Hyperon Production in Proton-Nucleus Collisions at a Center-of-Mass Energy of $\sqrt{s_{NN}} = 41.6$ GeV at HERA-B and Design of Silicon Microstrip Detectors for Tracking at LHCb

Dissertation

zur Erlangung des Doktorgrades
des Fachbereichs Physik der Universität Dortmund
ausgeführt am
Max-Planck-Institut für Kernphysik, Heidelberg

vorgelegt von
Michaela Agari
aus Gießen

Heidelberg
Juli 2006

Zusammenfassung

Themen dieser Arbeit sind Messungen von Hyperonenproduktion in Proton-Kern-Wechselwirkungen bei $\sqrt{s} = 41.6$ GeV mit dem Hera-B-Detektor am DESY, Hamburg, und das Design von Siliziumstreifensensoren für das LHCb-Experiment am CERN, Genf (Schweiz).

Λ, Ξ und Ω Hyperonen und ihre Antiteilchen wurden in $113.5 \cdot 10^6$ inelastischen Wechselwirkungen von Protonen mit festen Kohlenstoff-, Titan- und Wolfram-Targets rekonstruiert. Mithilfe dieser Datensätze konnten Antiteilchen-zu-Teilchen-Verhältnisse, Wirkungsquerschnitte sowohl über den kinematischen Messbereich von Hera-B integriert als auch differenziell als Funktion des Transversalimpulses, $d\sigma/dp_T^2$ (für Λ und Ξ), und der Rapidität, $d\sigma/dy$ (nur für Λ), gemessen werden, sowie die Abhängigkeit dieser Messgrößen von der Massenzahl des Targetkerns, parametrisiert nach dem Glauber-Modell. Die gemessenen Verhältnisse folgen dem gleichen Trend wie die Energieabhängigkeit der entsprechenden Messungen in Kern-Kern-Wechselwirkungen.

Silizumstreifensensoren wurden für das Spurrekonstruktionssystem des LHCb-Detektors entwickelt. Unter Zuhilfenahme von am CERN durchgeführten Strahltests wurde der Einfluss der Streifengeometrie und der Substratdicke auf die Eigenschaften des Sensors ermittelt, um das Optimum unter den gegensätzlichen Erfordernissen eines hohen Signal-zu-Rauschen-Verhältnisses, einer kleinen Anzahl an Auslesekanälen und einer niedrigen Spurbelegungsdichte zu erzielen. Der Detektor befindet sich momentan in der Bauphase, der Beginn des Messbetriebs ist für Herbst 2007 geplant.

Abstract

The topics of this thesis are the measurements of hyperon production in proton-nucleus collisions at $\sqrt{s} = 41.6$ GeV with the Hera-B detector located at DESY, Hamburg (Germany), and the design of silicon microstrip sensors for the LHCb experiment at CERN, Geneva (Switzerland).

Λ, Ξ and Ω hyperons and their antiparticles were reconstructed from $113.5 \cdot 10^6$ inelastic collisions of protons with fixed carbon, titanium and tungsten targets. With these samples, antiparticle-to-particle ratios, cross sections integrated for the accessible kinematic region of Hera-B and single differential cross sections as function of transverse momentum, $d\sigma/dp_T^2$ (for Λ and Ξ) and rapidity, $d\sigma/dy$ (for Λ only), have been been measured as well as the dependence of these quantities on the atomic number of the target nucleus, as parameterized using the Glauber model. The obtained ratios follow the same trend as found for the energy dependence of measurements from nucleus-nucleus collisions.

Silicon microstrip sensors have been designed for the tracking system of the LHCb detector. Evaluating the performance in beam tests at CERN, the strip geometry and sensor thickness were varied optimizing for a large signal-to-noise ratio, a small number of read-out channels and a low occupancy. The detector is currently being built to be operational for first proton-proton collisions in autumn 2007.

Contents

1 Introduction **1**
1.1 The Standard Model 1
1.2 Thesis Overview 3

2 CP Violation: Theory and Experiment **5**
2.1 The HERA-B Experiment 9
2.2 The HERA-B Detector 11
  2.2.1 The subdetectors 11
  2.2.2 The trigger and data acquisition systems 16
  2.2.3 Event reconstruction 21
2.3 The LHCb Experiment 25
2.4 The LHCb Detector 29
  2.4.1 The subdetectors 29
  2.4.2 The trigger and data acquisition systems 33
  2.4.3 The LHC Computing Grid 36

3 Silicon Sensors for the LHCb Tracking System **39**
3.1 Silicon Strip Detectors 40
  3.1.1 Signal Generation 40
  3.1.2 Noise 44
  3.1.3 Radiation Hardness 45
3.2 Detector Layout and Design Issues 48
  3.2.1 The Inner Tracker 49
  3.2.2 The Trigger Tracker 50
  3.2.3 Read-out Electronics 51
3.3 Sensor Design 53
  3.3.1 Beam Tests 54
  3.3.2 Laser Tests 57
  3.3.3 Radiation hardness tests 59
  3.3.4 Final sensor layout 59
3.4 Preparation and Analysis of Beam Test Measurements 60
  3.4.1 Design of a test set-up for prototype modules 60
  3.4.2 Software framework for beam test data analysis 63
  3.4.3 BEETLE chip pipeline homogeneity 65

4 Hyperon Production in pA collisions 75
- 4.1 Hyperon Production and Quark-Gluon Plasma . . . 76
  - 4.1.1 Hyperon Production in Proton-Nucleus Collisions . . . 76
  - 4.1.2 Quark-Gluon Plasma . . . 81
  - 4.1.3 Experimental Results for QGP . . . 86
- 4.2 Hyperon Reconstruction at HERA-B . . . 87
  - 4.2.1 The "Golden Minimum Bias" Data Sample 2002/2003 . . . 87
  - 4.2.2 Monte Carlo simulation . . . 88
  - 4.2.3 Signal preparation . . . 92
  - 4.2.4 Acceptance correction . . . 98
  - 4.2.5 Systematic errors . . . 109
  - 4.2.6 Antiparticle/Particle ratios . . . 123
  - 4.2.7 Inclusive cross section measurements . . . 127
  - 4.2.8 Differential cross sections . . . 131
  - 4.2.9 Cronin Effect . . . 140

5 Summary and Outlook 143

A List of Used Runs 147

Bibliography 160

List of Figures

2.1 The unitarity triangle. 7
2.2 Fitted constraints of the CKM triangle. 8
2.3 HERA-B: schematic view of the detector. 11
2.4 HERA-B: schematic view of the target. 12
2.5 HERA-B: Vertex detector system. 13
2.6 HERA-B: Outer Tracker, sketch of a honeycomb drift chamber. . . . 14
2.7 HERA-B: sketch of the RICH detector. 15
2.8 HERA-B: Schematic view of an ECAL module. 16
2.9 HERA-B: Isometric view of the muon system. 17
2.10 HERA-B: Sketch of the pretrigger conditions. 17
2.11 HERA-B: First Level Trigger, functional view 19
2.12 HERA-B: Sketch of the matching procedure of track segments. . . . 24
2.13 LHCb: Possible New Physics contributions in $B_d \rightarrow \Phi K_s^0$. 27
2.14 LHCb: Polar angles of $b\bar{b}$ pairs. 29
2.15 LHCb: schematic overview of the detector. 30
2.16 LHCb: Vertex Locator, r and ϕ sensor geometries 30
2.17 LHCb: Vertex Locator, schematic view of the vacuum vessel. 31
2.18 LHCb: Schematic view of the RICH detecors. 32
2.19 LHCb: Schematic view of the tracking system. 33
2.20 LHCb: Schematic view of the Electromagnetic Calorimeter. 34
2.21 LHCb: schematic view of the Muon system. 35
2.22 LHCb: Overview of the three trigger levels. 37

3.1 Landau distribution. 42
3.2 Layout of a silicon micro-strip sensor. 48
3.3 Two-sensor module of the LHCb Inner Tracker. 50
3.4 Front-end hybrid with three BEETLE chips. 50
3.5 Schematic view of the LHCb Inner Tracker boxes. 51
3.6 Layout of the LHCb Trigger Tracker. 52
3.7 Signal pulseshape with 500 μm sensor and BEETLE 1.2. 55
3.8 Signal-to-noise ratio with 500 μm sensor and BEETLE 1.2. 56
3.9 Signal-to-noise ratio as function of the inter-strip track impact. . . . 57
3.10 Testbeam set-up in an aluminum box. 58
3.11 Layout of the test beam set-up box. 62
3.12 Correlation of the ADC values of strips and neighbouring strips. . . 68

3.13 Pipeline structure of the Beetle 1.2. 69
3.14 Comparison of common mode noise and pipeline inhomogeneity. 70
3.15 Comparison of a calibration strip with others. 71
3.16 Pedestal values of first and last Beetle channels. 71
3.17 Total noise values of first and last Beetle channels. 72
3.18 Screen shot of the last channels of a Beetle chip. 73

4.1 Leading Feynman diagrams for $s\bar{s}$ production. 80
4.2 Phase diagram of matter. 82
4.3 Space-time evolution after an AA collision. 82
4.4 Examples of the data quality monitoring. 89
4.5 Comparison of real data taking and Monte Carlo simulation. 91
4.6 Event topologies of the hyperon decays under study. 95
4.7 Armenteros-Podolansky plot for K_S^0 and Λ. 96
4.8 Invariant mass spectra of $\Lambda/\bar{\Lambda}$ candidates. 99
4.9 Fitted invariant mass spectra of $\Lambda/\bar{\Lambda}$ candidates. 100
4.10 Invariant mass spectra of $\Xi/\bar{\Xi}$ candidates. 101
4.11 Fitted invariant mass spectra of $\Xi/\bar{\Xi}$ candidates. 102
4.12 Invariant mass spectra of $\Omega/\bar{\Omega}$ candidates. 103
4.13 Fitted invariant mass spectra of $\Omega/\bar{\Omega}$ candidates. 104
4.14 $\Lambda/\bar{\Lambda}$ reweighting as function of p_T^2 and rapidity. 108
4.15 $\Xi/\bar{\Xi}$ reweighting as function of p_T^2. 109
4.16 Λ acceptance as function of p_T^2 and rapidity. 110
4.17 $\bar{\Lambda}$ acceptance as function of p_T^2 and rapidity. 111
4.18 $\Xi/\bar{\Xi}$ acceptance as function of p_T^2. 112
4.19 p_T^2, y and x_F in data and Monte Carlo for $\Lambda/\bar{\Lambda}$. 115
4.20 $c\tau$ and ϕ in data and Monte Carlo for $\Lambda/\bar{\Lambda}$. 116
4.21 p_T^2, y and x_F in data and Monte Carlo for $\Xi/\bar{\Xi}$. 117
4.22 $c\tau$ and ϕ in data and Monte Carlo for $\Xi/\bar{\Xi}$. 118
4.23 Variation of the selection cut parameters for $\Lambda/\bar{\Lambda}$. 120
4.24 Variation of the selection cut parameters for $\Xi/\bar{\Xi}$. 121
4.25 Variation of the selection cut parameters for $\Xi/\bar{\Xi}$. 122
4.26 $\frac{\bar{\Lambda}}{\Lambda}$ at mid-rapidity vs $\sqrt{s_{NN}}$. 125
4.27 $\frac{\bar{\Lambda}}{\Lambda}$, $\frac{\bar{\Xi}}{\Xi}$ and $\frac{\bar{\Omega}}{\Omega}$ at mid-rapidity. 126
4.28 $\frac{\Xi}{\Lambda}$, $\frac{\bar{\Xi}}{\bar{\Lambda}}$, $\frac{\Omega}{\Xi}$ and $\frac{\bar{\Omega}}{\bar{\Xi}}$ at mid-rapidity. 126
4.29 A-dependence of the hyperon production cross sections. 128
4.30 Stability of the $\Lambda/\bar{\Lambda}$ cross section with time. 129
4.31 Stability of the $\Xi/\bar{\Xi}$ cross section with time. 130
4.32 $\Lambda/\bar{\Lambda}$ production cross section as function of p_T^2. 134
4.33 $\Lambda/\bar{\Lambda}$ production cross section as function of y. 135
4.34 $\Xi/\bar{\Xi}$ production cross section as function of p_T^2. 136
4.35 $\Xi/\bar{\Xi}$ production cross section as function of y. 137
4.36 $\Lambda/\bar{\Lambda}$: Effect of acceptance correction on the p_T^2 distribution. 138
4.37 $\Lambda/\bar{\Lambda}$: Effect of acceptance correction on the y distribution. 139
4.38 Atomic number dependence of the cross sections vs p_T^2. 141
4.39 Atomic number dependence of the cross sections vs rapidity. 142

List of Tables

1.1 The fundamental interactions 1
1.2 The fundamental particles 2

2.1 HERA-B: Target wire configuration in 2002/2003. 12
2.2 HERA-B: Overview of the trigger levels. 18
2.3 Annual signal yields of important B decay channels. 28

3.1 Geometrical parameters of the final sensor layout. 60

4.1 Ground state hyperons and their properties. 80
4.2 Summary of the statistics of the GMB data set. 88
4.3 Statistics of Monte Carlo generated events for. 93
4.4 Optimized selection criteria for the hyperon candidates. 105
4.5 Signal yields of reconstructed hyperons. 105
4.6 Total hyperon acceptances in the considered kinematic range. 112
4.7 Systematic error contribution from the comparison with MC. 114
4.8 Systematic error contribution from the variation of the selection cuts. 119
4.9 Hyperon production ratios. 124
4.10 Hyperon production cross sections. 131
4.11 A-dependence of the hyperon production cross sections. 131
4.12 Results of fits to the differential p_T^2 spectra. 132
4.13 $\Lambda/\bar{\Lambda}$ production cross sections at mid-rapidity. 133

A.1 List of runs used in this analysis. 149

Chapter 1

Introduction

1.1 The Standard Model

The current knowledge of fundamental particles and their interactions is summarized in the so-called Standard Model. It comprises the theory of strong interactions (quantum chromodynamics or QCD) and the unified theory of weak and electromagnetic interactions (electroweak theory). The fundamental forces are described by the exchange of mediating quanta, which are listed in Tab. 1.1[1]. These quanta are bosons, i.e particles with integral spin, whereas the other fundamental particles, quarks and leptons, are fermions and have half-integer spin. When quarks and leptons are arranged in terms of mass and charge (see Tab. 1.2, a pattern emerges: They group into three quark and lepton pairs, the so-called “families” or “generations”. Each quark pair comprises a quark carrying $+2/3$ of an elementary charge and one carrying the charge $-1/3$, while each lepton pair consists of a neutral particle, a neutrino, and a charged lepton. The number of leptons of one type (e, μ, τ) is conserved on the time scale of strong and weak interactions[2], but quarks can change into another type (the so-called flavour) through weak interactions. Quarks have never been

interaction	acts on	particles experiencing	particles mediating	mass (GeV/c^2)	J^P
gravitational	mass - energy	all	graviton (not yet observed)	0	2
strong	color charge	quarks, gluons	gluon (g)	0	1^-
electromagnetic	electric charge	electrically charged	photon (γ)	0	1^-
weak	flavour	quarks, leptons	W^+, W^-, Z^0	$\approx 10^2$	1

Table 1.1: The fundamental interactions

---

[1] Gravity is not part of the Standard Model.

[2] Measurements have found evidence for neutrino oscillations [Col01b]. Thus, the lepton number is not conserved in general.

found isolated, they are always confined in compound systems (hadrons). Hadrons are subdivided into two species: mesons and baryons. Since quarks carry the baryon quantum number $B = +1/3$ and antiquarks have $B = -1/3$, mesons, being composed of a quark and an antiquark have $B = 0$ and baryons, being assembled from three quarks, have $B = 1$. On earth, almost all baryonic matter consists only of the lightest quarks, u and d. The heavier quarks s, c, t and b can only be produced and studied in high energy experiments.

fermions	family			charge	color	weak isospin		spin
	1	2	3			left handed	right handed	
leptons	ν_e	ν_μ	ν_τ	0	–	1/2	–	1/2
	e	μ	τ	-1			0	
quarks	u	c	s	$+2/3$	r, g, b	1/2	0	1/2
	d	s	b	$-1/3$			0	

Table 1.2: The fundamental particles

Symmetries

In physics, the invariance of an observable under a symmetry transformation corresponds to a conservation law. For example, the invariance under translation in space is connected with the conservation of momentum. So, if a conservation law is found to be valid, conclusions about the nature of an interaction can be drawn [Per00]. The following three symmetry transformations play an important role in particle physics:

- **Charge conjugation *C*:** Transformation of all charge-like quantum numbers Q into $-Q$.
- **Parity *P*:** Reflection of all spatial coordinates at the origin ($\vec{x} \to -\vec{x}$).
- **Time reversal *T*:** Inversion of the direction of the time axis ($t \to -t$).

Postulating only minimal physical assumptions like locality and causality, the product of C, P and T is proven to be a good symmetry, as formulated in the CPT theorem [Wei95]. Up to now no experiment has shown a violation of it. However, the violation of the C symmetry can be found weak interactions, e.g. in applying charge conjugation to a neutrino: Since the chirality (i.e. the direction of its spin with respect to its momentum) is not altered by the C transformation, a left-handed neutrino (i.e. a neutrino with its spin antiparallel to its momentum) would be turned into a left-handed antineutrino, which does interact according to the Standard Model.

In the 1950s, P violation was observed in β decays from Co^{60} [WS50, FT57]. Subsequently, it was assumed that symmetry of the product of the C and P transformation, CP, would hold. But in 1964, CP violation was first discovered in the system of neutral K mesons [C$^+$64]. Therefore, if the CPT theorem holds, then also the T symmetry must be violated.

Particle Physics and the Universe

CP violation is one of the key ingredients to explain the matter-antimatter imbalance of the universe: In the Big Bang, matter and antimatter were initially created in equal amounts. During the following evolution of the hot and dense matter in the very early universe, the baryogenesis, an asymmetry between baryons and antibaryons was generated. In 1967, A.D. Sakharov formulated the necessary conditions for this asymmetry [Sak67]. They are:

- baryon number violation,
- C- and CP-symmetry violation and
- thermal non-equilibrium.

For baryon number non-conservation, no experimental evidence has been found yet, and the discovery of CP violation was mentioned above. Thermal non-equilibrium is needed to make the rate of pair-annihilation different from the one for pair creation. In the Standard Model it is also needed to generate a phase transition which induces baryon number violation.

Another phenomenon closely related to cosmology is a state of matter called quark-gluon plasma (QGP). Here, the energy density is so high that quarks and gluons are no longer confined in hadrons. It is assumed that in the first tens of microseconds after the Big Bang this state of matter was present until the temperature dropped below a critical value and baryogenesis took place, transforming a small fraction of the energy into matter and antimatter. Today, many experiments try to reach the energy density necessary for the formation of QGP in relativistic heavy-ion collisions. The aim is to study the underlying processes and apply this knowledge to the cosmological models describing the Big Bang.

1.2 Thesis Overview

The topics discussed in this thesis are related to both phenomena mentioned above: Precise measurements of CP violation in the sector of B mesons (i.e. mesons containing a b or $\bar{b}$ quark) are the aim of the LHCb experiment currently being constructed at the Large Hadron Collider (LHC) at CERN. Among other requirements, a highly efficient track reconstruction is necessary in order to be able to reconstruct B mesons from many different decay channels in the large quantities needed for precision measurements. The designing and testing of silicon microstrip sensors for the tracking system was a major part of the R&D program carried out before the construction of the LHCb detector could begin.

Very similar to LHCb, the initial aim of the HERA-B experiment was to measure CP violation in the neutral B meson system. But the experimental challenges of high particles densities and track multiplicities were not met by the chosen technologies, therefore, the design performance of the detector was never reached, and the initial physics goals were abandoned. Nonetheless, measuring at an energy and kinematic region not covered by other experiments, the collaboration could still contribute to a wide range of topics in the field of QCD and heavy flavour physics. One of the topics is the production of hyperons, i.e. baryons containing one or more strange quarks. The creation of strange quark pairs in hadron collisions and their hadronization presents a benchmark test for QCD-based models as used in the Monte Carlo event generators PYTHIA [Sjö94] and FRITIOF [Pi92]. So far, no satisfactory quantitative agreement of the models with experimental data has been found [A$^+$03e]. Furthermore, an increased strangeness production rate has been proposed as one of the signatures of the formation of QGP, therefore reference measurements at all availabe energies and kinematic regions present an important input to the search for QGP.

In this thesis, contributions to the R&D for the Silicon Tracker of the LHCb experiment are presented. The analysis of a large minimum bias data sample recorded in 2002 with the HERA-B detector is explained in detail and results for the production of hyperons created in proton-nucleus collisions using three different target nuclei are given. The document is structured as follows:

- Chapter 2 introduces briefly to the theoretical and experimental aspects of CP violation measurements and provides descriptions of the LHCb and HERA-B experiments.
- In chapter 3, the functional principles of silicon micro-strip sensors are described, followed by a review of the R&D program carried out for the LHCb Silicon Tracker. Furthermore, contributions to the design, testing and characterization of the prototype sensors are summarized.
- The measurements of hyperon production cross sections, both integrated for the kinematic region accessible for the HERA-B experiment and differential as function of kinematic variables, particle to antiparticle ratios of the reconstructed hyperon species and A-dependences of the measured quantities are presented in chapter 4.
- Chapter 5 provides the reader with a summary and an outlook.

Chapter 2

CP Violation: Theory and Experiment

The source of CP violation according to the Standard Model is the mixing of quarks in electroweak interactions [Nac91]. The electroweak quark eigenstates d', s' and b' are mixtures of the mass eigenstates d, s and b, and the correlation between them is described by the Cabibbo-Kobayashi-Maskawa (CKM) matrix [KM73]:

$$\begin{pmatrix} d' \\ s' \\ b' \end{pmatrix} = \begin{pmatrix} V_{ud} & V_{us} & V_{ub} \\ V_{cd} & V_{cs} & V_{cb} \\ V_{td} & V_{ts} & V_{tb} \end{pmatrix} \begin{pmatrix} d \\ s \\ b \end{pmatrix} \equiv \mathbf{V}_{CKM} \begin{pmatrix} d \\ s \\ b \end{pmatrix} \tag{2.1}$$

The square of matrix element V_{ij} is proportional to the transition probability of a quark of the type i into a quark of the type j by weak charged currents. Therefore, the CKM matrix has to be unitary.

One example for the mixture of quark flavours is the system of neutral B mesons[1]. Here, the mass eigenstates B_L ("light") and B_H ("heavy") can be written in terms of the flavour eigenstates B^0 and $\bar{B}^0$ as

$$|B_L\rangle = \quad p|B^0\rangle + q|\bar{B}^0\rangle, \tag{2.2}$$

$$|B_H\rangle = \quad p|B^0\rangle - q|\bar{B}^0\rangle, \tag{2.3}$$

where p and q obey the normalization condition

$$|q|^2 + |p|^2 = 1. \tag{2.4}$$

If $|q/p| = 1$, the mixture is maximal. An arbitrary linear combination of neutral B meson eigenstates,

$$a|B^0\rangle + b|\bar{B}^0\rangle, \tag{2.5}$$

is governed by a time-dependent Schrödinger equation

$$i\frac{d}{dt}\begin{pmatrix} a \\ b \end{pmatrix} = H \begin{pmatrix} a \\ b \end{pmatrix} \equiv (M - \frac{i}{2}\Gamma) \begin{pmatrix} a \\ b \end{pmatrix} \tag{2.6}$$

---

[1] For simplicity reasons, B^0 is used instead of B_d^0 sometimes in this thesis.

where M and Γ are 2×2 Hermitean matrices. A general time-dependent solution can be obtained with the ansatz $|B\rangle = a_H(t)|B_H\rangle + a_L(t)|B_L\rangle$ where

$$a_H(t) = a_H(0)e^{-iM_H t}e^{-\frac{1}{2}\Gamma_H t}, \; a_L(t) = a_L(0)e^{-iM_L t}e^{-\frac{1}{2}\Gamma_L t} \tag{2.7}$$

are the amplitudes of the two components. Thus, a state which is created as initially pure B^0 (at time $t = 0$, denoted as $|B^0_{phys}\rangle$), evolves with time as given by

$$|B^0_{phys}(t)\rangle = g_+(t)|B^0\rangle + (q/p)g_-(t)|\bar{B}^0\rangle \tag{2.8}$$

$$|\bar{B}^0_{phys}(t)\rangle = (p/q)g_-(t)|B^0\rangle + g_+(t)|\bar{B}^0\rangle \tag{2.9}$$

where

$$g_+(t) = e^{-iMt}e^{-\Gamma t/2}\cos(\Delta m_B t/2) \tag{2.10}$$

$$g_-(t) = e^{-iMt}e^{-\Gamma t/2}\sin(\Delta m_B t/2) \tag{2.11}$$

and $M = \frac{1}{2}(M_H + M_L)$, $\Gamma = \frac{1}{2}(\Gamma_H + \Gamma_L)$ and $\Delta m_B = m_H - m_L$.

In the case of the B system, the ratio q/p which determines the mixture is approximately given by

$$\frac{q}{p} \approx -\frac{|M_{12}|}{M_{12}} \tag{2.12}$$

where M_{12} is a matrix element of the matrix M. Since this is close to unity and $\Delta\Gamma_B = (\Gamma_H - \Gamma_L) \ll \Delta m_B$, a neutral B meson can oscillate from a pure B^0 into a (nearly) pure $\bar{B}^0$ and back before it decays [HQ98].

Via the unitarity condition, the matrix elements of the CKM matrix are correlated with each other. In total there are four independent parameters, three real angles and one complex phase. For CP violation to occur, this phase has to be different from 0 and π. In the Wolfenstein parametrization, the CKM matrix is expanded in terms of $\lambda = V_{us} = \sin\theta_C \approx 0.22$ where θ_C is the Cabibbo angle [Wol83]:

$$\mathbf{V}_{CKM} = \begin{pmatrix} 1-\frac{1}{2}\lambda^2 & \lambda & \lambda^3 A(\rho - i\eta) \\ -\lambda & 1-\frac{1}{2}\lambda^2 & \lambda^2 A \\ \lambda^3 A(1-\rho-i\eta) & -\lambda^2 A & 1 \end{pmatrix} + \mathcal{O}(\lambda^4), \tag{2.13}$$

where the three new parameters A, ρ and η are fixed by choosing $V_{cb} = \lambda^2 A$ and $V_{ub} = \lambda^3 A(\rho - i\eta)$. This representation shows the relative coupling strength between the different quark flavours.

From the unitarity of the CKM matrix, relations like the following can be obtained:

$$V_{ud}V^*_{ub} + V_{cd}V^*_{cb} + V_{td}V^*_{tb} = 0. \tag{2.14}$$

Omitting terms of $\mathcal{O}(\lambda^5)$ in equation (2.14) yields

$$V^*_{ub} - \lambda V^*_{cb} + V_{td} \approx 0. \tag{2.15}$$

This relationship can be visualized in a so-called unitarity triangle in the complex plane (Fig. 2.1) with the parameters ρ and η on the axes. Other relations from

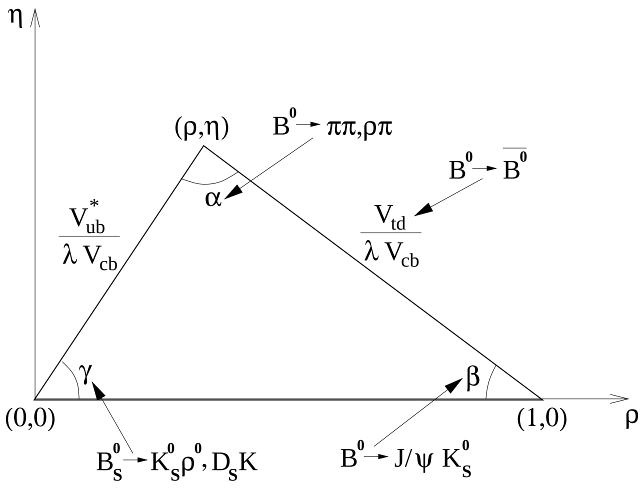

Figure 2.1: The unitarity triangle. Ways to access angles and side lengths are indicated.

the CKM matrix lead to similar triangles, all having the same area. In the case of CP invariance, this "CP violation area" would collapse to zero. The angles of the unitarity triangle can be extracted from special decay channels, some of them are also shown in Fig. 2.1. The one which is accessible most easily is the "gold-plated" decay $B^0/\bar{B}^0 \to J/\Psi K_s^0$ where both the B^0 meson and its antiparticle decay into the same CP eigenstate [BF98]. In this decay, no hadronic uncertainties are present which could spoil the precision of the measurement. The observed asymmetry A_{CP} of decay rates of particle and antiparticle (equation 2.16) yields the angle β of the unitarity triangle:

$$A_{CP}(t) = \frac{\Gamma\left(B^0(t) \to J/\Psi K_s^0\right) - \Gamma\left(\bar{B}^0(t) \to J/\Psi K_s^0\right)}{\Gamma\left(B^0(t) \to J/\Psi K_s^0\right) + \Gamma\left(\bar{B}^0(t) \to J/\Psi K_s^0\right)} = -\sin(2\beta)\sin(\Delta m_d t). \tag{2.16}$$

Here Δm_d is the mass difference between the B^0 and $\bar{B}^0$ mesons which determines the oscillation frequency between the two particles. This B^0 - $\bar{B}^0$ mixing was first observed by the ARGUS and CLEO collaborations [A$^+$87, A$^+$93].

Since both the B^0 and its antiparticle decay into the same final state, a means to distinguish B^0 and $\bar{B}^0$ decays had to be found. The so-called flavour-tagging exploits the fact that b quarks are produced in $b\bar{b}$ pairs. Hence, the flavour of one detected B meson determines the flavour of the other B. In addition to the reconstruction of the decay of one B into $J/\Psi K_s^0$, one has to identify a decay product of the other B meson, e.g. a lepton or a kaon. From the charge of the lepton or kaon, the flavour of this second B can be deduced. If the charge is negative, then the second B must contain a b quark; thus, the reconstructed signal B must contain a $\bar{b}$ and is therefore a B^0 and vice versa. Of course, this flavour-tagging is never perfectly efficient, hence an unavoidable fraction of mistags dilutes the purity of the samples of reconstructed decays.

A summary of ways to assess other parameters which constrain the CKM triangle can be found in [C$^+$05] together with a fit using results presented before or at the

FPCP conference in 2006. This fit is shown in Fig. 2.2, where the red-bordered area represents the allowed region for the top corner of the triangle, given by $(\bar{\rho}, \bar{\eta})$. The complementary area is excluded by the current experimental knowledge at 95 % confidence level. The purpose of this visualization of the measurements is to show whether or not the results are all compatible with the Standard Model description of CP violation. If the triangle would not close e.g. because the measured angles do not add up to 180°, then the Standard Model cannot account properly for the observed strength of CP violation and it has to be extended accordingly.

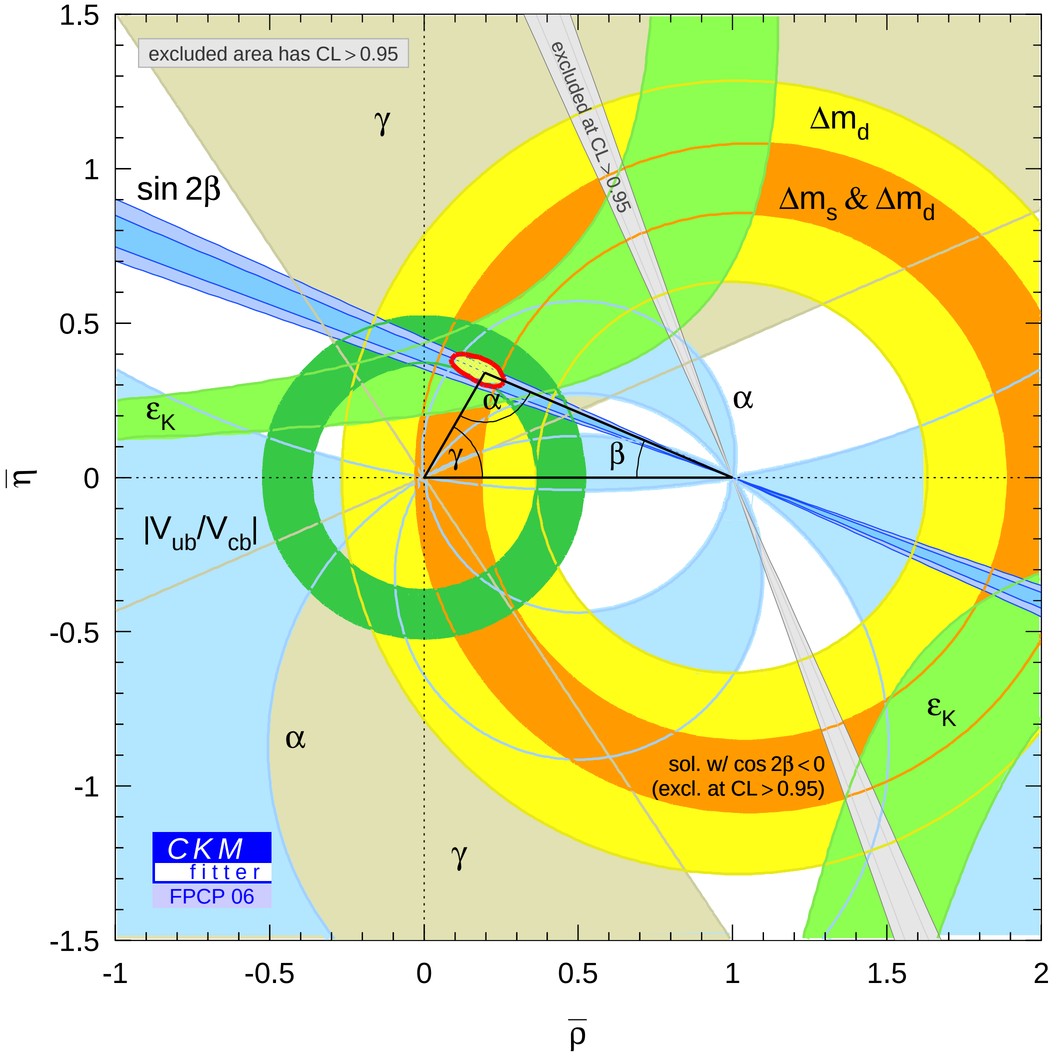

Figure 2.2: Fitted constraints of the CKM triangle. The constraints were deduced from results published before or at the FPCP conference, Canada, in 2006 [C+05]. The area outside of the red bordered region is excluded at 95 % confidence level.

2.1 The HERA-B Experiment

HERA-B was proposed in 1994 as a fixed target experiment at the HERA proton ring to study CP violation in the B meson system [A+94]. B mesons were produced in proton nucleon collisions at a center-of-mass energy of $\sqrt{s} = 41.6$ GeV. An interaction rate of 40 MHz, corresponding to a production rate of $b\bar{b}$ pairs of approximately 20 Hz, was envisaged in order to compete with the B factories BELLE and BABAR. The accompanying high particle densities and track multiplicities posed experimental and technological challenges that were unprecedented at that time, and the schedule was ambitous [A+95]. The foreseen interaction rate was never reached because some of the chosen technologies failed in the high radiation environment, and thus the detector and trigger system did not perform according to design values [HER00].

After the HERA upgrade shutdown in 2001, the detector was much improved compared to its status in 2000, but still not in the shape needed to compete with the B factories. However, since it was tuned for B physics, the energy and accessible kinematic range fills a gap left open by other experiments measuring pA collisions. Therefore it provides nonetheless the opportunity to contribute to a wide range of topics in the field of QCD and heavy flavour physics [HER00, col01a], as will be briefly summarized in the following.

- The production of J/Ψ and Υ decaying into e^+e^- or $\mu^+\mu^-$ pairs was studied [A+03b, A+06b]. The production rate of J/Ψ was measured relative to χ_c decays, while the Υ production rate was related to the J/Ψ production. In case of the Υ, the available statistics is small, but nonetheless, a value for the production cross section times branching fraction at mid-rapidity could be presented. Since the kinematic range of the detector acceptance lies in the central rapidity region, no systematic error due to extrapolation spoils the measurement. Therefore, the contribtutions are valuable, even for the small data sample in case of Υ.

- The production cross section of $b\bar{b}$ pairs was measured inclusively by searching for J/Ψs detached from the primary vertex which originate from the decay $b\bar{b} \to J/\Psi X$ where the J/Ψ subsequently decays into a lepton pair [A+03c, A+06a]. The results, together with the results of the J/Ψ and Υ production cross sections provide input to test models of heavy-quarkonium production.

- The production cross sections of the V^0 particles K^0_s, Λ and $\bar{\Lambda}$ [A+03a], as well as the polarization of Λ and $\bar{\Lambda}$ [A+06c], were measured as a function of the target material. The former results are important in the context of understanding production mechanisms in pA collisons. In the case of polarization, no existing model describes the observations, hence additional input from kinematic regions previously uncovered is very important.

- HERA-B could also contribute to the search for the flavour changing neutral current decay $D^0 \to \mu^+\mu^-$: An upper limit on the branching fraction for this decay modes was measured [A+04b]. In the Standard Model, the channel is strongly suppressed, but several extensions of it, including the Minimal Supersymmetric Standard Model, predict enhanced branching fractions, unfortunately still lower than the current experimental sensitivity.

- Upper limits for the central production of Θ^+ and Ξ^{--} pentaquarks[2] [A+04a] presented by the HERA-B collaboration were an important contribution since the paper was the first upper limit publication at variance with ten published papers claiming common production of either of the two particles. In the meantime, some more upper limits were published, questioning the discovery of the pentaquarks.

---

[2] Pentaquarks are baryons with at least five constituent quarks (four quarks and one antiquark, therefore the baryon number is unity).

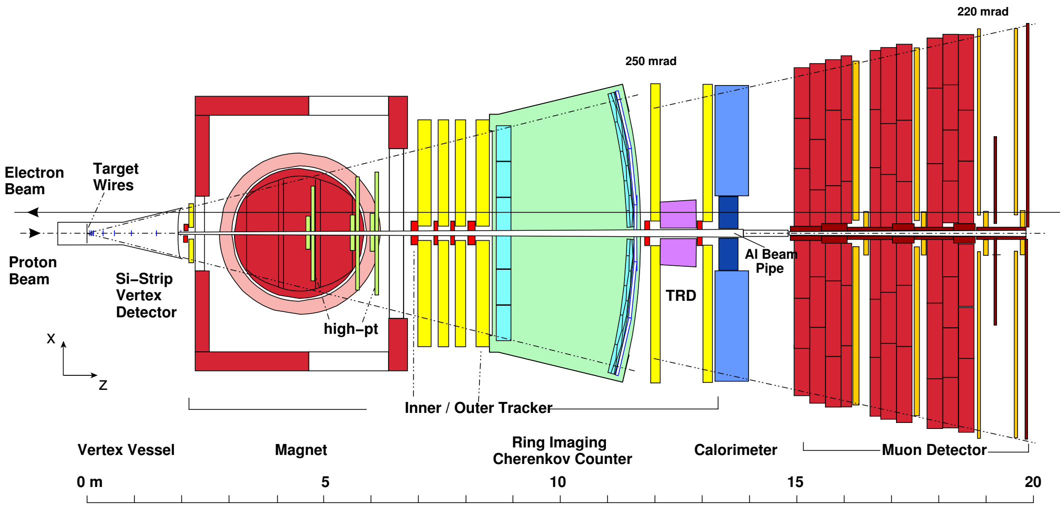

Figure 2.3: The HERA-B detector, schematic view

2.2 The HERA-B Detector

To measure the properties of the decay products from the beam target interaction, the HERA-B detector was built as a single-arm forward spectrometer. The aperture of the detector in the laboratory frame reaches from 15 up to 220 mrad. This corresponds to a solid angle coverage of 90% in the proton nucleon center-of-mass frame [A+95]. This large acceptance was originally forseen to enable the measurement of tracks with high transverse momentum which are common in B physics. But also other analyses profit now from the possibility to obtain measurements in the region of negative x_f values.

The coordinate system used in this thesis is defined as follows: The z axis points along the proton beam, y points upwards and x inwards with respect to the HERA ring, such that x, y and z form a righthanded coordinate system.

2.2.1 The subdetectors

The HERA-B detector consists of various subdetectors for tracking and particle identification purposes (Fig. 2.3). The main goal of the Vertex detector system (VDS) is to find and reconstruct primary and secondary vertices. The track parameters and momentum are obtained by matching track segments found in the VDS and the Inner and Outer Tracker (ITR and OTR) before and after the magnet. The aim of the High p_t chambers is to provide the trigger system with fast information about tracks with a high transverse momentum. Particle identification takes place in the Ring imaging Čerenkov counter (RICH). The energy of electrons and photons is measured in the electromagnetic calorimeter (ECAL). Muon candidates are identified and their track parameters are estimated (if needed for the trigger) with the muon system.

Wire Name	Material	Geometry
Inner 1	W	circular, diameter 50 μm
Outer 1	Ti	circular, diameter 50μm
Above 1	Al	ribbon, 50 $\times$ 500 μm^2
Below 1	C	ribbon, 100 $\times$ 500 μm^2
Inner 2	C	ribbon 100 $\times$ 500 μm^2
Outer 2	C	ribbon 100 $\times$ 500 μm^2
Above 2	Pd	circular, diameter 50 μm
Below 2	Ti	circular, diameter 50 μm

Table 2.1: Target wire configuration of the data taking period 2002/2003 [tar04]. The data used in this analysis were recorded with the target wires listed in bold print.

Target

HERA-B utilizes a wire target which is integrated into the detector and contained in the vacuum vessel of the Vertex detector system (see Fig. 2.5). By moving the target wires perpendiculary to the proton beam, the interaction rate can be adjusted to the desired level. To obtain a good spatial separation of the primary vertices, the target consists of two stations, each containing four independent wires, see Fig. 2.4 [Fun03]. In order to study nuclear dependences e.g. of quarkonium production, various wire materials are used. In Tab. 2.1, the wire configuration of the data taking period 2002/2003 is listed.

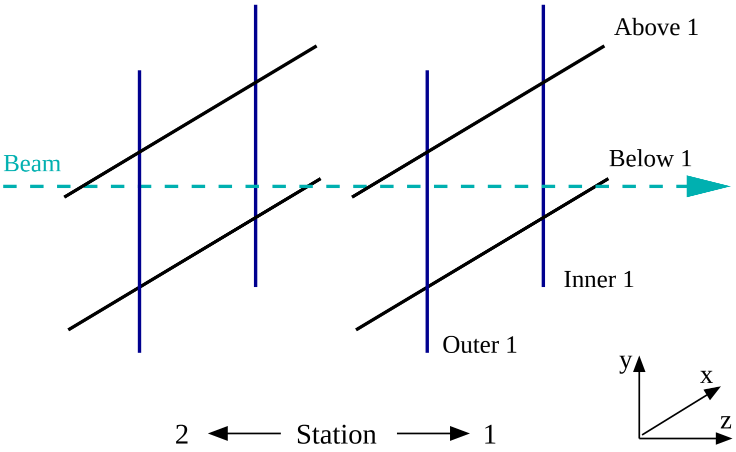

Figure 2.4: The HERA-B target, schematic view. The naming scheme of the target wires is indicated. The two stations are approximately 4 cm apart.

Vertex detector

The vertex detector system (Fig. 2.5) is situated directly behind the target (in z direction) and consists of 64 mostly double-sided silicon microstrip detector modules which are arranged in eight superlayers of four quadrants around the proton beam axis. The first seven superlayers are mounted inside the vacuum vessel in so-called

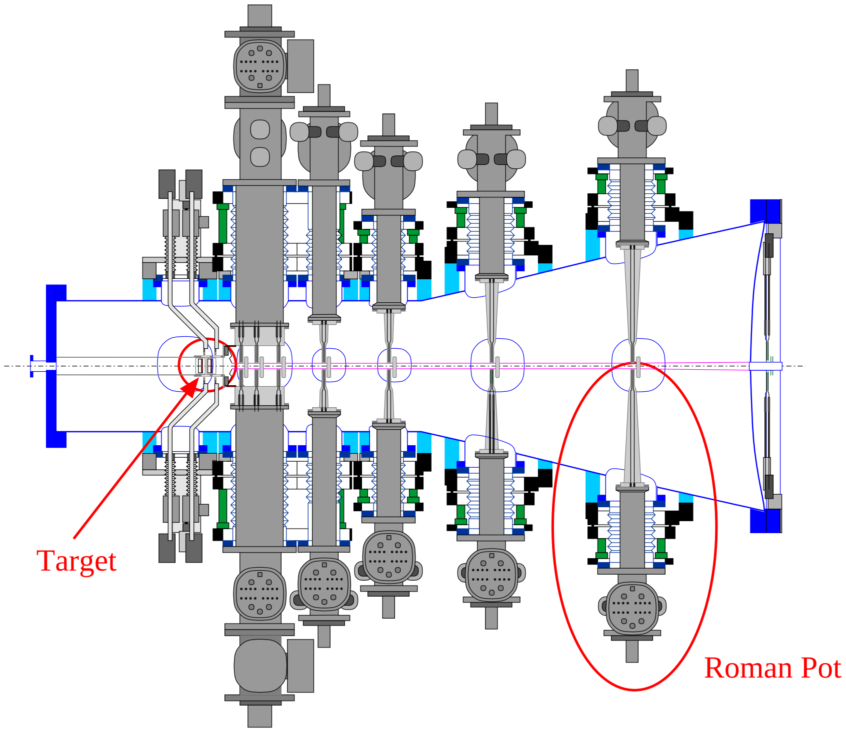

Figure 2.5: The Vertex detector system: the detector modules are mounted on roman pots located inside a vacuum vessel which also houses the target system (left).

roman pots [A$^+$03d]. The VDS provides a vertex resolution of $\mathcal{O}(700\ \mu\text{m})$ in the beam direction and of $\mathcal{O}(70\ \mu\text{m})$ perpendicular to the beam [HER00] which is needed to distinguish primary and secondary vertices. The high precision track information of the VDS is used at the higher trigger levels as well as in the offline analysis.

Magnet

To determine the track momentum, the spectrometer uses a dipole magnet of 2.2 Tm field integral. The momentum is calculated from the curvature in the xz plane of the particle trajectories in the magnetic field.

Main Tracker

In order to keep the occupancies below a level of 20 %, the main tracker is divided into parts with different granularity. The **Inner Tracker** covers a region of 6 - 30 cm around the proton beam, corresponding to polar angles between 10 and 100 mrad. It utilizes microstrip gas chambers combined with gas electron multiplier foils (MSGC-GEM) [B$^+$02a].

Originally, the Inner Tracker consisted of 48 detector modules in 10 supermodules, four of which were located inside the magnet. Since it proved difficult to integrate their data into the tracking algorithms, these were taken out during the HERA upgrade shutdown in 2001. Four of the remaining six supermodules are located between the magnet and the RICH and two between the RICH and the ECAL.

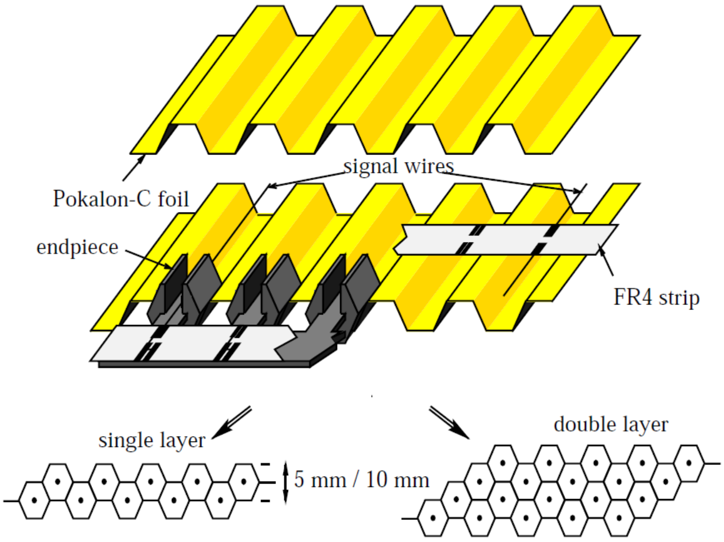

Figure 2.6: Schematic view of an Outer Tracker honeycomb drift chamber. Modules with cell heights of 5 mm (inner part) and 10 mm (outer part) are used.

Each supermodule consists of three layers which are rotated by 0° and ±5° about the y axis. The resulting spatial resolution is better than 100 μm in x direction and better than 1 mm in y direction.

The **Outer Tracker** uses honeycomb drift chambers [Ouc03]. Seven of the 13 superlayers used to be located inside the magnet (the so-called Magnet Chambers) but were taken out during the shutdown in 2001, four are placed in the field-free region between the magnet and the RICH (Pattern Chambers, PC) and two between RICH and ECAL (Trigger Chambers). Similar to the Inner Tracker, each superlayer is assembled of three layers rotated 0° and ±5° about the y axis. The OTR covers almost the whole geometrical acceptance of the experiment, down to 25 cm from the proton beam and up to the full aperture of 220 × 160 mrad. Using not only the spatial information but also the drift time[3] the measured hit resolution is 240 - 300 μm [HER00]. Four of the superlayers behind the magnet are also used in the First Level Trigger.

Ring Imaging Čerenkov counter

The ring imaging Čerenkov counter measures the velocity of charged particles close to the speed of light by utilizing the Čerenkov effect: Charged particles with a velocity $v > c/n$ passing through a medium with refractive index n emit a light cone with an opening angle $\cos\theta_C = c/nv$. Combined with the momentum of the particle, the particle mass can be calculated. The Čerenkov light is projected by a mirror system onto photomultipliers such that a given opening angle corresponds to a fixed ring radius (Fig. 2.7 (a)) [A$^+$04d]. The radiator medium of the HERA-B RICH is perfluorobutane gas (C_4F_{10}), resulting in an angular separation for particle

---

[3] The drift time is the time for the avalanche of electrons caused by a passing ionizing particle to reach the anode wire.

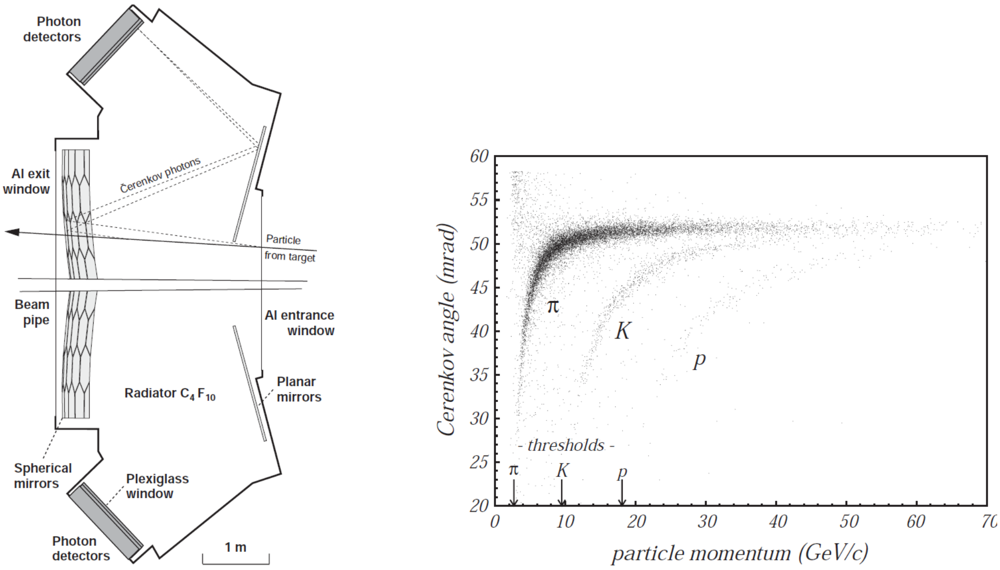

(a) (b)

Figure 2.7: The Ring Imaging Čerenkov Counter, schematic side view (a) and Čerenkov angles of various particles as function of momentum (b) [A$^+$04d].

momenta in the range from approximately 12 to 50 GeV/c as shown in Fig. 2.7 (b). For $\beta = 1$ particles, the Čherenkov angle is 51.5 mrad.

Electromagnetic calorimeter

The task of the electromagnetic calorimeter [A$^+$01] is to yield information about energy and position of electrons, positrons and photons. It provides fast pretrigger signals for the HERA-B trigger on single electrons or positrons or on electron/positron pairs coming from the J/Ψ decay. Furthermore, it offers an additional means for particle identification since it is designed to separate between hadrons and electrons.

The ECAL is a sampling calorimeter and has a modular structure of alternating layers of scintillator and converter materials, see Fig. 2.8. It consists of an inner, middle and outer part with different detector materials and granularities (decreasing from the inner to the outer regions. In the inner section, the containment depth is approximately 23 radiation lengths and the converter material is W-Ni-Fe metal alloy with a Molière radius[4] of about 1.3 cm, therefore the electromagnetic showers are deposited in a small spatial region. In the middle and outer sections, Pb is used as converter material, having a Molière radius of 3.5 cm and the containment is roughly 20 radiation lengths. The scintillation light is directed by wavelength shifting fibres to photomultipliers. The energy resolution of the ECAL is $\sigma(E)/E = (22.5 \pm 0.5)\%/\sqrt{E} \bigoplus (1.7 \pm 0.3)\%$ [HER00].

---

[4] The electromagnetic shower shape, to a good approximation, scales longitudinally with the radiation length, and laterally with the Molière radius.

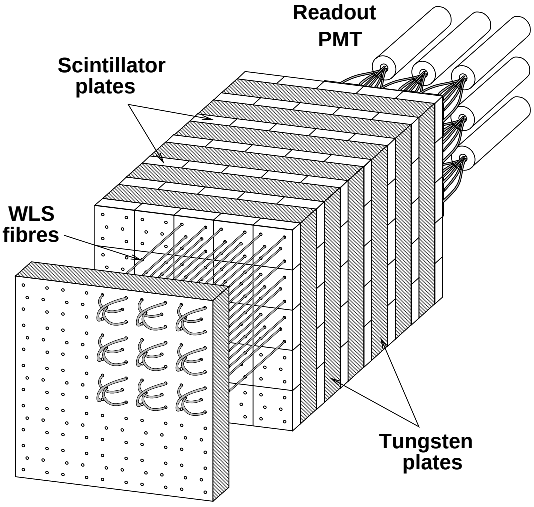

Figure 2.8: ECAL module: Scintillator and absorber layers are interleaved. Wavelength shifting fibres direct the scintillation light to the photomultipliers.

Muon system

The purpose of the muon system is to detect muons in the momentum range roughly from 4.5 GeV/c up to 200 GeV/c. Since the energy loss of muons in matter is very small compared to hadrons, a clean separation between the two can be obtained by placing an absorber of sufficient thickness in front of the muon detector planes.

The four superlayers of the muon system (MU1 - MU4) are divided into inner and outer parts; the former one covers the high occupancy region close to the beam pipe and consists of gas pixel chambers, and the latter covers polar angles up to 220 mrad in x direction and 160 mrad in y direction. The superlayers are interleaved with muon filters (iron and armored concrete blocks, MF1 - MF3 in Fig. 2.9). In the outer parts proportional wire chambers are used, organized in tube and pad chambers. The first two superlayers, MU1 and MU2, utilize three stereo layers of tube chambers, tilted by $0°$ and $\pm 20°$, while MU3 and MU4 consist of pad chambers, which are used by the muon pretrigger [E+01].

2.2.2 The trigger and data acquisition systems

In order to enrich a certain type of events in the recorded data sample at high interaction rates, a sophisticated trigger scheme was designed. At the first stage, the current event is searched for a signature easy to recognize by one of the pretriggers, e.g. an electron, a muon, an electron/positron pair or a high p_T track. The following pretriggers were used during the 2002/2003 data taking period:

- **The electron pretrigger**
  To find an electromagnetic shower with a minimum transverse energy, each ECAL cell is put in coincidence with its eight direct neighbours (Fig. 2.10(a)).

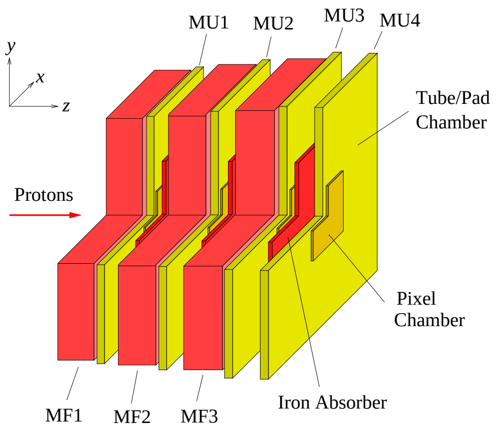

Figure 2.9: The muon system, isometric view (one quadrant omitted to provide an insight into the system.

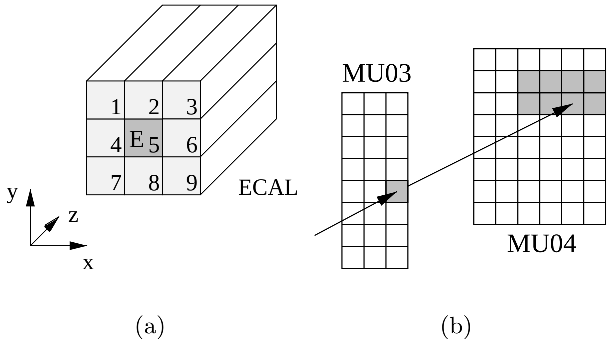

Figure 2.10: Sketch of the pretrigger conditions. The electron pretrigger searches for clusters where 50% of the energy is deposited in the central cell (a). The muon pretrigger picks up coincidences of hits in MU3 and MU4 (b).

If at least 50% of the energy of the cluster is deposited in the central cell and the total energy exceeds a threshold depending on the position of the cluster, then a trigger message is set off. The electron trigger can be used for triggering on electron/positron pairs e.g. from J/Ψ decays or on single high-p$_t$ photons or electrons.

- **The muon pretrigger**
  Looking for coincidences of hits on two pads in the muon chambers MU3 and MU4, the muon pretrigger detects three-dimensional muon track seeds (Fig. 2.10 (b)). The origin of the muon trajectories is required to be compatible with the target region.

During the following four trigger stages, the trigger decision (i.e. whether to keep the current event or not) is refined and the event is reconstructed in more and more detail. When the **First Level Trigger** (FLT) receives a message from one of the pretriggers search windows, the so-called "Regions of Interest" (RoI),

Level	Input	Latency	Reduction	Method
1	10 MHz	10 μs	200	Tracking, high p_t, di-lepton mass
2	20 kHz	$<$ 7 ms	100	Track re-fit, magnet tracking, vertexing
3	200 Hz			Event building

Table 2.2: Overview of the HERA-B trigger levels. Input rates, latency and reduction factors are listed together with the filter method used by each trigger stage [Sch06].

are defined. Then a coarse but fast track search is performed, starting from the RoIs found by the pretriggers and extrapolating the track seed towards the target region. After applying cuts on the transverse momentum and the invariant mass of track pairs, the remaining events are passed to the **Second Level Trigger** (SLT). Using the RoIs of the FLT, the SLT requests additional data and refines the trigger decision by utilizing the full chamber resolution and adding information of detector planes which are not connected to the FLT. After the SLT stage, the data from the complete detector are collected and the reconstructed event is written to storage.

An overview of the trigger levels, their input rates, computation times (i.e. the latency) and reduction factors can be found in Tab. 2.2. In case of the Minimum Bias data (see section 4.2.1), an interaction trigger was applied in order to reduce the fraction of empty events with respect to a purely random trigger, and the data were written to tape with a rate of 1kHz.

The First Level Trigger

Many of the track seeds from the pretriggers are caused by random coincidences or photon showers without an associated track. The FLT prolongates the track seeds and cluster candidates assuming their origin in the target region by adding hit information from selected superlayers behind the magnet. Since this has to be done very fast, the FLT is built as a network of specialized hardware boards, the so-called Track Finding Units (TFU), with data links for message exchange. Each TFU is assigned to a particular detector region, of which it receives hit information synchronously with each bunch crossing. When a pretrigger detects a signal, it sends a message to the corresponding TFU, which verifies the trigger decision, calculates the RoI for the next selected superlayer if necessary and sends a message to the TFU which is responsible for this region. This process is called FLT tracking, it ends when all selected layers behind the magnet are crossed or if a TFU cannot find a hit in the RoI on its detector plane. When a track has been confirmed a message is send to a Track Parameter Unit (TPU) which estimates the track parameters and rejects multiple reconstructed tracks (in cases of ambiguity). The trigger decision is taken by the Trigger Decision Unit (TDU) based on the track parameters, either on the number of reconstructed tracks (count trigger mode) or on kinematic properties, e.g. the invariant mass of track pairs (pair trigger mode). A functional view of the FLT network can be found in Fig. 2.11 [N02].

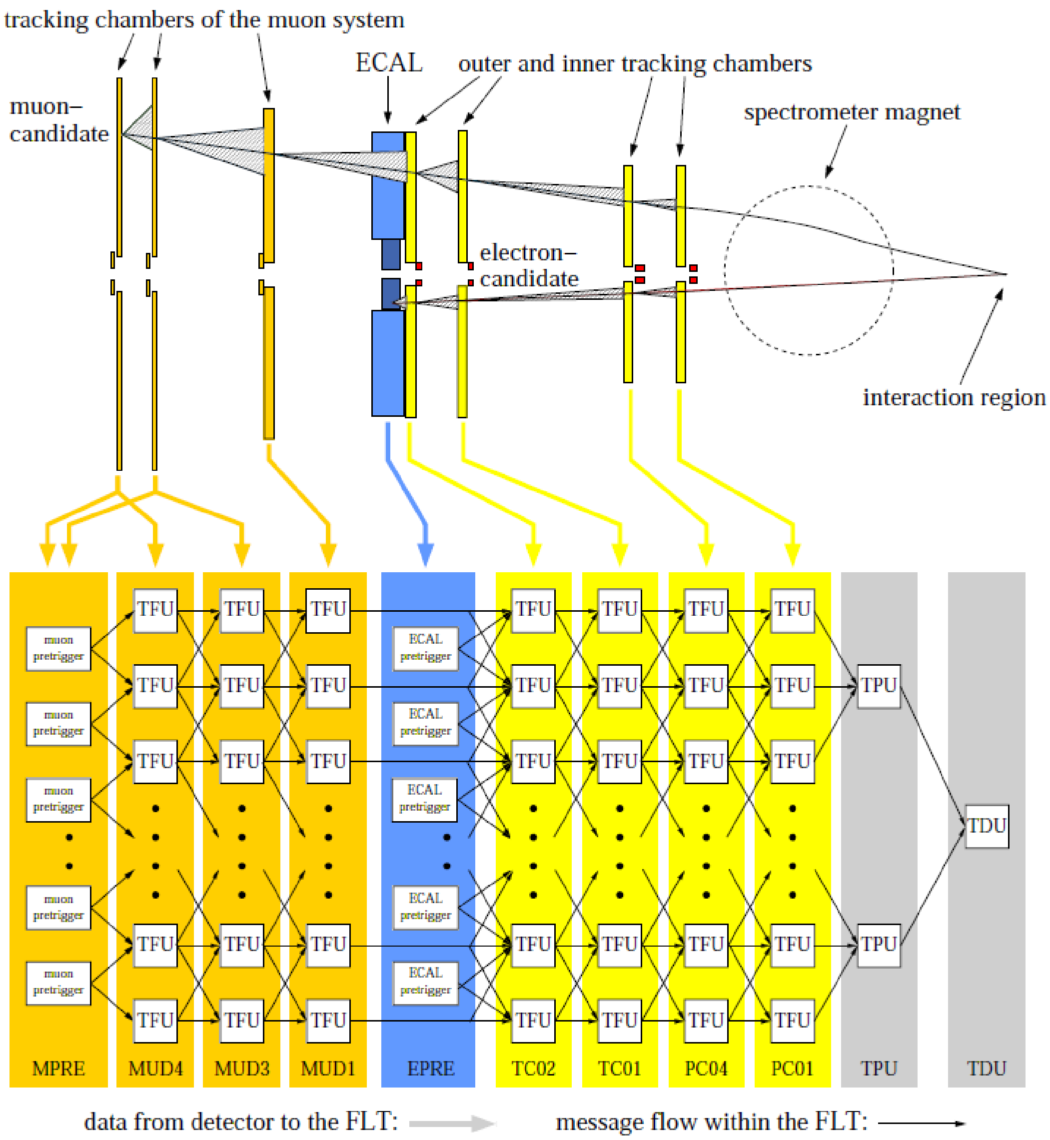

Figure 2.11: The First Level Trigger, functional view. The track search is based on pretrigger signals from the ECAL, the muon system or the high-p_t chambers (not shown in this picture). The corresponding TFU sends a message to the TFU which belongs to the next RoI, thus the tracks are extrapolated in target direction.

The Second and Third Level Trigger

Due to the course grained tracking done by the First Level Trigger, a large fraction of the track candidates are ghosts, i.e. combinations of hits belonging to different particles. In addition, most of the electron/positron pairs do not originate from the target but from photon conversions before or in the magnet. These events can be rejected by the SLT by performing the following steps [N+03]:

- The **Slicer** package requires that at least nine hits are found in four out of six superlayers and applies a fast pattern recognition in slices perpendicular to the xz plane, removing clone tracks.

- The **RefitX** and **RefitY** routines apply a simple Kalman filter method to refine the track candidates behind the magnet. The calculation is simplified by first using the hits in the horizontal plane that were already read out by Slicer (RefitX) and afterwards adding the y component determined from hits in the $\pm 5°$ stereo layers (RefitY). Only the best track candidates, according to their χ^2 and the number of crossed layers, are kept.

- The **L2Magnet** algorithm parametrizes the effective field integral of the magnet in terms of the track slopes and prolongates the track in an iterative procedure through the magnet towards the Vertex Detector.

- After the magnet, the track enters the VDS. Here, the **L2Sili** package takes care of the tracking, also using a Kalman filter algorithm. Tracks are kept if they have at least three hits in at least two superlayers both in x and y direction.

- Finally, for events with two trigger tracks coming from the same origin, the **L2Vertex** routine determines the vertex position and quality. Vertices of bad quality are discarded. Furthermore, it can be used to reject tracks from different wires when using multiple target wires.

The Third Level Trigger is the first system which has access to the data from every superlayer and is not restricted to information from the RoIs. Besides the option for refining the trigger decision, it does the so-called "event building", i.e. it assembles all data belonging to one event and sends them to the online reconstruction farm (4LT).

Instead of using specialized hardware, the Second and Third Level Trigger are implemented on a farm of 240 PCs which run a Linux operating system. This makes the system flexible, relatively cheap and easy to maintain.

The Fourth Level Trigger

At the Fourth Level Trigger the events accepted by SLT and TLT undergo a full reconstruction. If necessary for further suppression, the trigger decision can be refined once more by applying cuts on physical parameters. In addition event classification is performed and data for monitoring the performance, for calibration and for the detector alignment is collected. Finally accepted events are written to tape.

The data acquisition system

The data acquisition system (DAQ) is strongly interlaced with the trigger system. Its task is to move the event data from the detector to archive. At the same time, the synchronization of the subdetectors and their readout with respect to the bunch crossing of the proton beam has to be guaranteed. Handling 600000 readout channels at 10 MHz bunch crossing rate with a signal to background ratio of 10^{-10} the HERA-B DAQ resembles the systems designed for future LHC experiments. Its main parts are:

- The subdetector-specific front end driver boards (FED) provide a uniform interface, they send parts of the event data via the FLT to the **Fast Control System** (FCS), which in turn initiates the full readout of the data belonging to accepted events.
- Events which have been read out are buffered in the **Second Level Buffer** (SLB) where they are kept during the SLT step. It contains 1200 Digital Signal Processors (DSP)[5].
- As already mentioned, the SLT is implemented on a farm of 240 PCs with PCI interfaces to the DSPs, which run Linux as operating system. After being accepted by the SLT, all data of an event are extracted from the SLB via a switch by the event builder software (EVB) and submitted to the TLT process on the same CPU.
- After the TLT step, the data is transferred to the 4LT farm by a switched fast ethernet network for online reconstruction purposes. The 4LT farm is assembled of single and dual processor PCs with a total number of 200 CPUs, also running under Linux.

2.2.3 Event reconstruction

Both online and offline reconstruction of events at HERA-B are performed by ARTE, the Analysis and Reconstruction Tool [Art06]. While the online reconstruction is used for data quality monitoring (including e.g. invariant mass spectra of prevalent particles), the offline reconstruction prepares the information necessary for detailed analyses of the data. Track parameters are determined to the highest possible precision and every available information of the subdetectors is gathered. Apart from pure reprocessing, ARTE not only provides access to the data but also tools for the analysis itself.

ARTE, analysis and reconstruction tool

Before tracking programs can start their search for track patterns, the raw data from each subdetector system have to be prepared such that the detector information is translated into three-dimensional space points. For instance, in the case of the OTR, space points calculated from combined hit and drift time data (see page 14) are more precise than the hit information alone. In silicon detector layers and wire chambers, hits define only the position perpendicular to the silicon strips and wires, respectively. Here, three or more hits from differently oriented detector planes must be combined to form a space point.

---

[5] The DSPs are of the type ADSP-21060 SHARC. SHARC (Super Harvard Architecture) is a registered trademark of Analogue Devices Inc.

After the hit preparation, specialized software packages take care of the reconstruction of track segments, energy clusters in the ECAL and rings in the RICH. The detailed list of settings used for the second reprocessing can be found in [Rep06].

Software packages used in the forth and fifth reprocessing

- In the VDS, the **CATS** (Cellular Automaton for Tracking in Silicon) package [AKME02] uses a cellular automaton algorithm for pattern recognition. The track parameters are determined by a Kalman filter based fit method.
- Clusters of deposited energy in the ECAL are reconstructed by the **CARE** (Calorimeter Reconstruction) package. According to the amount of deposited energy and the distribution over the ECAL cells, the clusters are classified as electromagnetic or hadronic showers [A^+97].
- The track reconstruction in the main tracker is conducted by **OTR/ITR-CATS** [AEGK02] and **RANGER** [MS99]. In contrast to the VDS, track finding is more difficult due to the complicated geometry, the high occupancies and low efficiencies of the main tracker modules. Furthermore, a part of the main tracker is located inside the magnetic field. OTR/ITR-CATS utilizes a very similar algorithm as the CATS package for the VDS and performs the pattern recognition in the pattern tracker chambers (PC01-PC04, see Fig. 2.3). Due to detector inefficiencies that the algorithm can not handle, the resulting track segments do not always form complete tracks, therefore a simple track following mechanism combines corresponding segments before the tracks are prolongated into the trigger chambers by RANGER.

  Trigger tracks found by the Second Level Trigger are used as seeds for OTR/ITR-CATS in order to increase their reconstruction efficiency.
- The software package **RITER** [Pes01] is responsible for the particle identification with the RICH. RITER applies a track-based method: Starting from the center determined by a given track, RICH photons are histogrammed with respect to their radial distance to the center and weighted according to their significance. This is done in an iterative procedure for every charged track in the event, resulting in background-reduced picture of RICH rings. Together with the momentum information from the track, likelihoods for different particle hypotheses can be calculated.
- For the reconstruction of muon tracks, the **MUREC-B** (Muon Reconstruction) package [Fom99] is responsible. Reconstructed tracker segments are extrapolated by a Kalman filter algorithm into the Muon stations and hits inside search windows (accounting for the resolution of the extrapolation and for multiple scattering) are picked up. From the track fit and the number of associated hits, a likelihood for the track to be a muon track is calculated.
- The task of the **MARPLE** package is to match the track segments, ECAL clusters and RICH rings found in the subdetector systems into complete tracks. It comprises several subroutines specialized for matching of track segments of

different subdetectors or matching of segments with clusters or rings. E.g., for the matching of VDS and OTR Pattern Chamber segments, the coordinates and slopes are used to prolongate the segments into the middle of the magnet where cuts on the differences in x and y direction are applied (Fig. 2.12). Other matching procedures make use of momentum or energy information and the covariance matrices. The fitting procedure also employs a Kalman filter method [Igo98].

In this manner charged and neutral particles can be distinguished: Since only charged particles leave hits in the tracking devices, ECAL clusters without associated track segments can be regarded as belonging to neutral particles, in most cases photons.

- In many cases, the matching of the track segments is not unambiguous, i.e. one segment is shared between several tracks, the so-called clones. For physics analyses, this increases not only the combinatorics, which would be a nuisance in itself, but also contributes to the background: Since the reconstructed momenta of the tracks sharing e.g. a VDS segment are similar, they will also lead to similar invariant masses of the reconstructed particle under study. The tool **Cloneremove** [Ple01] selects among the clones the one with the best quality according to a figure of merit calculated from the number of hits in the subdectors, the presence of a RICH ring and an ECAL cluster and the number of degrees of freedom of the track fit. (In general, all tracks are kept in the data files, therefore, in contrast to the other software packages in this list, Cloneremove has to be applied each time the data are analysed.)

- The Vertexing package **Grover** [Eme02] searches for primary vertices[6] considering only tracks which have a maximal distance of $3.5\,\sigma$ to the target wire, where σ is the error of the intersection point of the track and the wire plane. The vertex fitting procedure employs a Kalman filter method taking only the geometrical track information into account, the track momenta are not used. To determine the precise target position in the coordinate system of the spectrometer, a wire-following procedure monitors the mean primary vertex position and utilizes it for internal alignment.

---

[6] The primary vertex finder of Grover uses the ROVER [E$^+$00] algorithm.

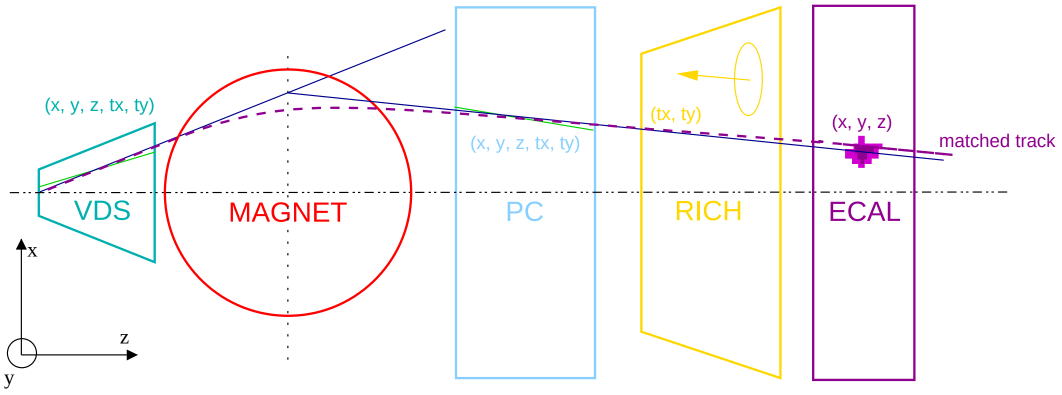

Figure 2.12: The matching of track segments. Track segments found in the VDS and the pattern chamber (PC) are prolongated to the middle of the magnet ($z = 4.55$ m) and cuts on the differences in x and y direction are applied.

2.3 The LHCb Experiment

LHCb is one of the four experiments currently being built at the Large Hadron Collider (LHC) at CERN. It was proposed in 1998 [LHC98] as a dedicated experiment to study CP violation in system of B mesons. While the dipole magnet is already installed and commissioned, all other subdetectors are being installed and expected to be ready for the first pp collisions in summer 2007 [LHC06]. The proton beams will collide head-on with a bunch crossing frequency of 40 MHz and an energy of 7 TeV each, resulting in a center-of-mass energy of 14 TeV.

The advantage of studying B physics at a hadron collider is that the visible cross section to produce $b\bar{b}$ pairs is relatively large: At LHCb, 10^{12} $b\bar{b}$ pairs are expected to be produced in one year of data taking[7], even though the luminosity will be kept at about $2 \cdot 10^{32}$ cm^{-2}s^{-1}, much lower than the luminosities foreseen for the other LHC experiments ATLAS and CMS. Since the center-of-mass energy is higher than those at the current B factories BABAR and BELLE, not only the light B mesons but also B_s and B_c (and their antiparticles) can be created. Thus, many other decay modes are assessible to measure different parameters of the Unitarity Triangle (UT). LHCb is designed to be able to determine all three angles with high statistics measurements. It will provide excellent tracking and vertexing precision, which is important for high mass and proper time resolutions, and an outstanding particle identification precision in order to distinguish between decay modes with similar topological signatures. Furthermore, the complete detector information is available at a relatively early trigger stage, thus many topological features of interesting decay modes can be used for the online event selection. At this stage, the trigger algorithms will run on a commodity computer farm, providing the flexibility to adapt the trigger criteria quickly to different physics goals.

LHCb will also contribute in the search for New Physics, not only because it can help to overconstrain the Unitarity Triangle by measuring all three angles, but it also offers redundant ways to measure the angles. Some of these ways are sensitive to New Physics, others are not, hence inconsistencies between redundant measurements could help to pin down an incompleteness of the Standard Model. Many proposed extensions to the Standard Model introduce new types of particles, which can influence the predicted rates for certain decays. In loop processes as depicted in Fig. 2.13(a), these possible new particles could appear as virtual particles as shown in Fig. 2.13(b) and cause deviations to the Standard Model description of these processes.

The main topics of the LHCb physics program are:

- **Measurement of the angle γ:** The angle γ of the UT is the one which is most difficult to assess with the current experiments [Har03]. LHCb will be able to perform redundant measurements of γ using the B_s decay channels $B_s^0 \to D_s^{\pm} K^{\mp}$ and their charge conjugated states (c.c.) [RAK92], the channels

---

[7] One year of data taking is usually considered to be 10^7 s.

$B_d^0 \to \pi^+\pi^-$ and $B_s^0 \to K^+K^-$ + c.c. [B+00] and the channels $B_d^0 \to \bar{D}^0 K^{*0}$ + c.c. [GW91]. The combination $\beta + \gamma$ is assessible through the decay channel $B_d^0 \to D^{*\pm}\pi^{\mp}$ + c.c. [Dun98].

- **Measurement of the angle β:** The "gold-plated" decay mode for β, $B_d^0 \to J/\Psi K_s^0$ (see section 2) will also be available at LHCb. In addition, β can also be measured in $B_d^0 \to \Phi K_s^0$ decays. For the former channel, high statistics measurements by the current B factories BaBar and Belle exist, hence it will serve as a test channel for the compatibility of the results. The latter one is sensitive to New Physics since the leading contribution is a so-called Penguin mode as shown in Fig. 2.13(a), where proposed new particles could have an impact on the decay rate. In the case of $B_d^0 \to J/\Psi K_s^0$, the main contribution comes from a so-called tree diagram where no loop processes are involved.

- **Measurement of the angle α:** The decays $B_d^0 \to \rho\pi^0 \to \pi^+\pi^-\pi^0$ and $B_d^0 \to \rho\rho \to 4\pi$ provide an unambigous way to extract the angle α applying a time dependend Dalitz plot analysis [SQ93, GL90].

- **B_s mixing:** The major channel to measure B_s mixing is $B_s \to D_s^-\pi^+$. Here, a recent measurment by CDF [A+06d] yields

$$\Delta m_s = \left(17.31^{+0.33}_{-0.18}\,(\text{stat.}) \pm 0.07\,(\text{syst.})\right)\ \text{ps}^{-1}, \tag{2.17}$$

  in agreement with the Standard Model prediction. LHCb will be able to contribute with a high statistics measurement, because for $\Delta m_s < 40\ \text{ps}^{-1}$, a 5σ observation will already be possible after 1/8 year of data taking [Sch02].

- **Rare B decays:** Decays like $B_s^0 \to \mu^+\mu^-$ + c.c. are suppressed in the Standard Model: The branching fraction according to the SM is in the order of 10^{-9}, but an enhancement is predicted by super-symmetric extensions. The current experimental upper limit is $1.5 \cdot 10^{-7}$ at 90 % confidence level [A+05a]. Here, LHCb should also be able to contribute significantly, but with the Monte Carlo simulated data currently available, a sensitivity study is still challenging [Sch02].

Table 2.3 presents the annual signal yields expected at LHCb for the decay channels listed above as given in [LHC03b].

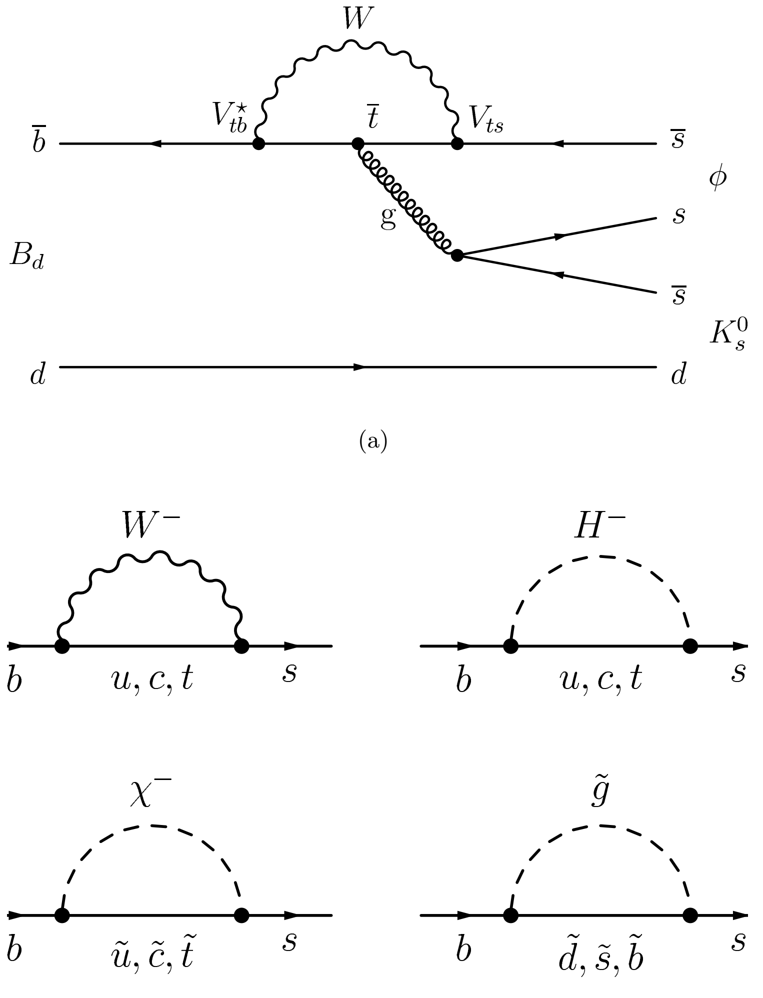

(a)

(b)

Figure 2.13: Feynman diagrams of the decay $B_d \to \Phi K_s^0$ (a) and possible New Physics contributions in the loop process (b): The exchange of a virtual Higgs (H^-), a virtual chargino (χ^-) and a virtual gluino ($\tilde{g}$) are shown. These particles have been proposed in extensions to the Standard Model.

decay channel	assumed visible BR $[10^-6]$	annual signal yield
$B_s^0 \rightarrow D_s^{\pm} K^{\mp}$	10.0	5.4 k
$B_d^0 \rightarrow \pi^+ \pi^-$	4.8	26 k
$B_s^0 \rightarrow K^+ K^-$	18.5	37 k
$B_d^0 \rightarrow \bar{D}^0 K^{*0}$	1.2	3.4 k
$B_d^0 \rightarrow D^{*\pm} \pi^{\mp}$	71.	206 k
$B_d^0 \rightarrow J/\Psi(\mu\mu) K_s^0$	19.8	216 k
$B_d^0 \rightarrow J/\Psi(ee) K_s^0$	20.0	25.6 k
$B_s^0 \rightarrow \Phi(\mu\mu) K_s^0$	31	100 k
$B_s^0 \rightarrow \Phi(ee) K_s^0$	31	20 k
$B_d^0 \rightarrow \rho\pi^0$	20	4 k
$B_s^0 \rightarrow D_s^- \pi^+$	120.	80 k

Table 2.3: Annual signal yields of important B decay channels and their assumed visible branching fractions [LHC03b]. The quoted yields include both the decays and their charge conjugates.

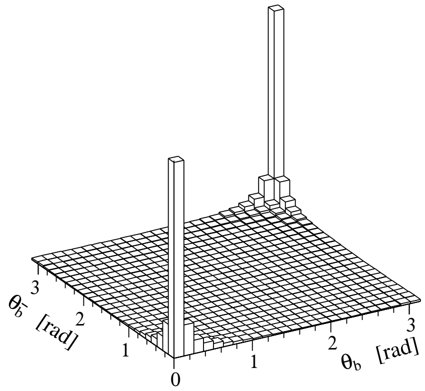

Figure 2.14: Polar angles (defined with respect to the beam axis in the pp center-of-mass system) of the b- and $\bar{b}$ hadrons as calculated by the PYTHIA event generator [LHC98].

2.4 The LHCb Detector

In contrast to the HERA-B detector, LHCb investigates decays of $b\bar{b}$ pairs created in head-on collisions of the proton beams of the LHC. The correlation of the polar angles of the emerging b- and $\bar{b}$ hadrons, shown in Fig. 2.14, is strongly peaked in forward and backward direction, thus both hadrons are produced predominantly in the same cone. Hence, LHCb was designed as a single-arm forward magnetic spectrometer covering one of the two cones with an angular aperture of approximately 10 - 300 (250) mrad in the bending (non-bending) plane.

2.4.1 The subdetectors

Very similar to HERA-B, LHCb possesses a vertex detector, called Vertex Locator (VELO), a tracking system with several subsystems (Trigger Tracker, Inner Tracker and Outer Tracker), a dipole magnet for momentum determination and various particle indentification systems. Two Ring Imaging Čerenkov Counters (RICH), a Electromagnetic Calorimeter and a Hadronic Calorimeter as well as a Muon detection system are being built. Fig. 2.15 shows a schematic overview of the detector.

Vertex Locator and Pile-Up Veto

The Vertex Locator consists of 21 stations with two half-disc shaped silicon sensors each. One half of the 300 μm thick sensors is covered with radial strips, the other half with circular strips, measuring the r and ϕ coordinates of the track impact points on the sensors (see Fig. 2.16). This geometry offers advantages for the tracking algorithm in the Level-1 trigger stage. Fig. 2.17 shows the VELO vaccuum vessel with the two additional stations (r-sensors only) used only for the so-called Level-0 Pile-Up Veto[8].

---

[8] See section 2.4.2 for a description of the LHCb trigger system.

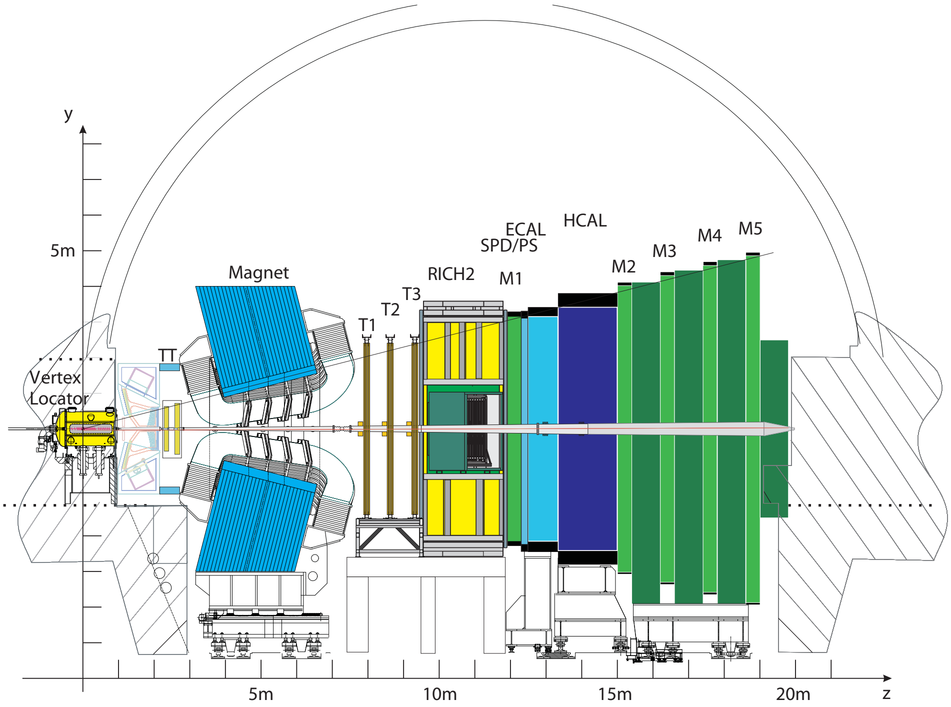

Figure 2.15: Schematic overview of the LHCb detector.

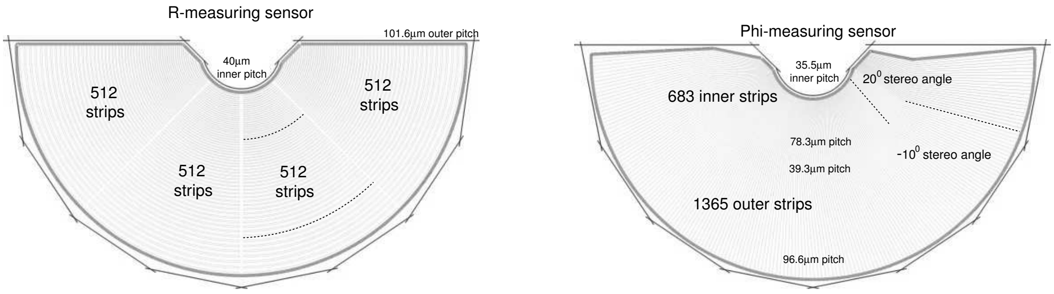

(a) (b)

Figure 2.16: Vertex Locator, r (a) and ϕ (b) sensor geometries [LHC03b].

Ring Imaging Čerenkov counters

LHCb has two Ring Imaging Čerenkov counters, RICH1 and RICH2, with make use of three different radiator media in order to provide clear π-K separation for the momentum range up to 150 GeV. RICH1, optimized for low momenta, is located directly behind the Vertex Locator and utilizes silica aerogel and C_4F_{10} as radiators, which cover the domain up to 50 GeV. RICH2 is designed for the high momentum range, hence its acceptance is limited to 120 mrad in horizontal and 100 mrad in the

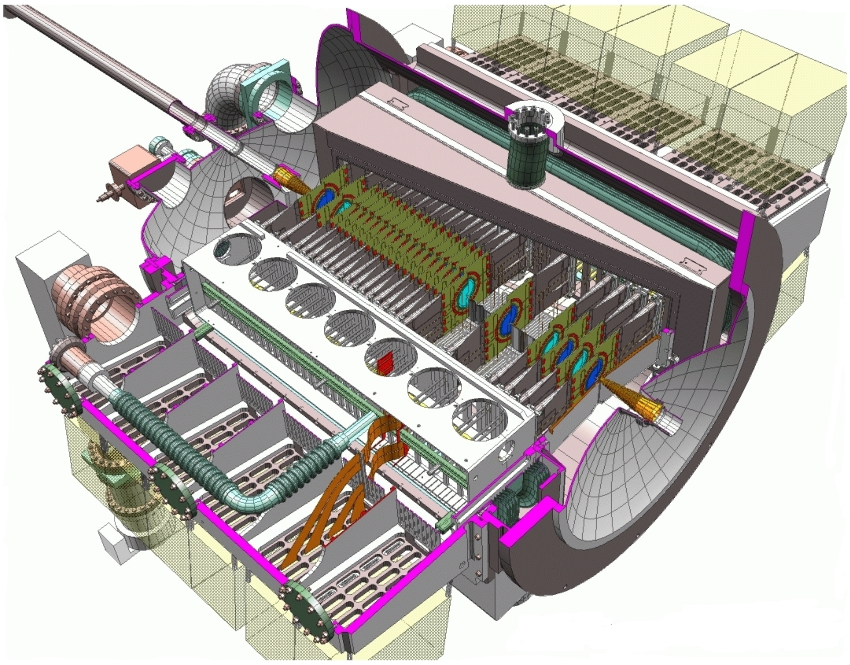

Figure 2.17: Schematic view of the Vertex Locator vacuum vessel [LHC03b].

vertical direction and its radiator is CF_4. In contrast to HERA-B, Hybrid Photo Diodes (HPDs) are employed to detect the photons of the Čerenkov light. In an HPD, photoelectrons created by incident photons on a photocathode are accelerated and focussed onto a silicon pixel sensor (see page 48).

Magnet

Because of higher particle momenta to be measured, LHCb needs a dipole magnet with a field integral of 4.2 Tm [LHC00b]. Nonetheless, it is designed as a warm magnet since a superconducting magnet has the disadvantages of slower ramping of the current and mechanical complexity.

Tracking system

The tracking system of LHCb consists of three subsystems: The Trigger Tracker [LHC03b] upstream of the magnet, the Inner Tracker and Outer Tracker downstream of the magnet. Trigger Tracker and Inner Tracker [LHC02] are being built from silicon strip sensors, hence both together are called **Silicon Tracker**. The Trigger Tracker covers the full acceptance of the spectrometer with four layers in two stations and provides a first momentum estimate for the Level 1 trigger to select high-p_T daughter tracks from B meson decays. Downstream of the magnet, the three stations (T1 - T3) of Inner and Outer Tracker will be crossed by the tracks. The region of high track density around the beam pipe is dealt with by the Inner Tracker. The Silicon Tracker project is described in detail in Chapter 3.

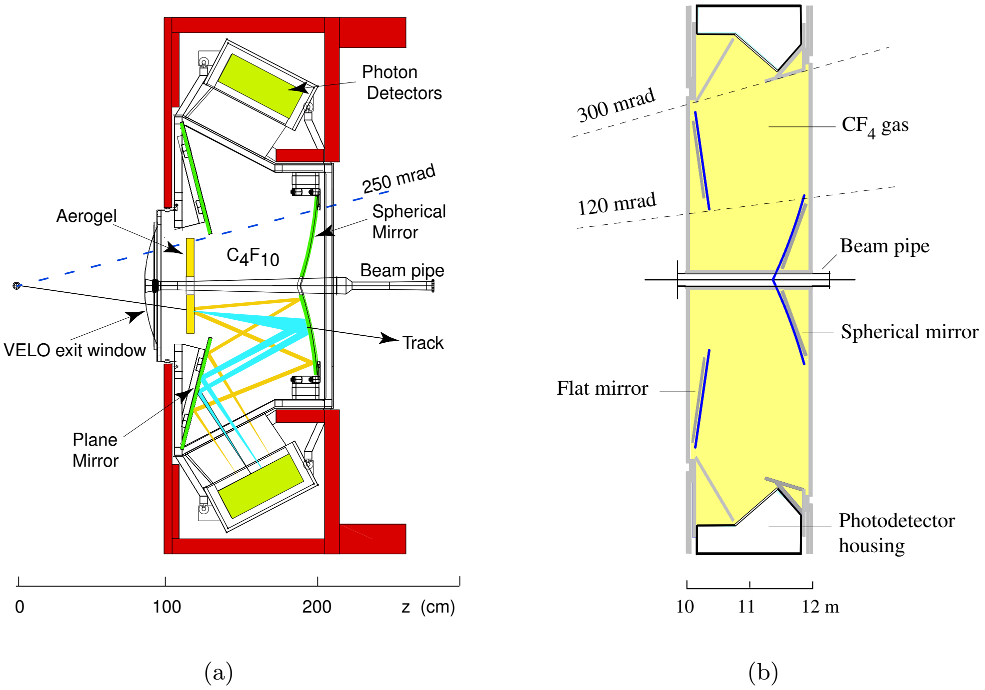

(a) (b)

Figure 2.18: Schematic view of RICH1 (a) and RICH2 (b) [LHC00c].

The **Outer Tracker** (OT) [LHC01b] covers the outer part of the acceptance using 5 mm wide straw drift tubes. The tubes are composed of carbon-doped polyimide film coated with an aluminium foil on the outside and flooded with CF_4 as drift gas around the gold-plated tungsten wires. Each of the three stations consists of four layers with two staggered layers of drift tubes.

Electromagnetic and Hadron Calorimeters

Similar to HERA-B, the LHCb calorimeters [LHC00a] are designed as sampling calorimeters. The calorimeter system is subdivided into a Scintillator Pad Detector (SPD), a Preshower Detector (PS), an Electromagnetic Calorimeter (ECAL) and a Hadronic Calorimeter (HCAL), . The SPD helps to separate charged particles, mainly electrons and positrons, from the neutral ones. The purpose of the PS is to improve the separation power for electrons and pions for the Level-0 trigger stage by measuring the much larger shower signal caused by the lead absorber between SPD and PS. The required energy resolutions of ECAL and HCAL of $\sigma_E/E = 10\%/\sqrt{E} \bigoplus 1.5\%$ and $\sigma_E/E = 80\%/\sqrt{E} \bigoplus 10\%$ can only be exploited in the offline reconstruction of tracks and clusters.

Technically, all four systems are very similar: They utilze alternating layers of scintillator and converter materials, so-called ”shashlik”-type modules. For PS and ECAL, lead is used as converting material, while the HCAL employs steel plates. The signal photons created inside the scintillator material is guided to photomultipliers by wavelength-shifting fibres. The cell sizes increase from the central region close to the beam pipe towards the outer regions in order to optimize the occupancy and the number of readout channels.

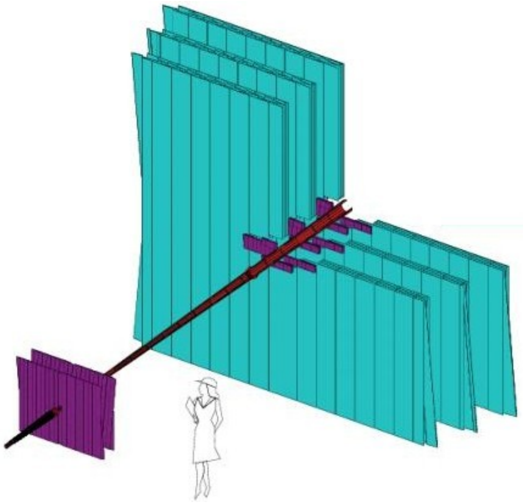

Figure 2.19: Schematic view of the LHCb tracking system: Silicon Tracker (consisting of Trigger Tracker and Inner Tracker, shown in purple) and Outer Tracker (in turquoise) [LHC01c].

Muon System

The Muon System [LHC01a] is an essential element of the trigger system of LHCb. Its task is to provide high-p_T muon candidates for the Level-0 trigger stage as well as efficient offline reconstruction of muons for the flavour-tagging of B meson decays.

After penetrating an absorber of sufficient thickness, most hadrons are filtered out and mainly muon tracks are left over. The LHCb muon system consists of five stations (M1 - M5): one station in front of the SPD detector and the others downstream of the HCAL. In this way, the calorimeters act as absorbing layer between M1 and M2. The interspaces between the four downstream stations are filled by 80 cm thick iron filters. To adapt to the occupancy gradient, the granularity of the detector is staggered in four regions (see Fig. 2.21). For all stations and regions except for the innermost region of M1, Multi-Wire Proportional Chambers (MWPCs) [LHC03a] are used, while the latter one will be build from triple Gas Electron Multipliers (GEMs) [LHC05] because MWPCs were proven to be not radiation-hard enough. Each station consists of two detecting layers and to increase the efficiency, a hit is accepted if at least one of the two corresponding read-out channels has fired.

2.4.2 The trigger and data acquisition systems

The fast increase in computing speed in the years since the HERA-B experiment was built brought a huge advantage for the design of the LHCb trigger and data aquisition: In contrast to the HERA-B trigger system, only the very first stage of the LHCb trigger system (Level-0 or L0) is being built from full custom electronics, the

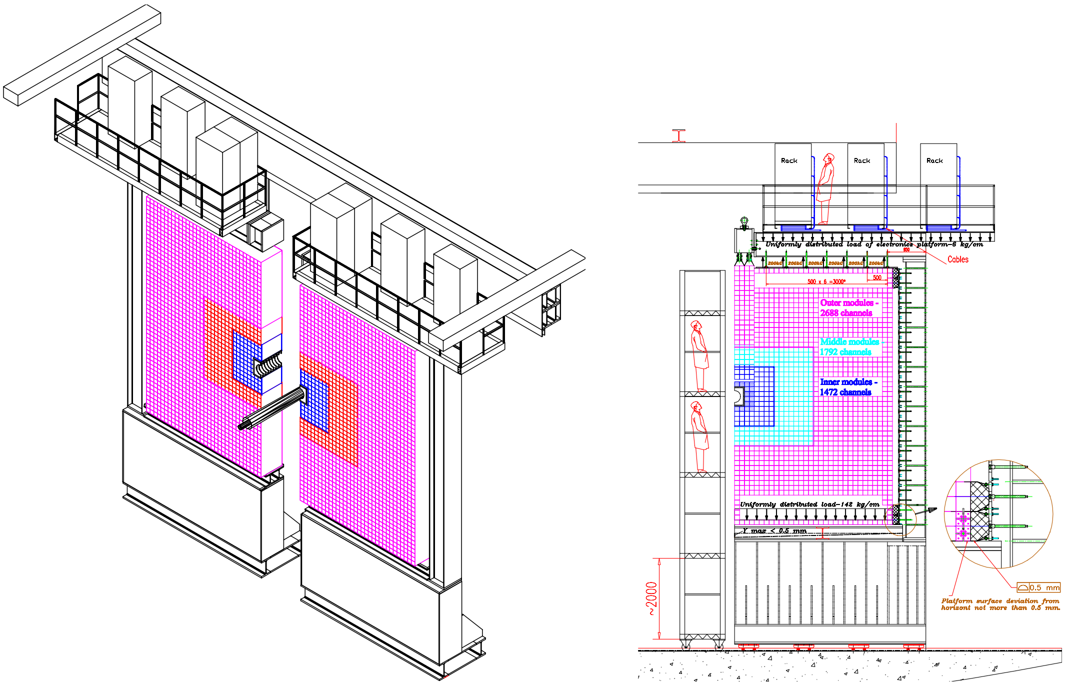

(a) view from behind (b) front view

Figure 2.20: The Electromagnetic Calorimeter: 3D view from behind the detector (a) and 2D front view (b) [LHC00a].

subsequent stages will be implemented on a large farm of commodity PCs [LHC03c]. This allows e.g. a flexible adaptation of the system to the beam conditions and further optimisation of the trigger algorithm.

While the LHC bunch crossing rate is 40 MHz, the rate of visible pp interactions[9] is only about 10 MHz. Fig. 2.22 presents a schematic overview over the three trigger levels: Level-0 is implemented in subdetector-specific custom electronis. Since B mesons are relatively heavy, their decay products have a high transverse momentum – thus the L0 trigger decision is based on either

- the hadron, electron or photon with the highest transverse energy (E_T) in the event, where the particle identification is based on the output of SPD, PS, ECAL and HCAL (see section 2.4.1), or
- the two muon with the highest transverse momentum in the event, as measured with the help of the stand-alone tracking algorithm of the Muon System.

Furthermore, it can reject events with charged track multiplicities above a given threshold, using the number of SPD cells with hits as a measure, and events with multiple interactions. The latter rejection is based on information provided by the

---

[9] An interaction is defined to be visible if it produces at least two charged particles with sufficient hits in the VELO and the tracking stations T1-T3 to allow them to be reconstructible.

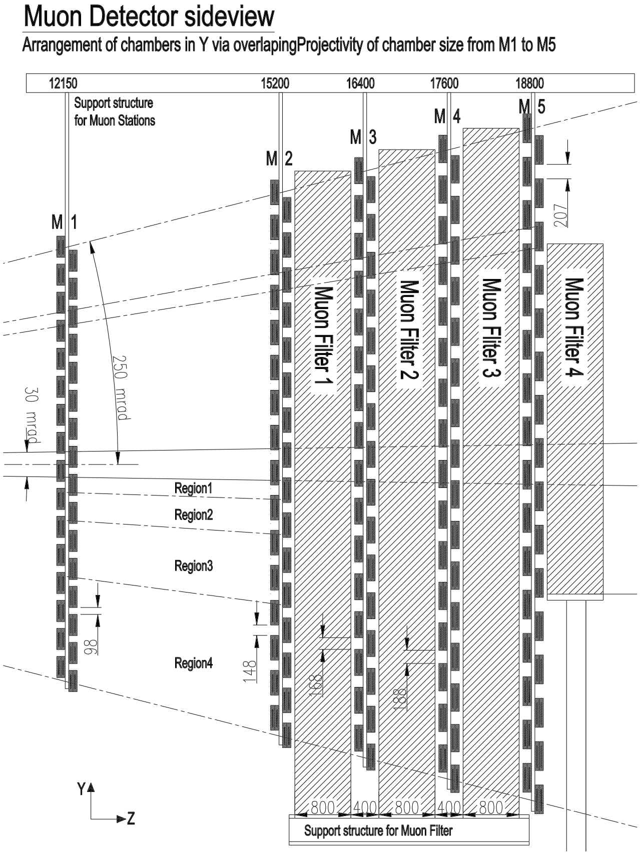

Figure 2.21: Schematic view of the Muon system [LHC01a]

Pile-Up System, i.e. positions of candidates of primary vertices along the beam direction and an estimate of the total multiplicity of charged tracks pointing backwards. As the first trigger stage, Level-0 runs synchronously with the LHC bunch crossing; thus, every 25 ns a trigger decision is taken by the L0 trigger decision unit (L0DU) and passed on to the Readout Supervisor [RJG01]. Here, the trigger decision can still be discarded if the readout rate has to be throttled in order not to overflow the buffers. If the trigger decision is positive, the Readout Supervisor requests the readout of the data from the Front-End electronics. The event output rate of Level-0 is about 1 MHz.

At the next level, Level-1, the remaining analogue data of the subsystems sending data to L1 is digitized, zero-suppressed and formatted and finally interfaced to the L1 trigger algorithm which runs on a commodity PC farm of $\sim$ 1600 nodes. This task is performed by the TELL1 board [B^{+}03a] used by all subsystems except the RICH. The L1 trigger algorithm adds tracks reconstructed in the VELO and matched to TT hits, ECAL clusters and muon candidates found at L0 to the L0 information. Here, the tracks have already a rough momentum estimate assigned. Events containing tracks with hight-p_T and significant impact parameter with respect to the primary vertex are selected. The output rate of Level-1 is approximately 40 kHz, but the feasibility of rates up to 1 MHz are currently discussed.

The aim of the high level trigger (HLT) is to provide an event selection as close to the offline selection as possible. Tracks and vertices are reconstructed with the data from all subsystems, thus refining the L1 trigger decision by an improved precision. Furthermore, selection cuts for specific final states will be applied in addition. The corresponding trigger algorithms run in parallel on the same PC farm as the L1 trigger (but with lower priority, in order not to cause bandwidth problems). Therefore, since no hardware limitations are involved, the output rate is flexible. Currently, an output rate of 2 kHz is foreseen, subdivided into four main streams [KF05]:

- **Exclusive B ($\sim$ 200 Hz):** The core physics program with exclusively reconstructed decays and control channels,
- D^* **($\sim$ 300 Hz):** Events with D^* decaying via D^0 into two hadrons, selected without applying cuts on the particle identification, for efficiency studies,
- **Di-muon ($\sim$ 600 Hz):** For measuring the uncertainty of lifetime measurements, and
- **Inclusive $b \rightarrow \mu$ ($\sim$ 900 Hz)**: Events with one muon with high transverse momentum and significant impact parameter, for systematic studies.

The output of the HLT is written to a mass storage system.

2.4.3 The LHC Computing Grid

The expected amount of data recorded per year by the four LHC experiments together will be roughly 15 PB. To analyze all this within a reasonable time, the strategy of Grid Computing was devised: The LHC Computing Grid project (LCG) will provide a common infrastructure organized in a hierarchical architecture of computing centres located around the globe. The raw data will initially processed and stored at CERN, but further processing, storage of the processed data and analysis will take place at local centres of the next hierarchical levels [Boa05]. Common application software is being developed, including core software libraries, tools and frameworks for data management and event simulation.

The order of magnitude of Monte Carlo simulated data needed for the analysis corresponds to the amount of real data taken, therefore the Monte Carlo production will be at least as demanding as the processing of the real data. The corresponding software framework and tools are being developed and tested: Each year, a large production of Monte Carlo events is carried out in so-called Data Challenges. In the 2004 LHCb Data Challenge, 187 million events were produced, resulting in 62 TB of data written to tape or disk. 50% of these data were produced by LCG resources.

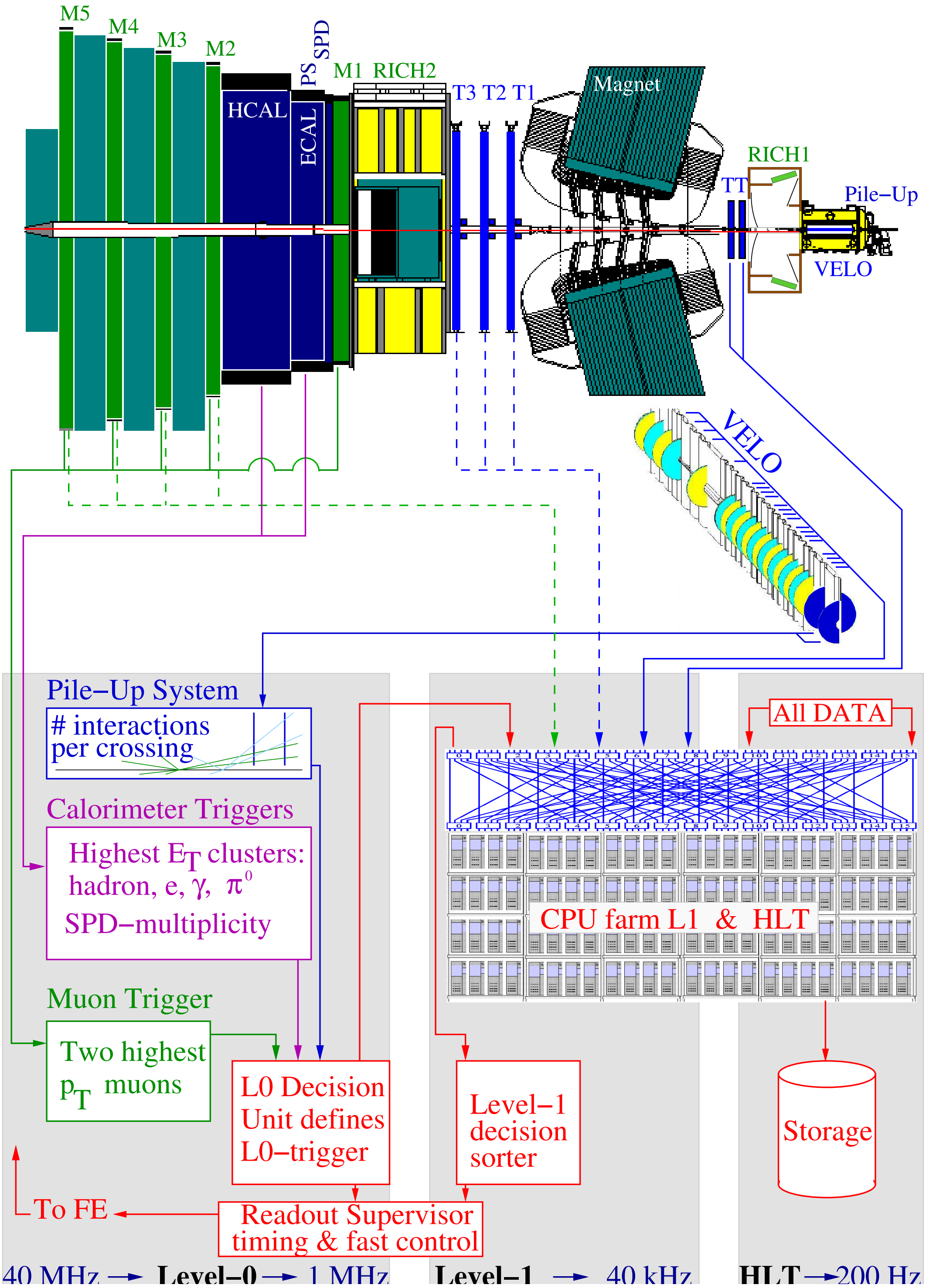

Figure 2.22: LHCb: Overview of the three trigger levels: L0 triggers on the highest E_T hadron, electron or photon or an the highest p_T muon, if the event is not rejected because of too high charged particle multiplicity. L1 adds information from the VELO and TT to the L0 data. At the HLT, all data in the event are used to improve the resolution, and channel specific selection cuts can be applied [LHC03c].

Chapter 3

Silicon Sensors for the LHCb Tracking System

Initially, in the LHCb Technical Proposal [LHC98], the tracking system was forseen to comprise 11 Inner and Outer Tracker stations, and the total radiation length accumulated in front of the second RICH detector (see chapter 2.3) was 40% of X_0[1]. By the time when the Outer Tracker Technical Design Report [LHC01b] was published, this fraction had already increased to 60% because of technological constraints. Since this would decrease the detector performance due to an enhancement of multiple scattering and higher occupancies of the tracking stations, considerable effort was put in a re-design of the detector with reduced accumulated radiation length.

The new design is described in detail in [LHC03b]. For the tracking system, basically the number of stations was drastically reduced: The stations inside the magnet were completely removed, the six stations behind the magnet were reduced to three and the two in front of the magnet were merged into one directly behind the exit window of the first RICH. While the three stations behind the magnet are separated into an inner region (Inner Tracker [LHC02]) and an outer region (Outer Tracker [LHC01b]), the one in front is not subdivided. This part of the tracking system provides input for the Level-1 Trigger and is therefore called the Trigger Tracker. Both the Inner Tracker and the Trigger Tracker are built using silicon micro-strip sensors.

This chapter provides a general description of the concept of semiconductor detectors [Leo92] and summarizes the main design issues for applications in particle physics. The R&D for the Inner Tracker and the Trigger Tracker is reviewed followed by a discussion of the final layout.

---

[1] The radiation length X_0 is defined as the distance over which the energy of an incident electron is reduced by a factor $1/e$ due to radiation loss only.

3.1 Silicon Strip Detectors

During the last decades, silicon detectors have become an important building block for particle physics experiments. At the LHC, they will not only be used for vertex detecors but also in the tracking systems. Their advantages are a high spatial resolution, their compact form and the fast response which allows high counting rates. If using appropriate designs, they show sufficient radiation hardness for several years of operation even under the harsh conditions in LHC experiments. A disadvantage is the need to cool the silicon sensors in order to achieve a better signal to noise ratio.

3.1.1 Signal Generation

When charged particles traverse matter, they deposit some fraction of their energy in collisions with electrons or nuclei of the material. Furthermore, they may emit Čerenkov radiation or bremsstrahlung or cause nuclear reactions. In a semiconductor like silicon, this energy deposition excites electrons from the valence band into the conduction band. The vacancy in the valence band is called a hole and also acts as a charge carrier. This electron-hole pair can recombine again or, the case exploited if used as a detector, the charges can be separated by an external electrical field and can be detected as a signal.

Energy Loss Distribution

The first quantum mechanical calculation of the energy loss of a charged particle traversing matter was performed by Bethe and Bloch [Leo92]. The result, the so-called Bethe-Bloch equation,

$$-\frac{dE}{dx} = 2\pi N_A r_e^2 m_e c^2 \rho \frac{Z}{A}\frac{z^2}{\beta^2}\left[\ln\left(\frac{2m_e\gamma^2 v^2 W_{max}}{I^2}\right) - 2\beta^2\right], \qquad (3.1)$$

(Here, N_A is Avogadro's number, r_e and m_e the classical electron radius and its mass, ρ the density of the absorbing material, Z and A its atomic number and weight, z the charge of the incident particle in units of e, $\beta = v/c$ and $\gamma = 1/\sqrt{1-\beta^2}$. I represents the mean excitation potential and W_{max} the maximum energy transfer in a single collision.)

describes the mean rate of energy loss. The average energy depostion for a finite thickness can be calculated by integrating equation 3.1. Since the collisions and the scattering inside the material are stochastical processes, theories were developed to calculate the probability density function for the energy loss. For thick absorbers, the number of collisions is large enough for the Central Limit Theorem to hold, and the energy loss distribution is simply Gaussian:

$$f(x,\Delta) \propto \exp\left(\frac{-(\Delta-\bar{\Delta})^2}{2\sigma^2}\right). \qquad (3.2)$$

(Here, x is the thickness of the absorber, Δ the energy loss in the absorber, $\bar{\Delta}$ the mean energy loss and σ is the standard deviation, depending on density, atomic number and weight and the thickness of the absorber.)

If N is too small for the Central Limit Theorem to apply, the calculation becomes more complicated. Depending on the ratio of the mean energy loss $\bar{\Delta}$, which can be obtained from Equ. 3.1 by integrating over the thickness x of the absorber, and the maximum energy transfer in a single collision W_{max},

$$\kappa = \frac{\bar{\Delta}}{W_{max}}, \tag{3.3}$$

different approximations can be used to ease the calculation. The Landau theory, applicable for $\kappa \leq 0.01$, assumes that the maximum energy transfer W_{max} is infinite, that the electrons can be treated as free particles and that the incident particle retains its velocity. The distribution can be expressed as

$$\begin{aligned} f(x,\Delta) &= \frac{\phi(\lambda)}{\xi} && (3.4)\\ \phi(\lambda) &= \frac{1}{\pi}\int_0^\infty e^{-u\ln u - u\lambda}\sin(\pi u)du && (3.5)\\ \lambda &= \frac{1}{\xi}\left[\Delta - \xi\left(\ln\xi - \ln\epsilon + 1 - C\right)\right] && (3.6) \end{aligned}$$

(Here, C is Euler's constant, ϵ is the minimum energy transfer still compliant with the assumption of free electrons, and ξ is the mean energy loss, approximated by considering only the first multiplicative term of the Bethe-Bloch equation 3.1 and ignoring the logarithmic variation (if β is close to unity, as given in high energy physics, then γ and v are large). Hence, $\xi \approx \bar{\Delta}$ and it depends on the thickness of the absorber, x.)

In contrast to Landau, Vavilov took into account the correct expression for the maximum energy transfer permitted in one collision. The asymetric form with the long tail (see Fig. 3.1) towards high energies is caused by the possibility to transfer a large amount of energy in one single collision. Thus, the tail is more prominent for light particles. The peak value of the distribution is the most probable energy loss and it is smaller than the mean energy loss.

Further corrections to the Landau and Vavilov distributions account for the fact that the electrons are not free but bound to the nuclei of the material traversed by the particle. The resulting distribution can be expressed as a convolution of a Gaussian with a Landau or Vavilov distribution. In addition, noise of the detector itself (see section 3.1.2) and of the read-out electronics can be incorporated.

$$\begin{aligned} f(x,\Delta) &= \frac{1}{\sigma_{tot}\sqrt{2\pi}}\int_{-\infty}^{\infty} f_{L,V}(x,\Delta')\,\exp\left(-\frac{(\Delta-\Delta')^2}{2\sigma_{tot}^2}\right)d\Delta' && (3.7)\\ \sigma_{tot}^2 &= \sigma_{ab}^2 + \sigma_{noise}^2 && (3.8) \end{aligned}$$

(Here, Δ is the actual energy loss, $f_{L,V}$ is the Landau or Vavilov distribution, σ_{ab} describes the effect of the atomic binding and σ_{noise} the noise contribution.)

For a detailed review on energy loss distribution in thin silicon sensors, see [Bic88].

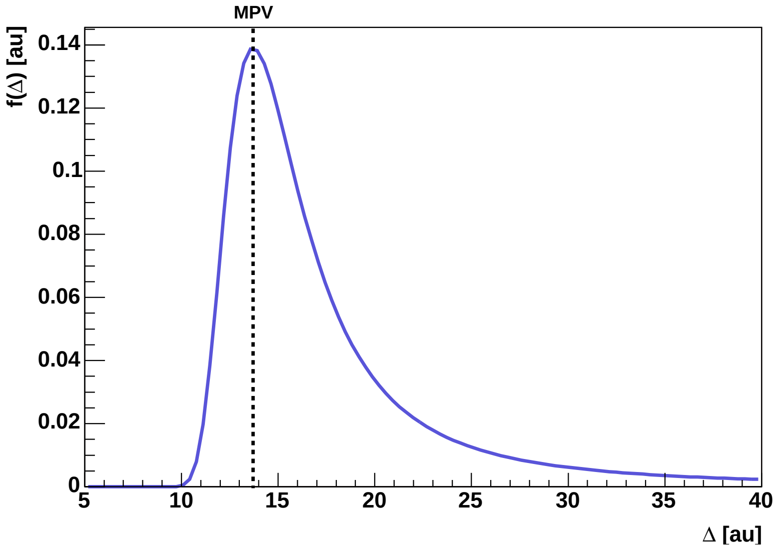

Figure 3.1: Landau distribution. The dashed line indicates the most probable energy loss.

Charge Transport

If an electric field is applied to a semiconductor, the drift velocities of electrons and holes (v_e and v_h) can be written as

$$v_e(x) = -\mu_e\, E(x), \tag{3.9}$$

$$v_h(x) = \mu_h\, E(x). \tag{3.10}$$

(Here, E is the electric field strength and μ_e and μ_h are the mobilities of electrons and holes.)

In general, the mobilities μ_e and μ_h depend on the temperature and on the applied electric field, but for silicon at normal temperatures and moderate field strengths ($E < 10^3$ V/cm) they are approximately constant [Leo92]. The drift velocity reaches its saturation value of about 10^7 cm/s at roughly $E = 10^4$ V/cm. In practice, the charge collection time of a typical semiconductor of a few 100 nm thickness (as used in particle physics) with saturated drift velocities amounts to a few nanoseconds.

The functionality of all modern silicon detectors is based on a semiconductor junction, showing the characteristic traits of a diode. Most sensors consist of a p-n junction, i.e. a juxtaposition of a p-type and an n-type[2] semiconductor. At the boundary between the two types, the electrons diffuse into the p-region and recombine with the holes, while holes diffuse into the n-region and capture electrons. Since the doped semiconductors were initially neutral, they accumulate now a non-zero net charge. The resulting field gradient eventually stops the diffusion process. The potential difference at the equilibrium is called contact potential. The region with accumulated space charge is drained of all mobile charge carriers (the so-called

---

[2] Doped semiconductors contain small amounts of impurities of material with one valence electron more (n-type, donor impurities) or less (p-type, acceptor impurities), which increases the abundance of electrons or holes as the majority charge carrier.

depletion zone), and as a consequence, all electron-hole pairs created by ionizing radiation will be swept out by the electric field.

The thickness of the depletion zone and the potential V can be calculated from the Poission equation, if the charge concentration $\rho(x)$ in that region is known:

$$\nabla^2 V = \frac{\rho(x)}{\epsilon} \tag{3.11}$$

(Here, ϵ is the permittivity of silicon.)

If the concentration of the donor impurities N_D is much higher than the acceptor concentration N_A as it is the case for n-type silicon sensors, then the width d of the depletion zone is approximately given by

$$d \simeq \left(\frac{2\epsilon V_0}{eN_D}\right)^{\frac{1}{2}} \tag{3.12}$$

(Here, V_0 is the contact potential and e is the charge of the electron.)

For the resulting electric field, we obtain:

$$-\frac{dV}{dx} = E(x) = \frac{2\epsilon V_0}{d^2}(x - d) \tag{3.13}$$

In general, the charge collection provided by the intrinsic electric field is not efficient and fast enough for the use in detectors. Furthermore, the small width of the corresponding depletion zone presents a large capacitance, increasing the noise in the read-out electronics. It is therefore required to apply in addition an external electric field in reverse bias (i.e. the cathode connects to the p-type side). The resulting width and electric field is given by equations 3.12 and 3.13 by replacing the contact potential V_0 by $V_B + V_0$. Thus, applying an external bias voltage has two favourable effects: It enlarges the width of the depletion zone and the higher voltage yields a more efficient charge collection. If the depletion zone extends over the whole thickness of the sensor, the corresponding voltage is called depletion voltage V_{dep}. Towards the edges of the depletion zone, the electric field and hence the charge collection efficiency decreases. Therefore the external bias voltage is usually chosen to be larger than the voltage needed to create a depletion zone of the same size as the sensor substrate. This is called over-biasing or over-depleting the detector and it ensures efficient collection over the whole sensor volume. In general, the applied bias voltage V_B is much higher than V_0, thus V_0 can be directly replaced by V_B in equations 3.12 and 3.13.

The capacitance of the depletion layer decreases with $C \propto V^{1/2}$ until the minimum value of

$$C = \epsilon \frac{A}{d_s} \tag{3.14}$$

(Here, A is the area of the depletion layer and d_s is the thickness of the silicon sensor.)

at the depletion voltage V_{dep} is reached. For n-type silicon, the typical values are $2.2\,(\rho V_0)^{-1/2}$ pF/mm^2 [Leo92], where ρ is the specific resistivity in Ωm. Therefore, by measuring the capacitance of a sensor as a function of the applied voltage, its depletion voltage can be determined.

Ideally, there is no current flowing through a reversed biased diode, but in reality, a small fluctuating current is conducted through the junction. This leakage current has various origins: One is the movement of the minority charge carriers (i.e. holes in the n-side and electrons from the p-side) which travel towards the opposite side. This effect typically contributes a few nA/cm^2. Another source is the thermal generation of electron-hole pairs at trapping centers (see section 3.1.3), hence its share depends on the density of such centers in the sensitive volume and generally amounts to a few μA/cm^2. Conducting channels on the surface of the sensor can also be a major source for leakage currents. Influencing factors can be the ambient atmosphere, the surface chemistry, possibly existing contaminants, and many more. A clean encapsulation and pure materials help to minimize the surface currents. At the detector output, the leakage current constitutes as noise at the detector output and hence presents a limit for the achievable sensitivity.

3.1.2 Noise

Another important property of any detector is its noise behaviour. In semiconductor detectors, the size of the signals generated by the traversing particles depends only on their type and energy and is not intrinsically amplified. Typical silicon sensors of a thickness of roughly a few hundred μm yield signals of $\mathcal{O}(10^4)$ electrons. Thus, the noise of detector and read-out electronics must be kept much smaller than the signal in order to obtain a clear separation between signal and noise. Furthermore, the distance between read-out electronics and sensors should be as short as possible. Since the signals from semiconductor detectors are charges, charge-sensitive preamplifiers are used.

The noise seen at the output of the charge-sensitive amplifier scales with the capacitance C_{det} of the detector at its input. Amplifiers are adjusted to the specific needs of the application by a feedback network[3] which feeds back a fraction of the output signal back to the input of the amplifier, thus the overall gain is reduced by this fraction. The fed back fraction of the signal depends on the capacitance inside the feedback network, C_{fb}, and the detector capacitance, C_{det}, as $(1+C_{det}/C_{fb})$ (to first order) [vB06]. Therefore, increasing C_{det} increases the fed back fraction and reduces the overall gain. Since this reduction in signal gain is more dominant than the change in noise from the amplifier, the signal-to-noise ratio is degraded. Thus, minimizing the detector capacitance helps to optimize the S/N performance of the system.

Several noise sources can be distinguished: thermal noise, shot noise and low-frequency voltage noise:

- **Thermal Noise**

  Thermal noise (also known as Johnson noise) is the noise generated by the thermal agitation of electrons in a conductor. The corresponding noise voltage

---

[3] Via a feedback network, the stability of the gain can be improved, the input and output impedances can be adjusted, the signal distortion and the internally generated noise can be reduced and the bandwidth increased [Sma04].

of a conductor of resitance R can be described by

$$\left\langle U_n^2 \right\rangle = 4\, kTR\Delta f \tag{3.15}$$

(Here, T is the absolute temperature, k the Boltzmann constant, and Δf the observing bandwidth.)

Since the thermal noise increases with temperature, cooling improves the noise performance of both sensor and read-out electronics. It is always present, even if no external voltage is applied and no DC current is flowing.

- **Shot Noise**

  Electrical current is carried in discrete charges, hence it is a statistical process and underlies random fluctuations. Their magnitude increases with rising current, thus care has to be taken to minimize the current flowing trough the detector, i.e. the leakage current in case of silicon detectors.

- **1/f Noise**

  While both thermal noise and shot noise show a flat frequency spectrum (hence called "white noise") and cannot be reduced by design, the so-called flicker or $1/f$ noise depends on the properties of a device. The phenomenon is common to most electronic systems and cannot be traced back to a single origin [Mil02]. One possible explanation arises from defects inside the silicon crystal (see section 3.1.3). At these sites charge carriers can be trapped for while until they are released after a certain lifetime. Since the charges arrive out of time with respect to the original signal, they contribute to the noise of the system. A superposition of many of these relaxation processes yields a noise distribution following a power law in $1/f$.

For a charge-sensitive amplifier as used in the BEETLE Front-end chip of LHCb, the thermal noise is the dominant part [Sma04].

3.1.3 Radiation Hardness

Radiation damage in silicon strip sensors is mainly caused by structural defects in the crystal lattice. Incident radiation can create point defects, e.g. vacancies in the lattice or atoms between the lattice positions, or dislocations if whole lines of atoms are displaced. Because of their masses, hadrons and heavy ions induce more damage than electrons or photons. The structural defects can form additional states in the energy gap between the conduction and the valence band. These states can act as centres for charge trapping or recombination. In the latter case, the detectable signal is deteriorated, while in the former case the signal loss depends on the trapping time: If the charge is released very soon, the detrimental effect can be little, but if it is trapped for a long time, it can not be detected, also resulting in a smaller signal. The existence of additional states within the band gap leads to an increased leakage current, an increased depletion voltage and reduced charge collection efficiency, i.e. a degradation in the energy resolution. Thus, the signal to noise ratio of a sensor decreases the more irradiation is accumulated. In general, the rising of leakage current and depletion voltage has the major impact on the degradation of the sensor performance while the effect of the lower charge collection efficiency plays a minor role. For fluences typical for 10 years of LHC conditions ($\mathcal{O}(10^{14})$ particles per cm^2, e.g. at the LHCb vertex detector) the collected charge of a minimum-ionizing-particle (mip) only drops to 90 % [L$^+$99].

It is common practice to relate the fluence of a given particle source to the equivalent fluence of neutrons with an energy of 1 MeV which induces the same damage. For a given equivalent fluence Φ_{eq}, the leakage current I of a fully depleted detector increases approximately as

$$I = \alpha \Phi_{eq} V \tag{3.16}$$

(Here, V is the sensor volume.)

The current-related damage rate α has been shown [L$^+$99] to be independent of the specific silicon material, the process technology and the particles used for irradiation. The equivalent fluence can be calculated from the fluence of the irradiation source by applying a "hardness factor" κ which is characteristic for the source:

$$\Phi_{eq} = \kappa \Phi_{tot} = \kappa \int \Phi(E) dE \tag{3.17}$$

(Here, $\Phi(E)$ is the energy distribution of the particles.)

κ can be determined by means of the displacement damage function $D(E)$, if the spectrum $\Phi(E)$ is known. $D(E)$ represents the possible damage caused by a particle of a specific type with energy E, and it is calculated from the individual reaction cross sections, the energy distribution of the recoils and the split-up into ionizing and non-ionizing energy loss, summing over all reaction channels available for the initial particle with the given energy. Then,

$$\kappa = \frac{\int D(E) \cdot \Phi(E) dE}{D_{neutron}(1\ \text{MeV}) \int \Phi(E) dE} \tag{3.18}$$

According to an ASTM standard [AST93], the displacement damage cross section for 1 MeV neutrons $D_{neutron}(1\ \text{MeV})$ is taken to be 95 MeVmb.

For high energy experiments like LHCb it is very important to know precisely which particles will be the main source of irradiation and what their energy spectra will be. Unfortunately, this can only be done by Monte Carlo simulations. For the LHCb Inner Tracker for instance, a 1 MeV neutron equivalent dose of 1.8×10^{13} cm^{-2} (including a safety factor of two) is expected for the innermost parts after ten years operation. To simulate the effect of this irradiation on the detector performance, it is customary to irradiate prototype sensors with a corresponding dose of one type of particles, e.g. protons. In addition to the immediate damage, long-term annealing effects have to be taken into account: With time and temperature, the distributed defects like interstitial atoms can move within the silicon lattice and "mend" it, such that the radiation damage is partly compensated. On the other hand, particles that are stopped inside the bulk of the substrate usually create point defects along their trajectory and a cluster of defects where they are stopped. This cluster can disassemble with time [L+99] and the defects distribute over the sensor, increasing the damage. This effect is called anti-annealing or reverse-annealing while the former is called beneficial annealing. Since the defects influence the effective number of charge carriers which can contribute to the signal generation, the resulting damage can be observed in a change of the effective doping concentration N_{eff} and hence a change in the depletion voltage. For a p-type sensor, this change in effective doping concentration can even lead to a type inversion of the bulk material after the absorption of a certain fluence. Since the annealing originates from the mobility of defects in the lattice, it strongly depends on the temperature.

Quantitatively, the change of N_{eff} is described as

$$\Delta N_{\text{eff}} = N_C(\Phi_{eq}) + N_a(\Phi_{eq}, t(T)) + N_Y(\Phi_{eq}, t(T)) \tag{3.19}$$

(Here, $t(T)$ indicates that the time dependence of the annealing process is a function of temperature.)

N_C is the stable component not subject to the annealing:

$$N_C = N_{C0}\left(1 - \exp\left(-c \cdot \Phi_{eq}\right)\right) + g_C \cdot \Phi_{eq} \tag{3.20}$$

N_a describes the short-term part of the annealing which decreases with a time constant of about two days. Hence this component will completely vanish during the yearly maintenance period of the experiment. N_Y presents the above mentioned reverse-annealing:

$$\begin{aligned} N_Y &= N_{Y\infty} \cdot (1 - \exp(-t/\tau)) \approx N_{Y\infty} \cdot \left(1 - \frac{1}{1 + t/\tau}\right) \\ N_{Y\infty} &= g_Y \cdot \Phi_{eq} \end{aligned} \tag{3.21}$$

(Here, $\tau(T)$ is the temperature-dependent time constant.)

Thus, N_Y starts from zero and saturates to the value $N_{Y\infty}$ after about 350 days at room temperature, when all defect clusters have disintegrated.

For radiation hardness tests, the temperature dependence of the annealing can be used to accelerate the annealing of irradiated prototypes in the laboratory in such a way that the expected annealing during the experiment is obtained within days or weeks at a correspondingly higher temperature (see section 3.3.3).

A possible improvement of the radiation hardness of silicon sensors can be achieved by enriching the silicon bulk material with oxygen. Though the resulting sensors show no improvement if irradiated with neutrons, they can endure up to thrice as many protons and pions to reach the same leakage current as standard silicon sensors. [L+01]. For a possible upgrade of the LHC, the expected equivalent fluences reach values of 10^{16} cm^{-2}. In this regime, the drop in charge collection efficiency due to defects and impurities can no longer be ignored. A possible workaround is to cool the sensors down to cryogenic temperatures, then the "de-trapping time", i.e. the time after which charge carriers leave the trapping sites, is so large that the trapped charge carriers effectively neutralize the trapping centres. The irradiation damage can thus be aleviated, the effect is therefore called the Lazarus effect [H+04]. Nonetheless, such a cooling of the detector presents a considerable operating expense.

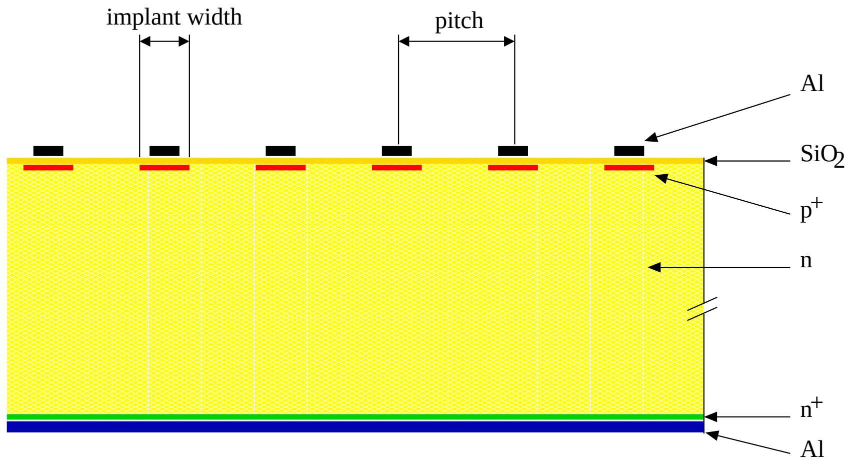

Figure 3.2: Layout of a silicon micro-strip sensor.

3.2 Detector Layout and Design Issues

In order to achieve a high spatial resolution, silicon sensors can be subdivided into strips or even pixels which are read out separately. The majority of sensors used in high-energy physics are p^+n single sided sensors which consist of p-type strips on n-type substrate. In Fig. 3.2, the typical profile of such a detector as used for the Inner Tracker and the Trigger Tracker is shown. The p-type strips are implanted into the high-ohmic n-type silicon bulk material. To collect the charge from the strips, the read-out electronics can be either connected directly to the implant (DC-coupling) or to aluminium strips on top of an additional SiO_2 layer (AC-coupling). The latter method provides an decoupling of the read-out electronics from the leakage current flowing through the sensor, and it is used both for the Inner Tracker and the Trigger Tracker.

The parameters that characterize the properties of the sensor are the thickness of the substrate, the pitch of the strips, their implant width and the width of the metal strip read-out electrodes, and of course the total length of the strips. Varying these parameters, the sensors can be optimized to their field of application. The impact of changes in the respective parameter can be summarized as follows:

- **Substrate thickness:** The thicker the substrate, the larger is the signal generated by traversing particles. Furthermore, the capacitance decreases with increasing substrate thickness, reducing the noise in the signal detection. On the other hand, thicker substrates also introduce more material and hence, due to multiple scattering of the tracks, deteriorate the momentum resolution of the tracking system. In addition, the amount of material also plays an important role for the performance of the calorimeters: More material in front of them increases the rate of e^+e^- pair creation and spoils the detection efficiency of photons. The sensors are therefore desired to be as thin as possible.

- **Strip length:** The longer the strips, the smaller is the number of read-out channels necessary to cover a given sensitive detector area, saving cost for the read-out system. Furthermore, it keeps the data volume low but is only feasible if the occupancy, i.e. the number of tracks passing through the detector in one event, is small enough. Otherwise ambiguities in the track reconstruction occur. Increasing the length of the strips also increases the capacitance of the sensor and hence the noise. The strips must therefore be optimized to be as long as possible without compromising the signal-to-noise performance and increasing the sensor occupancies to much.

- **Strip pitch:** The pitch is closely related to the spatial resolution of the sensor. If a very fine resolution is required, a small strip pitch is inevitable. However, for tracking systems like the Inner Tracker and the Trigger Tracker, the resolution is already limited by the amount of multiple scattering the tracks have undergone before. To achieve the required resolution is therefore not a problem, and other factors have to be considered. Again, the number of read-out channels and the occupancy have to be kept at a minimum, and the capacitance between the strips itself also plays a role in the total noise figure. Therefore, large strip pitches are favored as long as the occupancy does not increase too much.

- **Strip width:** The width of the metal strip AC-coupled to the implanted electrode has an impact on the charge collection behaviour in the gap between the implanted strips: A wider metal strip is expected to enhance the charge collection in the middle between two strips. On the other hand, the wider the strips are, the smaller is the distance between them and hence the interstrip capacitance increases.

In the next subsections, the layout of Inner Tracker and Trigger Tracker will be presented, followed by a description of the Front-end chip used for both detectors. The next section reviews the process of optimizing the sensor layout for both detectors. This order is to some extend arbitrary because the detector layout and partitioning is closely related to the sensor layout, and both evolved in parallel.

3.2.1 The Inner Tracker

The Inner Tracker covers a cross-shaped area around the beam pipe, its width being 125.6 cm in the bending plane (horizontal to the LHC ring), its height 41.4 cm in the non-bending plane. It comprises three stations with four active layers each. Two layers are oriented with their strips along the y axis of the LHCb coordinate system, and the other two layers are tilted by $\pm 5^\circ$. Each station is subdivided into four boxes housing sensor modules of different sizes: The boxes to the left and the right contain modules with two sensors bonded together as depicted in Fig. 3.3, resulting in doubled strip lengths. The boxes above and below the beam pipe contain single-sensor modules only. A schematic view of the IT boxes of one station is shown in Fig. 3.5. The modules consist of a support structure made from carbon fibre, a cooling balcony and a hybrid carrying three BEETLE Front-end chips (see section 3.2.3 and Fig. 3.4). The boxes are thermally insulated and will be flushed with dry nitrogen at a temperature of about 5° C.

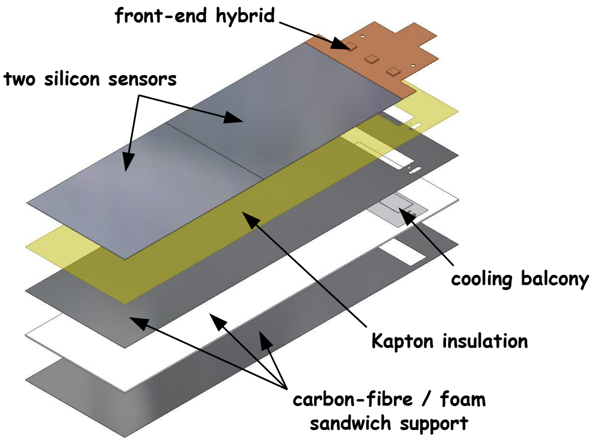

Figure 3.3: Two-sensor module of the LHCb Inner Tracker. Two sensors are bonded together, creating read-out strips of double length. The Front-end hybrid carries three Beetle chips, connected via a pitch adapter (not shown) to the read-out strips.

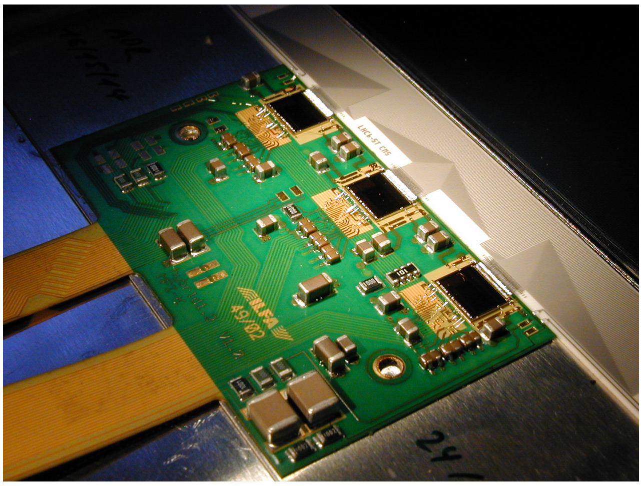

Figure 3.4: Front-end hybrid equipped with three Beetle chips, connected via a ceramic pitch adapter to the read-out strips of a silicon sensor.

3.2.2 The Trigger Tracker

In contrast to the Inner Tracker, the Trigger Tracker covers the whole acceptance of the LHCb detector [LHC03b], resulting in an active area of up to 157.2×132.4 cm^2 at a distance of 262 cm upstream of the interaction region. Since the TT data will already be used at the Level-1 trigger stage, the number of read-out channels had to be kept as small as possible without compromising the required occupancy. The solution is the layout presented in Fig. 3.6: It shows the four layers of the Trigger Tracker, segmented into read-out sectors shaded in different colors. The innermost sectors consist of only one sensor connected with a Kapton cable of 56.4 cm to the Front-end electronics which is located at the top and bottom ends of the modules,

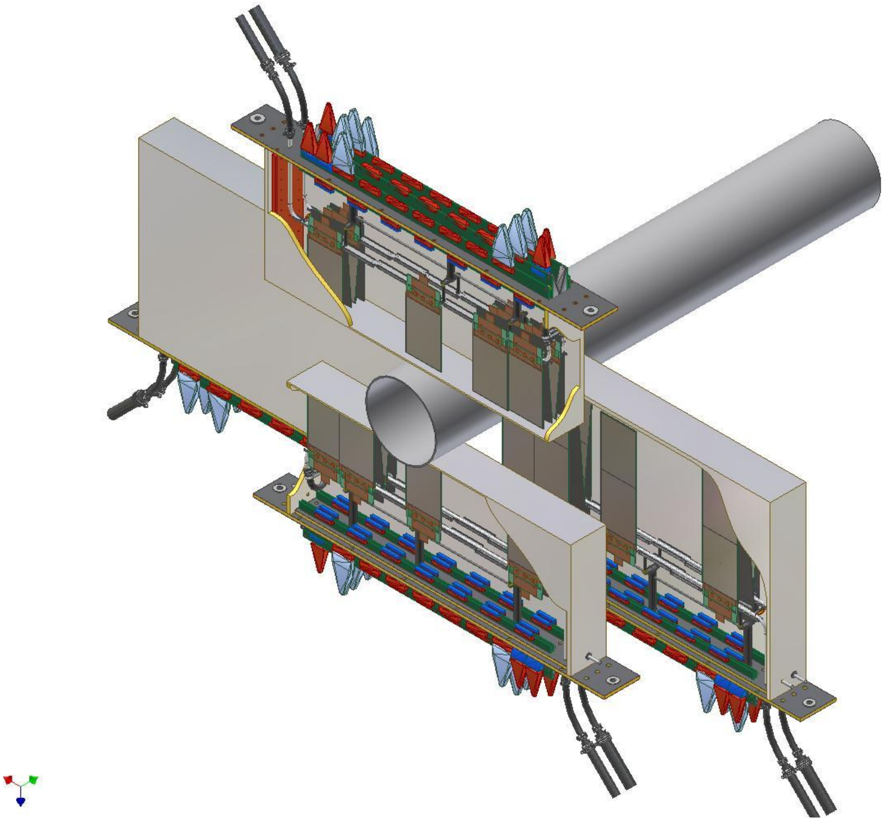

Figure 3.5: Schematic view of the LHCb Inner Tracker boxes of one station, placed around the beam pipe. The boxes are thermally insulated and will be flushed with cool dry nitrogen. The boxes to the left and right contain two-sensor modules while the top and bottom boxes are equipped with single-sensor modules.

i.e. outside of the detector acceptance. The next modules consist of two or three sensors, connected with 37.6 cm long Kapton cables to the read-out chips. The outer modules are built from four sensors and connect directly to the Front-end hybrid. The two middle layers are tilted with respect to the front and rear ones by ±5°. All four layers are enclosed in one common box, providing an ambient temperature of $< 5°$ C as well as electrical and optical insulation.

3.2.3 Read-out Electronics

The Beetle [Sch01], a custom Front-end chip, has been developed for the read-out of all silicon micro-strip sensors to be installed in the LHCb experiment. Its dynamic range is adapted to the signal range expected from the employed silicon sensors, i.e. ±10 times the charge of a minimum-ionizing particle crossing 150 μm of silicon substrate. It can store the analog signals collected from its 128 read-out channels for a latency of 4 μs, matching the latency of the Level-0 trigger decision. The multi-event buffer has a depth of 16 events, ensuring a deadtime below 1% at a read-out speed of 900 ns/event and a trigger rate of 1 MHz.

Each channel has a charge sensitive preamplifier and shaper with a peaking time

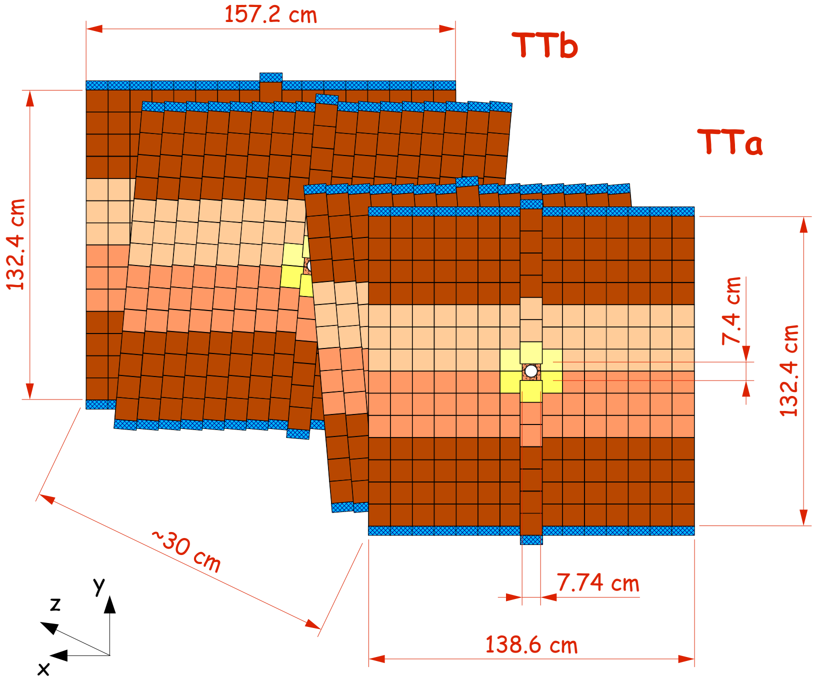

Figure 3.6: Layout of the LHCb Trigger Tracker. To cover the complete acceptance of LHCb, the last two layers are slightly wider than the first two. While the read-out strips of the first and the last layer are oriented vertically, the middle two are tilted by ±5°. Each rectangle corresponds to one silicon sensor, and the shading indicates the different read-out sectors.

of ≤ 25 ns, matching the LHC bunch crossing frequency of 40 MHz. The remaining signal detected 25 ns after the peaking time should be smaller than 30% of the peak signal, otherwise it would become very difficult at trigger level to distinguish whether a track segment belongs to the current event or the previous one. In the offline analysis, such ghost tracks could still be identified due to the smaller signal-to-noise ratios of all hits, but it would still increase the combinatorics for the tracking algorithms and hence increase the computing time for the reconstruction.

The chip can also run in binary mode, i.e. instead of analog signals, the discriminated output of the shaper is stored in the pipeline. There are several modes for the read-out multiplexing: The fastest analog read-out proceeds via four ports, each carrying 32 channels and control information for consistency checks. In binary mode, two ports carrying 64 channels can be used. The slowest mode is the single port mode, where all 128 channels are multiplexed to one read-out line.

A very important feature of the chip is its radiation hardness: For the application in the LHCb vertex detector, it has to be located close to the interaction point in a very harsh environment: 2 Mrad per year of operation is expected. Even at the position of the Inner Tracker, the accumulated dose is estimated to be 1 Mrad per year in the innermost part of the detector. Therefore, the Beetle was designed such that it can survive a total dose of 10 Mrad, sufficient for five years of operation inside the detector. To achieve this, the chip was fabricated in 0.25 μm CMOS technology, a process with an enhanced intrinsic radiation hardness. Furthermore, special design and layout techniques, e.g. enclosed gate structures, consistent use of guard rings and triple-redundant logic were applied. The actual radiation hardness of the chip (version 1.1) was tested up to 45 Mrad, showing no functional failures and only a slight degradation in the analog performance [Bau03]. While the chip version 1.3 already fulfils the requirements of VELO and Silicon Tracker, some minor modifications were introduced which might improve the performance further. Beetle chips of the version numbers 1.3, 1.4 and 1.5 were produced simultaneously, each in sufficient quantities for the supply of the experiment.

The Front-end chips are located on PCB hybrids [B+05c] as close as possible to the edge of the silicon sensors which they read out. In case of the Silicon Tracker, a ceramic pitch adapter matches the pitch of the Beetle input pads to the pitch of the silicon strips on the sensor. The hybrids are connected with low mass cables to service boxes outside of the acceptance of the detector, where the data are digitized before the optical transmission to the Level-1 electronics located inside the LHCb counting room.

3.3 Sensor Design

The research and design of the sensors was carried out in several steps: At first, prototype sensors segmented into regions with different strip geometries were tested for application at the Inner Tracker. After the decision to build the Trigger Tracker also with silicon sensors, thicker substrates had to be studied as well. Fortunately, it was possible to test samples of sensors designed for other experiments. The sensors were tested mostly at the CERN X7 testbeam facility in a 120 GeV π^- beam and with a laser set-up at the university of Zürich. Some of the prototypes were also exposed to high radiation doses in order to study their radiation hardness. As the Beetle read-out chip evolved, different versions of the chip were used for the tests. In the following, the results of the studies are summarized and the final layout is presented.

Common to all tests is the task of cluster finding: When a particle traverses the sensor, the released charge is not necessarily picked up only by on strip, but it can distribute over several strips. The signal charges for each read-out strip were extracted by subtracting the pedestal values from the raw data and then fitting a second- or third-order polynomial to account for the event-by-event common mode noise. After subtracting this common mode noise, the processed data are subject to the cluster finding algorithm. In order to detect the impact of the particle track as precise as possible, the charge sharing between the read-out strips was exploited: Instead of considering the coordinate of the strip with the largest signal as track impact position, all consecutive strips showing a signal were grouped into a hit cluster. The center-of-gravity of the signal charges gives measured track impact.

In this way, a resolution can be optained which is better than the resolution which would result from a binary read-out, i.e. dividing the strip pitch by $\sqrt{12}$.

After pedestal and common mode subtraction, the clustering algorithm first assigns a significance to each strip i to show a signal which was defined as d_i^2/n_i^2 where d_i is the ADC value after pedestal and common mode subtraction and n_i is the noise measured for this channel. All consecutive strips with a signal significance larger than a cut value, the seed-cut c_s, were joined into a cluster, and to reject noise clusters, the sum of the single strip significances also had to exceed a cut value, the χ^2-cut, to be accepted, i.e.

$$\begin{aligned} \frac{d_i^2}{n_i^2} &> c_s \ \forall\, i \\ \sum_i \frac{d_i^2}{n_i^2} &> c_{\chi^2}. \end{aligned} \tag{3.22}$$

In order to compare clusters composed of several strips with one-strip clusters, the signal-to-noise ratio was defined as S/N $= Q/\sigma$, where Q is the total cluster charge and

$$\sigma = \sqrt{\sum_i \frac{n_i^2}{n_s}}, \tag{3.23}$$

n_s being the number of strips in the cluster. Assuming that the noise is the same for all strips, the factor $\sqrt{n_s}$ normalises the S/N ratio such that for full charge collection effciency the value is independent of the cluster width and thus equivalent to the case where all charge is deposited on a single strip.

The parameters seed-cut and χ^2-cut of this cluster finding algorithm were tuned during the tests in order to perform realistic measurements close to the data processing of the full scale experiment. The tuning was done such that the highest efficiencies at still tolerable noise rates were obtained. Typical values for the cut parameters are seed-cut = 3 and χ^2-cut = 13 [A+02c].

More details of the data analysis are given in section 3.4.2.

3.3.1 Beam Tests

The first prototype sensors were purchased from the SPA Detector company, Kiev. The substrate thickness was 300 μm, the read-out pitch 240 μm and different strip geomeries were implemented: Implant widths of 48 μm, 60 μm and 72 μm were combined with 8 μm wider and 2 μm narrower metal strips. The prototypes were read out by HELIX chips[4] and tested with a ^{106}Ru β source, a laser system [B+01a] and at the T7 testbeam facility at CERN [B+01b]. The results indicated that the charge collection in the middle between two read-out strips was not fully efficient, since the observed signal-to-noise ratio plotted as function of the inter-strip position of the track impact on the sensor showed a dip between the strips, resulting in a hit finding efficiency reduced by up to 4% [B+01b]. A module assembled from three sensors, resulting in 20 cm long strips, yielded a signal-to-noise ratio (S/N) of 12 at a shaping time of about 50 ns.

---

[4] The HELIX chip is the predecessor of the Beetle chip, developed for the Hera-B experiment.

The same sensors were later tested at the X7 testbeam facility at CERN, read out for the first time with BEETLE chips of version 1.1. [G$^+$02]. A beam telescope provided by the LHCb VELO group was used to reconstruct the pion tracks and extrapolate them onto the active area of the sensors.

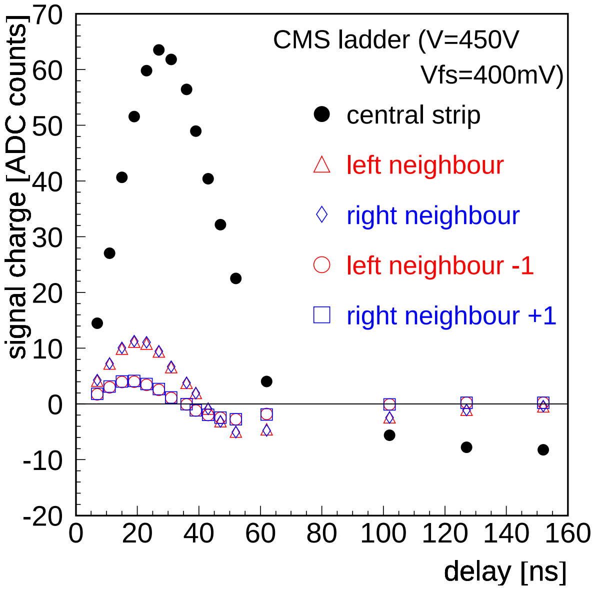

Figure 3.7: Signal pulseshape measured with the three-sensor 500 μm module and BEETLE 1.2. Superimposed are the pulseshapes obtained for the central strip of the cluster as well as the next and next-to-next neighbouring strips.

For the next beam test in May 2002 [A$^+$02c], prototype sensors featuring five different strip geometries were ordered from Hamamatsu photonics, Japan. They combined two strip pitches of 198 μm and 237.5 μm with implant widths of 50, 60, 70, and 85 μm, the metal strips always being 8 μm wider than the implants. Again, the signals were read out by BEETLE 1.1 Front-end chips. A beam telescope built from silicon sensors provided by the HERA-B vertex detector group was used to reconstruct the pion tracks. Data were taken for two different shaping times and as a function of the applied bias voltage. The single hit resolution of 17 μm of the HERA-B beam telescope allowed to study the signal charge collection and the hit efficiency as function of the distance to the next read-out strip.

The dip in S/N and efficiency in the inter-strip region which had been observed before [B$^+$01b] was confirmed and found to depend strongly on the strip geometry and only slightly on the bias voltage. For the wider pitch, the efficiency in the central region was about 3 % smaller than on top of a read-out strip, while for the narrow pitch, the effect amounted only to 1 %. Furthermore, the inter-strip hit finding efficiency was better for larger ratios of strip width over pitch. In this test, it was shown for the first time that the requirements for the Inner Tracker in terms of

S/N, efficiency and signal remaining after 25 ns (i.e. possible ghost hits in the next event) could be met also with two-sensor modules.

In May 2003, not only Inner Tracker prototype sensors were tested but also two sensors made from thicker substrates [A+03g]. In addition to a one-, a two- and a three-sensor module made of prototype sensors as described above, one module equipped with 410 μm thick sensors from the GLAST experiment and one module consisting of 500 μm thick sensors from the CMS experiment, each with three sensors, were tested. All modules were read out by Beetle 1.2. While the strips on the GLAST sensors had a pitch of 228 μm and an implant width of 56 μm, the CMS sensors had a pitch of 183 μm with an implant width of 46 μm. The resulting strip lengths of the three-sensor modules were 32.4 cm for the 320 μm module, 26.3 cm for the 410 μm module and 28.9 cm for the 500 μm module, leading to strip capacitances of up to 54.5 pF. The set-up including the beam telescope and four of the five modules under test was housed in a custom light-tight aluminium box (see Fig. 3.10 and section 3.4.1) built at the mechanical workshop of the Max-Planck-Institut für Kernphysik, Heidelberg.

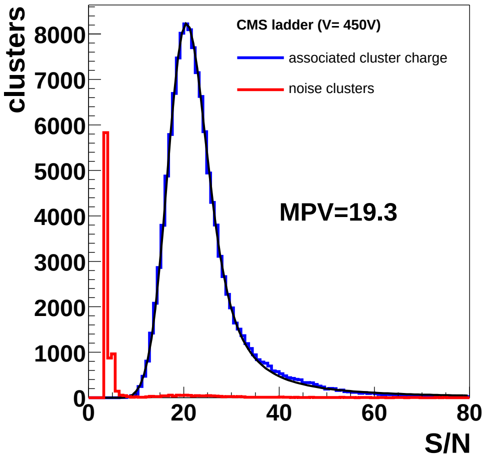

Figure 3.8: Signal-to-noise ratio measured with the three-sensor 500 μm module and Beetle 1.2. Superimposed are the well separated distributions for clusters associated to a measured track and the noise clusters.

High statistics data samples were recorded for two different voltages settings (1.5 and 2 times the respective depletion voltage), for three different shaping times and at several spots along the three-sensor modules. The shaping time of the Beetle 1.2 was found to be faster than the one measured with its predecessor, hence the requirements on the pulseshape could be met both for the IT and the TT, but in the latter case only with sensors which are at least 410 μm thick. The wealth of data allowed to characterize the S/N behaviour as function of the strip geometry, shaping time and applied bias voltage in such detail that reliable extrapolations to other sensor geometries were feasible. This was exploited in the development of the layout of the Trigger Tracker [GNS03]. Fig. 3.7 shows a typical pulseshape measurement, performed with the three-sensor 500 μm modules. From the shape, the rise time and the signal remaining 25 ns after the peaking time can be determined. Fig. 3.8 presents the signal-to-noise ratio obtained for this module. Here, a clear separation between the clusters associated with tracks reconstructed by the beam telescope and the noise clusters can be observed. In Fig. 3.9, S/N and the hit finding efficiency are depicted as function of the interstrip position, i.e. the value 0 on the abscissae corresponds to the center of one strip and the value 1 to the center of its right neighbour. Clearly, a dip in the S/N distribution in the central region is visible. Since the S/N values of this module are still high enough to distinguish real clusters from noise clusters, the efficiency is constant at a level of almost 100%. For modules with lower S/N, a dip in efficiency in the inter-strip region is observed.

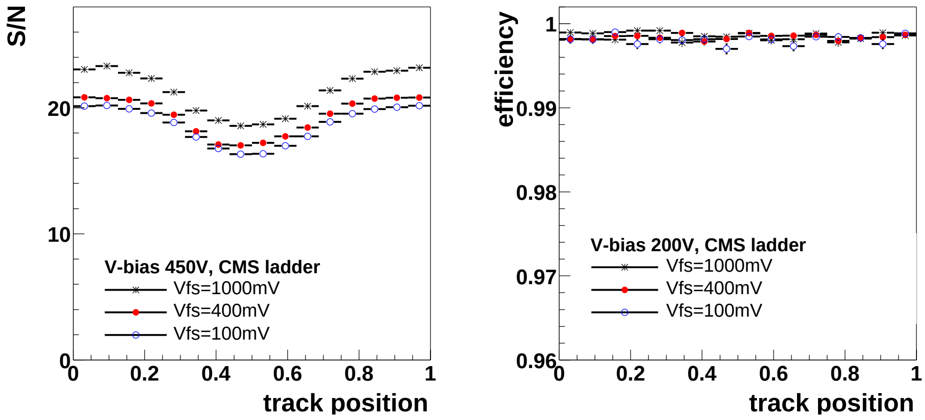

(a) S/N (b) efficiency

Figure 3.9: Signal-to-noise ratio measured with the three-sensor 500 μm module and Beetle 1.2 as function of the inter-strip impact of the track. Superimposed are the curves obtained with three different shaping times. While a slower shaping increases the collected signal, the efficiency cannot be improved further.

In the last beam test in July 2004 [A+04c], these extrapolations were tested for a module consisting of three CMS-type sensors connected via a 39 cm long Kapton cable to Beetle 1.3 read-out chips and found to be in excellent agreement with the measured data. For a shaping compliant with the LHCb requirements, S/N values of 16 close to the read-out strips and 13 in the centre between strips were found.

3.3.2 Laser Tests

The modules were also thoroughly tested in a laser set-up at the University of Zürich [B+03b, G+05]: The amplitude of pulses from 1064 nm Nd:YAG laser diode were adjusted such that the signal recorded with the sensors under test corresponded to the signal charge collected from a minimum ionizing particle traversing the sensor.

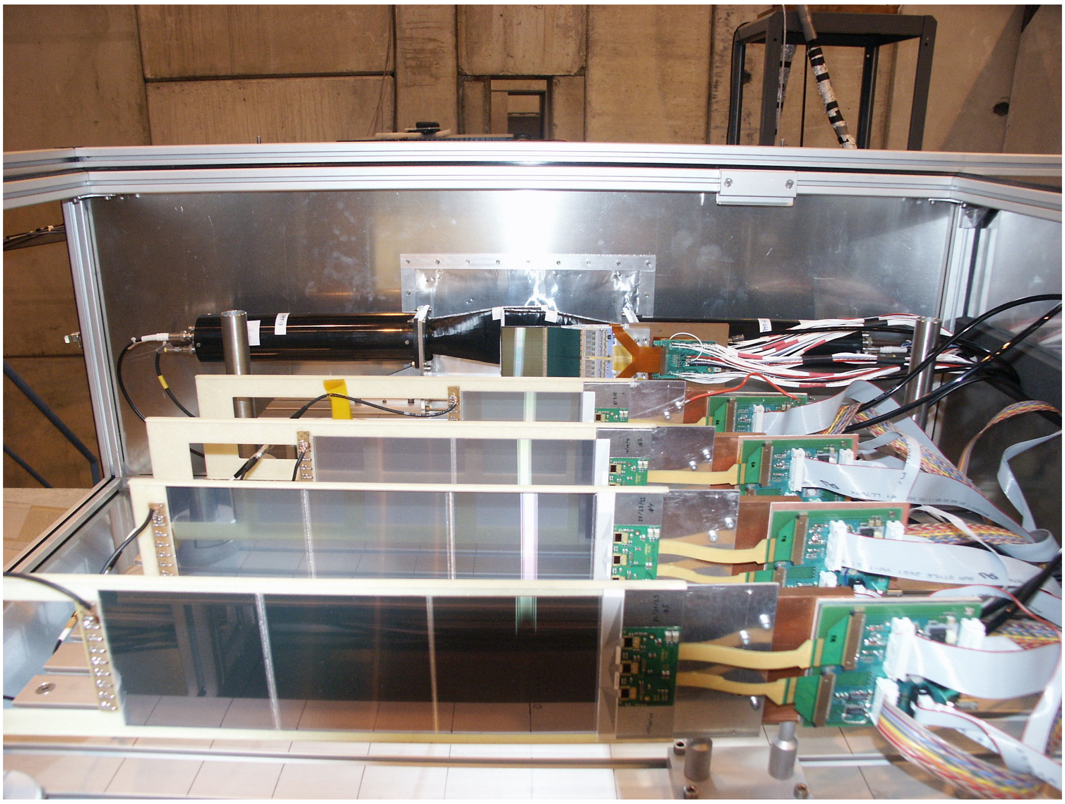

Figure 3.10: Testbeam set-up in a custom aluminum box. Viewing along the beam direction, four modules under test are shown: The three-sensor 500 μm module and the three-, two- and one-sensor 320 μm module. In front of the aluminium foil entrance window, one module of the Hera-B beam telescope and two scintillators used for triggering can be seen.

With a stepper motor moving the laser perpendicular to the strips in steps of 5 μm, the sensors could be tested over the whole width. A disadvantage of testing with a laser instead of a particle beam was that it does not penetrate the metal strips on top of the implanted electrodes. Therefore, tracks traversing the strips could not be simulated. A great advantage is that the set-up is freely available, while beam time at the X7 testbeam facility is usually rare.

The measurement program was very similar to the measurements carried out with the pion beam at CERN: Delay scans for different shaping times and voltage setting were performed in order to determine the pulse shape precisely. The rise time and the signal remaining after 25 ns could be measured as function of these parameters and as function of the sensor capacitance. Bias voltage scans yielded input about the optimal settings. The signal charge loss in the region between two read-out strips could also be quantified.

It has to be noted that the results obtained with the laser set-up are complementary to the testbeam results, since the charge density distribution caused by particles traversing a sensor is different compared to the charge profile caused by a laser pulse. Furthermore, a different data aquisition system was used. The laser tests therefore serve as important cross checks and complete the knowledge gained with the analysis of the beam test data. It increases the confidence in the understanding of the sensor properties that the results agree so well.

3.3.3 Radiation hardness tests

In order to assess the radiation hardness of the sensors, some of the modules were exposed to total doses of up to $6.3 \cdot 10^{13}$ protons per cm^2 (corresponding to about 20 years of operation inside the detector) using the 24 GeV proton beam at the T7 irradiation facility at CERN [LLV05]. Due to the inhomogeneous irradiation, the measurement of the depletion voltage after the irradiation was difficult, but it was concluded that the resulting depletion voltage was in any case lower than the original one. Thus, it will still be possible to overbias the sensors after many years of operation. The observation is in qualitative agreement with the so-called Hamburg model. From leakage current measurements, the damage constant α (see Equ. 3.16) and the hardness factor κ (see Equ. 3.17) could be determined and the resulting values of $\alpha = 2.78 \cdot 10^{-17}$ A/cm and $\kappa = 0.61$ are in agreement with existing data: Values of $\alpha = 2.54 \cdot 10^{-17}$ A/cm and $\kappa = 0.62$ have been published [B$^+$02b, L$^+$01]. The changes of sensor properties with the expected irradiation dose accumulated within the foreseen lifetime inside the experiment are thus well covered by the safety margins that were considered in the design of the sensors.

3.3.4 Final sensor layout

The final sensor layout was derived from the thorough evaluation of the results provided by extensive test with the 120 GeV π^- beam at CERN, the laser test in Zürich and the irradiation test [GNS03]. Simulations were carried out to understand and model the loss in signal charge observed for tracks traversing the sensors between the read-out strips [HL03], suggesting that the charge is trapped at the silicon-

type	overall size	thickness	strip pitch	strip width	no. of strips
1	78 mm × 110 mm	320 μm	198 μm	50(+8) μm	384
2	78 mm × 110 mm	410 μm	198 μm	50(+8) μm	384
3	94 mm × 96 mm	500 μm	183 μm	46(+12) μm	512

Table 3.1: Parameters and properties of the final sensor layout [B$^+$05b, B$^+$04]. The column concerning the strip width gives both the implant width and the width of the metal strips in parentheses. Sensors of type 1 and 2 are used for the one- and two-sensor modules of the Inner Tracker while all modules of the TT are built from type 3 sensors.

SiO_2 layer. This trapping cannot be overcome by applying higher bias voltages, in agreement with the results from beam and laser tests.

In order to maintain enough safety margin to be able to keep the sensors in operation for many years, the sensors designs listed in Table 3.1 were agreed on. Only the one-sensor modules of the Inner Tracker are build from the thinnest sensors. For the two-sensor modules, 410 μm thick substrates will be used, while for the Trigger Tracker, due to the length of the modules and the necessity to connect the innermost region with long Kapton cables to their read-out electronics, the 500 μm thick sensors must be employed.

3.4 Preparation and Analysis of Beam Test Measurements

The work summarized in this section covers a wide range of topics: The design of the transportable set-up for testing the prototype modules, both in beam tests and with cosmic rays, which has been used during the beam tests in 2003 and 2004, is described and explained. A software framework to process and analyze the recorded data was implemented, including the alignment with respect to the reference frame defined by the beam telescope and a new method to quantify the different noise contributions. In addition to a generic analysis of beam test data, properties of the Beetle chip, namely the homogeneity of the pipeline, were studied. Thus, the work covers main steps from the preparation of the data taking, the raw data processing providing the necessary information for any data analysis and finally, an example of a specific analysis topic.

3.4.1 Design of a test set-up for prototype modules

The experience of the early beam tests lead to the idea to design a robust box containing the basic infrastructure of the test set-up, in order to ease setting up the equipment. The layout of the box is shown in Fig. 3.11, while a picture including prototype modules for testing is presented in Fig. 3.10. The requirements met in the design of the box and the equipment are listed here:

- The general layout is the following: The beam enters the box through a thin aluminium foil entrance window. Then it traverses a pair of overlapping scintillators and a pair of double-sided silicon sensors of the beam telescope. Afterwards, it passes through the prototypes under test, before it traverses another pair of scintillators and the second half of the beam telescope. A four-fold coincidence of the scintillation counters triggered the events to be recorded while the beam telescope was used to reconstruct the tracks and extrapolate them to the prototype sensors. The beam leaves the box through an exit window (also made of thin aluminium foil), thus other experiments downstream of the box could take test data parasitically.

- The four scintillation counters were custom-made for the beam tests with an area matching precisely the sensitive area of the HERA-B sensor modules which served as a beam telescope. They were placed in overlapping pairs close to the entrance and exit windows of the box. In this way, the efficiency to trigger only on events which contain a track within the acceptance of the beam telescope was improved.

- The box had to be light-tight because incident light can lift electrons from the valence band into the conduction band of the silicon sensors and hence increase the leakage current strongly. At the same time, easy access was necessary in order to be able to change the positions of the modules quickly. Therefore, the box was equipped with a top lid, covering the whole area of the light-tight compartment, and a front lid, covering the front wall (left hand side in Fig. 3.11). Furthermore, the cables had to be routed through a slit padded with foamed rubber to ensure light-tightness.

- The whole box was built from metal in order to make it electrically conducting, and it was connected to ground during data taking. This is necessary to provide shielding from electromagnetic fields for the electronics.

- Both the beam telescope and the prototype modules are very lightweight, but the cables attached to the read-out electronics supplying the system with high voltage are very heavy and the optical fibres used for the read-out are very stiff. Thus, one end of the box was extended and provided a frame to which the cables could be fixed, such that they did not pull at the modules.

- With its adjustable feet, the box could be positioned such that the beam was centered on the beam telescope. For this purpose, alignment marks were attached to the box and to the platform carrying the prototype modules.

- Since the prototype sensors were wider than the acceptance of the HERA-B beam telescope, the platform was designed to be adjustable in height. In this way, the modules under test could be moved vertically and hence all strips of the sensors could be illuminated by the beam. In order to test all sensors of one module, the platform had horizontal slots perpendicular to the beam direction and the modules were mounted on carriers that could be moved along these slots.

- Since cosmic rays are available everywhere, they provided a means for a thorough system check before transporting the equipment to CERN. The box has

> additional feet at one end which allow to turn it and erect it such that cosmic rays could be used instead of the particle beam at X7. This gave us the opportunity to locate and solve problems in the set-up. However, the event rates obtained with cosmic rays are too small to collect the high statistics data samples that were needed for the R&D program of the Silicon Tracker.

The box was successfully used in the beam tests in 2003 and 2004.

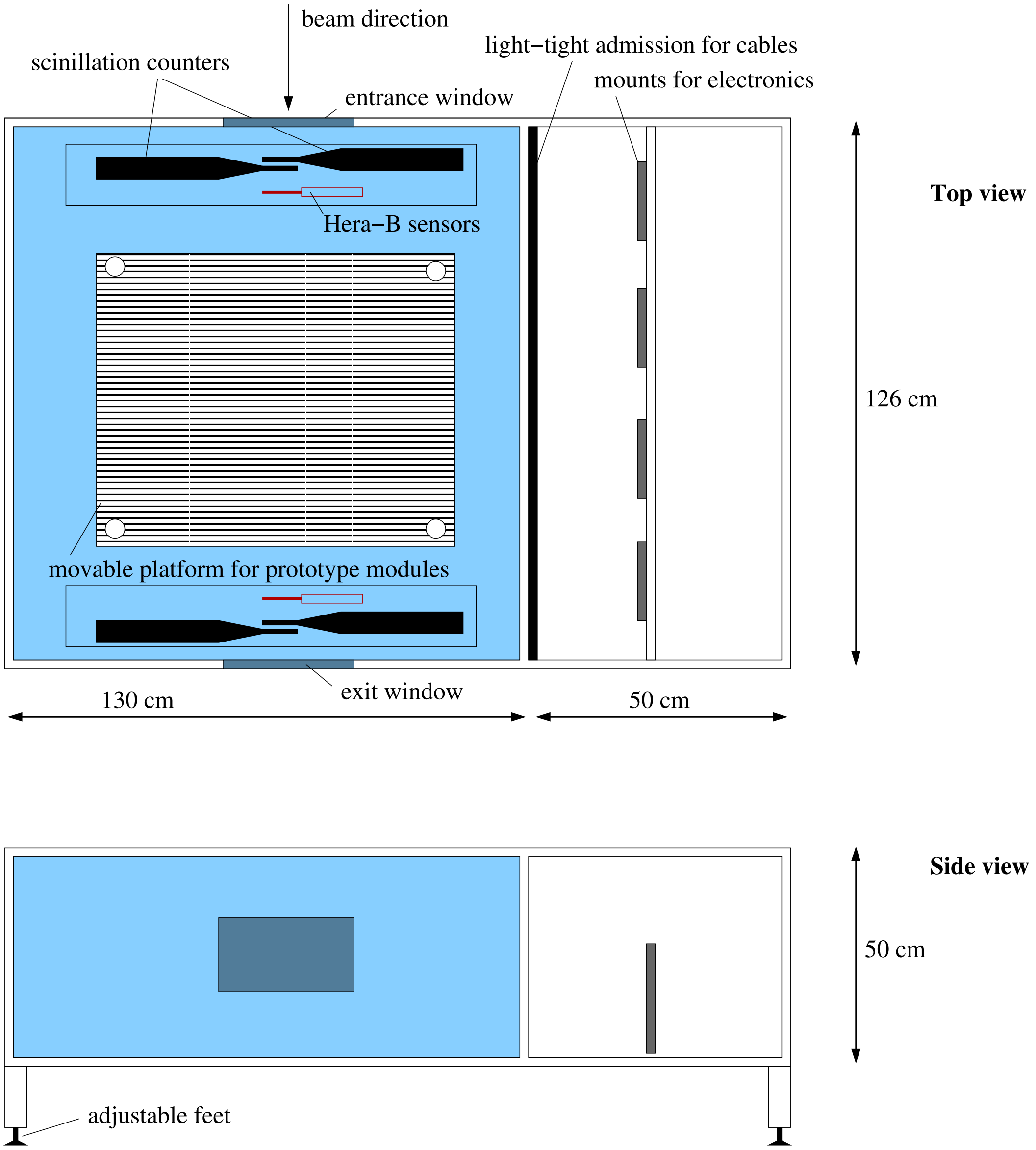

Figure 3.11: Layout of the test beam set-up box. It provides a light-tight compartment (shaded part) housing the scintillation counters for triggering, the HERA-B beam telescope and a movable platform for the prototype modules under test as well as mounts for the cables and electronics.

3.4.2 Software framework for beam test data analysis

For the beam test in May 2002, a new software framework written in C++ was developed. It comprised the implementation of the alignment of the prototype sensors with respect to the HERA-B beam telescope using reconstructed pion tracks, the raw data processing including pedestal and common mode noise subtraction and the reconstruction of the signal clusters. For the pedestal and common mode noise calculation, a new statistical method was implemented. The alignment of the beam telescope and the reconstruction of the pion tracks was provided by an external program [B+01b]. The main parts of the new software framework are summarized in the following:

- **Pedestal and common mode calculation:** Pedestals and noise were determined from the raw pulse heights for each strip i in an iterative procedure using a statistical method. The ADC value x of a strip ($x = \mathrm{adc}[i]$) is assumed to be composed of three different parts: pedestal (p), noise (σ_x) and common mode (c), where noise and common mode are assumed to be uncorrelated:

  $$x = p + a_x \cdot \sigma_x + b \cdot c \tag{3.24}$$

  The distributions of a_x and b are normalized to have an RMS equal to one. Similarly, one can write for the distribution of the mean ADC value y of its neighbouring strips ($y = (\mathrm{adc}[i-1] + \mathrm{adc}[i+1])/2$):

  $$y = q + a_y \cdot \sigma_y + b \cdot c \tag{3.25}$$

  From the distribution of y versus x (see Fig. 3.12(a)), one can determine

  $$\begin{aligned} \langle x \rangle &= p, \qquad (3.26)\\ \langle y \rangle &= q,\\ \langle x^2 \rangle &= p^2 + \sigma_x^2 + c^2,\\ \langle xy \rangle &= pq + c^2. \end{aligned}$$

  All other terms cancel if a_x, a_y and b are uncorrelated. Therefore, the average common mode c can be extracted from the correlation of x and y,

  $$\langle xy \rangle - \langle x \rangle \langle y \rangle = c^2, \tag{3.27}$$

  and the noise σ_x from

  $$\langle x^2 \rangle - \langle x \rangle^2 = \sigma_x^2 + c^2. \tag{3.28}$$

  In this way, pedestals and noise are determined (almost) independent of any assumptions about the shape of the baseline. The central area of the distribution of y versus x in Fig. 3.12 shows a two-dimensional Gaussian density as demonstrated by the projections. While the outliers correspond to hits, the noise and common mode are Gaussian distributed. For the pedestal and noise determination, a window of two RMS around the mean was used in order to reject the outliers.

- **Clustering:** The algorithm used for the reconstruction of hit clusters in the beam and laser test data was already described in section 3.3. It was also part of the implementation of this data processing and analysis package.

  Complementary to the cluster reconstruction, the signal charge and the signal-to-noise ratio was also determined by summing up the four closest strips around the track impact point on the strip[5]. In this way, the accuracy of the charge determination by the clustering could be determined, indicating room for improvement of the algorithm. The most-probable value (MPV) of the four-strip cluster charges were consistently larger than the MPV found by the clustering algorithm by roughly 10%, depending on the sensor geometry [A+03g]. This effect is due to charge sharing with the neighbouring strips. Since the amount of charge collected by the neighbouring strips is much smaller than on the main strip or strips, they are likely to be discarded by the cut removing the noise clusters.

- **Alignment:** For a scan of the hit finding efficiency as function of the track impact position on the sensor under test, a precise track reconstruction is needed and the positions of the prototype modules have to be determined accurately within the coordinate system of these tracks. Then the track impact positions on the sensors can be calculated and the distance to the closest hit cluster can be measured, indicating the spatial resolution of the sensor. The fraction of tracks, to which a hit can be associated yields the hit finding efficiency.

  Assuming a provisional alignment, starting from rough measurements of the geometry of the set-up, the residuals of the clusters reconstructed from the prototype modules with respect to the track impact point on the modules can be calculated. The residuals can be expressed in terms of the alignment parameters, i.e. the distance in beam direction with respect to the origin of the reference system of the beam telescope, a tilt angle correcting for rotations around an axis parallel to the strips on the sensors (effectively decreasing the visible pitch of the strips) and an offset necessary to define the position of the first strip of the sensor. The mean residual was then minimized in an iterative procedure, i.e. starting from the rough measurement of the sensor position, new aligment constants were calculated as described above. These were used as starting values for the next iteration. This procedure was then repeated until it converged.

The complete analysis of the data recorded during the 2002 beam test was analysed with this software package. For the following beam tests, it was adapted and extended to integrate modules with different geometries [A+03g], but the basic functionalities were left unchanged.

---

[5] This ensures the collection of the complete charge deposited within the sensor, since the average cluster extends over two to three strips, depending on the sensor geometry.

3.4.3 Beetle chip pipeline homogeneity

The Beetle Front-end chip, described in section 3.2.3, provides 128 channels for which it can store events of up to 160 sampling intervals. This is accomplished by a switched capacitor array of 130×187 cells acting as a ring buffer (pipeline) [Bau03]. The homogeneity of this pipeline, i.e. its uniform response of all cells of the array to incoming signals from the read-out strips of the attached silicon sensor, was studied using data recorded with Beetle chips of the version 1.2 during the 2003 beam test at the X7 test beam facility at CERN [A+03h]. This uniformity is important because a change in the data quality depending on the pipeline column in which the data were stored before being read out after a positive Level-1 trigger decision would be hard to control and very difficult to simulate in Monte Carlo studies. Different noise levels could for instance have an impact on the online track reconstruction on trigger level, because the threshold on the signal-to-noise ratio of hit clusters would be less sensitive in the distinction of real hit clusters from noise clusters. Therefore, the behaviour of all pipeline columns must not differ sizeably.

Variations along the columns

For the online processing of the data, it is foreseen to subtract the pedestal values measured for each channel, i.e. the mean pedestal for all pipeline cells storing data for that channel. If the variations along the columns would be large, then pedestal values measured for each cell of the pipeline must be used, increasing the computation time needed for this operation. If they are small, then the mean pedestal values per channel can be applied.

The following studies were carried out using a data sample recorded without the pion beam, i.e. without hits associated to tracks. In order to measure the variation of the pedestals across the pipeline, the pedestal value was determined for each pipeline cell separately. In Fig. 3.13(a), surface plots of the middle of the three Beetle chips (see Fig. 3.4) of the 320 μm two-sensor module are shown. The characteristic baseline shape of the Beetle 1.2 (noticeable in the global curvature) and slight channel-to-channel variations of the pedestals with the channel number can be observed. A subtraction of the mean pedestal value for each strip (i.e. averaged over all column numbers) helps to disentangle the variations along the pipeline column numbers from baseline shape and channel-to-channel deviations; the resulting histogram is depicted in Fig. 3.13(b). A clear pattern stands out (see also Fig. 3.13(c)): The pedestal differences along each column have a "slope" along the channels, and in general, positive and negative "slopes" alternate. Furthermore, the amplitude of the deviation from the mean pedestal seems to fluctuate periodically.

The remaining variations include in addition to the pipeline variations contributions from event-by-event common mode fluctuations. These are treated in the following way: A function is fitted to the pedestal subtracted raw data which is expected to describe the behaviour of the common mode. In our case, a second order polynomial is used, since it gives good efficiencies at a tolerable noise hit rate in the general analysis of the beam test data [A+03g]. This fitted function is then subtracted from the pedestal-subtracted raw data.

After common mode subtraction (see Fig. 3.13(d)), the striped structure of the pipeline has almost vanished. The vertical stripes belong to channels to which an additional circuitry for calibration purposes was bonded (see below). In Fig. 3.14(a), the common mode noise and the contribution of the pipeline inhomogeneity are compared. Here, the common mode noise was measured as the RMS of the common mode event-by-event corrections and the pipeline contribution was taken to be the difference of the pedestal value for each column number and the mean pedestal for all column numbers of one channel[6]. The similar curvatures of the two distributions suggests that the pipeline contribution is positively absorbed by the common mode correction. Which part is removed by the common mode correction is shown quantitatively in Fig. 3.14(b): Here, the grey shaded histogram shows the pipeline contribution as described above, while the blue line represents the data after mean pedestal and common mode correction averaged over all column numbers, representing the contribution of the pipeline inhomogeneity after common mode correction[7]. The mean spread of the data along the columns amounts to roughly 0.3 ADC counts, compared to a strip noise[8] of the order of 3.8 ADC counts as determined in [A$^+$03g]. Thus, the pronounced striped structure of the BEETLE pipeline does affect the data quality only marginally.

Calibration channels

For charge calibration, a few strips were bonded to a PCB at the sensor edge opposite to the readout chips (see Ref. [B$^+$03b] for more details). The influence of this additional connection on the pipeline homogeneity was already shown in Fig. 3.13(d). For low column numbers, the values after pedestal and common mode correction for the calibration channels are higher than the typical values, and for high column numbers they are systematically lower. A comparison of one of the calibration strips with the RMS of the data of all strips is presented in Fig. 3.15. This pattern is not unique for the calibration channels, in fact all channels have a certain structure along the columns; but the amplitude is much larger for those which have extra bonds for external charge injection. For a typical channel, the structure is less pronounced and, in addition, very similar to its neighbour channel. Therefore the applied common mode correction can level out the differences between the channels in general.

The cause for this effect on the pipeline is not known yet. An explanation could perhaps arise from the difference in capacity due to the additional connection. This hypothesis could be investigated with data from VELO sensors since they contain strips of different length and width over pitch (and therefore different strip capacitances) on one sensor.

Note that, as expected, the RMS of the data of all strips in Fig. 3.15 also shows the striped structure already observed in Fig. 3.13 (c).

---

[6] The common mode noise cancels out when calculating pedestal values.

[7] If the chosen common mode noise parametrization does not describe the common mode effects perfectly, a contribution of the common mode noise is still contained in the remaining noise component shown in Fig. 3.14(b).

[8] The total noise of a channel consists of a part correlated to the neighbouring channels, i.e. the common mode noise, and an uncorrelated part, the strip noise.

Edge channels

For a good performance of the detector, all channels from the first to the last must be fully functional. Therefore, it is important to test whether the edge channels indeed behave the same as the channels in between.

The first quantities to investigate are pedestal and total noise values. Fig. 3.16 displays the pedestal values for the first and last 10 channels of each BEETLE chip of the 410 μm module, while Fig. 3.17 shows the total noise defined as the sigma of a Gaussian fitted to the raw ADC value distribution of each channel. In general, the first channels of all Beetles behave in the same way as a typical channel. Note that for the 410 μm module, the first channel on the first BEETLE chip and the last channel on the third BEETLE chip coincide with the first and last strip of the sensor. Therefore, the abnormally high noise on the first channel on the first BEETLE might be caused by the sensor edge.

In our beam test data the last channels of each Beetle differed from the channels in between. Their pedestals were found to be systematically higher and their total noise lower than for a typical channel. The reason for this difference was found in the Beetle readout clock divider setting [Bau03], which is used if its read-out frequency is a fraction of its sampling frequency. In the beam test, data were sampled at 40 MHz and read out at 20 MHz, which means `RclkDiv = 1`. The effect of this setting on the last channel is shown in Fig. 3.18 in a screen shot of an oscilloscope displaying the analogue output signal of a Beetle chip at sampling and readout frequencies of 10 and 5 MHz (also corresponding to `RclkDiv = 1`). The signal is clearly not constant over the whole width of the 128^{th} channel (i.e. the period of data transmission), it is split into halves with two different levels. The same effect[9] can be observed when sampling at 40 MHz and reading out at 20 MHz, as in the test beam measurements. During the test beam data taking period, we adjusted the FADC sampling point to the second half of the signal window. Laboratory tests showed that digitizing the signal in the first half yields normal pedestal and noise values.

When `RclkDiv` is set to zero, i.e. the sampling and readout frequencies are the same, no level shift in the 128^{th} channel is visible. Therefore, all channels including the first and the last channel are fully operational for LHCb data taking.

In Fig. 3.18, two negative spikes are visible at the end of the data transmission. In consecutive readout, they can alter the first header bit in such a way that approximately the first third of the signal plateau is distorted. This should not cause problems in general, but if the readout frequency is much lower than the sampling frequency, it could be difficult to find a timing for the FADC which samples the first header bit and the last channel correctly.

---

[9] The effect should also be present in version 1.3 of the Beetle chip. On the last channel, data are only transmitted for a period of one `Sclk` cycle, afterwards the pipeamp reset potential `Vd` is sent (for the rest of the `Rclk` cycle). That means, e.g. for `Sclk/Rclk = 3` the fraction of time where the real signal is transmitted on the last channel shrinks to 1/3 of an `Rclk` cycle [DB03]. In the four port mode, every 32^{nd} channel is affected.

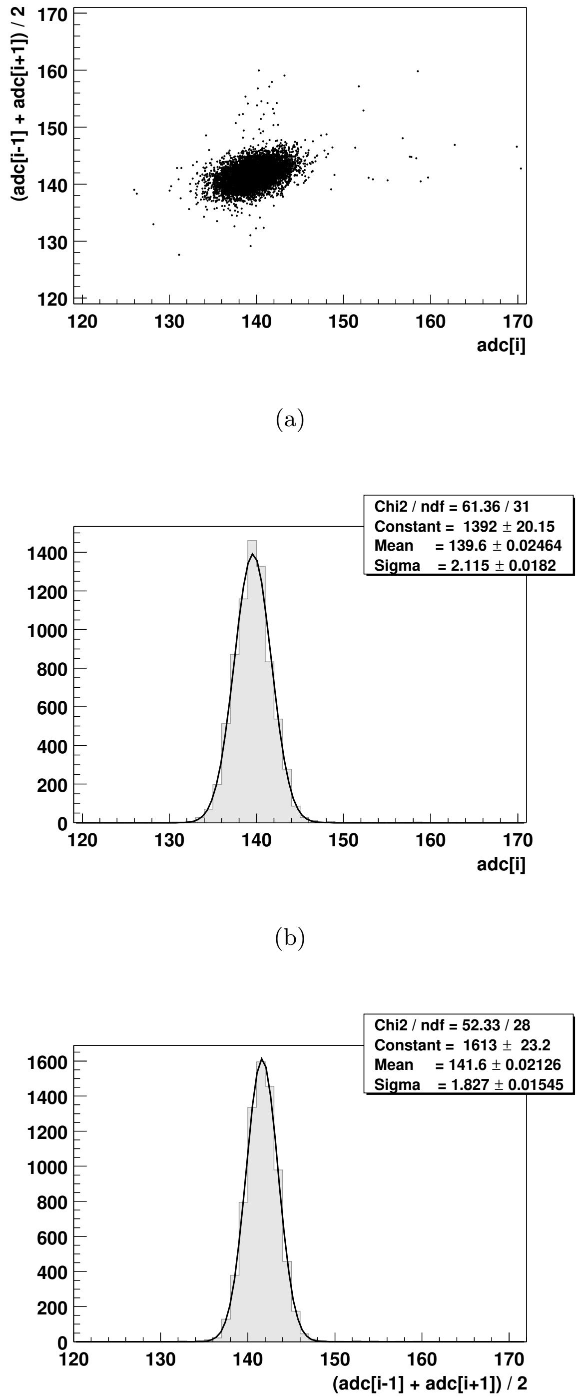

(a)

(b)

(c)

Figure 3.12: Correlation of the ADC value of one strip and the mean ADC value of its left and right neighbour strips (a). From the moments of this two-dimensional distribution, the strip noise and the average common mode noise can be determined. The projections on to the axes ((b) and (c)) show gaussian distributions.

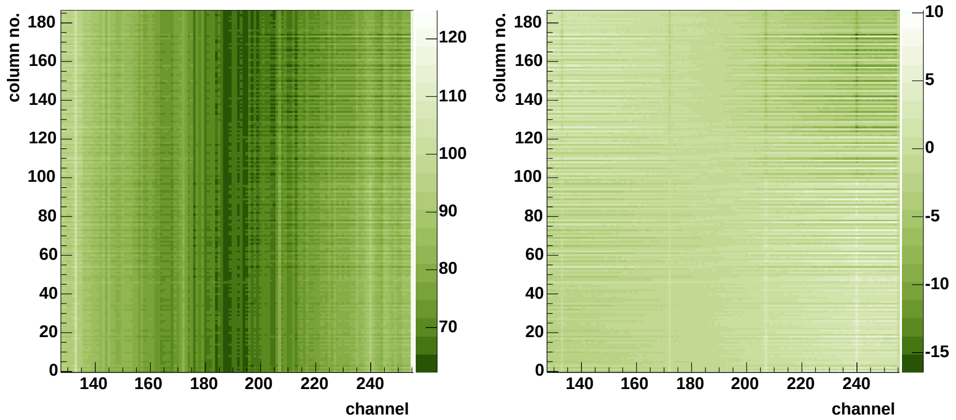

(a) Raw data averaged (pedestals).

(b) Pedestal subtracted.

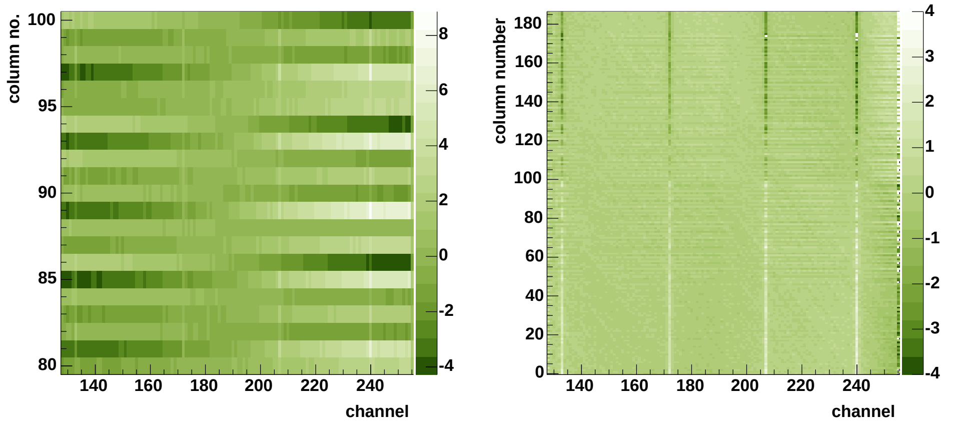

(c) Pedestal subtracted, zoomed in.

(d) Pedestal and common mode subtracted.

Figure 3.13: Pipeline structure of the Beetle 1.2 measured with a 320 μm module. The channel number refers to the numbering scheme of the module, i.e. the plots shows data from the second chip. The averaged raw data are plotted as a function of the channel and the pipeline column number (a). After pedestal subtraction, a pattern of stripes along the x axis becomes visible (b), which is shown in more detail in (c). The pattern almost vanishes after the subtraction of the common mode contribution (d). Now, some channels which had been prepared for a charge calibration display a different behavior then others.

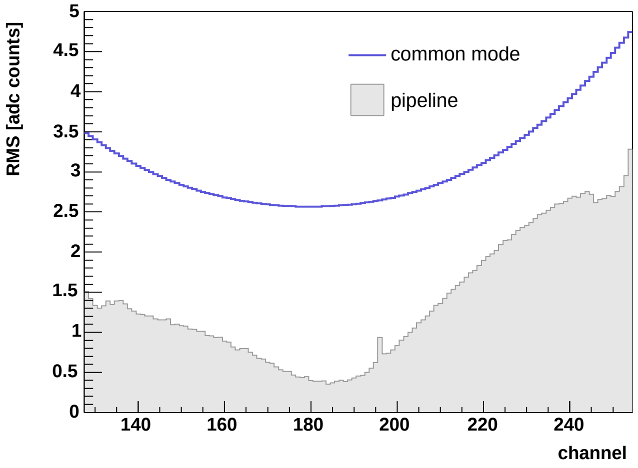

(a)

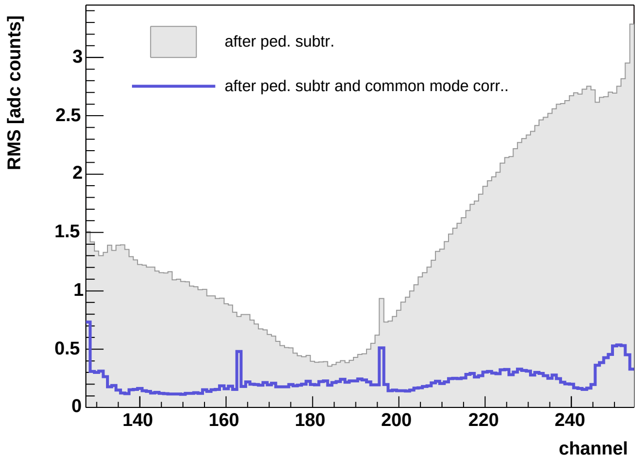

(b)

Figure 3.14: Comparison of common mode noise and pipeline inhomogeneity. In (a), the common mode noise (blue line) is measured in terms of the RMS of the event-by-event common mode corrections, while the pipeline inhomogeneity contribution (grey shaded histogram) is quantified by the RMS of the data averaged for all column numbers after subtraction of the mean pedestals. In (b), the pipeline contribution (grey shaded histogram) is shown again together with the averaged data after mean pedestal and common mode correction (blue line), i.e. the part of the pipeline inhomogeneities that is not absorbed in the common mode correction. The spikes belong to calibration channels (see text). For clarity reasons, results are shown for the 410 μm sensor, which is not divided into regions of different strip width and pitch.

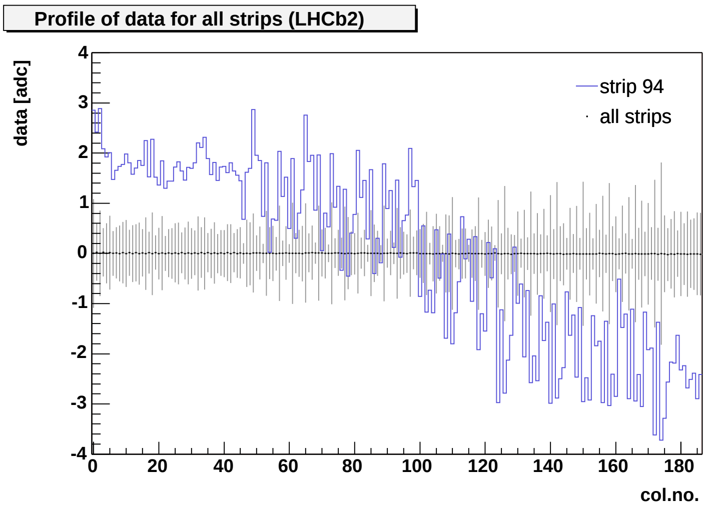

Figure 3.15: Data after pedestal and common mode subtraction for calibration strip 94 (blue line) in comparison with the RMS of the data of all strips (black markers: mean, error bars: RMS).

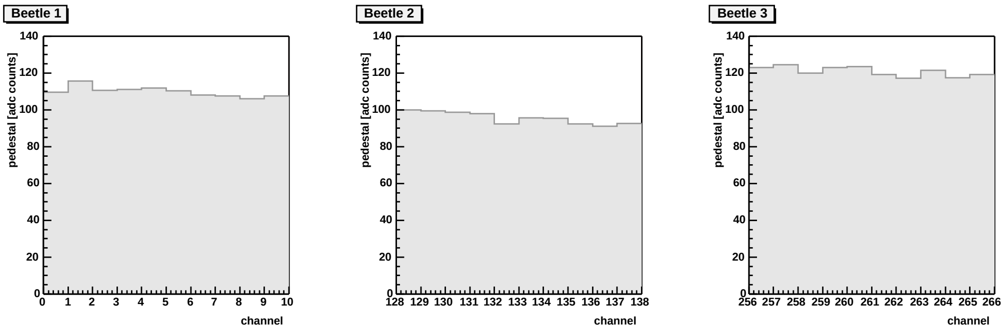

(a) lower edge of the Beetle chips

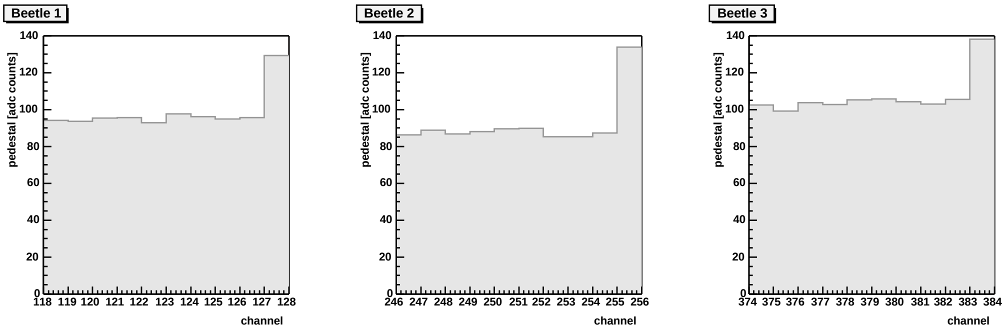

(b) upper edge of the Beetle chips

Figure 3.16: Comparison of first and last channels with other channels: Pedestals for the first (a) and last (b) 10 channels of each Beetle chip of the 410 μm module.

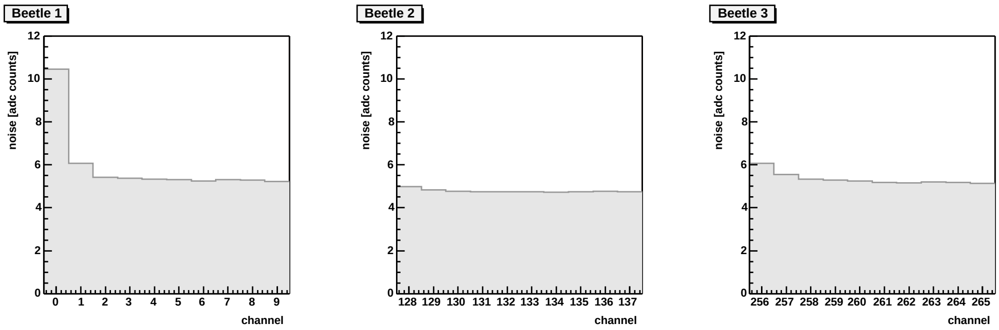

(a) lower edge of the Beetle chips

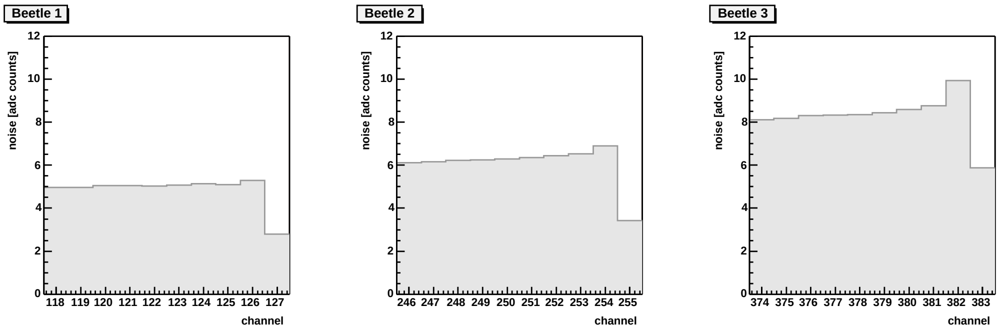

(b) upper edge of the Beetle chips

Figure 3.17: Comparison of first and last channels with other channels: Total noise for the first (a) and last (b) 10 channels of each Beetle chip of the 410 μm module.

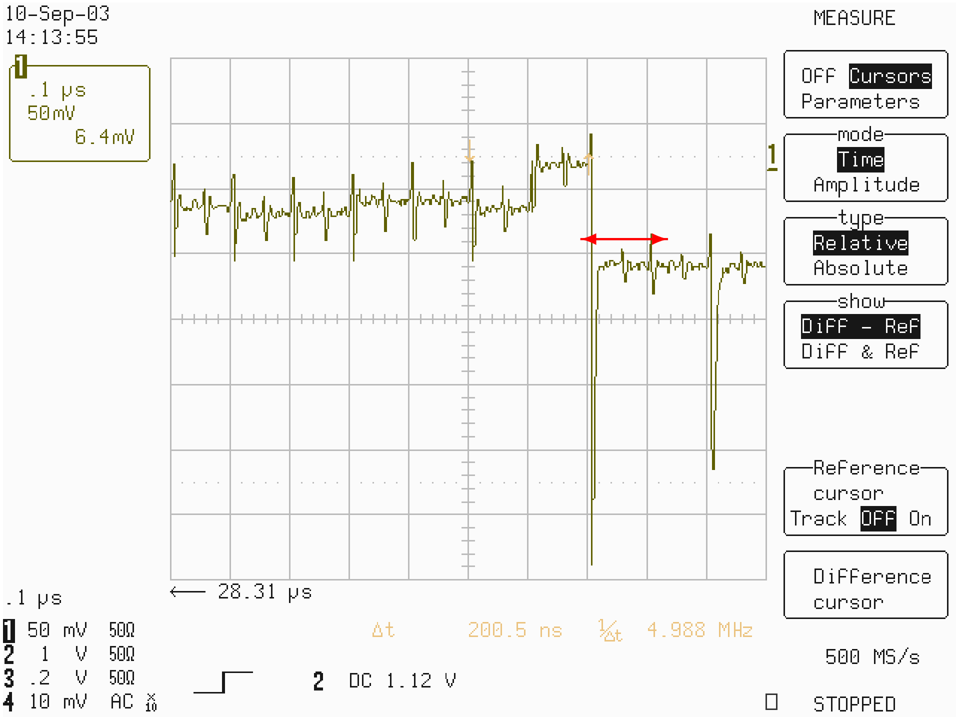

Figure 3.18: Screen shot of the last channels sampled at 10 MHz and read out at 5 MHz. The 128th channel is indicated with a red arrow. The signal transmitted for this channel is clearly not constant over its range. Thus, the ADC value of the signal depends on the FADC sampling point.

Chapter 4

Hyperon Production in *pA* collisions

This chapter presents the reconstruction of hyperons created in proton-nucleus collisions at a center-of-mass energy of $\sqrt{s} = 41.6$ GeV, recorded with the Hera-B detector. Hyperons are one of the possible probes for quark-gluon plasma (QGP) which is expected to form if the energy density is high enough. To meet this condition is the goal of four dedicated experiments at the heavy-ion collider RHIC at BNL. Since the lifetime of the plasma is presumably very short, experimental searches for QGP can only use final state observables to draw conclusions about the properties of the state of matter. Theoretical models are therefore needed in order to arrive at well founded interpretations of the experimental results. Input for these models is the understanding of the processes involved in nucleon-nucleon and nucleon-nucleus collisions. Since major parts of these model are phenomenological, measurements of particle production in *pA* collisions provide a very important input to refine the understanding of the underlying processes. The first section of this chapter gives an introduction to the present status of understanding of hyperon production and quark-gluon plasma.

The contribution of this thesis is presented in this chapter: Λ, Ξ and Ω baryons and their antiparticles were reconstructed in collisions of protons with targets of three different materials: carbon, titanium and tungsten. With the help of Monte Carlo simulations, total and differential cross sections and production ratios of the particles within the kinematic range of the experiment were evaluated as function of the atomic number of the target. The second section of this chapter describes the analysis in detail and presents the results.

4.1 Hyperon Production and Quark-Gluon Plasma

The relative production of baryons containing strange quarks is one of the signatures currently investigated in the search of quark-gluon plasma (QGP). In this state of matter, the energy density is so high that the confinement of quarks and gluons inside nucleons is expected to be revoked and the partons can move freely. The conditions for this were supposedly present shortly after the Big Bang, and theoretical models predict that they can be reached in high-energy heavy-ion collisions, too. In order to utilize hyperon production measurements as a probe for a possible observation of QGP, the production in nuclear matter at energies below the threshold for QGP formation has to be understood. In this section, models for the production of hyperons in hadron collisions and in QGP are briefly described. A short summary of recent results in the search for QGP is given.

4.1.1 Hyperon Production in Proton-Nucleus Collisions

In order to understand and describe particle production in proton-nucleus collisions, the understanding of the corresponding process in nucleon-nucleon collisions is a prerequisite. This section gives a short overview of theoretical descriptions of hadron production in general and hyperon production in pA collisions in particular.

Nucleon-nucleon collisions

In 1969, observations in deep inelastic electron-proton scattering indicated that hadrons can be viewed as systems of independent pointlike scattering centres (in the infinite momentum frame) - partons, which Bjorken and Paschos identified with quarks [BP69]. This model was then applied to the hadron production in the inclusive process $A + B \to C + X$ of hadrons C with very large transverse momenta ($p_T \gg 1$ GeV), yielding a power-law behaviour of the invariant inclusive cross section [BBK71]:

$$E\frac{d^3\sigma}{dp^3} \propto \frac{1}{p_T^4}. \tag{4.1}$$

While at low p_T an exponential fall-off had been measured, an excess at high p_T as resulting from a power-law was in fact measured at the CERN ISR, but in disagreement with the prediction, the observed cross section followed roughly a p_T^{-8} behaviour [A+73, B+73a, B+73b], indicating that the model was incomplete.

Subsequently, theoretical models based on the quark-parton model were more and more refined [G+90]. Four steps were identified which subdivide the underlying events of the collision into individual processes, each of which contributes to the kinematics of the final state particles produced in the collision. Since these processes are separated well enough in time, the global process can be represented by the product of the individual probability densities (factorization hypothesis). The four steps are

- initial state radiation before the scattering,
- hard scattering of at least two partons,

- the evolution of the partons after the hard scattering and finally
- the fragmentation of the free partons into hadrons.

A consistent description of the experimental observables can only be achieved if the contributions of all four steps are taken into account [vE04]. For the initial state effects, the structure of the nucleons as measured by deep-inelastic lepton-nucleon scattering experiments is a prerequisite. Two components are needed: The longitudinal momentum depends on the momentum fraction x of the scattered parton q with respect to the momentum of the nucleon. The probability for this process is described by the parton density distributions $q(x, Q^2)$, where Q^2 is the square of the momentum transferred between the projectile and the target parton. The transverse momentum is affected by the internal transverse momentum of the parton inside the nuclei[1] and by gluon radiation before the hard scattering. The latter contribution depends on Q^2 since more gluons are radiated if the transferred momentum is large.

During the hard scattering, the two scattering partons of the colliding proton-nucleon system acquire high transverse momenta, while the direction of motion of the spectating proton remnants remains basically unchanged. For large momentum transfers, i.e. $Q^2 \gg 1$ GeV^2, perturbative QCD can be applied and the differential cross sections can be calculated, resulting in a power-law behaviour. Taking the parton density distributions and the dependence of the strong coupling constant, α_s, on the transferred momentum into account, the resulting cross section is $\propto 1/p_T^n$ with values of n larger than 4, i.e. closer to the experimental findings than the first naive approach.

After the scattering process, hard processes can still change the kinematics of the scattered partons significantly: The partons loose energy by radiating gluons or creating quark-antiquark pairs. These branching processes are described by the Dokshitzer-Gribov-Lipatov-Altarelli-Parisi (DGLAP) relations [Dok77, GL72, AP77] which consider the probabilities of theses splitting processes and the momentum distributions associated with the created partons. During this evolution, the energy scale of the involved partons changes from a hard to a soft scale.

On the soft energy scale, α_S becomes large and therefore perturbative QCD is not applicable any longer. Phenomenological models had to be developed to cover this part of the process. One of the most successful models is the string fragmentation model, which is also used in the JETSET Monte Carlo software package [Sjö94] utilized in HERA-B [I$^+$99][2]. Here, the QCD color field between the partons wich move apart is described as a color flux tube stretched between them. The string constant of this tube is deduced from hadron spectroscopy to be roughly 1 GeV/fm. As the partons move away from each other, the potential energy stored in the string increases, and eventually the string breaks by the production of a new $q\bar{q}$ pair. The resulting string fragments may still have sufficient energy to create more $q\bar{q}$ pairs until only on-mass-shell hadrons remain. Since the newly-created hadrons are aligned with the original partons from the scattering process, they form a so-called jet of particles. The predicted properties of these jets have been studied in detail and

---

[1] From the uncertainty principle, a mean transverse momentum of $250 - 300$ MeV is expected for nucleons.

[2] JETSET is an integral part of the PYTHIA and FRITIOF [Pi92] packages.

agree well with experimental observations [G+90]. One property which is relevant for the results of this analysis is the prediction of a plateau of the production rate of particles at mid-rapidity.

Nucleus-nucleus collisions

The Glauber model [Gla59] is an ansatz to describe the dynamics of nucleus-nucleus collisions by considering collisions at the baryon level, i.e. the collision of the two nuclei is treated as a series of collisions of one or many of the constituents of the incident nucleus with the constituents of the target nucleus. In this way, knowledge gained e.g. by studying pp collisions can be utilized for pA and AA collisions. After the impact of a projectile nucleon onto a target nucleon, the resultant energetic baryon-like object can be regarded as a projectile object subsequently colliding with another nucleon of the target nucleus. Each collision contributes with the nucleon-nucleon cross section to the cross section of the whole process. The Glauber model takes the geometrical configuration of the colliding nuclei quantitatively into account by assuming a profile function [Cap91]

$$T_A\left(b\right) = \int dz \rho\left(b, z\right). \tag{4.2}$$

(Here, $\rho(b, z)$ is the nuclear density, b is the impact parameter and z the coordiate in direction of motion of the incident particle.)

From these profile functions, the average number of collisions along the path of the projectile particle, depending on the impact parameter between the incident particle and the target particle can be deduced. Multiplying the average number of collisions by the nucleon-nucleon cross section and integrating over all impact parameters, one arrives at the total cross section[3].

Phenomenologically, a common parametrization relating the cross section in pA collisions to the cross section in pN collisions is

$$\sigma_X^{pA} = \sigma_X^{pN} \cdot A^{\alpha_X} \tag{4.3}$$

(Here, A is the atomic number of the target material, σ_X^{pA} and σ_X^{pN} are the proton-nucleus and proton-nucleon cross sections for the production of a particle X.)

From geometrical considerations general limits for the parameter α_X, which describes the scaling with the atomic number of the target nucleus, can be deduced: If the production cross section in pN collisions is large, then the target nucleus can be approximated by a black disc and σ_X^{pA} scales with the surface of the nucleus, i.e. $\alpha_X \approx 2/3$. If it is very small (as it is the case for heavy quark production), then the cross section is proportional to the number of nucleons, i.e. $\alpha_X \approx 1$. Experimental findings at HERA energies yield $\sigma_{inel} \sim A^{0.711(1)}$ [Car03].

---

[3] A possible correction to this approach would be to take into account that one or more nucleons may become excited and hence contribute with a different cross section.

Hyperon Production

Hyperons are baryons with strangeness quantum number S different from zero. Tab. 4.1 presents the ground state hyperons and their basic properties. They are created mainly by annihilation of lighter quarks, as depicted in Fig. 4.1(a), or by gluon-gluon fusion, Fig. 4.1(b). The cross sections for these processes can be calculated using perturbative QCD. Here, all possibly contributing subprocesses are decribed using Feynman diagrams. Each vertex in such a diagram introduces a factor $\sqrt{\alpha}$, where α is the corresponding coupling constant, and propagator terms account for the energy and momentum transferred by the intermediating particles. Thus, the Feynman diagrams represent a series expansion in powers of the coupling constant. In case of strong interactions, the strong coupling constant α_s depends on the transferred momentum, hence it depends on the energy range whether the power series converges or not. The Feynman diagrams in Fig. 4.1 represent all leading order contributions to the processes mentioned above; adding them coherently and integrating them over the whole accessible phase space yields the cross section at leading order.

However, since the mass of the strange quark is of the order of Λ_{QCD}, pertubative methods are limited in precision. Therefore, leading order perturbative QCD calculations (pQCD) are expected to yield just a fraction of the complete result [GV02], i.e. the next-to leading order contribution will be of the same order of magnitude. One attempt to model the strangeness production in hadron collisions is therefore a combined model with two components, presented in [GV02]: The so-called leading twist component is based on the pQCD calculation and the higher-twist "intrinsic" component describes the hadronization of a sea $s\bar{s}$ pair from one of the colliding hadrons.

At hadron level, the elementary processes presented in Fig. 4.1 have to be embedded into the hadronic environment: This is achieved by the parton density functions describing the probability to scatter a parton with momentum fraction x depending on the momentum transfer, and by fragmentation functions describing the probabilities that a quark hadronizes into a given hadron species. The model of [GV02] assumes equal probabilities for all possible strange hadron species.

The intrinsic particle production component considers the wavefunction of a hadron as a superposition of Fock state fluctions, e.g. $\mid n_v\rangle$, $\mid n_v q\bar{q}\rangle$, $\mid n_v s\bar{s}\rangle$, $\mid n_v s\bar{s}q\bar{q}\rangle$, ... where n_v are the valence quarks of the hadron. When projectile and target hadrons scatter, the coherence of the Fock state is broken and the intrisic fluctuation hadronizes. This can either proceed in an uncorrelated way, similar to leading twist production, or by coalescence with spectator quarks from the wavefunction. In the latter case, if the minimal Fock state $\mid n_v s\bar{s}\rangle$ is part of the reaction, then the flavour of the final state hadron is correlated to the flavour of the projectile or the target, introducing a leading particle effect. Thus, in contrast to the uncorrelated fragmentation, where no particle species is favoured over another, in the coalescence mechanism some hadron types are created more abundantly than others, and - depending on the colliding particles - some may not created in this way

hyperon	quark content	S	I	mass [GeV]	life time [s]
Λ	uds	-1	0	1.115683(6)	2.632(20) $\cdot 10^{-10}$
Σ^+	uus	-1	1	1.18937(7)	0.8018(26) $\cdot 10^{-10}$
Σ^0	uds	-1	1	1.192642(24)	7.4(7) $\cdot 10^{-20}$
Σ^-	dds	-1	1	1.197449(30)	1.479(11) $\cdot 10^{-10}$
Ξ^0	uss	-2	1/2	1.31483(20)	2.90(9) $\cdot 10^{-10}$
Ξ^-	dss	-2	1/2	1.32131(13)	1.639(15) $\cdot 10^{-10}$
Ω^-	sss	-3	0	1.67245(29)	0.821(11) $\cdot 10^{-10}$

Table 4.1: Ground state hyperons and their properties [E+04]: constituent quark content, strangeness quantum number S, isospin I, invariant mass and life time. By convention, the s quark has a strangeness $S = -1$.

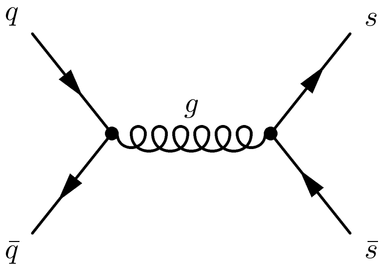

(a) $q\bar{q}$ annihilation.

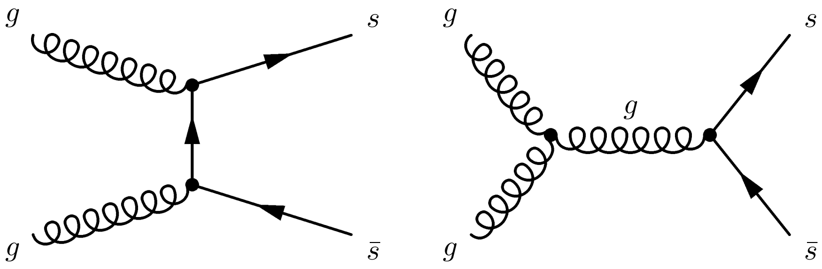

(b) gluonic processes.

Figure 4.1: Leading Feynman diagrams for $s\bar{s}$ production. The cross sections for the quark-antiquark annihilation (a) and the gluonic processes (b) are of the same order, but since there are only two different light quarks, the 8 different gluons make the gluon contribution the dominant one.

at all. In [GV02], the model is compared to hyperon/antihyperon asymmetries as function of the kinematic variable x_F (see section 4.2.4) measured in pion-proton collisions. With a suitable calibration of the relative contributions of the two different strangeness production schemes, some of the observed features could be reproduced by the model while others could not be accounted for, indicating room for improvement.

4.1.2 Quark-Gluon Plasma

If the energy density in a hadron collision is high enough, quarks and gluons are deconfined for a short while, i.e. they can interact as free particles. This new state of matter is called quark gluon plasma (QGP) and is extensively searched for by heavy-ion colliders. The properties of QGP are not directly accessible for measurements, therefore they have to be deduced from the final state. Models are therefore needed to describe the visible signatures of the QGP and to provide hints which observables are the most promising probes of the new state.

A useful phenomenological description of the confinement of quarks in hadrons is given by the bag model [C^+74]. Here, quarks are treated as massless particles inside a bag of finite dimension and as infinitely massive outside of the bag [Won94]. The balance of the bag pressure B, directed inbound, and the kinetic energy of the quarks, directed outwards, results in the confinement of the quarks, and deconfinement occurs if this balance is disturbed. The bag pressure B is a phenomenological quantity which takes the nonperturbative effects of QCD into account. From this simple model, an intuitive understanding arises of how QGP can be formed: If the pressure of the quark matter exceeds the bag pressure, then a transition into new phase of matter takes place.

Two extreme cases of high pressure are possible: Very high temperature and very high baryon number density. With rising temperature, the kinetic energy of the confined quarks and hence the pressure increases. If the baryon number density rises, the Pauli exclusion principle forces the quarks into higher energy levels, leading also to a pressure increase. In the former case, QGP with a net baryon number density of zero is possible, i.e. particles and antiparticles occur in equal numbers. In the latter case, since each quark carries a baryon number of 1/3, the high quark density corresponds to a high baryon density, i.e. the resulting QGP can have a non-zero net baryon number density. Fig. 4.2 depicts schematically the dependence of the phase transition on the temperature and the net baryon density of the system. In general, numerical calculations in the framework of lattice QCD yield values of $T \approx 170$ MeV $\approx 10^{12}$ K for the transition temperature, corresponding to energy densities of $\epsilon \approx 1$ GeV/fm^3 [Kar02].

In AA collisions of high energy, the energy density is expected to reach values high enough for quark gluon plasma to be formed. If the center-of-mass energy is in the order of $\sqrt{s_{NN}} \approx 5 - 10$ GeV per nucleon, then the so-called "nuclear stopping power" is assumed to be large enough to completely stop the colliding particles. As a result, a baryon-rich QGP is expected to be formed. For even higher values of $\sqrt{s_{NN}} > 100$ GeV, the particles cannot be stopped anymore but continue to move along their initial direction, leaving a QGP with very little or even zero baryon

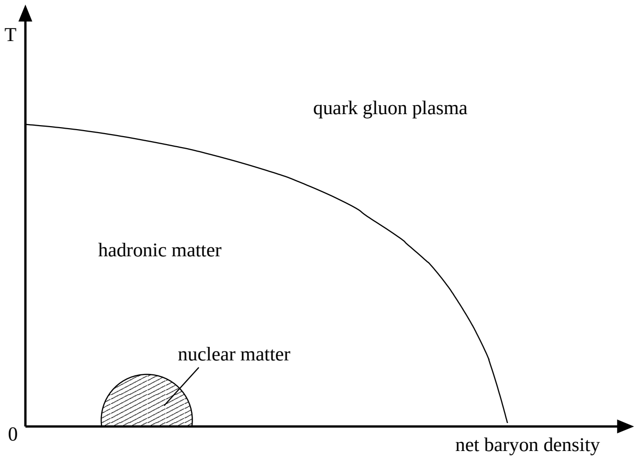

Figure 4.2: Phase diagram in the plane of temperature and net baryon density [Won94]. The phase transition of hadron matter to quark gluon plasma takes place if the temperature and/or the net baryon density exceed critical values.

content behind [Won94]. In any case, the energy density decreases rapidly as the system expands after the collision. Soon, the plasma hadronizes, i.e. a hot hadron gas is created where the quarks are confined again. This phase transition is called chemical freeze-out since the produced hadron species are already the ones of the final state. In the hot hadron gas, elastic interactions still take place until the energy density decreases such that these interactions stop, too. After this so-called thermal freeze-out, also the kinematics of the final state particles are fixed. The evolution of the system of colliding particles is schematically depicted in Fig. 4.3.

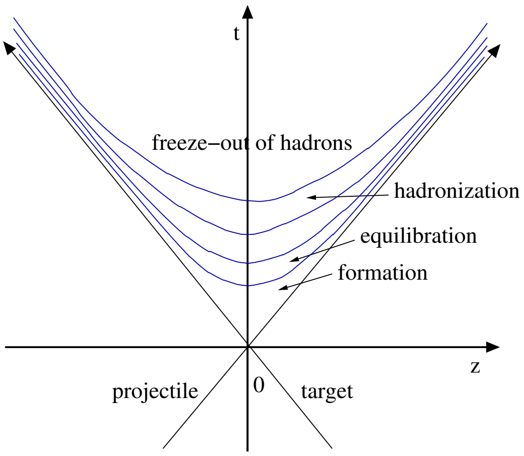

Figure 4.3: Space-time evolution of a system of colliding nuclei. If the energy density is high enough, QGP is formed after the collision. As the system cools down, the plasma hadronizes.

Probes for QGP

In order to unambigously prove that QGP was formed in a collision, many possible signatures are investigated. In general, the difficulties lie in the reliable prediction of how the effect differs from the case where no QGP was created. Reference measurements for comparison are a prerequiste, and the conditions of these measurements match those of the intended QGP measurement as close as possible. For instance, pA and pp collisions are often used as reference systems for AA collisions at similar or higher nucleon-nucleon center-of-mass energies. The comparison of results from pp and pA collisions helps to understand nuclear effects which have to be disentangled from possible QGP effects in AA collisions. Furthermore, if a prediction depends strongly on assumptions used in the model, this may lead to wrong interpretations of the results, if the assumptions were incorrect. Therefore, many different signatures have to be studied, and evidence for the observation of QGP can only be claimed if they deliver a consistent picture. Some of the most important probes proposed are:

- **Di-lepton production:** In the QGP, lepton pairs can be produced by fusion of quarks and anti-quarks. Since they interact only electromagnetically, the mean-free path is large enough such that the kinematics of the di-leptons are not altered too much. Therefore, their production rate and momentum distribution reflects the thermodynamical state of the medium in which they were produced.

- **J/Ψ suppression:** A J/Ψ particle is a bound state of a $c\bar{c}$ quark pair. Inside the QGP, the quarks and gluons are deconfined, therefore also the binding of the $c\bar{c}$ is weaker and the J/Ψ may become dissociated. Hence the J/Ψ production inside QGP is expected to be suppressed compared to collisions of lower energy density.

- **Photon production:** Similarly to the production of di-leptons, photons created trough quark-antiquark annihilation or in Compton processes of gluon scattering inside the plasma interact only electromagnetically with the surrounding particles and can therefore carry information about the thermodynamical state outside of the system.

- **Pion momentum correlations:** Here, the Hanbury-Brown-Twiss effect known from astrophysics is exploited. The intensity correlation of two photons emitted by the same source measured for different distances between the photon detectors provide information about the angular diameter of the source. In high energy physics, the momentum correlations of pairs of identical particles such as pions measured in coincidence are used to assess the matter distribution during the late stages of the reaction process.

- **Enhanced strangeness production:** The high energy density in QGP allows for an abundant production of $s\bar{s}$ quark pairs, and since the expected QGP life time in AA collisions is expected to be roughly 10^{-23} s, i.e. much shorter than the typical time scale of weak interactions of 10^{-10}, strict strangeness conservation can be safely assumed [PKR86]. That means that the enhanced production of strange quarks leads to an enhanced production of strange particles in the final state of the collision. This will be described in more detail in the following.

Enhanced hyperon production

In the high energy density regime present in QGP, strange quark-antiquark pairs can be produced easily by annihilation processes of lighter quark-antiquark pairs (see Fig. 4.1(a)) or by gluons (Fig. 4.1(b)). The cross sections for both processes are of the same order, but since there are 8 different gluons and only two different light quarks, the gluonic production of strange quark-antiquark pairs dominates.

At first, immediately after the formation of QGP, the newly created phase space for strange quarks and antiquarks is empty. Subsequently, the production of $s\bar{s}$ pairs via the processes describes above starts to fill this phase space until chemical equilibrium is reached or until the QGP transfoms into a hot hadron gas, where the energy density is too low to create strange particles. Chemical equilibrium is given when the production and decay rates of a particle are the same, i.e. when both processes balance each other and the particle densities are constant in time. It has been estimated that the equilibration time amounts to about $\tau \sim 10$ fm/c at a temparature of $T = 200$ MeV, while typical interaction times in heavy-ion collisions are roughly 5 - 10 fm/c. Therefore, the system might not reach the chemical equilibrium before the plasma breaks down. For temperatures of $T = 400$ MeV, however, the phase space of $s\bar{s}$ pairs should definitely saturate [PKR86]. Thermal equilibrium, i.e. the levelling of the momentum distributions of the different particle species trough interactions, is reached very quickly after the formation of the QGP.

The $s\bar{s}$ pairs created in the QGP enter the final state of the collision in the form of strange particles, i.e. as strange mesons and baryons (hyperons) and their antiparticles. For these to be formed, additional light quarks and antiquarks are needed, therefore the densities of u, $\bar{u}$, d and $\bar{d}$ quarks in the system determine the hadron composition of the final state. For instance, if the plasma has a negligible baryon number density, then the densities of quarks and antiquarks are the same and the production rates of particles and their antiparticles are the very similar. On the other hand, if the quarks are more numerous than the antiquarks, the production ratios of antihyperons to hyperons will be smaller. The latter are therefore very good measures both for the proof that a QGP was formed and also for the diagnosis how baryon-rich the QGP was. Ratios of hyperons of the same type, e.g. $\bar{\Lambda}/\Lambda$, $\bar{\Xi}/\Xi$ and $\bar{\Omega}/\Omega$ as well as ratios of hyperons with different strangeness content, e.g. Ξ/Λ, Ω/Ξ (and the corresponding ratios of the antiparticles) are considered.

The coalescence model [Bia98, Z^{+}00] predicts relations between antibaryon to baryon ratios of different species, but only assuming deconfined quarks and neglecting the gluonic degrees of freedom. The advantage of the model lies in its simplicity: It is based on the assumption that the probability of creating a baryon with a given quark content is proportional to the probability that three quarks with appropriate quantum numbers are found in the same small phase space volume (and correspondingly for antibaryons). The resulting relations[4] are

$$\begin{aligned} p &= \omega_p \cdot (b_q q)^3 \\ \Lambda, \Sigma &= \omega_\Lambda \cdot (b_q q)^2 \cdot (b_s s) \\ \Xi &= \omega_\Xi \cdot (b_q q) \cdot (b_s s)^2 \\ \Omega &= \omega_\Omega \cdot (b_s s)^3 \end{aligned} \qquad (4.4)$$

(Here, q and s are the relative probabilities to find a light (i.e. a u or d quark) and a strange quark in the suitable phase space region and the ω_i are proportionality factors accounting for properties of the baryon type, assumed to be equal for baryon and antibaryon.)

The parameters b_x are derived from the requirement that the numbers of the constituent quarks do not change during the hadronization:

$$\begin{aligned} s &= 3\Omega + 2\Xi + (\Lambda, \Sigma) + \bar{K} + \eta \\ \bar{s} &= 3\bar{\Omega} + 2\bar{\Xi} + (\bar{\Lambda}, \bar{\Sigma}) + K + \eta \\ q &= 3p + 2(\Lambda, \Sigma) + \Xi + K + \pi^d \\ \bar{q} &= 3\bar{p} + 2(\bar{\Lambda}, \bar{\Sigma}) + \bar{\Xi} + \bar{K} + \pi^d \end{aligned} \qquad (4.5)$$

(Here, x is the relative number of directly produced particles of a hadron species x.)

Inserting Equ. 4.4 into Equ. 4.5, one obtains a set of non-linear equations for the b_x normalization constants. The ω_i in Equ. 4.4 are difficult to calculate, but if only ratios of antibaryons to baryons are considered, they cancel out, together with the b_x:

$$\begin{aligned} \frac{\bar{p}}{p} &= \frac{\bar{q}^3}{q^3} \\ \frac{\bar{\Lambda}}{\Lambda}, \frac{\bar{\Sigma}}{\Sigma} &= \frac{\bar{p}}{p} \cdot D \\ \frac{\bar{\Xi}}{\Xi} &= \frac{\bar{p}}{p} \cdot D^2 \\ \frac{\bar{\Omega}}{\Omega} &= \frac{\bar{p}}{p} \cdot D^3 \end{aligned} \qquad (4.6)$$

where

$$D = \frac{b_q q \cdot b_{\bar{s}} \bar{s}}{b_{\bar{q}} \bar{q} \cdot b_s s} \qquad (4.7)$$

Comparing the predictions with experimental results from CERN SPS [K+97, B+97, C+99], [Bia98] found that the measured ratios from Pb-Pb collisions can be well described by the coalescence model, while the agreement with p-Pb data is poor. Also for preliminary data from Au-Au collisions at RHIC, the results are well described by the model predictions [Z+01] indicating that the model assumption of deconfined quarks is justified.

---

[4] The coalescence model only counts quarks, therefore no distinction between the Λ and the Σ and the neutral and charged Ξ hyperons is made. In case of deconfined quarks, however, all measurements should yield the same value D.

4.1.3 Experimental Results for QGP

First experiments searching for quark gluon plasma were carried out at the AGS at BNL (at an energy of $\sqrt{s_{NN}} = 5$ GeV per nucleon in the center-of-mass system and the SPS at CERN ($\sqrt{s_{NN}} = 17.2$ GeV). They found a very dense state of matter, possibly partonic, but no definite conclusions could be drawn from the results [Sat03]. The system of colliding heavy ions seemed to evolve from a short period of deconfinement into a thermalized system with collective behaviour, but did not show both at the same time. It was therefore anticipated that QGP should be found by future experiments at higher energy densities at the RHIC collider at BNL, or even at the LHC at CERN.

In autumn 2005, all four heavy-ion experiments at RHIC, STAR, PHENIX, BRAHMS and PHOBOS, published a critical summary of the results obtained during the first three years of operation at RHIC [A+05b, A+05c, A+05d, B+05a]. The goal of the RHIC measurement program is not only to find evidence for the formation of QGP, but also to characterize it in terms of experimental observables. Data were taken in the range of $\sqrt{s_{NN}} = 130$ GeV to $\sqrt{s_{NN}} = 200$ GeV, for p-p, d-Au and Au-Au collisions. The results of all four experiments agree very well in almost all measured channels, increasing the significance of the measurements.

The measurement programs covered charged particle multiplicities, transverse energy, yield ratios, two-particle correlations and suppression of particles at high p_T. The initial energy densities which were achieved in central collisions reached values as high as at least 5 GeV/fm^3, well above the threshold, beyond which the formation of QGP was predicted, of roughly 1 GeV/fm^3 [Kar02]. Fits of statistical models to the relative abundances of particles consisting of the three lightest quarks suggest that chemical equilibrium was formed at a temperature of $T \approx 175$ MeV, one of the conditions for QGP. In contrast to the expectations, however, the newly formed state of matter did not show properties of an ideal gas of non-interacting partons, but rather as a coherent state like a fluid, where the mean free path of the particles is short. Furthermore, no sign of a clear phase transition was observed, all observables evolved smoothly as function of the energy.

It is therefore a matter of intensive debates as to whether the results prove the formation of QGP in heavy-ion collision data at RHIC, but all publications agree that a new state of matter has been found which behaves different to any other state that has been investigated before. The main problem is that so far the theoretical understanding does not seem solid enough to rule out hadronic descriptions for the new state of matter. As the precision and the wealth of measurements increase further, the theoretical models also will have to evolve until a definite conclusion can be drawn.

4.2 Hyperon Reconstruction at HERA-B

The "Golden Minimum Bias" data sample taken in December 2002 was searched for reconstructible Λ, Ξ and Ω hyperon candidates. In order to separate the hyperon signals from the combinatorial background, selection cuts on variables describing the kinematics and the topology of the decays under study were necessary. For the correction for the limited acceptance of the detector, Monte Carlo simulated events were used. This section presents the data and Monte Carlo samples and describes the optimization of the selection cuts and the acceptance correction. The results obtained for particle ratios, total and differential cross sections are presented and compared with published values.

4.2.1 The "Golden Minimum Bias" Data Sample 2002/2003

During the HERA upgrade shutdown in 2001, the HERA-B detector was improved compared to its status in 2000. After re-commissioning, a period of data taking followed from November 2002 to March 2003. During that time, different trigger schemes were applied: Single and double electron and muon triggers (i.e. one or two electron or muon candidates were required in each event), an interaction trigger and a pseudo-random trigger. While the latter just recorded random events synchronously to the bunch crossing, the interaction trigger demanded at least 20 hits in the RICH detector and/or 1 GeV of energy deposit in the inner region of the ECAL. The purpose of this trigger was to suppress empty events and enrich minimum bias events with respect to the pseudo-random trigger. In fact, the fraction of empty events for the pseudo-random runs is about 90 % while it is of the order of 10 % for the interaction triggered runs.

In December, after thorough testing, a large sample of interaction triggered runs was recorded, consisting of about 65 million events taken with a carbon (C) target, 55 million events taken with a tungsten (W) target and 23 million events taken with a titanium (Ti) target. The interaction rate of ~ 1 MHz was chosen such that the majority of the events contain only one interaction. These data are called the "Golden Minimum Bias" data sample.

Among the minimum bias runs of this period are so-called transparent runs, taken with the pseudo-random trigger but for each event a flag was set indicating which trigger would have given a positive decision. Other runs were recorded with two target wires simultanously. These two classes of runs were excluded from the analysis because their characteristics are different from the other runs and the statistics is so small that the effort of a specific Monte Carlo simulation is not justified.

The quality of the data and especially its stability was monitored by histogramming some crucial parameters with respect to time, e.g. the number of primary vertices and their position, the number of hits in each subdetector per event, the number of reconstructed tracks, their geometrical distribution within the acceptance, and the quality of their reconstruction, i.e. the number of hits associated with each track and the fit and matching quality. On the basis of this data quality monitoring, one run from the list of "Golden Minimum Bias" runs [MBa06], namely run 20711, had to be excluded because the average position of the primary vertices jumped from the nominal target wire to another wire towards the end of the run. In Fig. 4.4, two examples of the data quality monitoring are given: in (a), the position of the primary vertices in beam direction is plotted as a function of the run number. As mentioned before, run 20711 shows a different average position as the other runs recorded with the carbon target wire. Fig. 4.4(b) presents the stability of the relative momentum resolution $\Delta p/p$. A summary of the accumulated statistics of the selected runs is given in Table 4.2 while a complete list of all used runs can be found in appendix A.

For the offline reconstruction of the data, the so-called reprocessing, the best knowledge available of the detector is applied. Noisy detector components are masked, inefficiencies are taken into account. The latest calibration brings out the best results in the measured data. The alignment of the subdetector modules and of the subdetectors with respect to each other is optimized. In this analysis, the fifth reprocessing (repro5) of the data samples was used [Rep06]. Major changes with respect to the previous reprocessings, important for this analysis were:

- The Inner Tracker was excluded from the reconstruction because of its unstable behaviour which was too complex to be taken into account in the Monte Carlo simulation.
- For the Vertex detector, a wrong geometry file (inconsistent with the detector alignment) was used in repro4; this mistake was corrected in repro5.

Other changes included an updated ECAL calibration, new alignments for the Outer Tracker and the target system as well as a new masking scheme of unreliable VDS read-out chips and MUON and RICH channels.

target wire/material	no. of runs	no. of events	$\mathcal{L}$ [μ b^{-1}]
b1/C	22	$50.9 \cdot 10^6$	242.7 ± 12.7
b2/Ti	6	$17.4 \cdot 10^6$	29.5 ± 1.5
i1/W	16	$45.2 \cdot 10^6$	28.4 ± 1.1
sum	44	$113.5 \cdot 10^6$	300.6 ± 12.8

Table 4.2: Summary of the statistics and and the recorded luminosity of the ”Golden Minimum Bias” data sample recorded in December 2002. A detailed list of all runs can be found in appendix A. For an overview of the target system and the naming scheme of the target wires, see 2.2.1.

4.2.2 Monte Carlo simulation

Monte Carlo simulations are the standard tool to study the feasibility of a measurement and the complex characteristics of high-energy physics experiments. Monte Carlo event generators attempt to simulate the underlying physical processes as precisely as possible, incorporating the latest interaction models as well as the knowledge gained from previous measurements. The generated events are then passed through a detector simulation, which tries to transform the physical truth into raw

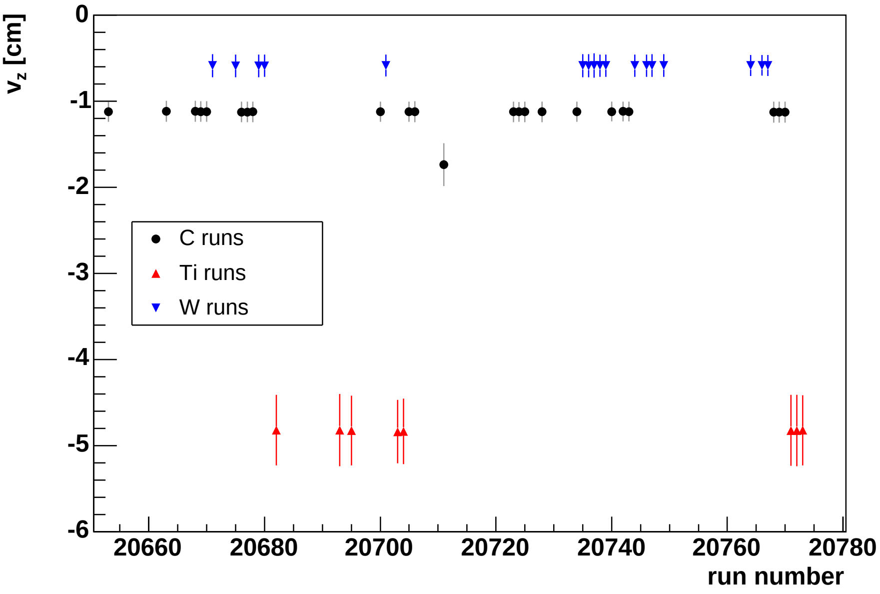

(a) z position of the primary vertices.

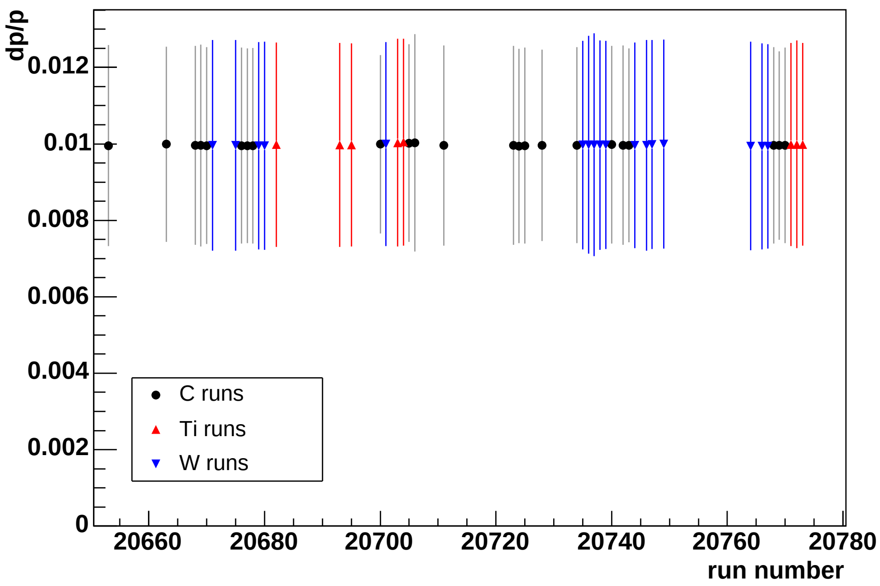

(b) momentum resolution $\Delta p/p$.

Figure 4.4: Examples of the data quality monitoring. The position of the primary vertices in beam direction is shown in (a), the momentum resolution $\Delta p/p$ is presented in (b) as a function of the run number. The error bars represent the RMS spread within each run.

data as the detector would measure it, taking the detector acceptance, inefficiencies and resolutions into account. In this way, the Monte Carlo simulation provides an important instrument to understand the properties of the physical signals observed in a measurement, a valuable cross check for verification. Furthermore, the efficiency of analysis routines can be evaluated by applying them to simulated events. Without Monte Carlo simulations, a correction for the limited detector acceptance which in general strongly depends on the kinematics of the process under study would be very difficult or not possible at all.

On the other hand care has to be taken if conclusions are to be drawn from Monte Carlo simulations: Thorough tests have to be performed that the properties of the simulated particles are close enough to the ones of the real particles seen in the data. Since they usually do not match perfectly, the use of a Monte Carlo simulation often introduces a bias. It is a very important part of every analysis to assess this bias and calculate its contribution to the systematic error of the measurement.

The software package HBGEAN [Now94], based on the standard detector description tool GEANT [GEA94], was written to simulate the response of the HERA-B detector. While propagating the simulated tracks through the detector, it does not only generate hits on sensitive detector planes but considers also the momentum change due to multiple scattering within the material crossed by the tracks. To achieve a realistic simulation of the detector response, the material description fed into HBGEAN must correspond precisely to the accumulated matter inside the detector and to the efficiencies and resolutions of the measuring components. In a first step, the tracks are propagated through the acceptance of the detector and along their way, changes in momentum and direction caused by multiple scattering are calculated and the intersections with sensor modules are stored as so-called Monte Carlo impact points (MIMP). The second step is the digitization – the translation of the Monte Carlo impact points into hits the detector would measure. To account for the non-perfect efficiency, some of the MIMPs are discarded. The resolution of the detector planes is taken into account by smearing the position of the generated hit according to a Gaussian error distribution. The resulting hits are then treated in the same way as the measured data, i.e. the full reconstruction chain is applied (as described in section 2.2.3). A comparison of real data taking and Monte Carlo simulation is schematically depicted in Fig. 4.5.

Another important point is that the real data do not always contain a single interaction per recorded event, i.e. interactions pile up in the events. In fact, the number of interactions per Minimum Bias event follows a Poissonian distribution [Bru05]. This pile-up is considered by combining Monte Carlo truth events during the reconstruction phase such that the resulting distribution shows the same pile-up as the data.

For Monte Carlo simulations of Minimum Bias events at HERA-B, the event generator FRITIOF [Pi92] is utilized [I+99]. FRITIOF is able to perform the simulation of nuclear effects like energy loss and multiple scattering of partons crossing the target nucleus. In order to enrich the fraction of events containing the particles under study, all events which did not contain a Λ, Ξ or Ω hyperon were discarded before reconstruction. This is a well feasible method for Λs and Ξs, but for Ωs the computing time was very long and thus the available sample is not very large.

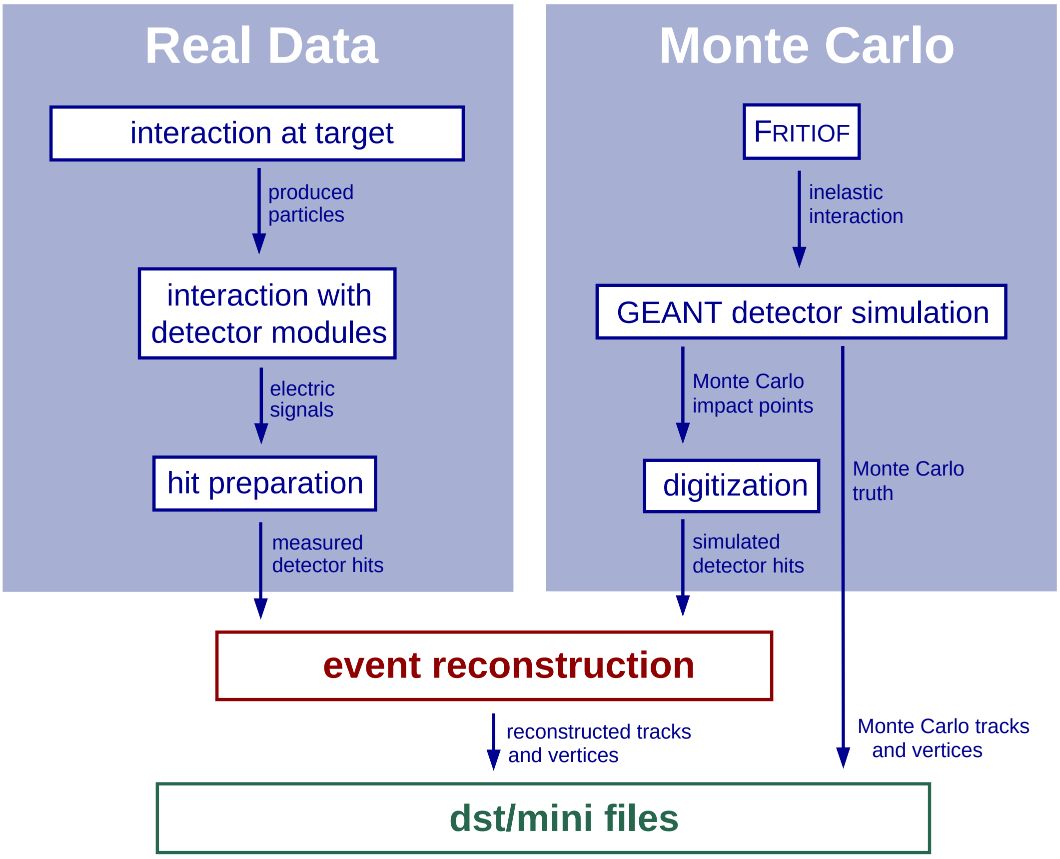

Figure 4.5: Comparison of real data taking and Monte Carlo simulation. Instead of a real interaction at the target wire, the Monte Carlo event consists of generated tracks for which hits in the detector planes are simulated. These hits are then processed in the same way as real events.

However, it turns out that the resulting kinematic distributions of the generated particles are not fully consistent with the ones of the measured particles, therefore the simulated events have to be re-weighted in order to match the real data. This process is described in detail in section 4.2.4.

The large $\Lambda/\bar{\Lambda}$ sample was generated by Esben Klinkby for the purpose of Λ polarization studies [Kli04]. Unfortunately, when he started with the tungsten sample he did not implement the mixing of different events, therefore this sample contains only events with exactly one interaction. This has to be corrected for, and will be described in section 4.2.4. During the reconstruction of the carbon sample, the mixing procedure was applied. Since the statistics of $\Lambda/\bar{\Lambda}$ from the titanium minimum bias data sample is much lower than that of the carbon and tungsten samples, no attempt of a polarization measurement was made and hence no corresponding MC sample generated. For this analysis, the $\Lambda/\bar{\Lambda}$ acceptance therefore had to be interpolated between the two other materials. Furthermore, the $\Lambda/\bar{\Lambda}$ transverse momentum distribution was brought more in line with the one observed in the real data by applying a rejection method during the generation of the events. Nonetheless, the resemblance of data and Monte Carlo could be improved further by introducing event weights as described in section 4.2.4.

The $\Xi/\bar{\Xi}$ and the $\Omega/\bar{\Omega}$ samples were generated with the standard HERA-B Monte Carlo tools and settings; no tuning was applied at this stage. Table 4.3 lists the available statistics for all particles and target materials.

4.2.3 Signal preparation

Starting from carefully selected events, the procedure to reconstruct hyperon candidates is described. Criteria based on track and vertex quality and on the event topologies are defined and optimized in order to enhance the visible signal above background. The resulting signal peaks are presented.

Event and track selection

In order to ensure a well defined data quality, events were selected according to the following criteria: First of all, the events had to be triggered by the interaction trigger, and MC events had to fulfil equivalent conditions, respectively. Only events originating from nominally filled HERA bunches were accepted, since the luminosity determination is based on this selection as well [Bru05]. Finally, they had to contain exactly one reconstructed primary vertex. The reason for this latter requirement was that some of the variables needed for the separation of the signal from the background are defined with respect to the primary vertex. Since there are very few events with more than one reconstructed primary vertex[5], the extra effort and complexity to handle this case would not be justified. The quality criteria applied for the track selection are typical HERA-B specifications: A track had to have at least 6 hits in the VDS and 11 hits in the OTR.

---

[5] Note that in many cases where an event contains more than one interaction the corresponding primary vertices are reconstructed as one because they lie very close together.

Particle	Target	pile-up	no. of events generated
Λ	C	0.1675	$5690 \cdot 10^3$
	Ti	-	-
	W	0.0	$4943 \cdot 10^3$
$\bar{\Lambda}$	C	0.1675	$3448 \cdot 10^3$
	Ti	-	-
	W	0.0	$2542 \cdot 10^3$
Ξ^-	C	0.18	$800 \cdot 10^3$
	Ti	0.17	$439 \cdot 10^3$
	W	0.16	$1621 \cdot 10^3$
$\bar{\Xi}^+$	C	0.18	$543 \cdot 10^3$
	Ti	0.17	$384 \cdot 10^3$
	W	0.16	$1102 \cdot 10^3$
Ω^-	C	0.18	$298 \cdot 10^3$
	Ti	0.17	$149 \cdot 10^3$
	W	0.16	$299 \cdot 10^3$
$\bar{\Omega}^+$	C	0.16	$299 \cdot 10^3$
	Ti	0.17	$149 \cdot 10^3$
	W	0.18	$299 \cdot 10^3$

Table 4.3: Statistics of Monte Carlo generated events for the different particles and target materials. Each event contains a signal particle and a Poissonian distributed Minimum Bias event to account for the event pile-up found in the real data. Unfortunately, no sample for the titanium target exists for $\Lambda/\bar{\Lambda}$.

Signal reconstruction

The hyperon decay channels which are most easily to reconstruct at a fixed target experiment like Hera-B are

- $\Lambda \to p\pi^-$,
- $\Xi^- \to (\Lambda \to p\pi^-)\,\pi^-$,
- $\Omega^- \to (\Lambda \to p\pi^-)\,K^-$,

and their charge conjugated equivalents (c.c.). All final state products are long-lived charged particles which are well observable with the detector. Furthermore, these are the main decay channels of the hyperons: The branching ratios are (63.9 ± 0.5) % for $\Lambda \to p\pi$, (99.887 ± 0.035) % for $\Xi \to \Lambda\pi$, and (67.8 ± 0.7) % for $\Omega \to \Lambda K$. The decay topologies offer sufficient distinguishing marks for the hyperon candidates to be separated from the combinatorial background, therefore only tracking information and no additional information about the particle identity, e.g. based on RICH rings, ECAL clusters or hits in the MUON system, are needed to reconstruct the particles. This simplicity eases the Monte Carlo simulation.

Fig. 4.6 depicts schematically the topologies of the decays under study. Also shown are the definitions of some of the variables that can be utilized to cut on in order to isolate the signal events from background events. The first obvious quantity to consider is the distance of closest approach of the tracks, d_{ca}, since it decides whether or not it is possible to form a vertex. A major part of the combinatorial background can be removed by requiring this distance to be small. After calculating the track parameters of the hyperon candidate from the assumed daughter tracks, it can be tested whether or not it points back to the primary vertex, i.e. whether its impact parameter with respect to the primary vertex is small. On the other hand, impact parameters of the daughter tracks should not point back (or at least not both at the same time) because of the relative momentum. One can therefore demand the sum or the product of the impact parameters to be higher than a given cut value. In practice, the product turned out to be the more efficient cut parameter.

A popular method in the analysis of V_0 particles[6] is shown in the so-called Armenteros-Podolansky plot [T+53]: The transverse momentum is plotted against the asymmetry of the longitudinal momenta of the daughter particles, where both quantities were measured with respect to the flight direction of the mother particle (Fig. 4.7). Three prominent bands are visible in this plot: One band symmetrical with respect to the origin and two bands to the left and the right hand side. The latter ones correspond to $\bar{\Lambda}$ (left) and Λ (right) while the one in the center originates from K^0_S particles decaying into a charged pion pair. In the region where the Λ bands overlap with the K^0_S band, they are kinematically indistinguishable from each other. Therefore, for all Λ and $\bar{\Lambda}$ candidates the invariant mass was calculated assuming that both daughter tracks are pions (i.e. applying the K^0_S mass hypothesis) and if

---

[6] V_0 particles are neutral particles which decay into two charged particles, first observed in bubble chambers where the neutral track is invisible and the oppositely charged tracks give a signature which resembles the letter V.

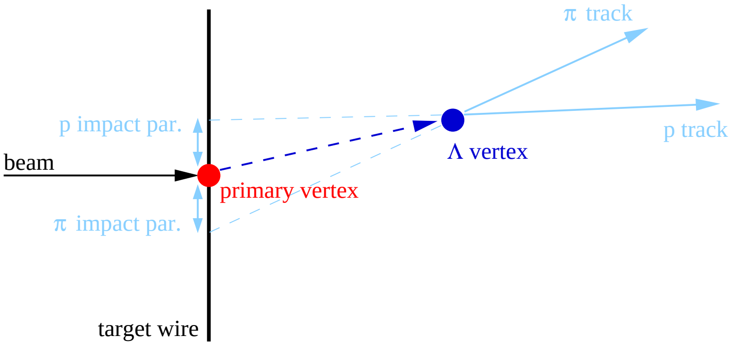

(a) $\Lambda \rightarrow p\pi$

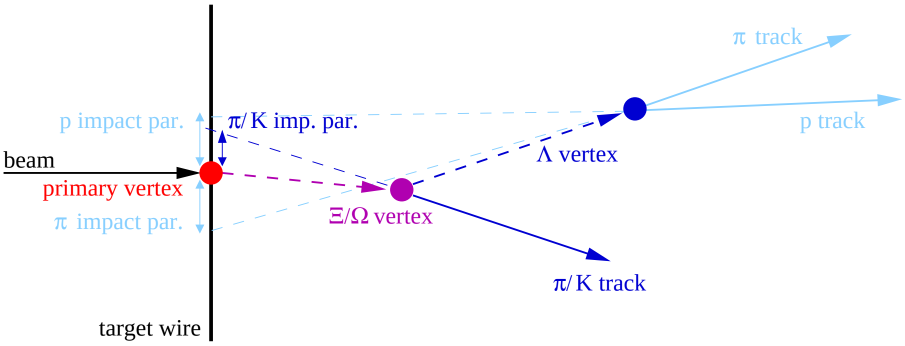

(b) $\Xi \rightarrow \Lambda\pi/\Omega \rightarrow \Lambda K$

Figure 4.6: Event topologies of the decays $\Lambda \rightarrow p\pi$ (a) and $\Xi \rightarrow \Lambda\pi/\Omega \rightarrow \Lambda K$ (b). Ξ and Ω decay into a Λ and a pion or a kaon while the Λ subsequently decays into a proton and a pion. The solid lines refer to measurable tracks while the dashed lines represent tracks which have to be deduced from the measured ones. Some of the geometrical parameters utilized as selection cuts are indicated.

the result lay in the region of the K^0_S mass, the respective candidate was excluded from the analysis.

Conversions of γs into electron-positron pairs can also be mistaken for a two-body decay of a heavier particle, but the relative transverse momentum of the outgoing tracks with respect to the mother track direction is small, therefore requiring p_T to be larger than 0.01 GeV is sufficient to remove this possible background. Another cut is related to the fact that tracks which decay far downstream of the target can not leave enough hits in the vertex detector for a track segment to be reconstructible, thus candidates with vertices further apart than 1m from the primary vertex are discarded. The removal of candidates whose vertices are of bad quality can be achieved by cutting on the probability of the vertex fit.

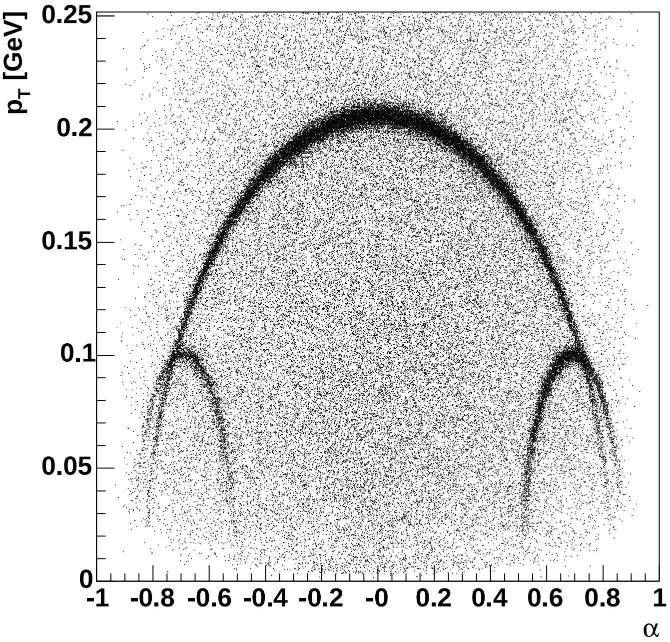

Figure 4.7: Armenteros-Podolansky plot for K^0_S and Λ [T+53]. The transverse momentum is plotted against the longitudinal momentum asymmetry $\alpha = (p_l^+ - p_l^-)/(p_l^+ + p_l^-)$ of the daughter tracks, both quantities were measured with respect to the mother particle track.

The following list summarizes all generic cuts which were applied before optimizing the additional topological cuts as described in the next section:

- Event selection: Only events triggered by the interaction trigger, originating from a nominally filled HERA bunch and containing exactly one reconstructed primary vertex were accepted.

- Track selection: Tracks with at least 6 hits in the VDS and 11 hits in the OTR were selected for the analysis.

- The distance between the primary vertex and the decay vertices of the hyperons had to be smaller than 1 m.
- The probability of each vertex fit had to be at least 0.001.
- The momentum component of the Λ daughter tracks perpendicular to the flight direction of the Λ (one of the variables of the Armenteros-Podolanski plot) had to at least 0.1 GeV.
- Λ candidates were rejected when the invariant mass calculated under the assumption that both tracks are pions (K_s^0 hypothesis) was between 0.485 GeV and 0.515 GeV (i.e. in the K_s^0 mass region).
- The Ξ and Ω decay vertices had to lie upstream of the decay vertex of the Λ candidate used in the reconstruction.

Cut optimization

The question how the cut values should be chosen is a very delicate one: It is very difficult not to be biased when judging whether a change of a cut improved the signal significance. It is always possible that the increase in the observed signal is due to a fluctuation in the background only. In principle, the Monte Carlo simulation can be exploited for this purpose, but for pure signal Monte Carlo, the amount of background in the peak region is often much lower than in Minimum Bias events. Therefore, the effects of varying the cut values were evaluated by blindly optimizing the significance Σ of the signal, i.e.

$$\Sigma := \frac{S}{\sqrt{S+B}}. \tag{4.8}$$

(Here, S is the number of reconstructed signal peak entries found in the Monte Carlo simulation and B is the number of background entries underneath the peak reconstructed in the data. Both signal and background were integrated in the 3σ range around the particle mass.)

The Monte Carlo signal statistics was scaled such that the reconstructed Monte Carlo signal was similar to the signal reconstructed in the data. In this way, fluctuations in the data could not artificially increase the signal, and the underestimated background in the signal MC was compensated for by considering the real background from the data. The optimization was carried out in the following way: For each cut variable, several possible values were set. All combinations of the cut sets were then applied to the hyperon candidates in data and Monte Carlo. The number of background events was determined from fitting a straight line to the sidebands left and right of the peak (grey area e.g. in Fig. 4.8) and integrating the fit function in the peak region (blue area underneath the peak). The number of signal events was evaluated by counting the entries in the peak region and subtracting the previously obtained background entries. The peak region was defined by the 3σ interval around the peak where peak position and σ were typical values taken from fits of the sum of a Gaussian and a straight line to the invariant mass distributions. For each of the tested cut sets, the significances were calculated according to Equ. 4.8, and the one with the largest value was taken to be the optimized one. If the optimization procedure returned a cut set where one of the cut variables was at the edge of the range of tested values, the corresponding range was extended and another iteration carried out, until all cut values were inside the range. This was done for particles and antiparticles separately, and similar cut sets were found to be optimal for both. In order to arrive at one cut set, the combination which yielded the highest value of the sum of significances Σ for particle and antiparticle was decided on to be the optimal cut set. Since (except for the case of $\Omega/\bar{\Omega}$) the analysis was in general not limited by statistics, absolutes cut values were chosen instead of significance levels, where the cut value is considered in units of its error. The latter option has the disadvantage to be less robust against difficulties in the error determination.

For Λ and $\bar{\Lambda}$, one run (namely the run 20653 recorded with the carbon target wire) was sufficient to determine the optimized cut set, while for $\Xi/\bar{\Xi}$ all carbon runs had to be used to obtain enough statistics. In the case of $\Omega/\bar{\Omega}$, the statistics was too low to evaluate the effect of slight changes in the cut values, i.e. it was impossible to distinguish the effect of changing the cut values from fluctuations in background and signal. Therefore, a cut set similar to the one found in the $\Xi/\bar{\Xi}$ cut optimization was chosen. In addition to the cuts also applied in the Ξ selection, kinematic reflections from the Ξ decays were supressed by requiring that the invariant mass calculated assigning the pion mass to the kaon track candidate is larger than 1.34 GeV, i.e. the candidates being incompatible with a Ξ or $\bar{\Xi}$ hypothesis.

In the case of Ξ and Ω hyperons, the impact parameters of the Λ daughter tracks can be easily calculated with respect to the primary vertex or the Ξ or Ω vertex. The latter would be the natural choice for a selection cut parameter, but since the flight distance to the target is longer the impact parameters have higher values. To decide which of the two is the better reference point for the cut, both variants were tested. The result was that the cut set defined with respect to the primary vertex gives slightly higher signal significances as well as more signal entries in the peak. Therefore, in the following all impact parameters are evaluated with the primary vertex as reference point as depicted in Fig. 4.6.

In addition to the cuts applied in the selection of secondary Λ candidates for the Ξ and Ω reconstruction, a cut on the product of the proper lifetime $c\tau$ and the component of the momenta of the daughter tracks perpendicular to the flight direction of the Λ (one variable of the Armenteros-Podolansky plot) was applied for the Λ signal preparation. Table 4.4 summarizes the optimized cut sets for the three hyperons; the same values were used for all three target materials. Table 4.5 presents the signal yields obtained with these selection cuts.

4.2.4 Acceptance correction

A reliable correction for the limited detector acceptance can only be achieved if the Monte Carlo simulation closely matches the data. Any deviation contributes to systematic error of the measurement. Thus, in order to obtain an as small as possible systematic error, the consistency of the properties of the simulated particles with the observed ones is often improved by reweighting the Monte Carlo generated events such that distributions of kinematic variables agree better. In the case of $\Lambda/\bar{\Lambda}$, the

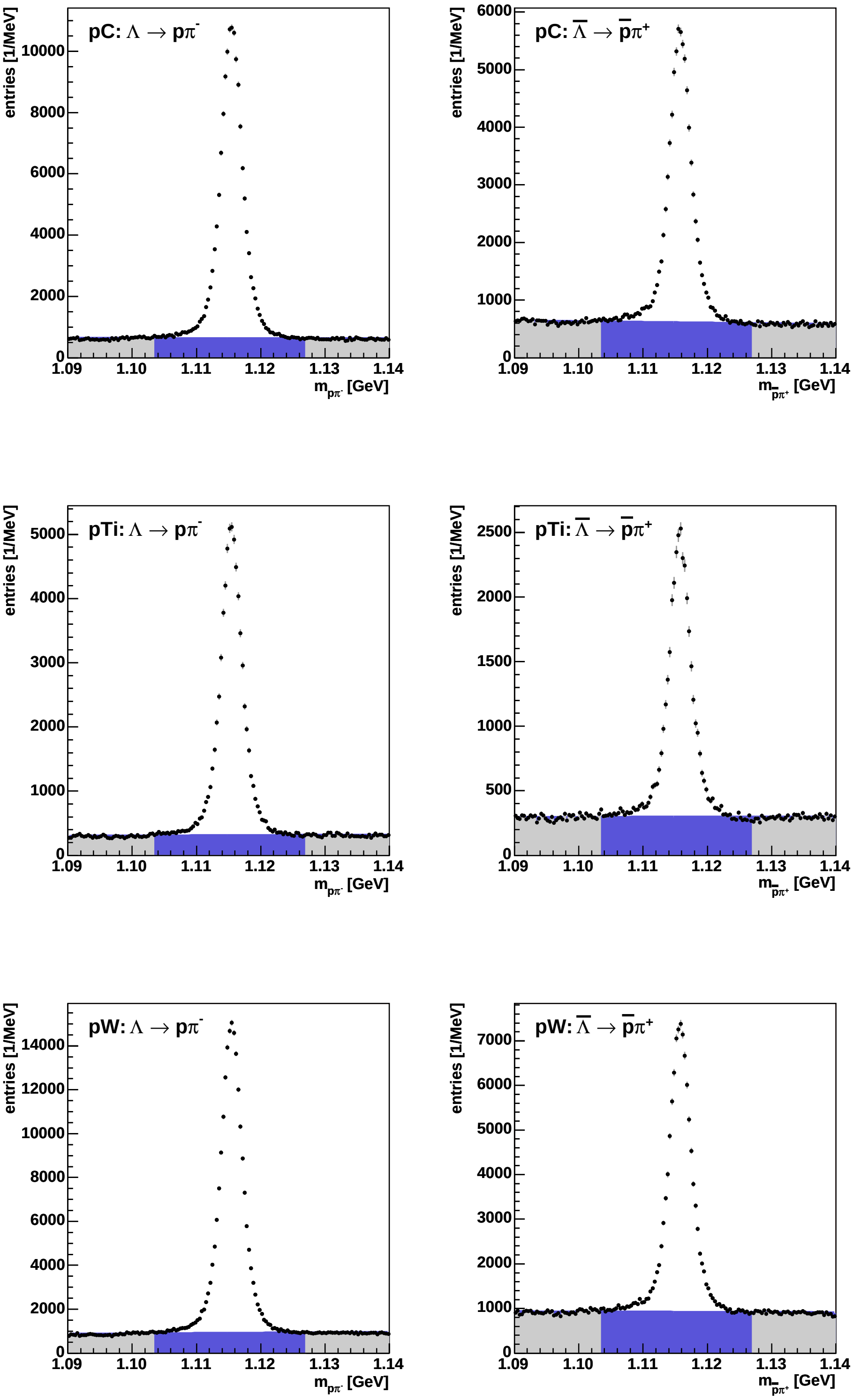

Figure 4.8: Invariant mass spectra of Λ (left column) and $\bar{\Lambda}$ (right column) candidates reconstructed for the three target materials carbon, titanium and tungsten. The area underneath the signal peaks indicates the interval of the signal and background determination while the background fits were based on the grey shaded side bands.

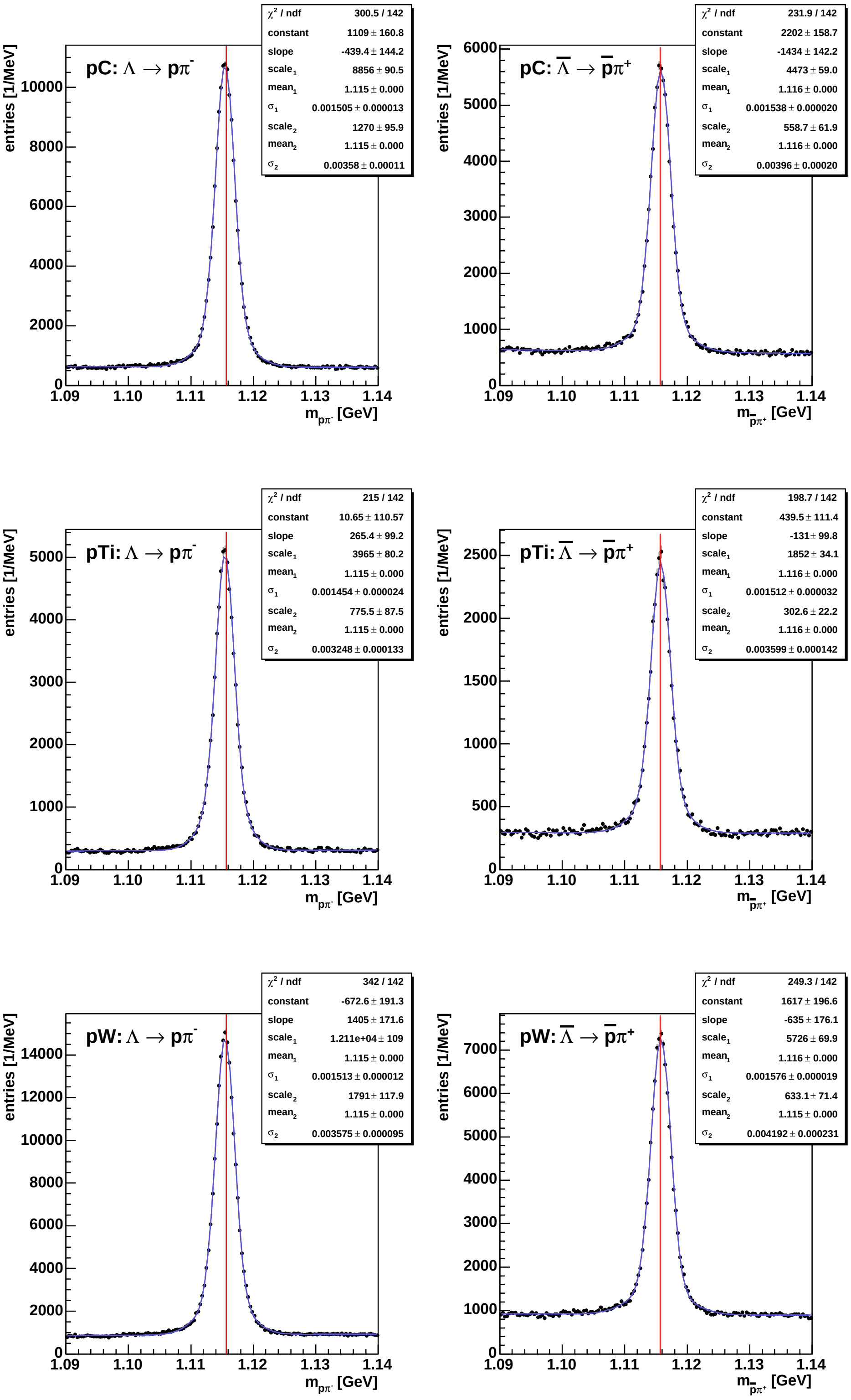

Figure 4.9: Invariant mass distributions of Λ (left column) and $\bar{\Lambda}$ (right column) candidates. Superimposed are fits of the sum of a linear background and two Gaussians. The vertical red line indicates the invariant mass value listed by the PDG [E⁺04].

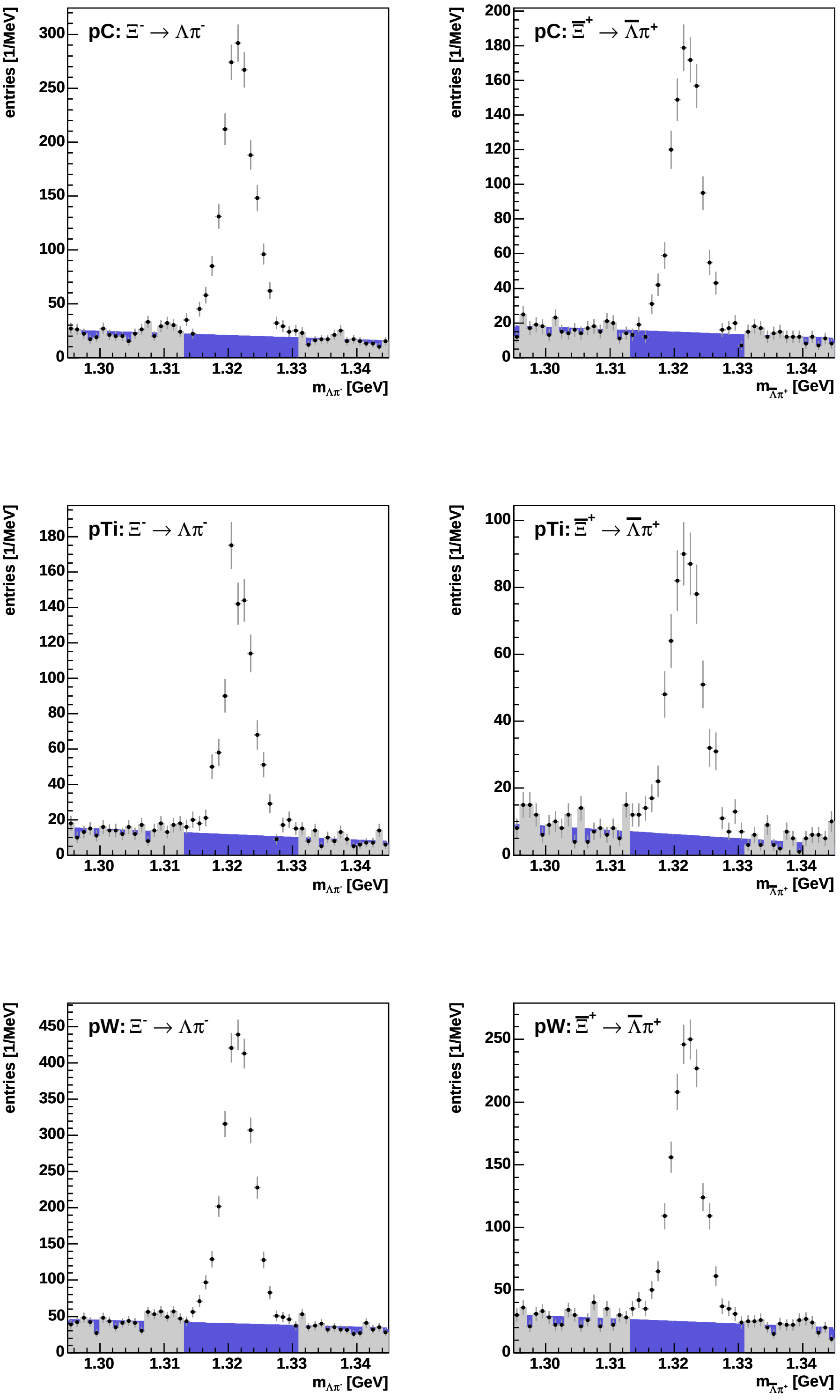

Figure 4.10: Invariant mass spectra of Ξ (left column) and $\bar{\Xi}$ (right column) candidates reconstructed for the three target materials carbon, titanium and tungsten. The area underneath the signal peaks indicates the interval of the signal and background determination while the background fits were based on the grey shaded side bands.

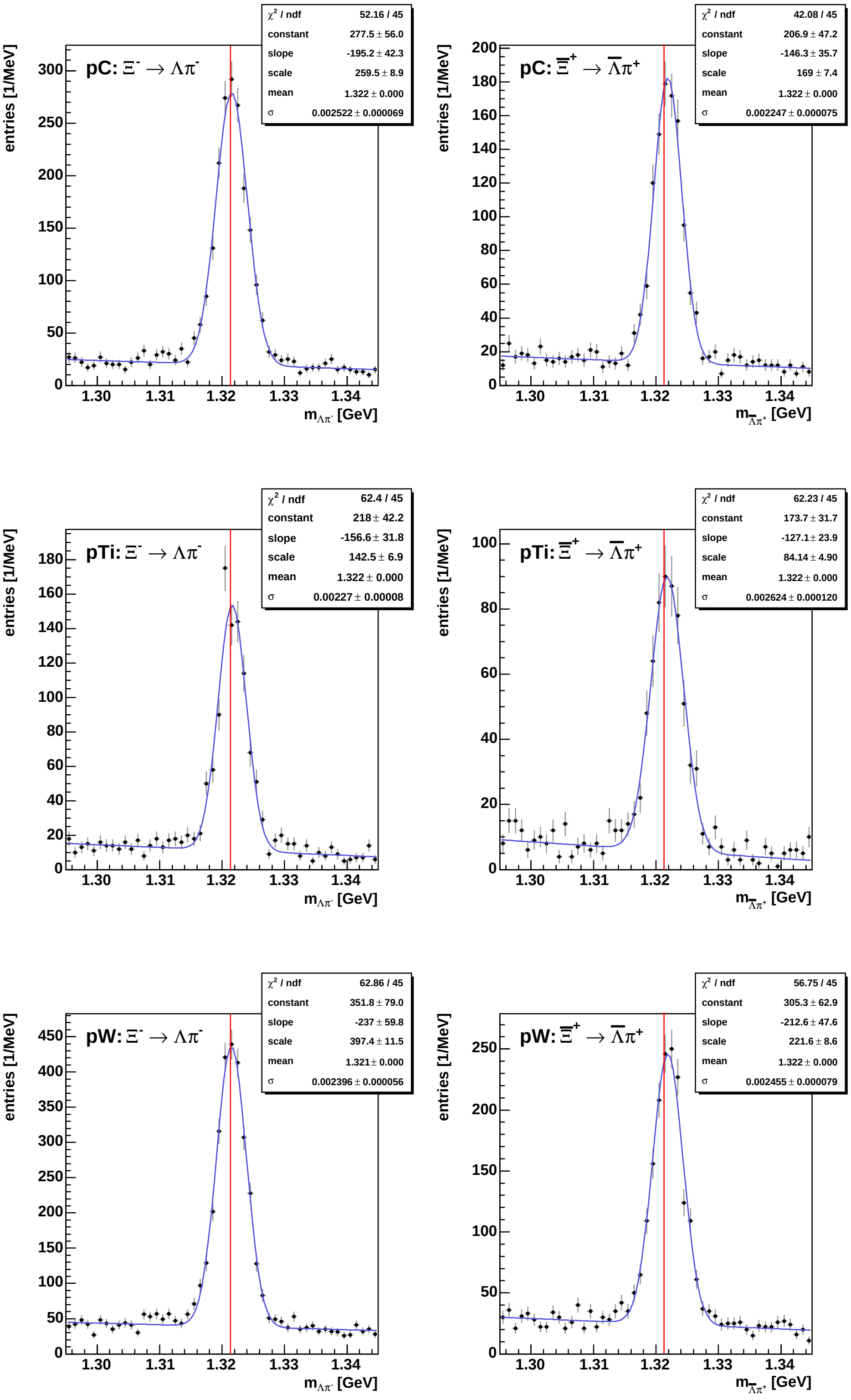

Figure 4.11: Invariant mass distributions of Ξ (left column) and $\bar{\Xi}$ (right column) candidates. Superimposed are fits of the sum of a linear background and a Gaussian. The vertical red line indicates the invariant mass value listed by the PDG [E+04].

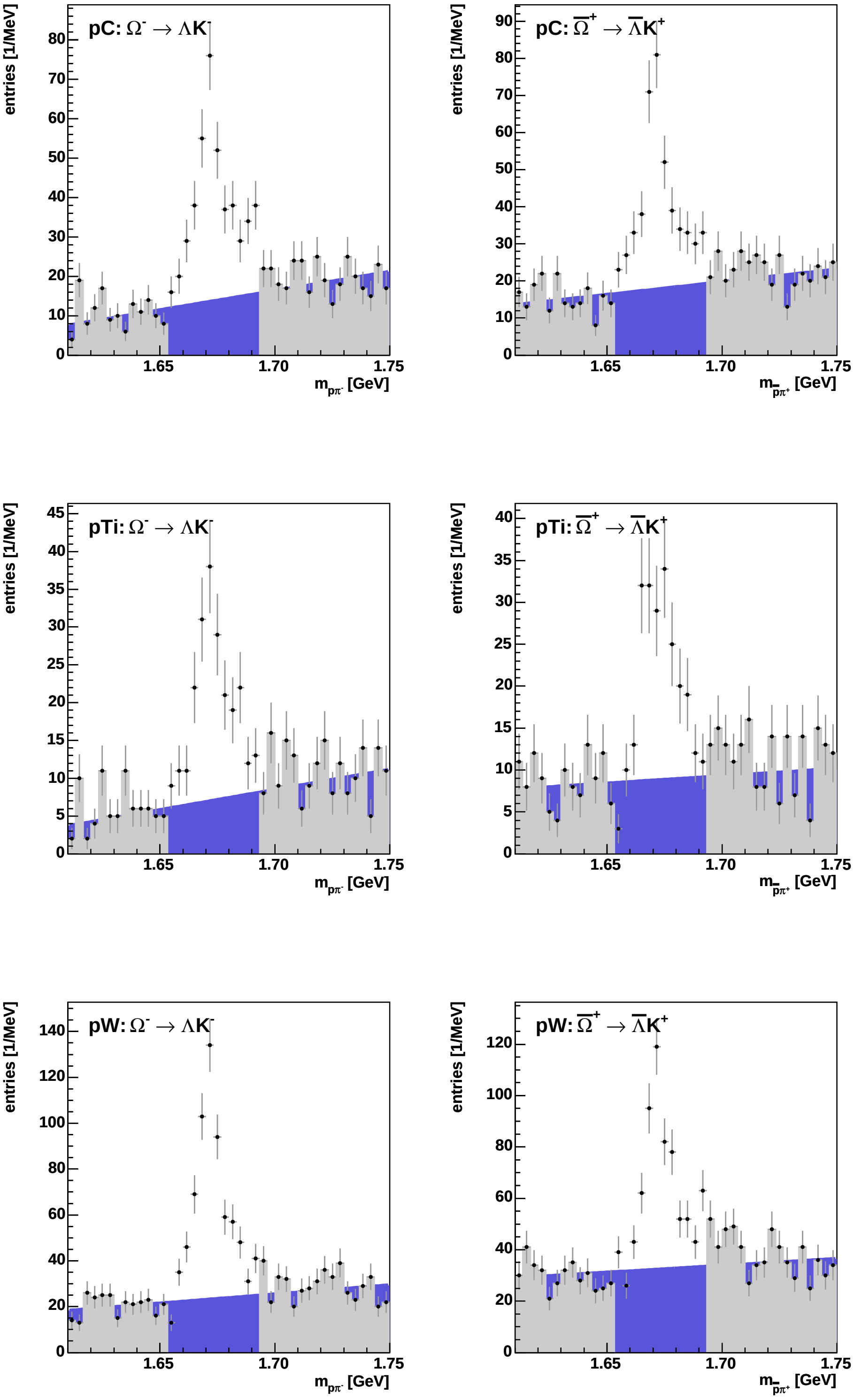

Figure 4.12: Invariant mass spectra of Ω (left column) and $\bar{\Omega}$ (right column) candidates reconstructed for the three target materials carbon, titanium and tungsten. The area underneath the signal peaks indicates the interval of the signal and background determination while the background fits were based on the grey shaded side bands.

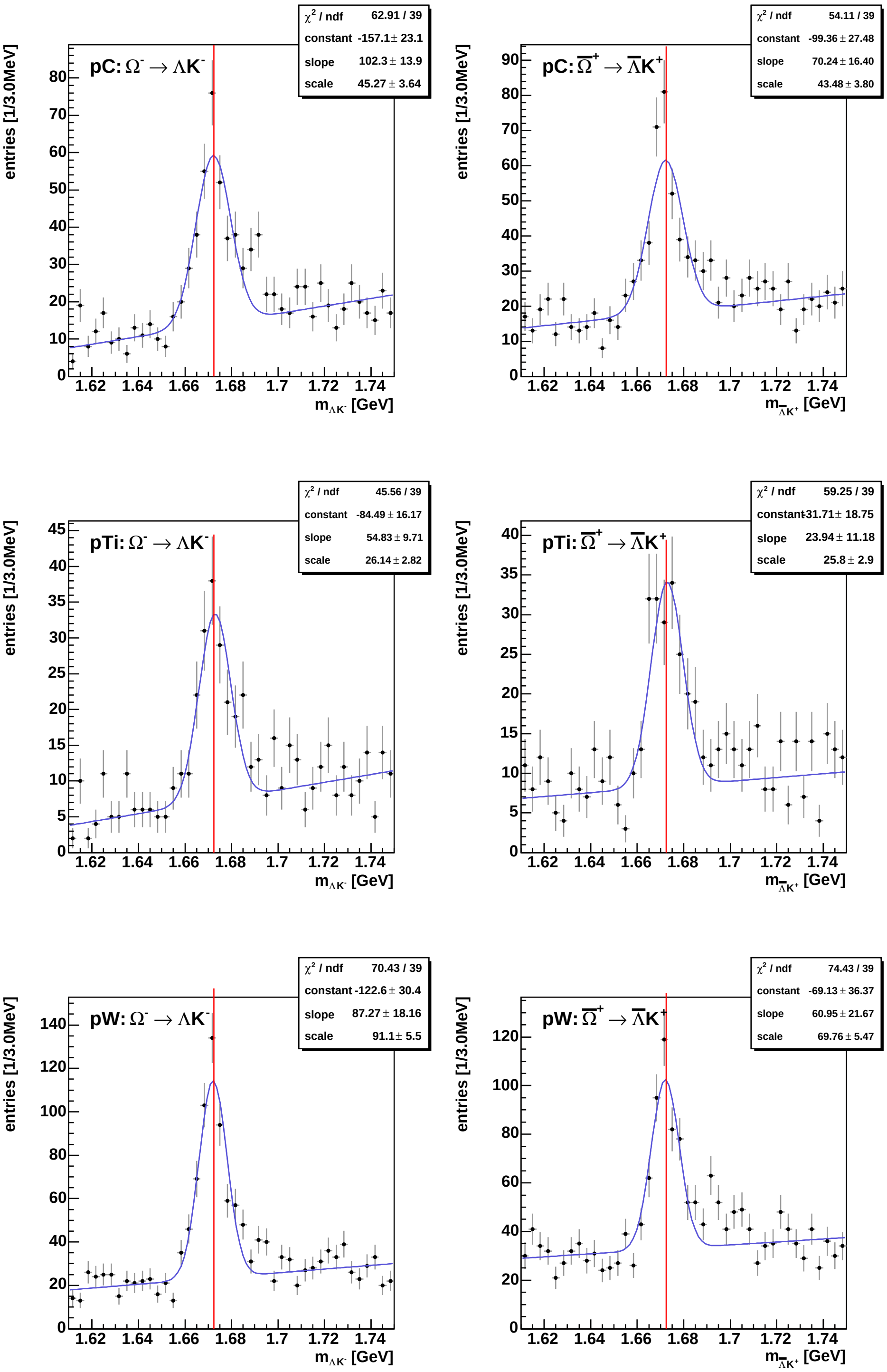

Figure 4.13: Invariant mass distributions of Ω (left column) and $\bar{\Omega}$ (right column) candidates. Superimposed are fits of the sum of a constant background and a Gaussian, where the mean and the width have been taken from a fit to the sum of the Ω and $\bar{\Omega}$ histograms. The vertical red line indicates the invariant mass value listed by the PDG [E⁺04].

cut parameter	$\Lambda/\bar{\Lambda}$	$\Xi/\bar{\Xi}$	$\Omega/\bar{\Omega}$
$d_{ca} <$	0.06 cm	0.12 cm	0.10 cm
$\mathrm{imp}_{\Lambda/\Xi/\Omega} <$	-	0.10 cm	0.10 cm
$\mathrm{imp}_{\pi/K} >$	-	0.20 cm	0.20 cm
$\mathrm{imp}_p \times \mathrm{imp}_\pi$ (from $\Lambda/\bar{\Lambda}$) $>$	0.014 cm^2	0.025 cm^2	0.015 cm^2
d_{ca} of $\Lambda/\bar{\Lambda} <$	-	0.30 cm	0.20 cm
$c\tau \times p_T >$	0.06 cm·GeV	-	-
$m(\Lambda, \pi) >$	-	-	1.34 GeV

Table 4.4: Optimized selection criteria for the reconstruction of hyperon candidates. The same cuts were applied for particles and antiparticles and for the different target materials. For a description of the cut variables, see page 94.

particle	target	signal entries
Λ	C	130087 ± 447
	Ti	60334 ± 309
	W	178993 ± 531
$\bar{\Lambda}$	C	65658 ± 364
	Ti	27915 ± 247
	W	83326 ± 431
Ξ^-	C	1687 ± 53
	Ti	873 ± 38
	W	2444 ± 68
$\bar{\Xi}^+$	C	966 ± 42
	Ti	575 ± 30
	W	1432 ± 52
Ω^-	C	260 ± 30
	Ti	130 ± 22
	W	442 ± 37
$\bar{\Omega}^+$	C	268 ± 32
	Ti	124 ± 23
	W	357 ± 41

Table 4.5: Signal yields of reconstructed hyperons in the 2002/2003 minimum bias data.

abundant statistics admits to study the acceptance in two dimensions, i.e. in two different kinematic variables which are independent of each other. Hence also the reweighting was carried out in the same two variables. The statistics of Ξ and $\bar{\Xi}$ candidates does not permit a two-dimensional treatment, here only one-dimensional reweighting and acceptance correction was performed. Finally, the statistics of the Ω hyperons is so small that no differential distribution could be measured. Here, one can make use of the weight set applied in the reweighting of $\Xi/\bar{\Xi}$ to estimate the systematic error due to the non-perfect matching of data and Monte Carlo.

The kinematic variables which are usually compared are:

p_T: the component of the particle momentum perpendicular to the beam direction

y: the rapidity:

$$y = \frac{1}{2} \ln \left(\frac{E + p_z}{E - P_z} \right) \tag{4.9}$$

(Here, E is the energy of the particle.)

x_F: the Feynman variable x_F is defined by

$$x_F = \frac{p_z}{p_{z\ max}}. \tag{4.10}$$

In the center-of-mass system (cms), equation 4.10 yields

$$x_F \approx \frac{2p_{z\ cm}}{\sqrt{s}}. \tag{4.11}$$

(Here, $p_{z\ max}$ is the maximal kinematically allowed value of p_z, the momentum component parallel to the beam direction, and $\sqrt{s}$ is the total energy in the cms.)

While x_F is a useful variable for the analysis in the very forward ($x_F \rightarrow 1$) and backward regions ($x_F \rightarrow -1$) of the phase space, the rapidity is a better suited variable for experiments like HERA-B measuring in the central phase space region, i.e. at $y_{cms} = 0$. Thus, p_T^2 and rapidity were chosen as kinematic variables for the acceptance correction of Λ and $\bar{\Lambda}$, and x_F distributions are only shown for comparison.

Reweighting

For the reweighting of Λ and $\bar{\Lambda}$, the two-dimensional differential distributions of p_T^2 versus rapidity were plotted for the carbon and tungsten data and Monte Carlo samples in the following way: For each bin in p_T^2 and y, an invariant mass histogram was filled and evaluated as described above. The binning in the two variables was chosen such that in each histogram there was enough statistics to yield a seizable signal. In order to ensure the correct normalization of the weights, the histograms were then scaled such that the total signal statistics in data and Monte Carlo was the same. The ratio of data and Monte Carlo histograms was applied to the Monte Carlo simulated events as a matrix of weights, i.e. in the following, to each Monte Carlo Λ and $\bar{\Lambda}$ the value of the bin corresponding to its p_T^2 and y values was assigned as a weight. In Fig. 4.14, the weight matrices are depicted for Λ (top) and $\bar{\Lambda}$ (bottom) from the carbon sample. The weight maps for the tungsten sample do not deviate significantly from the ones obtained for carbon, therefore they are not shown here. In the Λ weight map, an underestimation of the production rate of up to ~ 40 % by the Monte Carlo simulation at low p_T^2, especially towards higher rapidity values, can be observed. Furthermore, a smaller fraction of simulated Λs is reconstructed in the high p_T^2 region compared to the data. The latter deviation is not observed for $\bar{\Lambda}$, while the mismatch in the region of low p_T^2 and high rapidity is also found.

This indicates that the excess of Λs reconstructed in the data at high p_T^2 might be caused by a leading particle effect which is not present for $\bar{\Lambda}$.

The reweighting of the Ξ and $\bar{\Xi}$ Monte Carlo samples was conducted analogously in the variable p_T^2 only. The weights for the carbon sample are plotted in Fig. 4.15. The titanium and tungsten sample yield very similar weight distributions, which are not shown here. Obviously, the p_T^2 spectra from the Monte Carlo simulation are slightly to steep, therefore the simulated production rate of Ξ and $\bar{\Xi}$ is overestimated at low p_T^2 and underestimated at high p_T^2.

It was attempted to fit the weight distributions in order to avoid additional systematic effects due to the binning, but finally, the deviations to the data when applying the fitted weighting functions to the Monte Carlo sample were similar or even larger than the ones resulting from the matrix method. Therefore the idea was abandoned and the binned weights were applied.

Acceptance determination

In order to evaluate the acceptance as a function of y and p_T^2 (Λ) or of p_T^2 only (Ξ), a similar procedure as for the reweighting was carried out: The acceptance is the ratio of the signal seen in Monte Carlo reconstructed in exactly the same way as the data and applying the same cuts and the signal originally generated in each bin. Unfortunately, pile-up influences the acceptance because the increase in track multiplicity leads to more combinatorial background and probably a lower track reconstruction efficiency due to mismatched track segments. Therefore, since the $\Lambda/\bar{\Lambda}$ tungsten MC sample was reconstructed without pile-up, this effect had to be studied and corrected for using the carbon sample. Here, the acceptance was determined for the whole sample (i.e. with pile-up) and for the sub-sample of events containing exactly one interaction (without pile-up, corresponding to the tungsten sample). Assuming then the same behaviour of the acceptance versus pile-up, the tungsten MC was scaled with the ratio of the resulting value with pile-up divided by the one without. The size of this correction amounts to roughly 7%. The missing titanium $\Lambda/\bar{\Lambda}$ sample was compensated for by interpolating between the carbon and the tungsten sample. Since the multiplicity increases proportional to the logarithm A where A is the number of the target material, the acceptance a was interpolated as

$$a_{Ti} = a_C + \frac{\log A_{Ti} - \log A_C}{\log A_W - \log A_C} \cdot (a_W - a_C)\,. \tag{4.12}$$

The error on the acceptance for the titanium sample was estimated by the standard deviation of a flat distribution between the values found for carbon and tungsten, i.e.

$$\Delta a_{Ti} = \frac{a_C - a_W}{\sqrt{12}} \tag{4.13}$$

For the two-dimensional acceptance correction in y and p_T^2, Equ. 4.12 and 4.13 were applied to each bin. The resulting acceptance maps for Λ and $\bar{\Lambda}$ are shown in Fig. 4.16 and Fig. 4.17, respectively. Although the p_T^2-rapidity distributions of both particles generated by the Monte Carlo look different, especially in the region of low

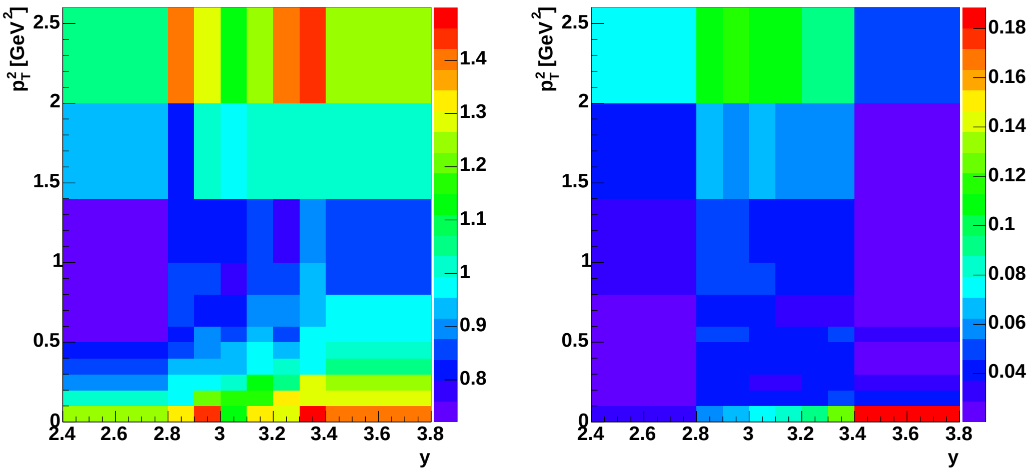

(a) Λ map of weights.

(b) Relative errors of the Λ weights.

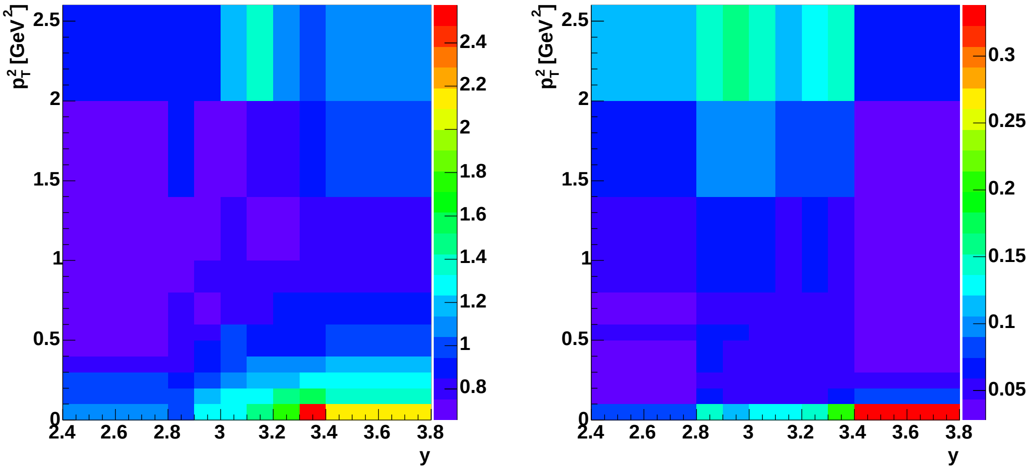

(c) $\bar{\Lambda}$ map of weights.

(d) Relative errors of the $\bar{\Lambda}$ weights.

Figure 4.14: $\Lambda/\bar{\Lambda}$ reweighting as function of p_T^2 and rapidity. The weights determined for each bin are shown in (a) and (c) while the corresponding relative errors are displayed in (b) and (d) for Λ and $\bar{\Lambda}$, respectively.

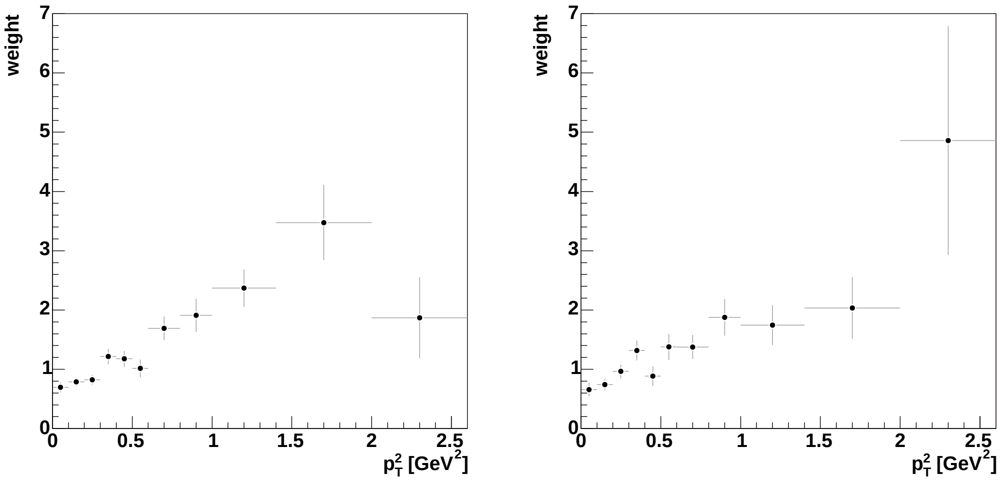

(a) Ξ reweighting.

(b) $\bar{\Xi}$ reweighting.

Figure 4.15: $\Xi/\bar{\Xi}$ reweighting as function of p_T^2.

p_T^2 and low rapidity, the acceptance as function of the two variables agrees both qualitatively and quantitatively. There is a core region at moderate p_T^2 and rapidity values where the acceptance is roughly 10 %, and it decreases towards lower and higher values of both variables. Towards high p_T^2 and low rapidity values, it decreases more rapidly and vice versa.

In the case of Ξ and $\bar{\Xi}$, the pile-up applied during the Monte Carlo reconstruction was different from the values measured later in the course of the luminosity determination (see Table 4.3 and Appendix A). Since the tools for correction in the case of the $\Lambda/\bar{\Lambda}$ sample were already implemented, they were now utilized for Ξ, $\bar{\Xi}$ (and Ω, $\bar{\Omega}$, too) to compensate for these deviations, even if the effect was small: roughly 1%. The measured acceptance as function of p_T^2 is shown in Fig. 4.18 for the runs recorded with the carbon target. In the region of moderate p_T^2, the acceptance has its maximum of roughly 2 %, while it decreases to values of about 1 % towards the low and the high edge of the considered p_T^2 range. The observed fluctuations are most probably due to the limitations from statistics which enter both the determination of the reweighting and the acceptance.

4.2.5 Systematic errors

Apart from measurement errors due to the limited statistics of real and Monte Carlo simulated data, systematic errors arise from the fact that it is impossible to simulate the detector with perfect precision. Furthermore, the kinematics of the simulated and real particles may deviate from each other. The choice of the selection cut set may be sensitive to this deviation and influence the acceptance determination. In addition to the differences between the real and the simulated hyperons, general

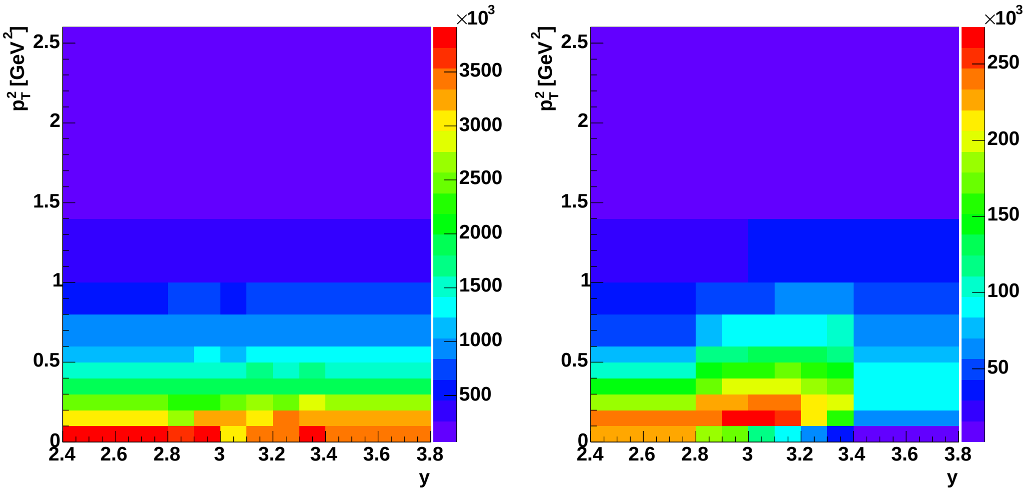

(a) Λ, before reconstruction.

(b) Λ, after reconstruction.

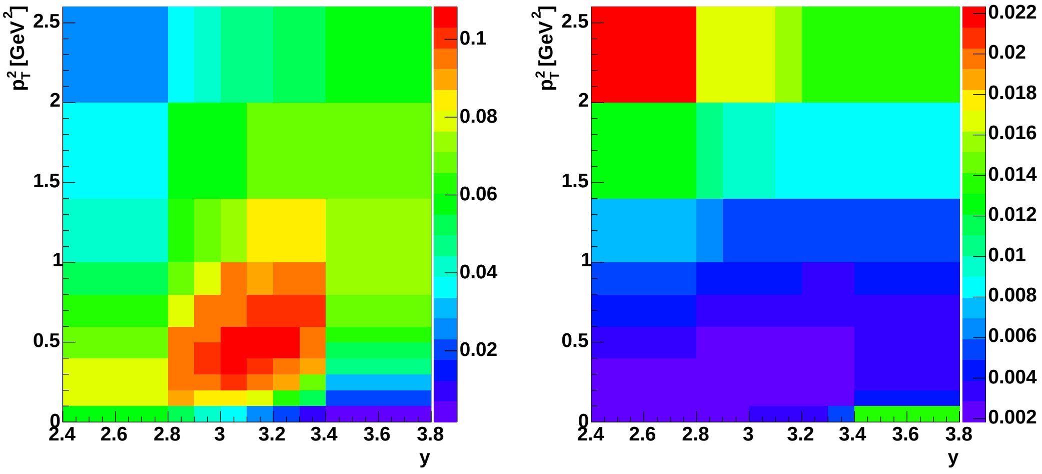

(c) Λ acceptance.

(d) Relative error of the Λ acceptance.

Figure 4.16: Λ acceptance as function of p_T^2 and rapidity. The distribution of Monte Carlo generated Λs after applying the reweighting is shown in (a), the resulting distribution after the reconstruction is displayed in (b). The acceptance, i.e. the ratio of these two histograms is presented (c) together with its relative errors (d).

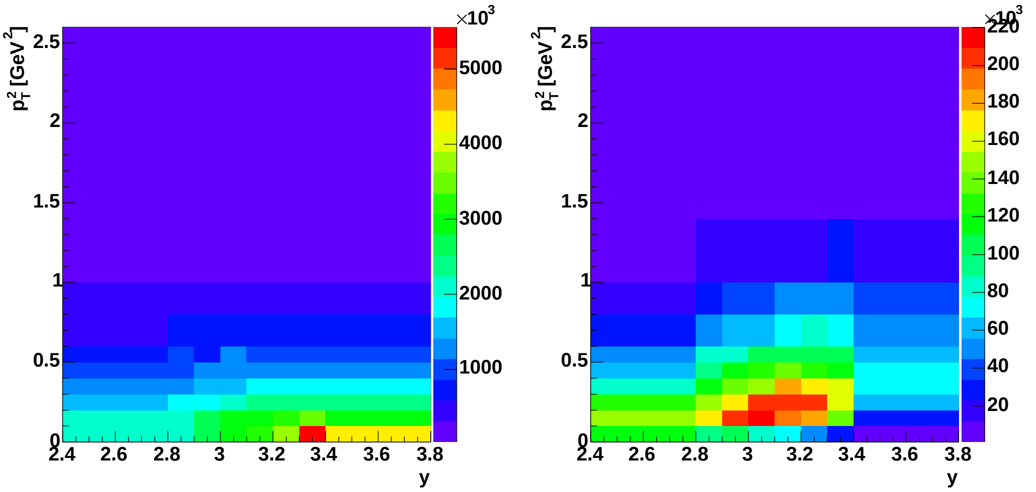

(a) $\bar{\Lambda}$, before reconstruction.

(b) $\bar{\Lambda}$, after reconstruction.

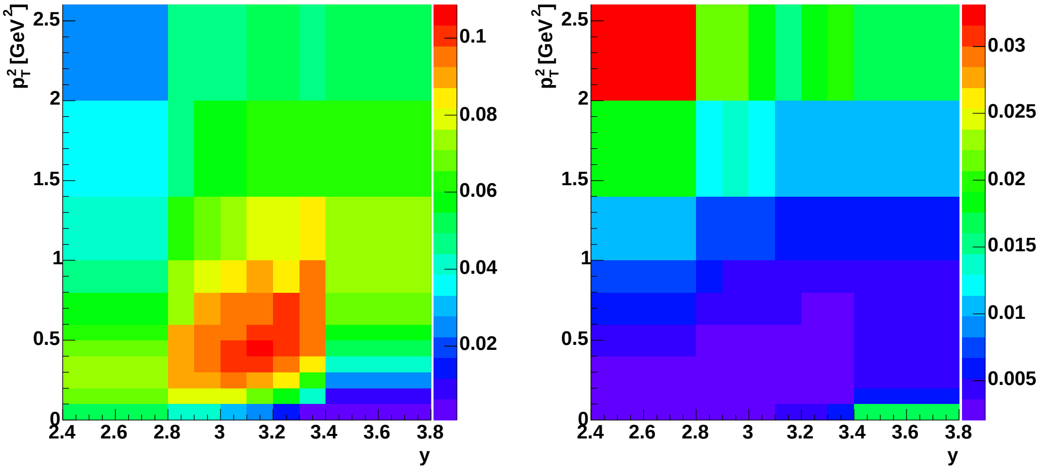

(c) $\bar{\Lambda}$ acceptance.

(d) Relative error of the $\bar{\Lambda}$ acceptance.

Figure 4.17: $\bar{\Lambda}$ acceptance as function of p_T^2 and rapidity. The distribution of Monte Carlo generated $\bar{\Lambda}$s after applying the reweighting is shown in (a), the resulting distribution after the reconstruction is displayed in (b). The acceptance, i.e. the ratio of these two histograms is presented (c) together with its relative errors (d).

	C	Ti	W
Λ	0.062735(9)	0.0642(8)	0.06559(1)
$\bar{\Lambda}$	0.056551(9)	0.0574(5)	0.05828(1)
Ξ^-	0.01545(2)	0.01660(3)	0.01381(1)
$\bar{\Xi}^+$	0.01438(2)	0.01503(2)	0.01257(1)
Ω^-	0.01432(3)	0.01659(6)	0.01517(4)
$\bar{\Omega}^+$	0.01515(3)	0.01714(6)	0.01528(4)

Table 4.6: Total hyperon acceptances in the considered kinematic range of ($0.0\text{GeV}^2 < p_T^2 < 2.6\text{GeV}^2$) and ($2.4 < y < 3.8$) in the HERA-B laboratory system. The errors are statistical only.

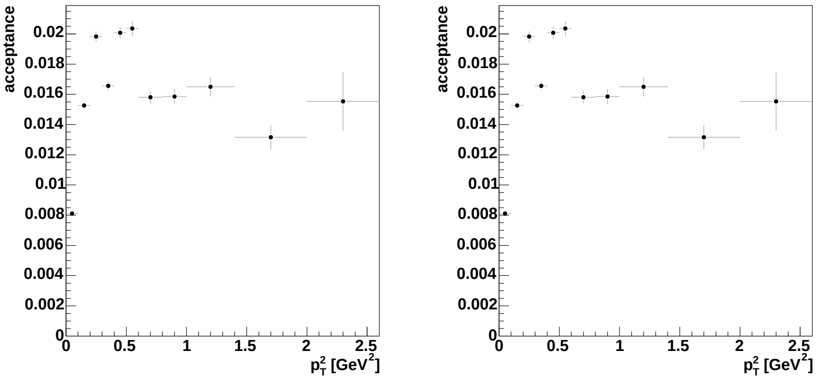

(a) Ξ acceptance.

(b) $\bar{\Xi}$ acceptance.

Figure 4.18: $\Xi/\bar{\Xi}$ acceptance as function of p_T^2.

properties of the concomitant event can also have an impact on reconstruction efficiencies and precisions. In this analysis, the following contributions to the systematic error were evaluated:

- The general agreement of Monte Carlo simulation and data was tested by comparing the differential distributions of the following kinematic variables: the transverse momentum p_T^2, the rapidity y, Feynman x_F (see page 106), the proper lifetime $c\tau$ and the azimuthal angle ϕ.
- The influence of the selection cut values was studied by varying each cut parameter. The behaviour of the ratio of the signal entries reconstructed for data and MC reveals the dependence of the acceptance determination on the cut values.
- Errors on external input to the measurements as the error on the luminosity determination and the branching fractions of the reconstructed decays also have to be considered.

The total systematic error was determined by adding all contributions quadratically.

Comparison of data and Monte Carlo simulation

A powerful means for the comparison of two distributions with statistics N_1, N_2 is the so-called Kolmogorov- Smirnov test [Pre92]. Here, a measure for the deviation between the distributions which are functions of the variable x is computed from the maximum difference of the corresponding cumulative distribution functions $S_{N_i}(x)$:

$$D = \max_{-\infty < x < +\infty} \mid S_{N_1}(x) - S_{N_2}(x) \mid \tag{4.14}$$

(Here, $S_{N_i}(x)$ is the fraction of data points left of x.)

If D is non-zero, a probability can be calculated that both distributions are still compatible within their statistical errors:

$$prob(D > observed) = Q_{KS}\left(\sqrt{\tfrac{N_1 N_2}{N_1+N_2}}D\right) \tag{4.15}$$

where

$$Q_{KS}(\lambda) = 2\sum_{j=1}^{\infty}(-)^{j-1}e^{-2j^2\lambda^2} \tag{4.16}$$

In order to measure the deviation between the kinematics of hyperons in the data and in the simulation, the Kolmogorov-Smirnov test was applied in the following way: In Equ. 4.15 the errors are assumed to behave as $\sqrt{N}$, where N is the statistics in each bin, while in the case of reconstructed hyperon signals, the error on the number of entries in the peak, S, is computed as follows:

$$\Delta S = \sqrt{(\Delta N_{SB})^2 + (\Delta B)^2} \tag{4.17}$$

(Here, N_{SB} is the number of entries in the peak region before background subtraction and B is the number of background events in the same range.)

Thus, ΔS behaves different than $\sqrt{S}$. Therefore, the equivalent statistics S_e for each bin has to be calculated by satisfying

$$\frac{\Delta S}{S} = \frac{1}{\sqrt{S_e}}. \tag{4.18}$$

The total equivalent statistics was calculated by summing up the equivalent statistics of each bin. Second, the probability that the distribution of Monte Carlo simulated and real data hyperons are consistent was determined using Equ. 4.15, replacing N_1 and N_2 by their corresponding equivalent statistics. If this probability was smaller than 0.5, i.e. smaller than its expectation value, the equivalent statistics of the data sample was modified by a factor a such that Equ. 4.15 yielded 0.5. This factor a gives the ratio of systematic and statistical error which can then be applied to each signal independently:

$$(\Delta S_e)^2_{tot} = (\Delta S_e)^2_{syst} + (\Delta S_e)^2_{stat} = \frac{1}{a}(\Delta S_e)^2_{stat}. \tag{4.19}$$

Therefore, adopting the same relation for the real statistics:

$$(\Delta S)_{syst} = \sqrt{\frac{1}{a} - 1} \cdot (\Delta S)_{stat} = b \cdot (\Delta S)_{stat}. \tag{4.20}$$

This was applied to the differential distributions of p_T^2, y, x_F, $c\tau$ and ϕ, and, in order to have a conservative estimate of the error, the maximum value of b was taken as the systematic error arising from the deviation between the data and the Monte Carlo simulation. These values are listed for $\Lambda/\bar{\Lambda}$ and $\Xi/\bar{\Xi}$ and for the different target materials in Table 4.7. In the case of $\Lambda/\bar{\Lambda}$, the contribution to the total error is roughly $3-5$ times as high as the statistical error, while for $\Xi/\bar{\Xi}$, where the statistics is much lower, the share is of the same order as the statistical uncertainties.

Target	b_Λ	$b_{\bar{\Lambda}}$	b_Ξ	$b_{\bar{\Xi}}$
C	2.7	5.1	1.0	1.7
Ti	-	-	0.8	1.5
W	3.0	5.8	1.6	1.6

Table 4.7: Contribution to the systematic error from the deviation between Monte Carlo simulation and real data for $\Lambda/\bar{\Lambda}$ and $\Xi/\bar{\Xi}$. Listed are the ratios b_X of the systematic error assessable in the comparison of differential distributions of kinematic variables with respect to the statistical errors (see page 113).

Variation of the selection cuts

The influence of the cut parameters chosen for the signal preparation was tested by evaluating the ratio of signal events observed in data and in the Monte Carlo simulation, N_{data}/N_{MC}, since this shows whether the reconstruction efficiency changes in

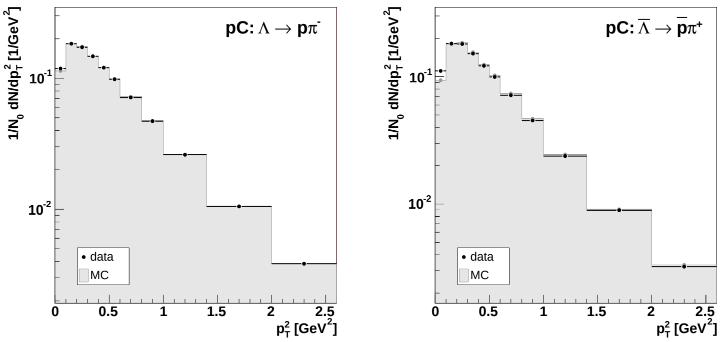

(a) Λ: p_T^2 (b) $\bar{\Lambda}$: p_T^2

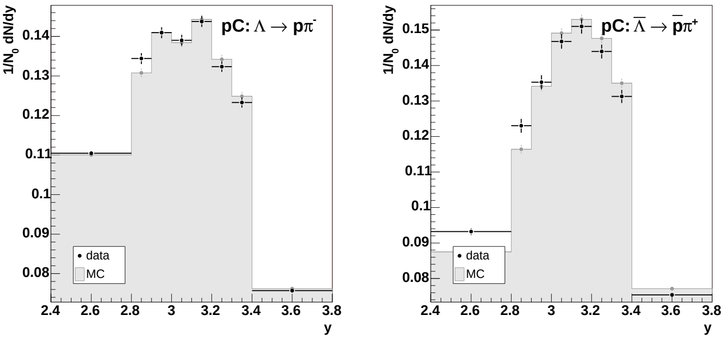

(c) Λ: rapidity (d) $\bar{\Lambda}$: rapidity

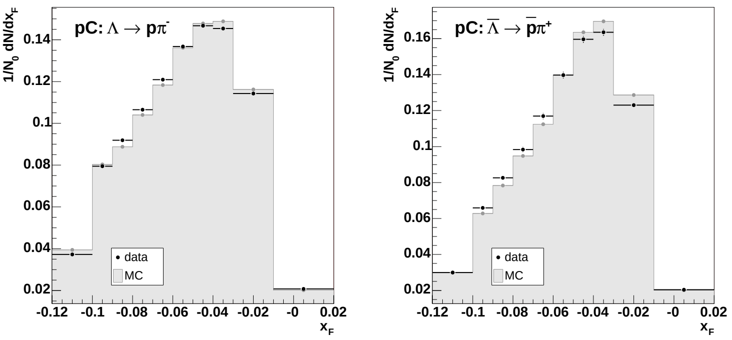

(e) Λ: x_F (f) $\bar{\Lambda}$: x_F

Figure 4.19: Comparison of data and Monte Carlo of the p_T^2, y and x_F distributions of $\Lambda/\bar{\Lambda}$. The error bars show the statistical errors only.

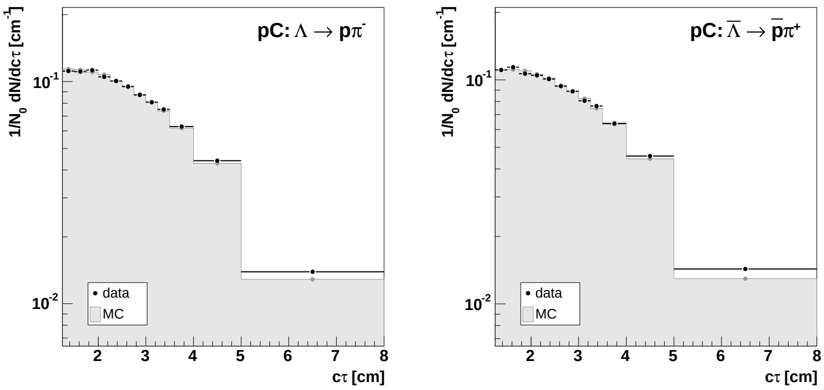

(a) Λ: $c\tau$ (b) $\bar{\Lambda}$: $c\tau$

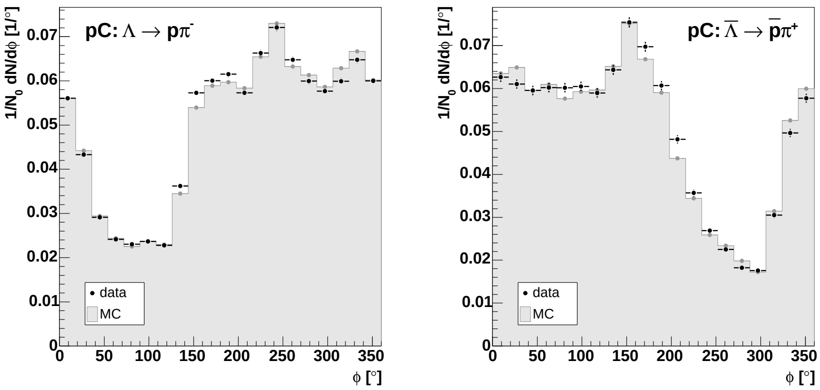

(c) Λ: ϕ (d) $\bar{\Lambda}$: ϕ

Figure 4.20: Comparison of data and Monte Carlo of the $c\tau$ and ϕ distributions of $\Lambda/\bar{\Lambda}$. The error bars show the statistical errors only.

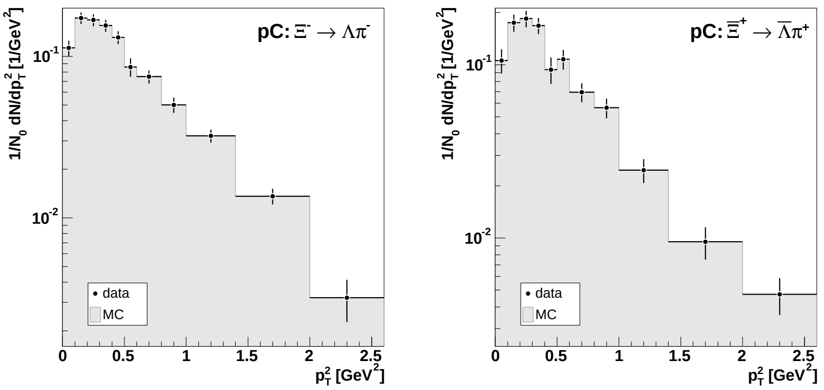

(a) Ξ: p_T^2 (b) $\bar{\Xi}$: p_T^2

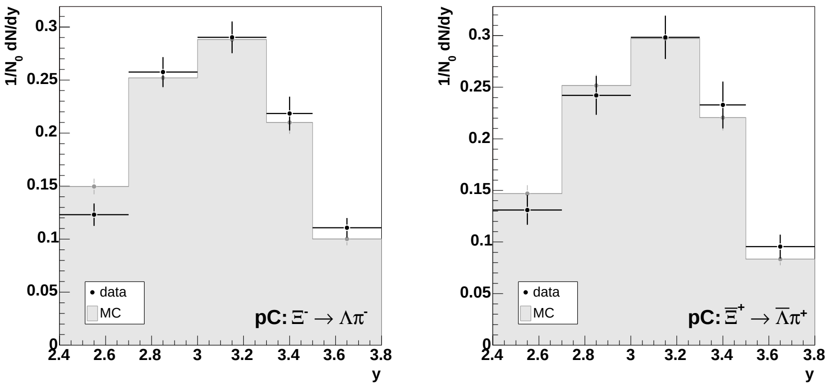

(c) Ξ: rapidity (d) $\bar{\Xi}$: rapidity

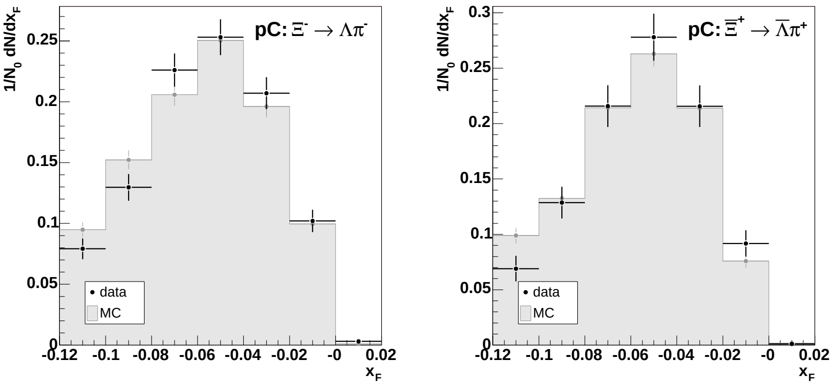

(e) Ξ: x_F (f) $\bar{\Xi}$: x_F

Figure 4.21: Comparison of data and Monte Carlo of the p_T^2, y and x_F distributions of $\Xi/\bar{\Xi}$. The error bars show the statistical errors only.

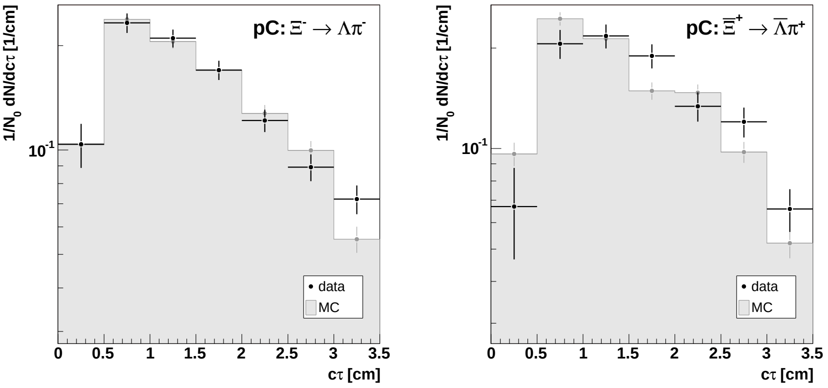

(a) Ξ: $c\tau$ (b) $\bar{\Xi}$: $c\tau$

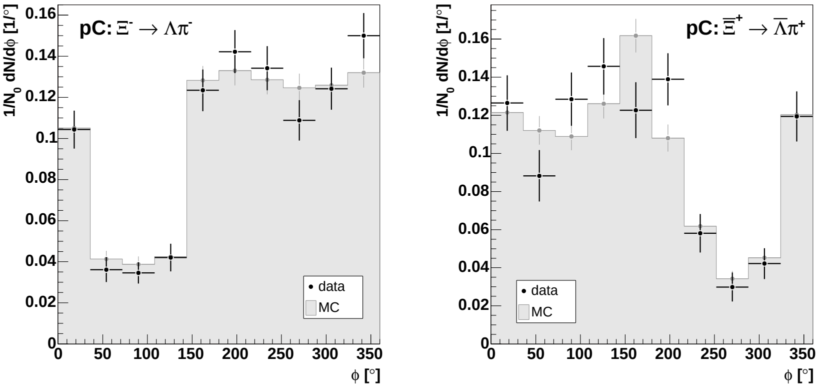

(c) Ξ: ϕ (d) $\bar{\Xi}$: ϕ

Figure 4.22: Comparison of data and Monte Carlo of the $c\tau$ and ϕ distributions of $\Xi/\bar{\Xi}$. The error bars show the statistical errors only.

the same way for the two samples. The selection cuts listed in Table 4.4 were varied in ten steps each while the other parameters were kept at their nominal values, and the resulting ratios were plotted as a function of the cut parameter under study. The plots are shown in Fig. 4.23 for $\Lambda/\bar{\Lambda}$ and Fig. 4.24 and 4.25 for $\Xi/\bar{\Xi}$, respectively. In the case of $\Lambda/\bar{\Lambda}$, no dependence of N_{data}/N_{MC} on the cut parameters was found while for $\Xi/\bar{\Xi}$, an increase of the ratio can be observed if the cuts on the distance of closest approach of the tracks in the $\Xi/\bar{\Xi}$ vertex or on the impact parameter with respect to the primary vertex are tightened. A possible explanation could be that there are more candidates among the combinatorial background which can be rejected by tighter cuts in the real data compared to the Monte Carlo simulated data. Nonetheless, the cut values that were found by the optimization procedure all lie in plateau regions where the ratios show a stable behaviour. To assess the systematic error associated with the cut variation quantitatively, the RMS scatter of the obtained ratios serves as a measure. Similar as before, the maximum contribution of all parameters was adopted as share to the total systematic error; the results are listed in Table 4.8. As can be expected from the plots in Fig. 4.23, there is only a very small contribution below 1% in the case of $\Lambda/\bar{\Lambda}$, but for $\Xi/\bar{\Xi}$, systematic uncertainties of up to 10% are found.

Target	σ^{Λ}_{cut}	σ^{Λ}_{cut}	σ^{Ξ}_{cut}	σ^{Ξ}_{cut}
C	$\leq 1\%$	$\leq 1\%$	7%	10%
Ti	-	-	5%	3%
W	$\leq 1\%$	$\leq 1\%$	5%	7%

Table 4.8: Contribution of the variation of the selection cuts for $\Lambda/\bar{\Lambda}$ and $\Xi/\bar{\Xi}$ to the systematic error: The ratio of signal entries reconstructed in the data and the Monte Carlo simulation was determined for ten different values of each cut variable. The maximum RMS scatter of these distributions was taken as a measure for the associated systematic error.

Systematic error for $\Omega/\bar{\Omega}$

In the case of $\Omega/\bar{\Omega}$, the total signal statistics is very low. The consequence is that it is impossible to plot differential distributions of kinematic variables and that the evaluation of a variation of the selection cuts is very difficult. Therefore, it is not feasible to compare data and Monte Carlo at the same level as for $\Lambda/\bar{\Lambda}$ and $\Xi/\bar{\Xi}$. As already mentioned, no reweighting procedure could be applied because of the low number of signal entries. Since the kinematics of the decay $\Omega \to \Lambda K$ is not so different from the decay $\Xi \to \Lambda\pi$, the weights obtained for $\Xi/\bar{\Xi}$ were applied to $\Omega/\bar{\Omega}$ in order to estimate the systematic error arising from the Monte Carlo simulation of the detector acceptance. The resulting acceptances with and without reweighting differed by up to 20%. This was therefore assumed to be the total systematic error for the $\Omega/\bar{\Omega}$ measurements.

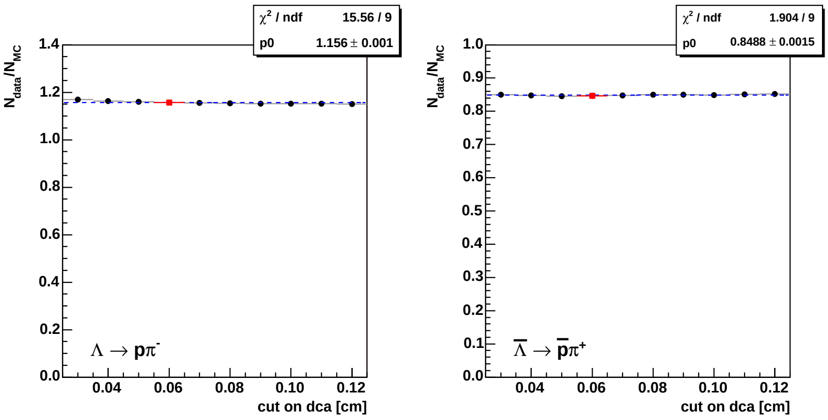

(a) distance of closest approach of the daughter tracks

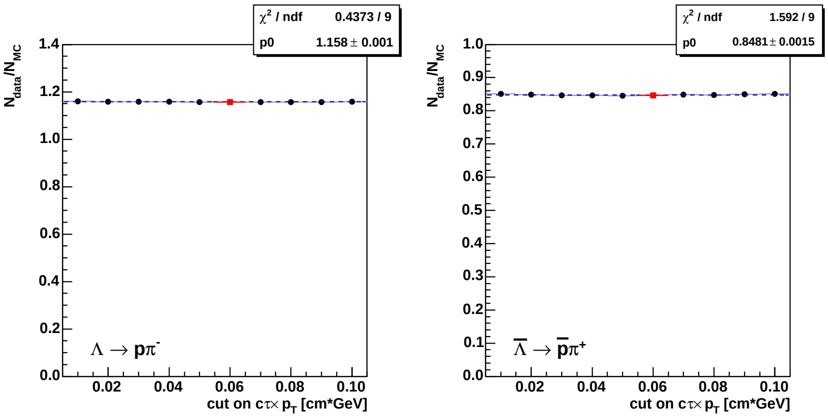

(b) $c\tau \times p_T$

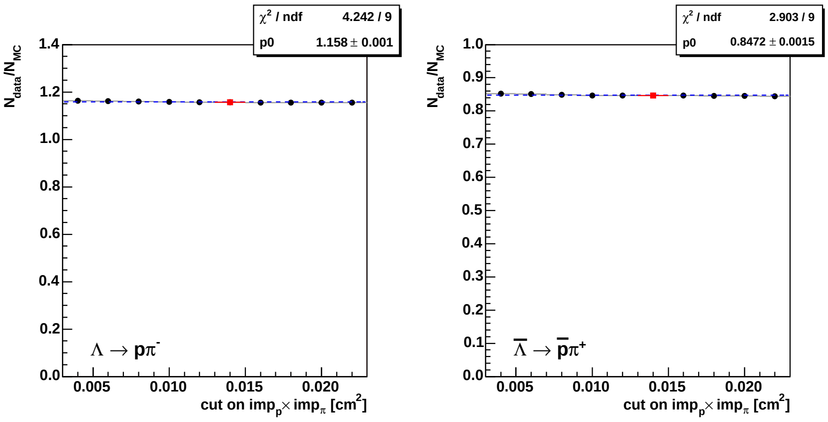

(c) product of p and π impact parameters

Figure 4.23: Variation of the selection cut parameters $\Lambda/\bar{\Lambda}$. The ratio of reconstructed signal entries of data and Monte Carlo is plotted versus the different cut parameters (all other cut variables were kept at the standard values).

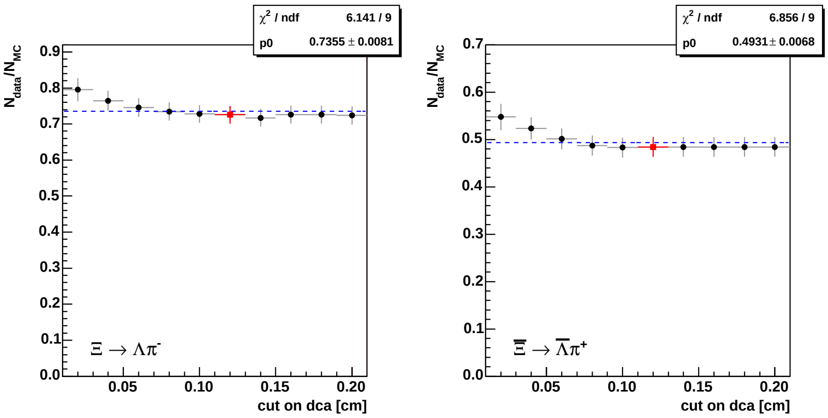

(a) distance of closest approach of the daughter tracks

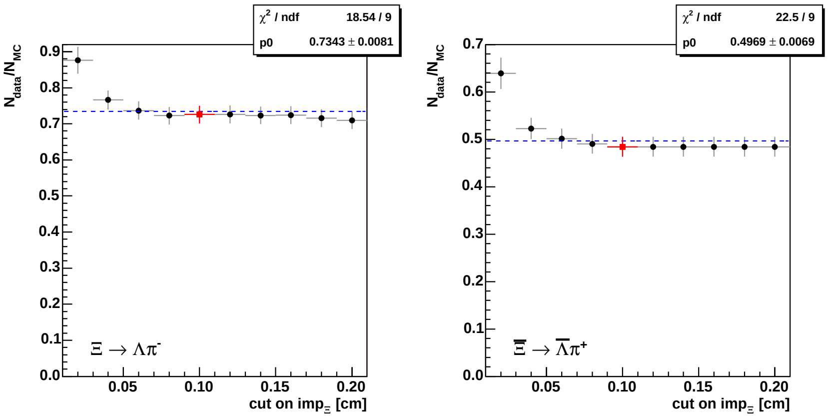

(b) $\Xi/\bar{\Xi}$ impact parameter

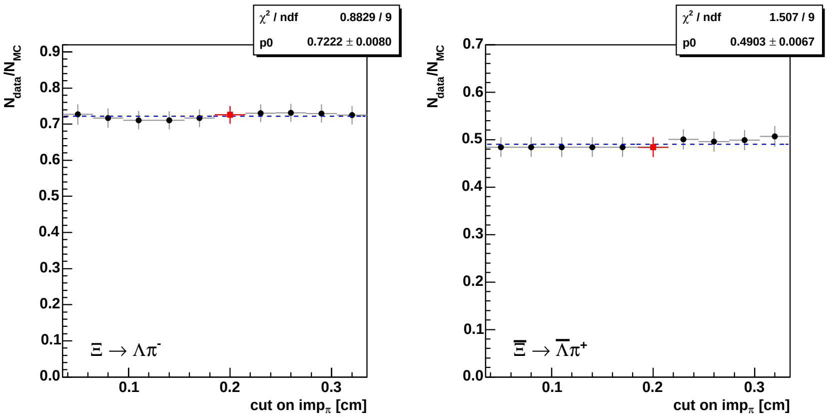

(c) $\Xi/\bar{\Xi}$: impact parameter of π

Figure 4.24: Variation of the selection cut parameters for $\Xi/\bar{\Xi}$. The ratio of reconstructed signal entries of data and Monte Carlo is plotted versus the different cut parameters (all other cut variables were kept at the standard values).

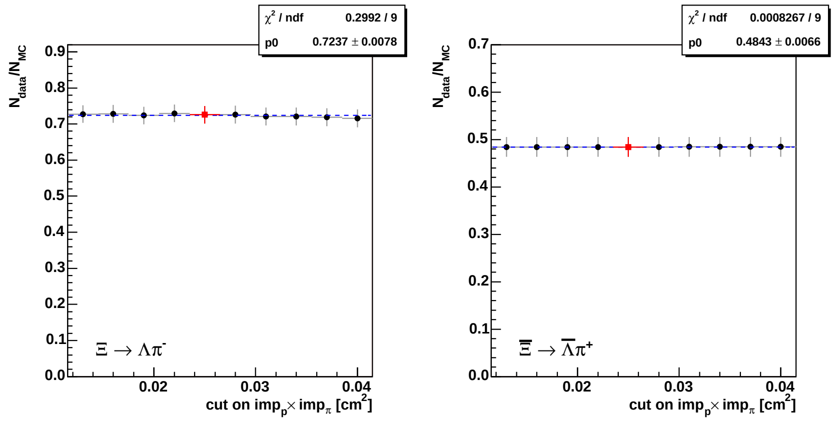

(a) product of p and π impact parameters

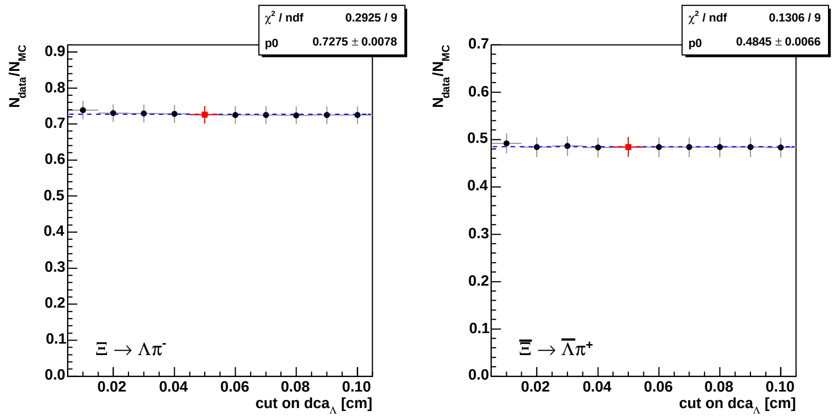

(b) $\Xi/\bar{\Xi}$: $\Lambda/\bar{\Lambda}$ vertex quality

Figure 4.25: Variation of the selection cut parameters for $\Xi/\bar{\Xi}$. The ratio of reconstructed signal entries of data and Monte Carlo is plotted versus the different cut parameters (all other cut variables were kept at the standard values).

4.2.6 Antiparticle/Particle ratios

For the measurement of the production ratios of antihyperons and hyperons, only the reconstructed signal yields and the acceptances determined by means of the Monte Carlo simulation are needed for the final results:

$$\frac{\bar{H}}{H} = \frac{N_{\bar{H}}}{N_H} \cdot \frac{a_H}{a_{\bar{H}}} \tag{4.21}$$

(Here, N_X is the reconstructed signal for particle X and a_X is the acceptance for the decay channel considered for the reconstruction of X.)

The branching fractions and the luminosity values do not enter the calculation, hence the total error depends only on the uncertainties due to the Monte Carlo simulation and the limited statistics. Table 4.9 lists the ratios measured in the kinematic range defined earlier, i.e. within the rapidity range of $(2.4 < y < 3.8)$ and the p_T^2 region of ($0.0\ \text{GeV}^2 < p_T^2 < 2.6\ \text{GeV}^2$) in the HERA-B laboratory frame, with their statistical and systematic errors. Within these errors, no dependence on the target material is observed. Therefore, the mean for the three data samples (weighted according to their statistics) was used when comparing the results of this analysis in the following with published values.

In Fig. 4.26, the weighted mean of the $\bar{\Lambda}/\Lambda$ ratios for the three targets is presented together with previous results from experiments utilizing proton-proton (pp), proton-nucleus (pA) and nucleus-nucleus (AA) collisions and measuring over a wide range of energies: The CERN experiments NA57 [F+02, S+04], NA49 [K+02a, M+03] and WA97 [C+99] at SPS measure at energies of 40 to 158 A GeV corresponding to nucleon-nucleon center-of-mass energies ($\sqrt{s_{NN}}$) of approximately 8.8 to 17.2 GeV and the experiment E802 at BNL AGS at $\sqrt{s_{NN}} = 5.4$ GeV [C+02]. PHENIX and STAR, experiments at the heavy ion collider RHIC, operate with Au-Au collisions at $\sqrt{s_{NN}} = 130$ GeV [A+02a, A+02b, A+03f]. The published HERA-B result of 2003 [A+03a] is shown as well as the result of this analysis; both measured values are statistically compatible with each other. With respect to the other experimental results, the HERA-B values fit in the general trend of the energy dependence of $\frac{\bar{\Lambda}}{\Lambda}$. Comparing the curves for pp, pA and AA collisions, one might find an indication that they are shifted slightly in energy. This is also suggested by results of NA49 [K+02a] and NA57 [F+02] which indicate that going from p-p over p-Pb to Pb-Pb collisions, the ratio $\bar{\Lambda}/\Lambda$ decreases by roughly 60 % in each step.

Fig. 4.27 shows a comparison of the ratios $\frac{\bar{\Lambda}}{\Lambda}$, $\frac{\bar{\Xi}}{\Xi}$ and $\frac{\bar{\Omega}}{\Omega}$ measured in this analysis with values obtained by other experiments in AA collisions at different center-of-mass energies. Also here, the results fit in the general context, but for a precise extrapolation of the AA values to the energy of HERA-B in order to observe a possible deviation for pA collisions, more data are needed.

Calculating the double ratios $\frac{\bar{\Xi}/\Xi}{\bar{\Lambda}/\Lambda}$ and $\frac{\bar{\Omega}/\Omega}{\bar{\Xi}/\Xi}$, one obtains the parameter D of the coalescence model described on page 84f, see Equ. 4.7. If quark deconfinement would be reached at HERA-B energies, both double ratios would yield the same value for D, according to the model. Using the weighted mean of all target materials, we get

$$\frac{\bar{\Xi}/\Xi}{\bar{\Lambda}/\Lambda} = 1.25 \pm 0.15,$$

Target	ratio of	result
C	$\bar{\Lambda}/\Lambda$	$0.560 \pm 0.004_{stat} \pm 0.010_{syst}$
	$\bar{\Xi}/\Xi$	$0.62 \pm 0.03_{stat} \pm 0.12_{syst}$
	Ξ/Λ	$0.053 \pm 0.002_{stat} \pm 0.006_{syst}$
	$\bar{\Xi}/\bar{\Lambda}$	$0.058 \pm 0.003_{stat} \pm 0.009_{syst}$
	$\bar{\Omega}/\Omega$	$0.97 \pm 0.16_{stat} \pm 0.28_{syst}$
	Ω/Ξ	$0.24 \pm 0.03_{stat} \pm 0.06_{syst}$
	$\bar{\Omega}/\bar{\Xi}$	$0.39 \pm 0.05_{stat} \pm 0.10_{syst}$
Ti	$\bar{\Lambda}/\Lambda$	$0.517 \pm 0.010_{stat} \pm 0.022_{syst}$
	$\bar{\Xi}/\Xi$	$0.73 \pm 0.05_{stat} \pm 0.11_{syst}$
	Ξ/Λ	$0.056 \pm 0.003_{stat} \pm 0.006_{syst}$
	$\bar{\Xi}/\bar{\Lambda}$	$0.079 \pm 0.004_{stat} \pm 0.010_{syst}$
	$\bar{\Omega}/\Omega$	$0.92 \pm 0.23_{stat} \pm 0.26_{syst}$
	Ω/Ξ	$0.22 \pm 0.04_{stat} \pm 0.05_{syst}$
	$\bar{\Omega}/\bar{\Xi}$	$0.28 \pm 0.05_{stat} \pm 0.06_{syst}$
W	$\bar{\Lambda}/\Lambda$	$0.524 \pm 0.003_{stat} \pm 0.009_{syst}$
	$\bar{\Xi}/\Xi$	$0.64 \pm 0.03_{stat} \pm 0.09_{syst}$
	Ξ/Λ	$0.065 \pm 0.002_{stat} \pm 0.006_{syst}$
	$\bar{\Xi}/\bar{\Lambda}$	$0.080 \pm 0.003_{stat} \pm 0.009_{syst}$
	$\bar{\Omega}/\Omega$	$0.80 \pm 0.11_{stat} \pm 0.23_{syst}$
	Ω/Ξ	$0.24 \pm 0.02_{stat} \pm 0.05_{syst}$
	$\bar{\Omega}/\bar{\Xi}$	$0.30 \pm 0.04_{stat} \pm 0.07_{syst}$

Table 4.9: The ratios of the production rates of Λ, $\bar{\Lambda}$, Ξ, $\bar{\Xi}$, Ω and $\bar{\Omega}$ are listed together with their statistical and systematic errors. The ratios were measured in the kinematic range of ($0.0\ \mathrm{GeV}^2 < p_T^2 < 2.6\ \mathrm{GeV}^2$) and ($2.4 < y < 3.8$) in the HERA-B laboratory system.

$$\frac{\bar{\Omega}/\Omega}{\bar{\Xi}/\Xi} = 1.33 \pm 0.28.$$

With the large errors on the $\bar{\Omega}/\Omega$ ratio, the resulting error on the second double ratio is too large to allow conclusions to be drawn from a comparison of the two values. An agreement is not expected, however, it can not be excluded.

With the data available, also ratios of different hyperon species were determined: $\frac{\Xi}{\Lambda}$, $\frac{\Omega}{\Xi}$ and the ratios of the corresponding antiparticles. In this case, the branching fractions and their errors have to be taken into account, too, and Equ. 4.21 becomes

$$\frac{\bar{H}_x}{H_y} = \frac{N_{\bar{H}_x}}{N_{H_y}} \cdot \frac{BR(\bar{H}_x \rightarrow ...)}{BR(H_y \rightarrow ...)} \cdot \frac{a_{H_y}}{a_{\bar{H}_x}} \tag{4.22}$$

(Here, $BR(X \rightarrow ...)$ is the branching fraction for the decay channel considered for the reconstruction of X.)

Since the branching fraction for the decay $\Lambda \rightarrow p\pi^-$ (and it charge conjugate) occurs in all reconstructed decays, it drops out in Equ. 4.22. Fig. 4.28 presents a comparison of these ratios as a function of the nucleon-nucleon center-of-mass energy of the collisions. It is difficult to find a general trend of the measured values: While NA57 and WA97 observe (mostly) significantly different values for particle and antiparticle ratios, the results presented by the STAR collaboration and in this analyis are similar. Certainly, more measurements are necessary in order to decide how our results classes with the values from AA collisions.

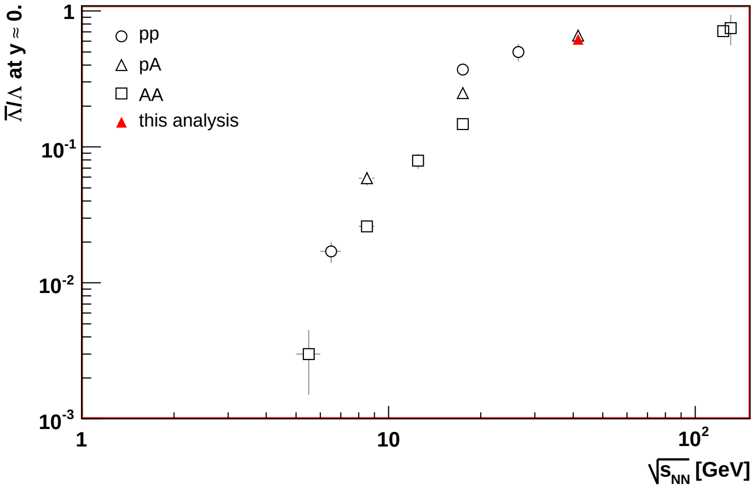

Figure 4.26: $\frac{\bar{\Lambda}}{\Lambda}$ at mid-rapidity as a function of the nucleon-nucleon center-of-mass energy. Results for pp, pA and AA collisions, taken from [F$^+$02, S$^+$04, K$^+$02a, C$^+$99, C$^+$02, M$^+$03, A$^+$02a, A$^+$02b, A$^+$03f], are presented together with the weighted mean of the results for the three target materials of this analysis.

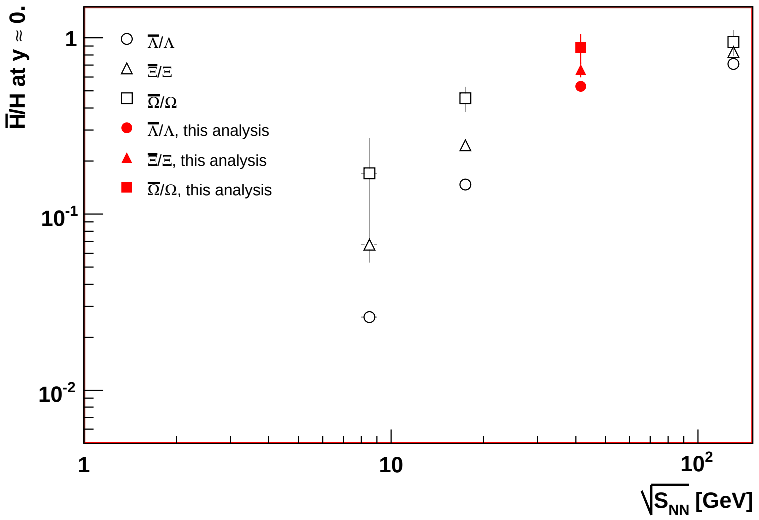

Figure 4.27: $\frac{\bar{\Lambda}}{\Lambda}$ (strangeness $S = 1$) , $\frac{\bar{\Xi}}{\Xi}$ ($S = 2$) and $\frac{\bar{\Omega}}{\Omega}$ ($S = 3$) at mid-rapidity. Results for AA collisions, measured by NA57 and WA97 in Pb-Pb collisions at $\sqrt{s_{NN}} =$ 8.8 GeV and 17.2 GeV [S$^+$04, C$^+$99] and by PHENIX and STAR in Au-Au collisions at $\sqrt{s_{NN}} = 130$ GeV [A$^+$02a, A$^+$03f] are presented together with the weighted mean of the results for the three target materials of this analysis ($\sqrt{s_{NN}} = 41.6$ GeV).

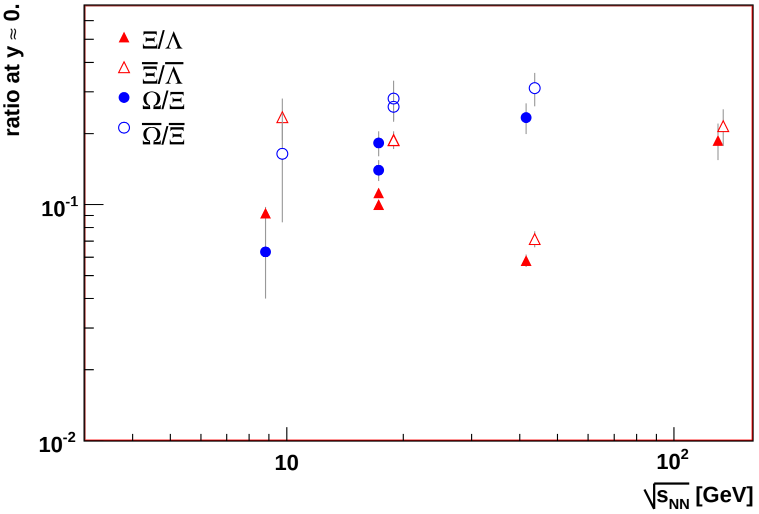

Figure 4.28: $\frac{\Xi}{\Lambda}$, $\frac{\bar{\Xi}}{\bar{\Lambda}}$, $\frac{\Omega}{\Xi}$ and $\frac{\bar{\Omega}}{\bar{\Xi}}$ at mid-rapidity. Results for AA collisions, measured by NA57 and WA97 in Pb-Pb collisions at $\sqrt{s_{NN}} = 8.8$ GeV and 17.2 GeV [S$^+$04, C$^+$99] and by STAR in Au-Au collisions at $\sqrt{s_{NN}} = 130$ GeV [A$^+$03f] are presented together with the weighted mean of the results for the three target materials of this analysis ($\sqrt{s_{NN}} = 41.6$ GeV). For a better visibility, the ratios of the antiparticles were shifted slightly towards higher energies.

4.2.7 Inclusive cross section measurements

The measurement of the total cross section of a particle X requires more ingredients than the preparation of the signals and the acceptance determination by means of a Monte Carlo simulation. The branching fraction of the decay under study ($X \to yz$ in this example) and the recorded luminosity of the analysed data samples are necessary, too:

$$\sigma_X^{pA} = \frac{N_X}{a_X \cdot BR(X \to yz) \cdot \mathcal{L}} \tag{4.23}$$

(Here, N_X is the number of reconstructed X particles, a_X the acceptance of X particles within the kinematic range, $BR(X \to yz)$ the branching fraction of the decay under study, and $\mathcal{L}$ is the integrated luminosity of the data sample.)

A description of the luminosity determination and a table of the luminosity values of the ”Golden Minimum Bias” data sample is given in Appendix A. The branching fractions were already mentioned earlier, see page 94. Table 4.10 lists the cross sections measured for the $\Lambda/\bar{\Lambda}$, $\Xi/\bar{\Xi}$ and $\Omega/\bar{\Omega}$ hyperons in this analysis.

Since the data sample contains events recorded with three different target materials, the dependence of the production cross section on the atomic number A of the target nuclei can be measured. Usually, a power law dependence is assumed:

$$\sigma^{pA} = \sigma^{pN} \cdot A^{\alpha}. \tag{4.24}$$

(Here, A is the atomic number of the target material, σ^{pA} is the cross section per nucleus, and σ^{pN} is the cross section per nucleon.)

In Fig. 4.29, the logarithm of the measured cross section values is plotted versus the logarithm of the atomic number of the target material. These plots were then fitted by straight lines, yielding fit values for the parameters σ^{pN} and α as in Equ. 4.24. The results are listed in Table 4.11.

To test the stability of the measurement, the cross sections were calculated for each run independently and plotted as function of the run number, see Fig. 4.30 for $\Lambda/\bar{\Lambda}$ and Fig. 4.31 for $\Xi/\bar{\Xi}$, respectively. In the case of $\Xi/\bar{\Xi}$, some runs had to be omitted due to too low statistics. The error bars in these plots correspond to the statistical error only, and at the far left, the cross section measured for the complete data sample is shown for comparison (here including the systematic error). For Λ and $\bar{\Lambda}$, the measured cross sections are perfectly stable within the statistical errors, while for Ξ and $\bar{\Xi}$, some runs show deviations. The same fit ranges for the background determination have been applied as in the measurement of the total cross sections, but the statistical fluctuations expecially in the shape of the side bands of each run are large, and therefore the background estimate is not stable. Nonetheless, the overall stability tested by fitting a constant is satisfactory. The number of reconstructed Ω and $\bar{\Omega}$ hyperons was too small to perform this test.

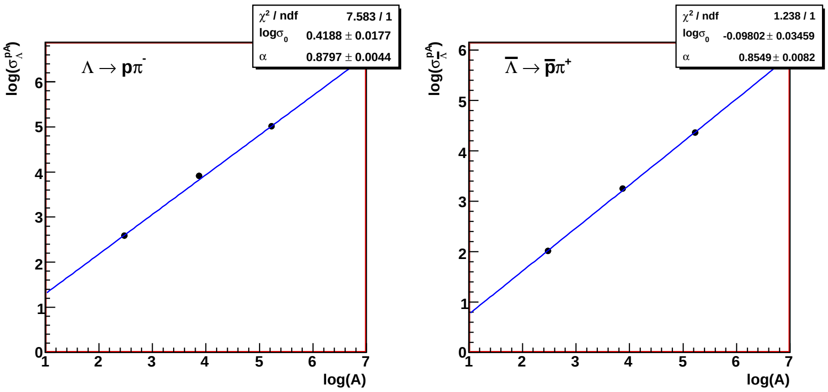

(a) $\Lambda/\bar{\Lambda}$

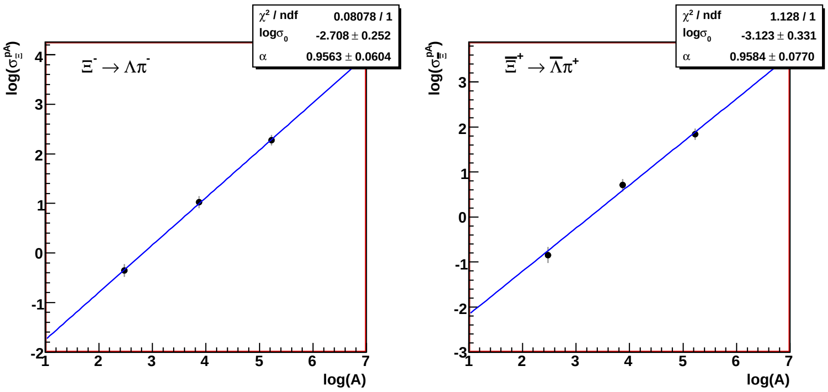

(b) $\Xi/\bar{\Xi}$

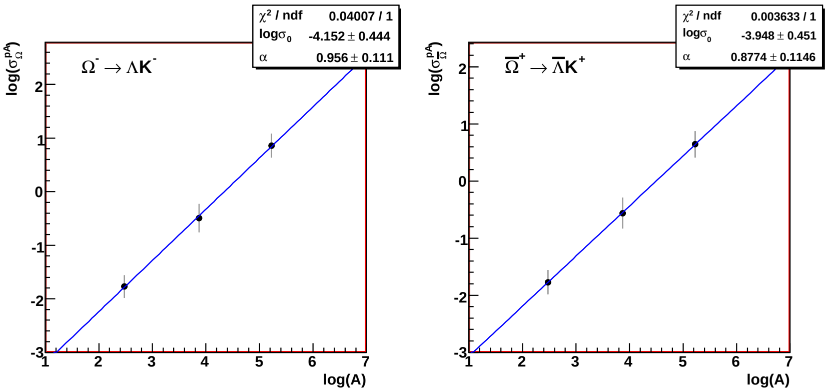

(c) $\Omega/\bar{\Omega}$

Figure 4.29: A-dependence of the hyperon production cross sections in the considered kinematic range. The function fitted to the measured values is given in Equ. 4.24.

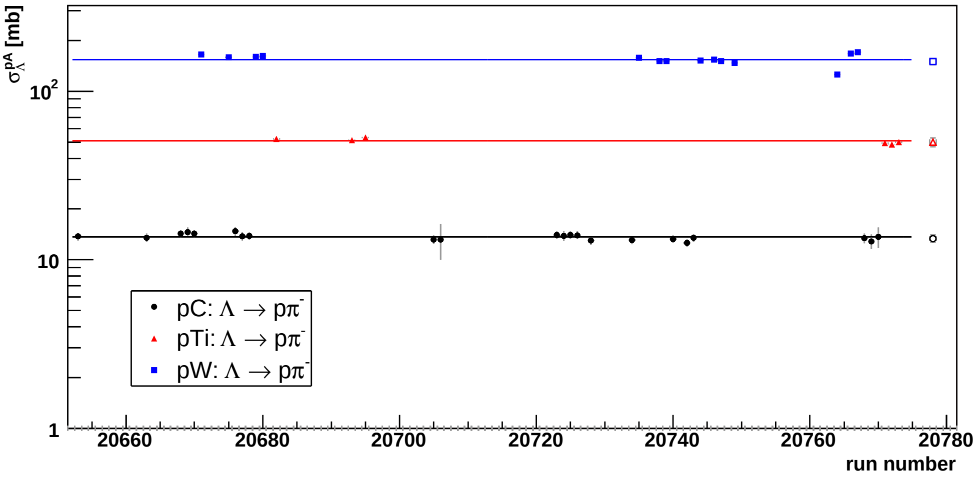

(a) Λ

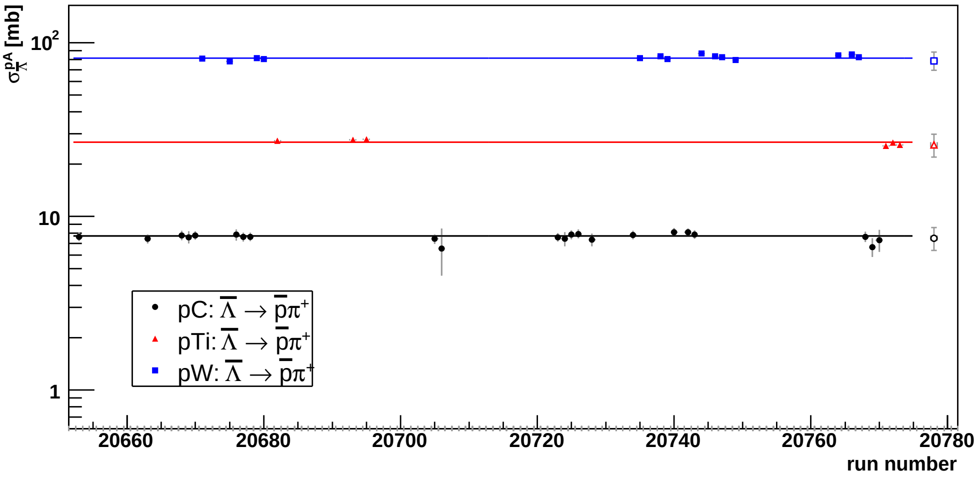

(b) $\bar{\Lambda}$

Figure 4.30: Stability of the $\Lambda/\bar{\Lambda}$ cross section with time. The cross section of Λ (a) and $\bar{\Lambda}$ (b) was evaluated for each run separately and plotted with statistical errors as function of the run number which increases with the recording date. The cross section of the whole data samples are shown with total errors at the right hand side of the plots.

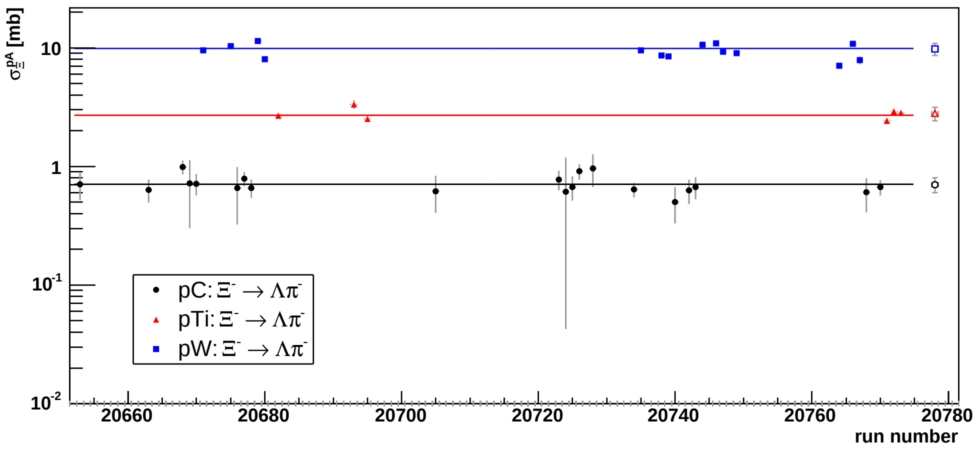

(a) Ξ

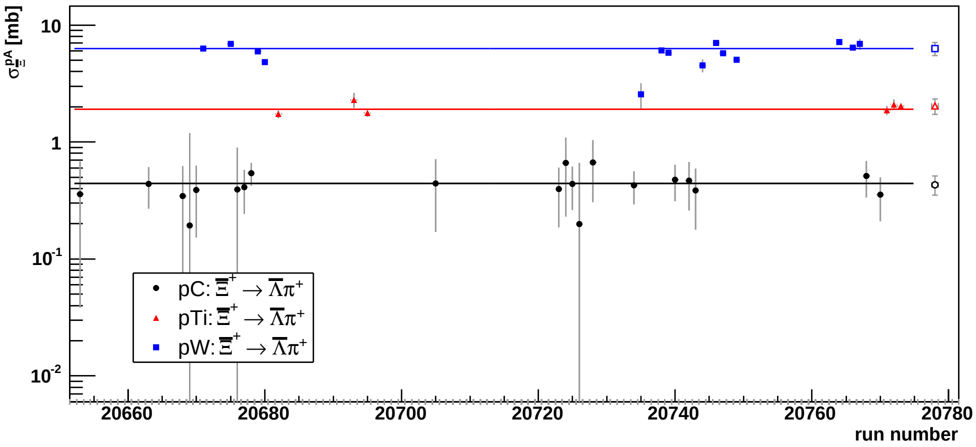

(b) $\bar{\Xi}$

Figure 4.31: Stability of the $\Xi/\bar{\Xi}$ cross section with time. The cross section of Ξ (a) and $\bar{\Xi}$ (b) was evaluated for each run separately and plotted with statistical errors as function of the run number which increases with the recording date. The cross section of the whole data samples are shown with total errors at the right hand side of the plots.

Target	Particle	σ_X^{pA} [mb]
C	Λ	$13.37 \pm 0.05_{stat} \pm 0.72_{syst}$
	$\bar{\Lambda}$	$7.49 \pm 0.04_{stat} \pm 0.41_{syst}$
	Ξ	$0.70 \pm 0.04_{stat} \pm 0.09_{syst}$
	$\bar{\Xi}$	$0.43 \pm 0.03_{stat} \pm 0.07_{syst}$
	Ω	$0.17 \pm 0.02_{stat} \pm 0.04_{syst}$
	$\bar{\Omega}$	$0.17 \pm 0.02_{stat} \pm 0.03_{syst}$
Ti	Λ	$49.93 \pm 0.69_{stat} \pm 2.89_{syst}$
	$\bar{\Lambda}$	$25.82 \pm 0.32_{stat} \pm 1.56_{syst}$
	Ξ	$2.79 \pm 0.19_{stat} \pm 0.32_{syst}$
	$\bar{\Xi}$	$2.03 \pm 0.15_{stat} \pm 0.26_{syst}$
	Ω	$0.61 \pm 0.11_{stat} \pm 0.13_{syst}$
	$\bar{\Omega}$	$0.57 \pm 0.11_{stat} \pm 0.12_{syst}$
W	Λ	$150.18 \pm 0.45_{stat} \pm 6.15_{syst}$
	$\bar{\Lambda}$	$78.67 \pm 0.41_{stat} \pm 3.35_{syst}$
	Ξ	$9.75 \pm 0.48_{stat} \pm 1.01_{syst}$
	$\bar{\Xi}$	$6.28 \pm 0.34_{stat} \pm 0.75_{syst}$
	Ω	$2.36 \pm 0.22_{stat} \pm 0.48_{syst}$
	$\bar{\Omega}$	$1.90 \pm 0.23_{stat} \pm 0.39_{syst}$

Table 4.10: The production cross sections of Λ, $\bar{\Lambda}$, Ξ, $\bar{\Xi}$, Ω and $\bar{\Omega}$ are listed together with their statistical and systematic errors. The cross sections were measured in the kinematic range of ($0.0\ \mathrm{GeV}^2 < p_T^2 < 2.6\ \mathrm{GeV}^2$) and ($2.4 < y < 3.8$) in the HERA-B laboratory system.

Particle	σ^{pN} [mb]	α
Λ	1.52 ± 0.07	0.880 ± 0.004
$\bar{\Lambda}$	0.91 ± 0.05	0.855 ± 0.008
Ξ	0.07 ± 0.02	0.96 ± 0.06
$\bar{\Xi}$	0.04 ± 0.01	0.96 ± 0.08
Ω	0.016 ± 0.007	0.96 ± 0.11
$\bar{\Omega}$	0.019 ± 0.009	0.88 ± 0.11

Table 4.11: A-dependence of the hyperon production cross sections. The parameters σ^{pN} and α are taken from fits of the function given in Equ. 4.24 to the measured values, see Fig. 4.29.

4.2.8 Differential cross sections

Differential p_T^2 spectra are often parameterized with the function

$$\frac{d\sigma}{dp_T^2} = \left(1 + \left(\frac{p_T}{p_0}\right)^2\right)^{-\beta} . \tag{4.25}$$

Unfortunately, this function has the disadvantage that the parameters p_0 and β are strongly correlated. Another form of parameterization which is equivalent to

Equ. 4.25 is

$$\frac{d\sigma}{dp_T^2} = \left[1 + \left(\frac{\sqrt{\pi}}{2}\frac{\Gamma(\beta - 1.5)}{\Gamma(\beta - 1)}\right)^2 \frac{p_T^2}{\langle p_T\rangle^2}\right]^{-\beta} \tag{4.26}$$

Here, the parameter $\langle p_T\rangle$, being the mean transverse momentum, has a physical meaning and is very stable over a wide range of β values. This form was therefore applied to fit the measured differential p_T^2 spectra.

In the case of $\Xi/\bar{\Xi}$, the errors are larger and the fits are not sensitive to the parameter β anymore. Therefore, Equ. 4.26 was considered in the limit of β approaching infinity:

$$\left.\frac{d\sigma}{dp_T^2}\right|_{\beta\to\infty} = \exp\left(-\frac{\pi}{4}\frac{p_T^2}{\langle p_T\rangle^2}\right). \tag{4.27}$$

In this way, at least the parameter $\langle p_T\rangle$ can be extracted from the measured differential p_T^2 cross section of $\Xi/\bar{\Xi}$.

Fig. 4.32 and Fig. 4.34 show the cross sections as function of p_T^2 for $\Lambda/\bar{\Lambda}$ and $\Xi/\bar{\Xi}$, respectively. On the error bars, the statistical and systematic errors are superimposed: The inner part with the perpendicular ticks states the statistical error while the full length of the error bars corresponds to the total error. The statistical errors for $\Lambda/\bar{\Lambda}$ are so small that the systematic error is the main error contribution, only in the lowest p_T^2 bin both components are comparable in size. The results of the fits of Equ. 4.26 and Equ. 4.27 are summarized in Table 4.12. The $\chi^2/n.d.f.$ values are much smaller than 1, indicating that the errors are overestimated. In the case of the systematic error, that might be the case due to the fact that they were estimated for the whole spectra (see section 4.2.5), not bin by bin.

Target	Particle	$\langle p_T\rangle^2$ [GeV^2]	$\langle p_T\rangle$ [GeV]	β	$\chi^2/n.d.f.$
C	Λ	0.45 ± 0.01	0.67 ± 0.01	5.1 ± 0.8	1.134/8
	$\bar{\Lambda}$	0.39 ± 0.01	0.62 ± 0.01	4.7 ± 0.7	0.3194/8
	Ξ	0.46 ± 0.03	0.69 ± 0.02	-	4.989/9
	$\bar{\Xi}$	0.42 ± 0.05	0.65 ± 0.04	-	3.965/9
Ti	Λ	0.50 ± 0.02	0.71 ± 0.01	4.3 ± 0.7	0.7697/8
	$\bar{\Lambda}$	0.42 ± 0.02	0.65 ± 0.02	4.1 ± 0.8	1.561/8
	Ξ	0.61 ± 0.07	0.78 ± 0.04	-	2.712/9
	$\bar{\Xi}$	0.45 ± 0.06	0.67 ± 0.04	-	2.018/9
W	Λ	0.57 ± 0.02	0.75 ± 0.01	3.8 ± 0.4	1.189/8
	$\bar{\Lambda}$	0.48 ± 0.02	0.69 ± 0.01	3.5 ± 0.4	0.6564/8
	Ξ	0.69 ± 0.06	0.83 ± 0.04	-	1.598/9
	$\bar{\Xi}$	0.57 ± 0.06	0.75 ± 0.04	-	6.296/9

Table 4.12: Results of fits to the differential p_T^2 spectra. The fitted functions are given in Equ. 4.26 for $\Lambda/\bar{\Lambda}$ and Equ. 4.27 for $\Xi/\bar{\Xi}$, respectively.

The measured cross sections as function of rapidity are shown in Fig. 4.33 for $\Lambda/\bar{\Lambda}$ and in Fig. 4.35 for $\Xi/\bar{\Xi}$. Here, no standard parameterization exists, therefore the shape of the distribution as predicted by the Monte Carlo was compared to the

Target	$\sigma_{\Lambda}^{pA}\big\vert_{y=0}$ [mb]	$\sigma_{\bar{\Lambda}}^{pA}\big\vert_{y=0}$ [mb]
C	10.1 ± 0.6	6.5 ± 0.4
Ti	36.9 ± 2.1	22.6 ± 1.6
W	107.1 ± 4.6	65.2 ± 3.3

Table 4.13: $\Lambda/\bar{\Lambda}$ production cross sections at mid-rapidity. The differential cross sections as function of rapidity were extrapolated to central rapidity by fitting Equ. 4.28 to the measured distributions.

resulting distributions found in the data. The following function was chosen to fit the data:

$$\frac{d\sigma}{dy} = p_0 + p_1 \cdot (y - y_{cms})^2 \,. \tag{4.28}$$

Here, y_{cms} is the rapidity of the HERA-B center-of-mass system. Thus the parameter p_0 yields the cross section at $y = 0$ in the rest frame of the collision. Table 4.13 lists the extrapolated cross sections for Λ and $\bar{\Lambda}$ at mid-rapidity. The values amount to roughly 70% of the cross section value for the full range (see Table 4.10 with the values for the whole kinematic range under study). The shape of the distributions differs strongly for Λ and $\bar{\Lambda}$: While the cross section increases with rapidity for $\bar{\Lambda}$, it is relatively flat for Λ, i.e. there is only a small curvature measured by the parameter p_1 in Equ. 4.28. In fact, p_1 is negative for the carbon data sample, compatible with zero for the titanium sample and positive for the tungsten data. This indicates that a leading particle effect influences the shape of the rapidity distribution of Λ, which depends on the atomic number of the target nucleus. Since $\bar{\Lambda}$ is an anti-baryon, no leading particle effect can be expected in pA collisions. The Monte Carlo simulation describes this behaviour very well both for Λ and $\bar{\Lambda}$.

The comparison of the Monte Carlo prediction and the measured differential cross section as function of rapidity for $\Xi/\bar{\Xi}$ reveals that the one-dimensional reweighting and acceptance correction in one kinematic variable has only limited power to improve the agreement in other variables and hence the reliability of the measurement. The predicted shape and the measured one deviate significantly, therefore a different fit function than in the case of $\Lambda/\bar{\Lambda}$ matches the data: a general second order polynomial,

$$\frac{d\sigma}{dy} = p_0 + p_1 \cdot y + p_2 \cdot y^2. \tag{4.29}$$

For a robust measurement of the differential cross section using the complete available kinematic range, one has to verify that the shape of the distribution is stable with respect to other kinematic variables. Due to the limited detector acceptance, the reconstruction efficiency is a complicated function of the kinematic range chosen for the analysis. This can be seen in the left columns of Fig. 4.36 and Fig. 4.37, respectively, where the p_T^2 and rapidity distributions of Λ and $\bar{\Lambda}$ for different bins in rapidity and p_T^2 are superimposed. The black markers give the average values while their error bars represent the RMS spread of the measured values in the respective bin. The shape of the distributions strongly depends on the bin of the other variable, and the spread is large. After the acceptance correction (right column

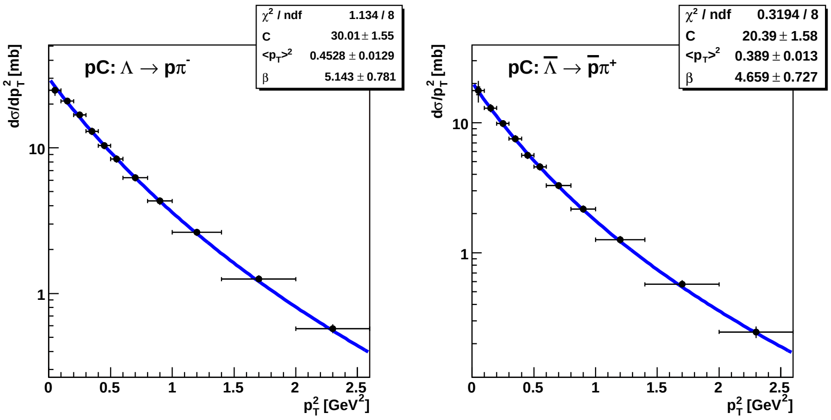

(a) C

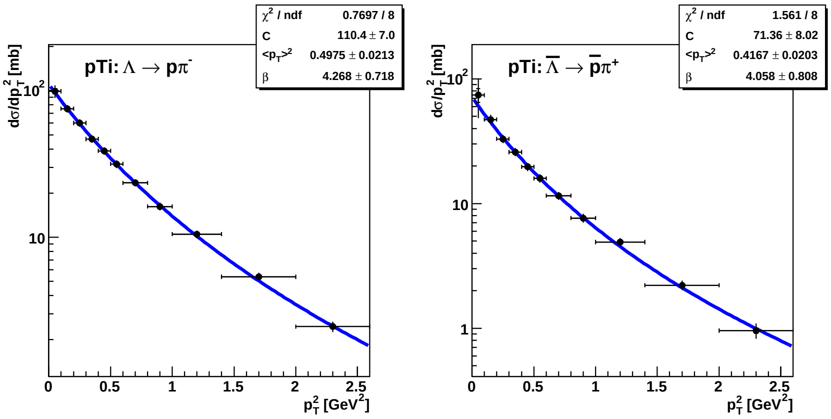

(b) Ti

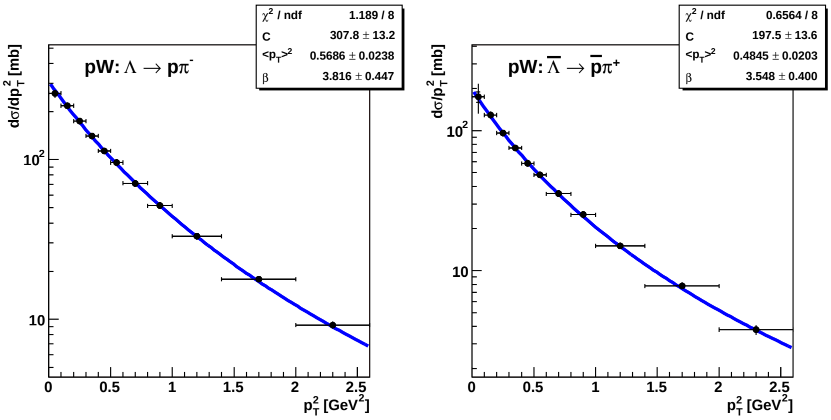

(c) W

Figure 4.32: $\Lambda/\bar{\Lambda}$ production cross section as function of p_T^2. The error bars show the statistical errors (with perpendicular ticks) as well as the total error (full length of the error bars).

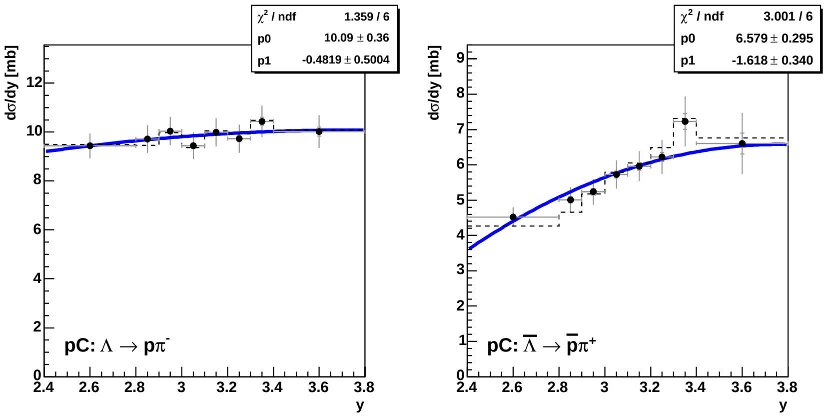

(a) C

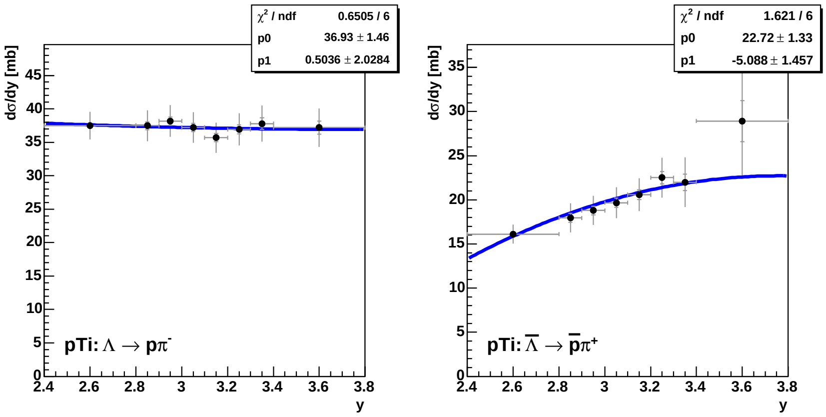

(b) Ti

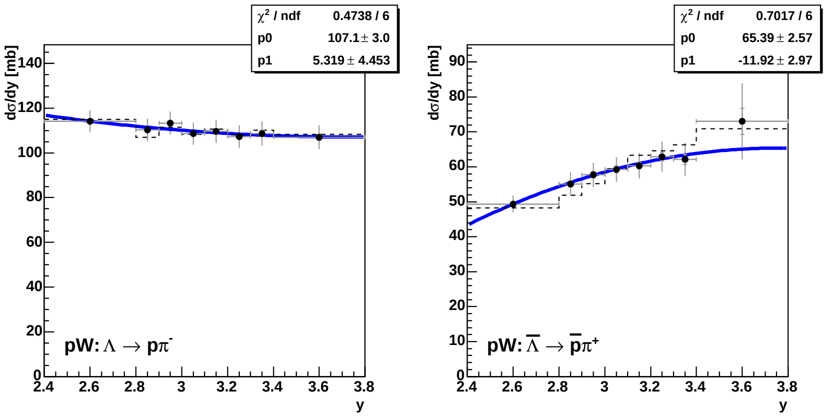

(c) W

Figure 4.33: $\Lambda/\bar{\Lambda}$ production cross section as function of rapidity. The dashed line represents the Monte Carlo prediction. The error bars show the statistical errors (with perpendicular ticks) as well as the total error (full length of the error bars).

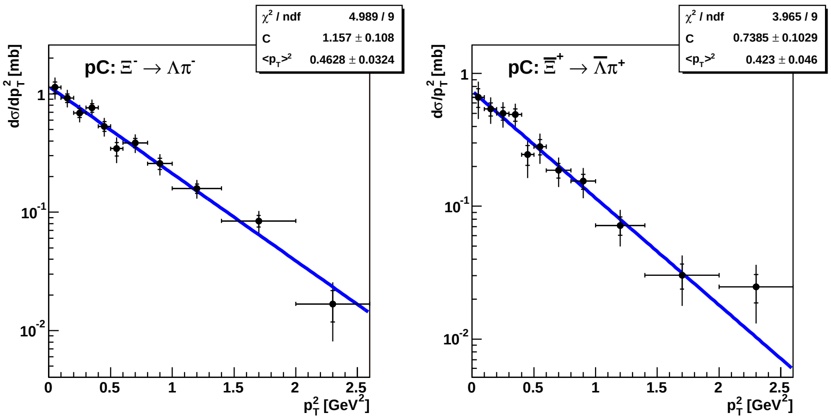

(a) C

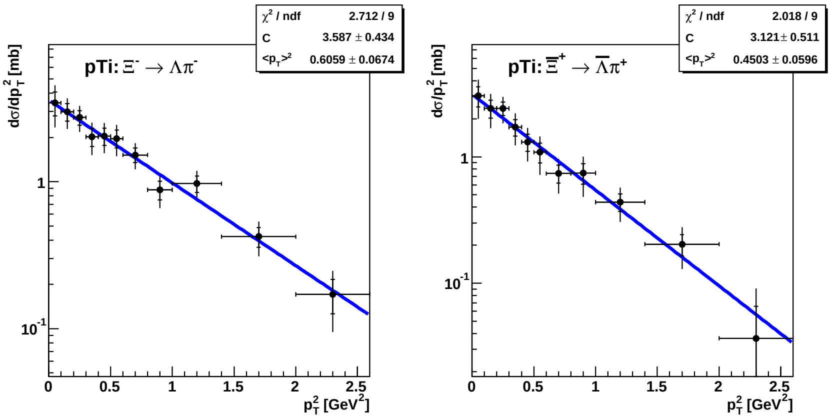

(b) Ti

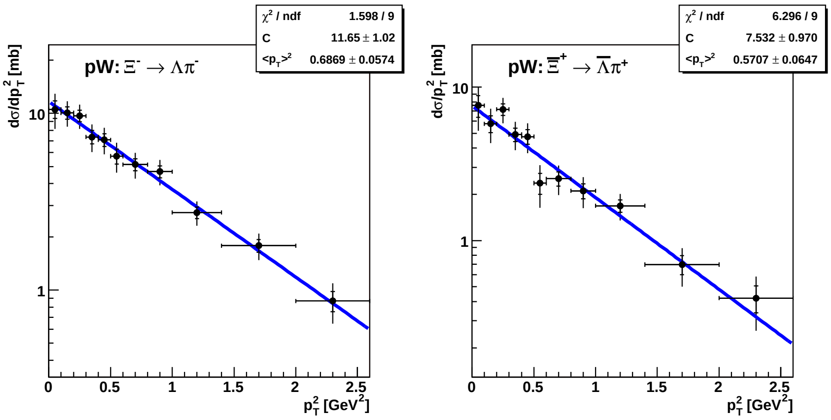

(c) W

Figure 4.34: $\Xi/\bar{\Xi}$ production cross section as function of p_T^2. The error bars show the statistical errors (with perpendicular ticks) as well as the total error (full length of the error bars).

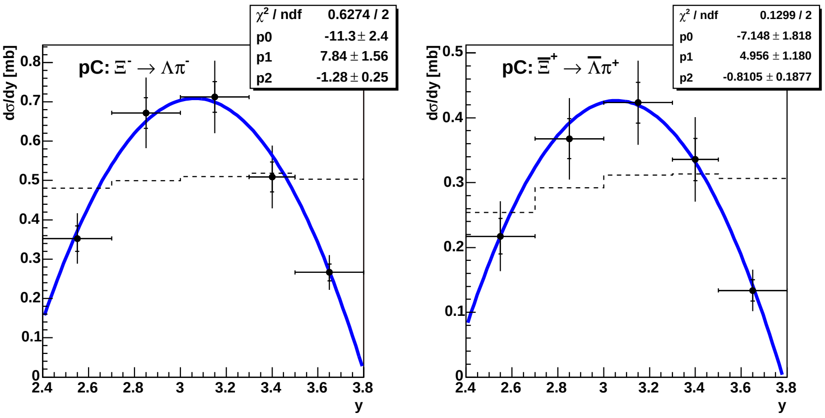

(a) C

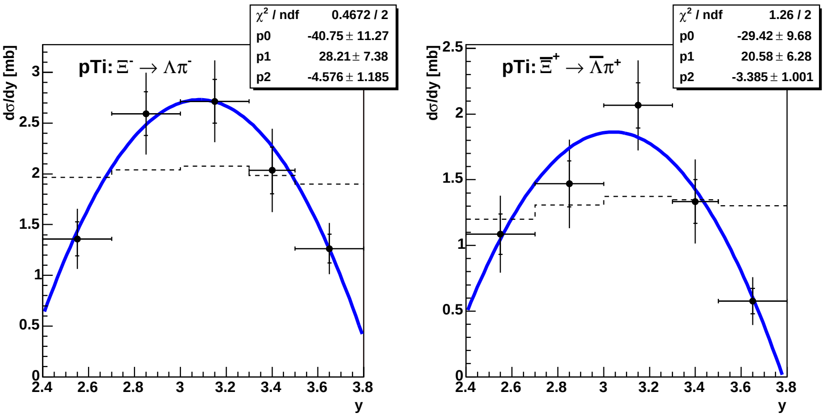

(b) Ti

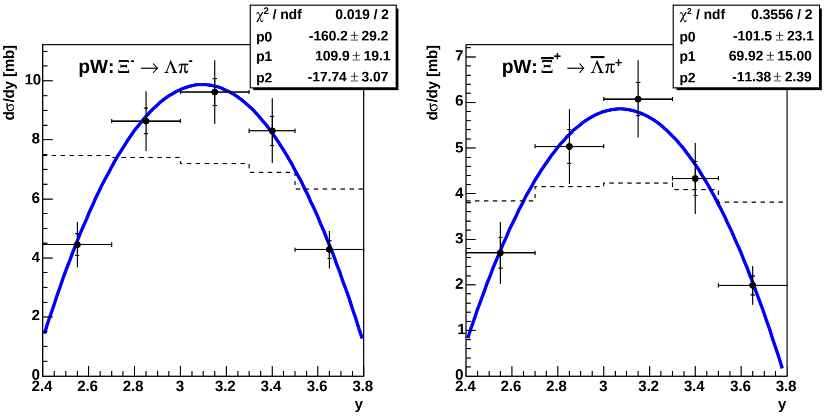

(c) W

Figure 4.35: $\Xi/\bar{\Xi}$ production cross section as function of rapidity. The dashed line represents the Monte Carlo prediction. The error bars show the statistical errors (with perpendicular ticks) as well as the total error (full length of the error bars).

of Fig. 4.36 and Fig. 4.37) was applied, all distributions have a very similar shape and the spread per bin decreases strongly, i.e. the dependence on the other variable vanishes. Therefore, the whole kinematic range can be employed to measure the $\Lambda/\bar{\Lambda}$ differential cross sections in p_T^2 and rapidity.

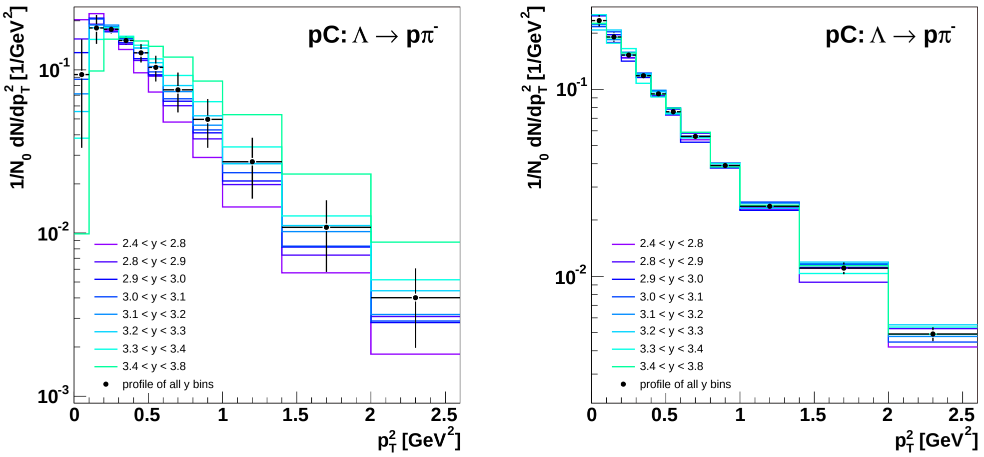

(a) Λ, before acceptance correction (b) Λ, after acceptance correction

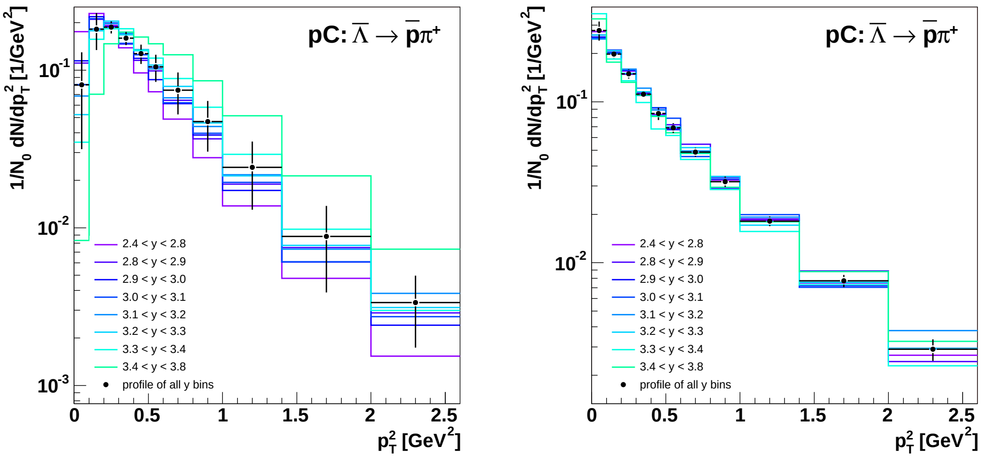

(c) $\bar{\Lambda}$, before acceptance correction (d) $\bar{\Lambda}$, after acceptance correction

Figure 4.36: $\Lambda/\bar{\Lambda}$: Effect of the acceptance correction on the p_T^2 distribution. The differential p_T^2 spectra for all rapidity bins are plotted as well as their profile, before applying the acceptance correction ((a) and (c)) and afterwards ((b) and (d)).

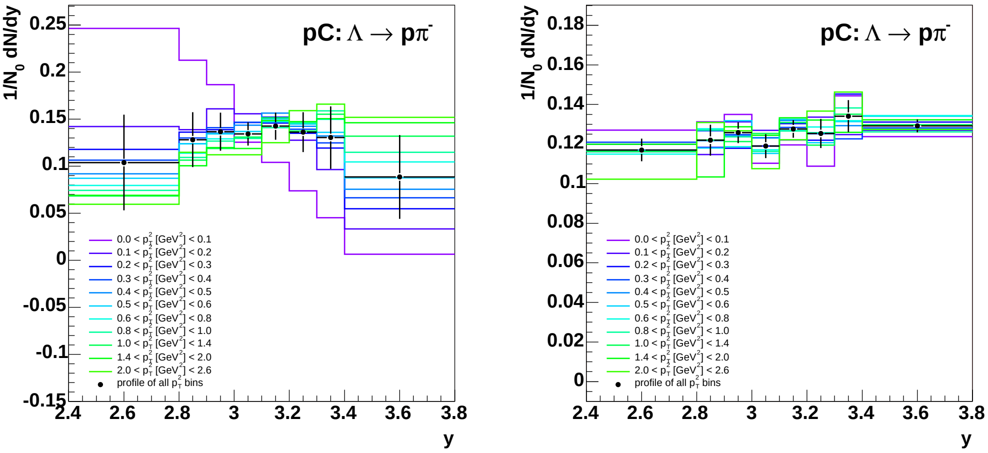

(a) Λ, before acceptance correction (b) Λ, after acceptance correction

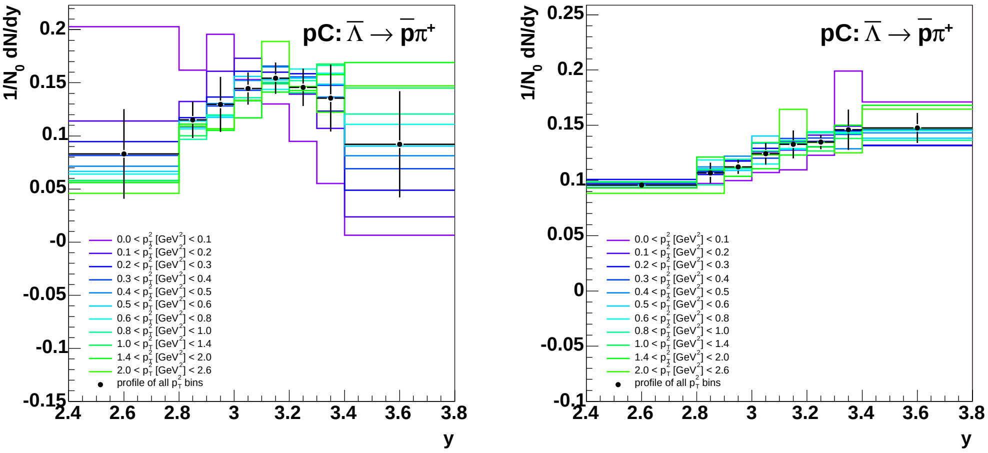

(c) $\bar{\Lambda}$, before acceptance correction (d) $\bar{\Lambda}$, after acceptance correction

Figure 4.37: $\Lambda/\bar{\Lambda}$: Effect of the acceptance correction on the rapidity distribution. The differential rapidity spectra for all p_T^2 bins are plotted as well as their profile, before applying the acceptance correction ((a) and (c)) and afterwards ((b) and (d)).

4.2.9 Cronin Effect

The availability of differential cross section measurements as function of p_T^2 and rapidity for different target materials allows to study the behaviour of the A-dependence of the cross section as function of these variables. Usually, if comparing collisions of protons with two different target nuclei, the ratio of the two differential cross section measurements normalized to the atomic numbers of the targets is plotted, e.g.

$$R\left(p_T\right) = \frac{B}{A}\frac{d\sigma_X^{pA}/d^2p_T}{d\sigma_X^{pB}/d^2p_T}. \tag{4.30}$$

(Here, A and B are the atomic numbers of the two target materials, and σ_X^{pA} and σ_X^{pB} are the measured production cross sections of particle X.)

If the cross section would simply scale with the atomic number of the target nucleus, then $R(p_T) = 1$, but for $A > B$, a suppression is observed at small p_T and an enhancement at moderate p_T with $R(p_T) \to 1$ for $p_T \to \infty$. This behaviour is called Cronin effect [C⁺75], for which a full theoretical understanding is still missing [K⁺02b]. In this analysis, we are able to compare results obtained with three different target materials, therefore the A-dependence of the cross section was measured by applying Equ. 4.24 for each bin in p_T^2 and rapidity separately. Fig. 4.38 shows the variable α describing the influence of the number of nucleons on the cross section of $\Lambda/\bar{\Lambda}$ and $\Xi/\bar{\Xi}$ as a function of p_T^2. For $\Lambda/\bar{\Lambda}$, α increases clearly with p_T^2, approaching one in the last bin of the measured range – equivalent to $R(p_T) = 1$ in Equ. 4.30. In the case of $\Xi/\bar{\Xi}$, the error bars are too large to definitely state an increase since it would still be possible to fit a constant to the measured data points.

With respect to rapidity, the measured distributions of α are flat as shown in Fig. 4.39, i.e. no enhancement with increasing atomic number of the target material was found.

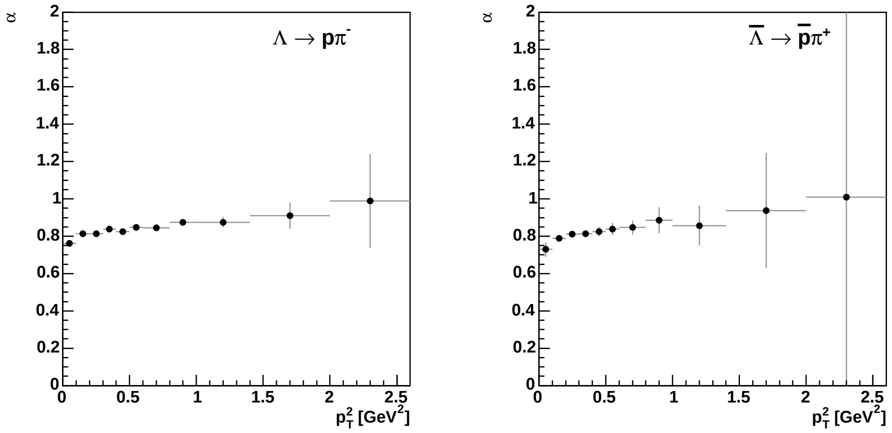

(a) $\Lambda/\bar{\Lambda}$

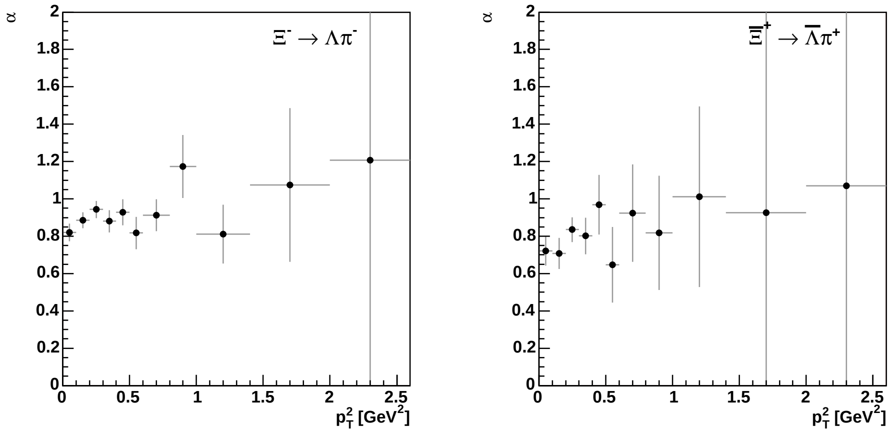

(b) $\Xi/\bar{\Xi}$

Figure 4.38: Atomic number dependence of the $\Lambda/\bar{\Lambda}$ (a) and $\Xi/\bar{\Xi}$ (b) cross sections as function of p_T^2. For each bin, the parameter α was extracted from fits of Equ. 4.24 to the cross section values measured for the different target materials.

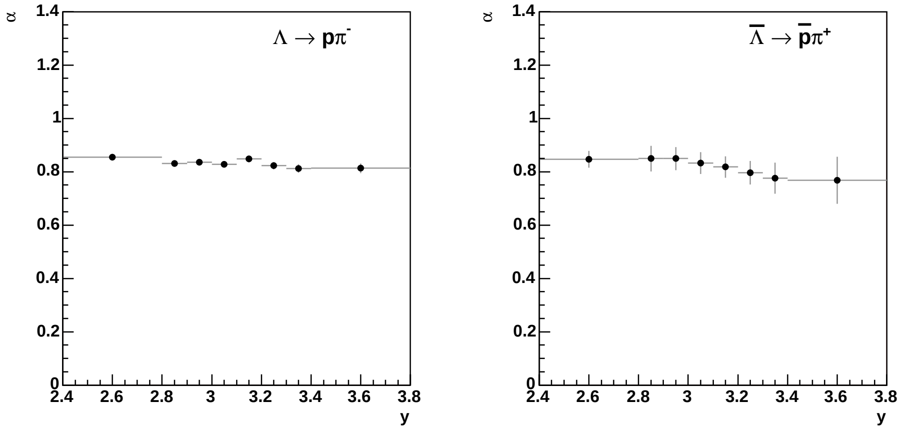

(a) $\Lambda/\bar{\Lambda}$

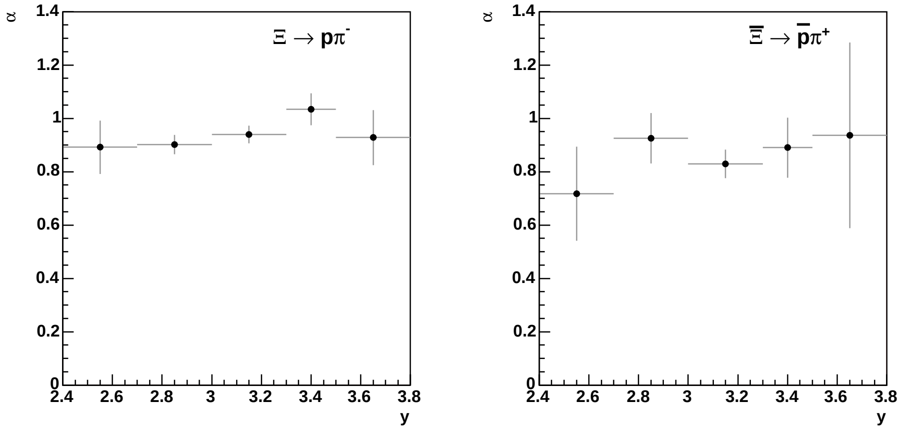

(b) $\Xi/\bar{\Xi}$

Figure 4.39: Atomic number dependence of the $\Lambda/\bar{\Lambda}$ and $\Xi/\bar{\Xi}$ cross sections as function of rapidity. For each bin, the parameter α was extracted from fits of Equ. 4.24 to the cross section values measured for the different target materials.

Chapter 5

Summary and Outlook

In this thesis, we have presented results from two topics of particle physics: The design of silicon microstrip sensors for the tracking system of the LHCb experiment at CERN and the measurement of hyperon production in proton-nucleus collisions at $\sqrt{s} = 41.6$ GeV with the HERA-B detector at DESY. Although LHCb will study head-on collisions of protons and HERA-B investigated interactions of protons with fixed targets, the general structure of the detectors is very similar, since both were optimized for the analysis of B decays.

Both provide a vertex detector for a precise measurement of the primary vertices, an efficient tracking system to reconstruct the charged particle tracks, a magnet to measure the momenta of these tracks and a particle identification system which is divided into Ring Imaging Čerenkov counters, calorimeters and muon systems.

After the lessons learned with the Inner Tracker of the HERA-B detector, it was decided to build the Inner Tracker and the Trigger Tracker of LHCb from silicon microstrip sensors, which have been proven to be radiation hard enough to sustain a few years of operation under LHC conditions without a significant performance degradation.

We have reviewed the basic properties of silicon sensors, introduced the custom developed Front-end chip BEETLE and motivated the criteria for the optimization process: Apart from being highly efficient, the sensors must be as thin as possible to reduce the multiple scattering of the charged particle tracks and the pair creation of photons. The shaping of the signals must be so fast that after 25 ns, i.e. when the next proton bunches collide, the signal must have dropped significantly, because otherwise it would require additional effort to find out which hits or tracks belong to the current event. While this could be dealt with during the offline reconstruction of the data, it would be very difficult at trigger level. Since the required resolution is not very high, the choice of the strip pitch is mainly determined by the constraints to have a high hit-finding efficiency also in the middle between two read-out strips (favouring a small pitch) and to minimize the number of read-out channels in order to save cost.

In comprehensive tests, several prototype sensors, combining different substrate thicknesses and different strip geometries in terms of strip pitch, implant width and width of the metal strip providing the AC-coupled read-out of the signal, were evaluated. Modules were built from up to three sensors bonded together creating read-out strips of up to 32.4 cm length and a capacitance of up to 54.5 pF. The sensors were tested with a 120 GeV π^- beam at CERN, with a laser set-up at the University of Zürich (Switzerland) and with a radioactive source. In each test, the latest version of the BEETLE chip at a time was used, and the recorded data were also analyzed to study properties of the chip itself, providing valuable input for improvements implemented in the following versions. The knowledge gained in all these tests provided a thorough understanding of the dependence of the sensor performance on the applied bias voltage, the shaping time, the strip geometry, the thickness and the accumulated radiation dose. This provided a solid base for the extrapolation of the expected performance of the Silicon Tracker over several years of operation in LHCb.

After finishing the mass production of Inner Tracker and Trigger Tracker modules (currently underway), the next step will be the mechanical integration and the commissioning of the detector before tracks can be reconstructed from the first proton-proton collisions expected in autumn 2007.

Using only information provided by the tracking system of HERA-B, Λ, Ξ and Ω hyperons and their antiparticles have been reconstructed from the large minimum bias data sample recorded during the data taking period 2002/2003. It comprises roughly 51 million events taken with a carbon target, 17 million events taken with a titanium target and 45 million events recorded with a tungsten target. The main decay channels of all three hyperon species contain only charged tracks in their final state: $\Lambda \rightarrow p\pi^-$, $\Xi^- \rightarrow \Lambda(\rightarrow p\pi^-)\pi^-$, $\Omega^- \rightarrow \Lambda(\rightarrow p\pi^-)K^-$ and the charge conjugated decays have been searched for in the data. The signal events were separated from the large combinatorial background mainly by exploiting the topology of the decay modes. In total, roughly 550,000 Λ and $\bar{\Lambda}$ decays have been reconstructed, 6,000 Ξ^- and $\bar{\Xi}^+$ and 1,600 Ω^- and $\bar{\Omega}^+$ in the kinematic range of $2.4 < y < 3.8$ (corresponding to $-1.4 < y_{cms} < 0.0$ in the center-of-mass system) and $0 < p_T^2 < 2.6$ GeV^2.

The large $\Lambda/\bar{\Lambda}$ sample provides not only the advantage of small statistical errors in the measurements, but also the opportunity to precisely assess the agreement of the Monte Carlo description with the data. Comparing the two-dimensional differential distributions in p_T^2 and rapidity, a disagreement can be observed, which is corrected for by a reweighting of the Monte Carlo events in the same variables. Comparisons of resulting distributions of other kinematic variables show that still no perfect agreement is obtained. From these deviations, the contribution of the Monte Carlo simulation to the total systematic error was evaluated.

Since the statistics of Ξ^- and $\bar{\Xi}^+$ are much smaller than of $\Lambda/\bar{\Lambda}$, the reweighting of the Monte Carlo sample and the acceptance correction was only performed in one variable, p_T^2. In the case of Ω^- and $\bar{\Omega}^+$, the statistics was too small to compare differential distributions, therefore a systematical error was estimated from the deviation between results obtained without a reweighting and by applying the weights determined for Ξ and $\bar{\Xi}$. Additional contributions to the systematic error of the measurements were deduced from the variation of the selection cuts, and for the cross section measurements, errors on the branching fractions and the luminosity determination have to be considered. The measurements of Λ and $\bar{\Lambda}$ are dominated by the systematic error, while in case of Ξ and Ω, the statistical errors almost of the same magnitude.

Acceptance corrected antiparticle to particle ratios yield information about leading particle effects: If one or more valence quarks of the produced hyperon could originate from the colliding primary particles, then its production rate will be higher than in the case where all three valence quarks have to be created in the collision. For pA collisions, this effect can be quantified by comparing ratios of the production rates of antiparticles and particles. The ratios for all three target materials have been measured and within the errors, no dependence on the atomic number A was observed. Weighted with their errors, the mean value of the three measurements of $\frac{\bar{\Lambda}}{\Lambda}$ was compared to published results obtained in pp, pA and AA collisions at different energies. Our value fits well into the general trend of the energy dependence of the ratio. The curves for pp, pA and AA results seem to be slightly shifted in energy. The mean ratios for all three hyperon species were compared to results from AA collision measurements at different energies, and also here, our results follow the trend, but for a precise extrapolation of the AA values to the HERA-B energy, more data are needed. Ratios between different hyperon species, namely $\frac{\Xi}{\Lambda}$,$\frac{\Omega}{\Xi}$ and the ratios of the corresponding antiparticles, were also measured and compared to results from Pb-Pb and Au-Au collisions at different energies. Here, it is difficult to find a general trend.

For the kinematic region accessible for HERA-B (see above), integrated production cross sections of the three hyperon species have been measured. Applying a parametrization following the Glauber model, the dependence of the production cross section on the atomic number A of the target nucleus has been fitted to $\sigma_X^{pA} = \sigma_X^{pN} \cdot A_X^{\alpha}$ (here, X denotes the particle species). Thus, apart from estimates for the respective proton-nucleon cross sections, the parameter α describing the scaling of the cross section with A can be extracted from the fits. While $\alpha(\Lambda) = 0.880 \pm 0.004$ and $\alpha(\bar{\Lambda}) = 0.85 \pm 0.07$, it is compatible with 1 for Ξ, Ω and their antiparticles.

We have also measured the differential cross sections in p_T^2 for Λ, $\bar{\Lambda}$, Ξ^- and $\bar{\Xi}^+$ and in rapidity for Λ and $\bar{\Lambda}$. The p_T^2 distributions have been fitted with the phenomenological ansatz

$$\frac{d\sigma}{dp_T^2} = \left[1 + \left(\frac{\sqrt{\pi}}{2}\frac{\Gamma(\beta - 1.5)}{\Gamma(\beta - 1)}\right)^2 \frac{p_T^2}{\langle p_T \rangle^2}\right]^{-\beta} . \tag{5.1}$$

Due to the larger error bars in case of Ξ^- and $\bar{\Xi}^+$, the fit was not sensitive to the parameter β, hence the ansatz was considered in the limit of β approaching infinity. In this way, the mean transverse momenta $\langle p_T \rangle$ could be extracted from the fits. As a general trend, slightly smaller values for antiparticles compared to the particles were observed. Furthermore, the mean p_T increases with increasing atomic number of the target nucleus. This was studied in more detail by fitting the A-dependence of the p_T^2 distribution in each bin with the parameterization according to the Glauber model and plotting the parameter α as function of p_T^2, i.e. measuring the A-dependence as function of p_T^2. Starting from $\alpha \sim 0.8$ at $p_T^2 = 0$, it increases to $\alpha \sim 1.0$ in the last p_T^2 of the measured range. This effect is called Cronin effect.

The differential distributions as function of rapidity are different in shape for Λ and $\bar{\Lambda}$: While the $\bar{\Lambda}$ distributions all show qualitatively the same shape which can be described well by a constant offset and a parabola centered at y_{cms}, the curves for Λ are almost flat except for a slight curvature. Going from $A = 12$ for carbon to $A = 74$ for tungsten, the parabolic term changes its sign from negative to positive in the limited phase space accessible by HERA-B. This indicates an A-dependent leading particle effect in the Λ production. From the fits to the differential rapidity distributions, cross section values at y_{cms} were derived for Λ and $\bar{\Lambda}$. Measuring the dependence of α as function of rapidity results in flat distributions. For Ξ^- and $\bar{\Xi}^+$, the error bars are too large to measure α as a function of p_T^2 and rapidity, the distributions are compatible with constants.

The influence of the pile-up of events on the acceptance of the hyperon decays considered in this thesis indicates that the agreement of Monte Carlo simulation and data also in parameters describing the accompanying event (e.g. track multiplicities) is of great importance. In this thesis, only signal Monte Carlo data have been used. For a cross check, it would be very profitable to compare the acceptance obtained with the current Monte Carlo to results from minimum bias Monte Carlo simulations. Unfortunately, especially in the case of Ω and $\bar{\Omega}$, the statistics needed for such a sample would be very large.

Hyperon production has been studied for different reasons: It serves as an important benchmark test for QCD-based models as used in the Monte Carlo event generators PYTHIA and FRITIOF. As we have observed when comparing distributions of kinematic variables, there is still room for improvement in the agreement of the model prediction and the data. Hyperons are strange particles, and an enhanced strangeness production has been proposed as one of the signatures of the formation of QGP. Therefore, reference measurements at all availabe energies and kinematic regions and in pp, pA and AA collisions provide a prerequisite for the interpretation of data from experimental searches for QGP.

Appendix A

List of Used Runs

This appendix gives a short introduction to the luminosity determation at HERA-B and lists the data sample used in this analysis (Table A.1).

Luminosity Determination at HERA-B

The luminosity $\mathcal{L}$, defined as

$$\mathcal{L} = \frac{N}{\sigma} \tag{A.1}$$

(Here, N is the number of events of a given type and σ is the corresponding cross section.)

is a process independent measure for the amount of data taken. At HERA-B, the total inelastic cross section σ^{pA}_{inel}, extrapolated to the kinematic range of the experiment [Car03], and the number of recorded inelastic interactions is used to determine the luminosity [Bru05], which in turn provides input for other cross section measurements. To separate inelastic events from other events, the Interaction Trigger was applied, which requires more than 20 hits in the RICH and/or more than 1 GeV of energy released in the inner ECAL. It has to be taken into account that one recorded event can contain more than one interaction; this is done by assuming that the number of interactions per event follows a single Poissonian distribution:

$$P\left(n, \lambda\right) = \frac{\lambda^n e^{-\lambda}}{n!}. \tag{A.2}$$

(Here, n is the number of interactions per event and λ the average number of interactions per bunch crossing.)

The efficiency ϵ^n_{trig} to trigger on an event with n interactions is parameterized using the efficiency ϵ_{trig} to select an event with a single interaction by the factorization ansatz

$$\epsilon^n_{trig} = 1 - \left(1 - \epsilon_{trig}\right)^n . \tag{A.3}$$

The total number of inelastic events can be deduced from

$$N_{inel} = N_{BX} \cdot \lambda, \tag{A.4}$$

where N_{BX} is the number of bunch crossings, and the number of triggered events N_{IA} recorded in the same period of data taking:

$$\begin{aligned} N_{IA} &= N_{BX} \cdot \sum_{n=0}^{\infty} \left(P\left(n, \lambda\right) \cdot \epsilon_{trig}^{n} \right) && \text{(A.5)} \\ &= N_{BX} \cdot \left(1 - e^{-\epsilon_{trig}\lambda} \right) && \text{(A.6)} \end{aligned}$$

By measuring ϵ_{trig} and λ, the luminosity of the data sample is

$$\mathcal{L}_{IA} = \frac{N_{IA} \cdot \lambda}{\left(1 - \exp\left(-\epsilon_{trig} \cdot \lambda\right)\right) \cdot \sigma_{inel}^{pA}} \tag{A.7}$$

The trigger efficiency ϵ_{trig} is studied with the help of the so-called transparent runs, i.e. runs taken with a pseudo-random trigger (synchronized to the bunch crossings), while the interaction trigger only set a flag indicating whether each event would have triggered or not. Then the number of events with interaction trigger flag were compared with those selected by applying the trigger conditions offline. The average number of interactions per bunch crossing is then using equations A.4 and A.6:

$$\lambda = -\frac{1}{\epsilon_{trig}} \log \left(1 - \frac{N_{IA}}{N_{BX}} \right) \tag{A.8}$$

The runs used for this analysis and their corresponding luminosities are listed in tabel A.1.

run	target wire/ material	IA rate [MHz]	date	no. of events	$\mathcal{L}_{IA}$ [mb^{-1}]	$\sigma_{\mathcal{L}_{IA}}$ [mb^{-1}]
20653	b1/C	1.36	2002/12/09	1734726	7602.8	357.6
20663	b1/C	0.55	2002/12/12	4003955	16151.8	871.9
20668	b1/C	0.56	2002/12/12	2288926	9145.3	482.1
20669	b1/C	0.57	2002/12/12	418950	1693.6	80.1
20670	b1/C	0.68	2002/12/12	2583625	10643.6	536.5
20671	i1/W	0.93	2002/12/12	2629628	1391.5	72.0
20675	i1/W	1.28	2002/12/13	7733657	4205.6	282.7
20676	b1/C	0.82	2002/12/13	675437	2770.9	146.7
20677	b1/C	0.90	2002/12/13	4568646	19176.9	1082.1
20678	b1/C	0.88	2002/12/13	5121506	21470.3	1102.7
20679	i1/W	1.27	2002/12/13	8675028	4731.4	172.7
20680	i1/W	1.32	2002/12/13	1376041	748.2	34.7
20682	b2/Ti	0.96	2002/12/13	5497551	8052.9	373.0
20693	b2/Ti	0.98	2002/12/15	573379	821.3	43.5
20695	b2/Ti	0.99	2002/12/15	4724521	6835.6	318.5
20705	b1/C	0.79	2002/12/15	1303905	5416.2	270.5
20706	b1/C	0.78	2002/12/15	38141	155.1	30.0
20723	b1/C	0.92	2002/12/17	2848025	11833.0	607.6
20724	b1/C	0.96	2002/12/17	277936	1156.2	53.6
20725	b1/C	0.96	2002/12/17	3148178	12703.7	659.3
20726	b1/C	1.51	2002/12/17	1994465	8244.5	416.4
20728	b1/C	0.78	2002/12/17	453635	1786.6	89.2
20734	b1/C	0.78	2002/12/17	7438284	30713.4	1669.5
20735	i1/W	0.80	2002/12/18	1043289	535.4	19.2
20736	i1/W	1.27	2002/12/18	15461	8.3	4.2
20737	i1/W	1.29	2002/12/18	18920	10.4	4.0
20738	i1/W	1.27	2002/12/18	2082766	1130.0	41.9
20739	i1/W	1.20	2002/12/18	7005917	3782.6	130.7
20740	b1/C	0.74	2002/12/18	3786598	15607.4	785.4
20742	b1/C	0.73	2002/12/18	2714468	11169.7	538.8
20743	b1/C	0.75	2002/12/18	3647125	14997.6	765.3
20744	i1/W	1.18	2002/12/18	362345	193.4	6.7
20746	i1/W	1.23	2002/12/18	5013042	2703.7	111.7
20747	i1/W	1.26	2002/12/19	6219769	3399.5	152.9
20749	i1/W	1.24	2002/12/19	3898581	2124.2	91.1
20764	i1/W	0.86	2002/12/20	4184930	2175.2	81.9
20766	i1/W	0.98	2002/12/20	2366338	1227.6	43.4
20767	i1/W	1.16	2002/12/20	137940	72.3	3.1
20768	b1/C	0.89	2002/12/21	2435408	9568.6	588.4
20769	b1/C	0.89	2002/12/21	236469	902.1	67.8
20770	b1/C	0.89	2002/12/21	7867549	29766.7	4213.9
20771	b2/Ti	1.09	2002/12/21	2707272	3787.1	222.0
20772	b2/Ti	1.09	2002/12/21	1677012	2299.7	145.2
20773	b2/Ti	1.10	2002/12/21	5656409	7668.2	524.4

Table A.1: List of runs used in this analysis. The quoted values were taken from [MBa06, Bru05].

Bibliography

[A+73] B. Alper et al., *Particle composition at high transverse momenta in p-p-collisions in the central region at the CERN ISR*, Phys. Lett. **B 44** (1973), 521. 76

[A+87] H. Albrecht et al., *Observation of* B^0 *-* $\bar{B}^0$ *mixing*, Phys. Lett. **B 192** (1987), 245. 7

[A+93] M. Artuso et al., *Two measurements of* B^0 *-* $\bar{B}^0$ *mixing*, Phys. Rev. Lett. **71** (1993), 1680. 7

[A+94] H. Albrecht et al., *HERA-B – An experiment to study CP violation in the B system using an internal target at the HERA proton ring*, Tech. Report DESY-PRC 94/02, Desy, 1994. 9

[A+95] H. Albrecht et al., *HERA-B – An experiment to study CP violation in the B system using an internal target at the HERA proton ring*, Technical Design Report DESY-PRC 95/01, Desy, 1995. 9, 11

[A+97] V. Alberico et al., *The Reconstruction for the Electromagnetic Calorimeter of the HERA-B Experiment*, Proceedings of the VII International Conference on Calorimetry in High Energy Physics (J. Rutherfoord E. Cheu, T. Embry and R. Wigmans, eds.), World Scientific, 1997, p. 537. 22

[A+01] G. Avoni et al., *The electromagnetic calorimeter of the HERA-B experiment*, Nucl. Instrum. Meth. **A461** (2001), 332. 15

[A+02a] K. Adcox et al., *Measurement of* Λ *and* $\bar{\Lambda}$ *Particles in Au+Au Collisions at* $\sqrt{s_{NN}} = 130\ GeV$, Phys. Rev. Lett. **89** (2002), 092302. 123, 125, 126

[A+02b] C. Adler et al., *Midrapidity* Λ *and* $\bar{\Lambda}$ *Production in Au+Au Collisions at* $\sqrt{s_{NN}} = 130\ GeV$, Phys. Rev. Lett. **89** (2002), 092301. 123, 125

[A+02c] M. Agari et al., *Test Beam Results of Multi-Geometry Prototype Sensors for the LHCb Inner Tracker*, LHCb Note 2002-058 (2002). 54, 55

[A+03a] I. Abt et al., *Inclusive* V^0 *production cross sections from 920 GeV fixed target proton-nucleus collisions*, Eur. Phys. J. C (2003), no. 29, 181. 9, 123

[A$^+$03b] I. Abt et al., *J/ψ Production via χ_c Decays in 920 GeV pA Interactions*, Phys. Lett. **B 561** (2003), 61. 9

[A$^+$03c] I. Abt et al., *Measurement of the $b\bar{b}$ production cross section in 920 GeV fixed-target proton-nucleus collisions*, Eur. Phys. J. **C 26** (2003), 345. 9

[A$^+$03d] I. Abt et al., *Update on the performance of the HERA-B vertex detector system*, Nucl. Instrum. Meth. **A511** (2003), 24. 13

[A$^+$03e] M. I. Adamovich et al., *V^0, Ξ^+ and Ω^- inclusive production cross-sections measured in hyperon experiment WA89 at CERN*, Eur. Phys. J. **C26** (2003), 357. 4

[A$^+$03f] J. Adams et al., *Strange antiparticle-to-particle ratios at mid-rapidity in $\sqrt{s_{NN}} = 130$ GeV Au+Au collisions*, Phys. Lett. **B 567** (2003), 167. 123, 125, 126

[A$^+$03g] M. Agari et al., *Test-beam measurements on prototype ladders for the LHCb TT station and Inner Tracker*, LHCb Note 2003-082 (2003). 56, 64, 65, 66

[A$^+$03h] M. Agari et al., *Studies of the Beetle 1.2 Pipeline Homogeneity*, LHCb Note 2003-155 (2003). 65

[A$^+$04a] I. Abt et al., *Limits for the Central Production of Θ^+ and Ξ^{--} Pentaquarks in 920-GeV pA Collisions*, Phys. Rev. Lett. **93** (2004), 212003. 10

[A$^+$04b] I. Abt et al., *Search for the flavor-changing neutral current decay $D^0 \to \mu^+\mu^-$ with the HERA-B detector*, Phys. Lett. **B 596** (2004), 173. 10

[A$^+$04c] M. Agari et al., *Measurements of a prototype ladder for the TT station in a 120 GeV/c pi$^-$ beam*, LHCb Note 2004-103 (2004). 57

[A$^+$04d] I. Arino et al., *The HERA-B ring imaging Cerenkov counter*, Nucl. Instrum. Meth. **A516** (2004), 445. 14, 15

[A$^+$05a] A. Abulencia et al., *Search for $B^0_s \to \mu^+\mu^-$ and $B^0_d \to \mu^+\mu^-$ Decays in $p\bar{p}$ Collisions with CDF II*, Phys. Rev. Lett. **95** (2005), 221805. 26

[A$^+$05b] J. Adams et al., *Experimental and theoretical challenges in the search for the quark-gluon plasma: The STAR Collaboration's critical assessment of the evidence from RHIC collisions*, Nucl. Phys. **A757** (2005), 102. 86

[A$^+$05c] K. Adcox et al., *Formation of dense partonic matter in relativistic nucleus-nucleus collisions at RHIC: Experimental evaluation by the PHENIX Collaboration*, Nucl. Phys. **A757** (2005), 184. 86

[A$^+$05d] I. Arsene et al., *Quark-gluon plasma and color glass condensate at RHIC? The perspective from the BRAHMS experiment*, Nucl. Phys. **A757** (2005), 1. 86

[A+06a] I. Abt et al., *Improved measurement of the $b\bar{b}$ production cross section in 920 GeV fixed-target proton-nucleus collisions*, Phys. Rev. **D 73** (2006), 052005. 9

[A+06b] I. Abt et al., *Measurement of the Upsilon production cross section in 920-GeV fixed-target proton nucleus collisions*, hep-ex/0603015, 2006. 9

[A+06c] I. Abt et al., *Polarization of Λ and $\bar{\Lambda}$ in 920 GeV fixed-target proton-nucleus collisions*, Physics Letters B, Article in Press (2006). 9

[A+06d] A. Abulencia et al., *Measurement of the B_s-$\bar{B}_s$ Oscillation Frequency.* 26

[AEGK02] I. Abt, D. Emelyanov, I. Gorbunov, and I. Kisel, *Cellular automaton and Kalman filter based track search in the HERA-B pattern tracker*, Nucl. Instrum. Meth. **A490** (2002), 546. 22

[AKME02] I. Abt, I. Kisel, S. Masciocchi, and D. Emelyanov, *CATS: A cellular automaton for tracking in silicon for the HERA-B vertex detector*, Nucl. Instrum. Meth. **A489** (2002), 389. 22

[AP77] G. Altarelli and G. Parisi, *Asymptotic freedom in parton language*, Nucl. Phys. **B 126** (1977), 298. 77

[Art06] *ARTE - Analysis and Reconstruction Tool of HERA-B*, http://www-hera-b.desy.de/subgroup/software/, 2006, retrieved January 2006. 21

[AST93] *ASTM E722-93: Standard practice for characterizing neutron fluence spectra in terms of an equivalent monoenergetic neutron fluence for radiation testing of electronics*, American Society for Testing and Materials, Annual Book of ASTM Standards (1993), 1993. 46

[B+73a] M. Banner et al., *Large transverse momentum particle production at 90 in proton-proton collisions at the ISR*, Phys. Lett. **B 44** (1973), 537. 76

[B+73b] F.W. Büsser et al., *Observation of π^0 mesons with large transverse momentum in high-energy proton-proton collisions*, Phys. Lett. **B 46** (1973), 471. 76

[B+97] C. Bormann et al., *Kaon-, Λ and $\bar{\Lambda}$-production in Pb + Pb-collisions at 158 GeV per nucleon*, J. of Phys. G **23** (1997), 1817. 85

[B+00] P. Ball et al., *B decays at the LHC*, hep-ph/0003238, 2000. 26

[B+01a] C. Bauer et al., *Characterization of Inner Tracker Silicon Prototype Sensors Using a ^{1}06Ru-source and a 1083 nm Laser System*, LHCb Note 2001-121 (2001). 54

[B+01b] C. Bauer et al., *Test beam results on Inner Tracker silicon prototype sensors*, LHCb Note 2001-135 (2001). 54, 55, 63

[B$^+$02a] Y. Bagaturia et al., *Studies of aging and HV break down problems during development and operation of MSGC and GEM detectors for the inner tracking system of HERA-B*, Nucl. Instrum. Meth. **A490** (2002), 223. 13

[B$^+$02b] D. Bechevet et al., *Results of irradiation tests on standard planar silicon detectors with 7-10 MeV protons*, Nucl. Instr. Meth. **A479** (2002), 487. 59

[B$^+$03a] A. Bay et al., *Common L1 read out board for LHCb specification*, LHCb Note 2003-007 (2003). 35

[B$^+$03b] R.P. Bernhard et al., *Measurements of Prototype Ladders for the Silicon Tracker with Laser*, LHCb Note 2003-075 (2003). 57, 66

[B$^+$04] G. Baumann et al., *Quality Assurance of 100 CMS2-OB2 Sensors*, LHCb Note 2004-105 (2004). 60

[B$^+$05a] B.B. Back et al., *The PHOBOS perspective on discoveries at RHIC*, Nucl. Phys. **A757** (2005), 28. 86

[B$^+$05b] G. Baumann et al., *Pre-Series Sensor Qualification for the Inner Tracker of LHCb*, LHCb Note 2005-037 (2005). 60

[B$^+$05c] A. Bay et al., *Hybrid Design, Procurement and Testing for the LHCb Silicon Tracker*, LHCb Note 2005-061 (2005). 53

[Bau03] D. Baumeister, *Development and Characterisation of a Radiation Hard Readout Chip for the LHCb-Experiment*, Ph.D. thesis, Universität Heidelberg, 2003. 53, 65, 67

[BBK71] S. M. Berman, J. D. Bjorken, and J. B. Kogut, *Inclusive Processes at High Transverse Momentum*, Phys. Rev. D **4** (1971), 3388. 76

[BF98] A.J. Buras and R. Fleischer, *Heavy Flavors II*, ch. Quark Mixing, *CP* Violation and Rare Decays After the Top Quark Discovery, p. 65, World Scientific, 1998. 7

[Bia98] A. Bialas, *Quark model and strange baryon production in heavy ion collisions*, Phys. Lett. **B 442** (1998), 449. 84, 85

[Bic88] H. Bichsel, *Straggling in thin silicon detectors*, Rev. Mod. Phys. **60** (1988), no. 3, 663. 41

[Boa05] LCG Editorial Board, *LHC Computing Grid Technical Design Report*, CERN-LHCC-2005-024 (2005). 36

[BP69] J. D. Bjorken and E. A. Paschos, *Inelastic Electron-Proton and γ-Proton Scattering and the Structure of the Nucleon*, Phys. Rev. **185** (1969), 1975. 76

[Bru05] M. Bruschi, *Luminosity determination at HERA-B*, HERA-B Internal Note 05-011 (2005). 90, 92, 147, 149

[C+64] J. H. Christenson et al., *Evidence for the 2π Decay of the K_2^0 Meson*, Phys. Rev. Lett. **13** (1964), 138. 3

[C+74] A. Chodos et al., *New extended model of hadrons*, Phys. Rev. **D9** (1974), 3471. 81

[C+75] J.W. Cronin et al., *Production of hadrons at large transverse momentum at 200, 300, and 400 GeV*, Phys. Rev. **D11** (1975), 3105. 140

[C+99] R. Caliandro et al., *Λ, Ξ and Ω production at mid-rapidity in Pb-Pb and p-Pb collisions at 158 A GeV/c*, J. Phys. G **25** (1999), 171. 85, 123, 125, 126

[C+02] B. A. Cole et al., *Recent results from experiment E859 at the BNL AGS*, Nucl. Phys. **A590** (2002), 179. 123, 125

[C+05] J. Charles et al., *CP violation and the CKM matrix: assessing the impact of the asymmetric B factories*, Eur. Phys. J. **C41** (2005), 1. 7, 8

[Cap91] A. Capella, *A-Dependence in Hadron-Nucleus Collisions*, Nucl. Phys. **A525** (1991), 133. 78

[Car03] J. Carvalho, *Compilation of cross sections for proton?nucleus interactions at the HERA energy*, Nucl. Phys. **A725** (2003), 269. 78, 147

[col01a] HERA-B collaboration, *Update of status and plans for 2001/2*, HERA-B Internal Note 01-064 (2001). 9

[Col01b] G.P. Collins, *SNO nus is good news*, Scientific American **285** (2001), 00368733. 1

[DB03] S. Löchner D. Baumeister, *Private communication*, September 2003. 67

[Dok77] Yuri L. Dokshitzer, *Calculation of the structure functions for deep inelastic scattering and e^+e^- annihilation by perturbation theory in quantum chromodynamics.*, Sov. Phys. JETP **46** (1977), 641. 77

[Dun98] Isard Dunietz, *Beautiful CP violation*, Nucl. Instrum. Meth. **A408** (1998), 14. 26

[E+00] D. Emeliyanov et al., *Primary Vertex Reconstruction by ROVER*, HERA-B Internal Note 00-139 (2000). 23

[E+01] V. Eiges et al., *The muon detector at the HERA-B experiment*, Nucl. Instrum. Meth. **A461** (2001), 104. 16

[E+04] S. Eidelman et al., *Review of Particle Physics*, Physics Letters **B592** (2004), 1+. 80, 100, 102, 104

[Eme02] D. Emeliyanov, *The Grover vertexing package*, Web page (status: June 2005) (2002). 23

[F+02] K. Fanebust et al., *Results on hyperon production from NA57*, J. Phys. G **28** (2002), no. 7, 1607. 123, 125

[Fom99] B. Fominykh, *MUREC-B*, Talk given at the HERA-B Software meeting, June 23, 1999. 22

[FT57] J. I. Friedman and V. L. Telegdi, *Nuclear Emulsion Evidence for Parity Nonconservation in the Decay Chain* $\pi^+ \to \mu^+ \to e^+$, Phys. Rev. **106** (1957), 1290. 2

[Fun03] Michael Funcke, *Strahlphysikalische Aspekte des Targetbetriebs bei Hera-B*, Ph.D. thesis, Universität Dortmund, 2003. 12

[G+90] W.M. Geist et al., *Hadronic production of particles at large transverse momentum: Its relevance to hadron structure, parton fragmentation and scattering*, Phys. Rep. **197** (1990), 263. 76, 78

[G+02] T. Glebe et al., *First measurements on Inner Tracker silicon prototype sensors using the BEETLE v1.1 readout chip*, LHCb Note 2002-018 (2002). 55

[G+05] J. Gassner et al., *Measurements of Prototype Ladders for the TT station with a Laser*, LHCb Note 2004-102 (2005). 57

[GEA94] *GEANT 3.21 Detector Description and Simulation Tool*, CERN Program Library Long Writeup W5013, 1994. 90

[GL72] V. N. Gribov and L. N. Lipatov, *Deep inelastic e p scattering in perturbation theory*, Sov. J. Nucl. Phys. **15** (1972), 438. 77

[GL90] M. Gronau and D. London, *Isospin analysis of CP asymmetries in B decays*, Phys. Rev. Lett. **65** (1990), 3381. 26

[Gla59] R.J. Glauber, *Lectures on Theoretical Physics*, Interscience, N.Y., 1959. 78

[GNS03] J. Gassner, M. Needham, and O. Steinkamp, *Layout and Expected Performance of the LHCb TT Station*, LHCb Note 2003-140 (2003). 56, 59

[GV02] T.D. Gutierrez and R. Vogt, *Asymmetries between strange and antistrange particle production in pion-proton interactions*, Nucl. Phys. **A705** (2002), 396. 79, 81

[GW91] M. Gronau and D. Wyler, *On determining a weak phase from cp asymmetries in charged b decays*, Phys. Lett. **B265** (1991), 172. 26

[H+04] J. Härkönen et al., *Recent results from the CERN RD39 Collaboration on super-radiation hard cryogenic silicon detectors for LHC and LHC upgrade*, Nucl. Instr. Meth. **A535** (2004), 384. 47

[Har03] N. Harnew, *B physics at the LHC*, Frascati Phys. Ser. **31** (2003), 289. 25

[HER00] HERA-B collaboration, *Report on status and prospects*, Tech. Report DESY-PRC 00/04, Desy, 2000. 9, 13, 14, 15

[HL03] S. Heule and F. Lehner, *Simulation of signal generation in silicon microstrip detectors for the Silicon Tracker of the LHCb experiment*, LHCb Note 2003-159 (2003). 59

[HQ98] P.F. Harrison and H.R. Quinn (eds.), *The BaBar physics book: Physics at an asymmetric B factory*, SLAC-R-0504, 1998. 6

[I$^+$99] J. Ivarsson et al., *PYTHIA and FRITIOF: Event Generators for HERA-B*, HERA-B Internal Note 99-067 (1999). 77, 90

[Igo98] O. Igonkina, *MARPLE -Version 1.03-*, HERA-B Internal Note 98-129 (1998), for a more recent online reference see (status: June 2005): http://www-hera-b.desy.de/subgroup/software/arte/MARPLE/. 23

[K$^+$97] M. Kaneta et al., *Particle ratios from central Pb + Pb collisions at the CERN SPS*, J. of Phys. G **23** (1997), 1865. 85

[K$^+$02a] K. Kadija et al., *Strange particle production in p+p, p+Pb and Pb+Pb interactions from NA49*, J. Phys. G **28** (2002), no. 7, 1675. 123, 125

[K$^+$02b] B. Z. Kopeliovich et al., *Cronin Effect in Hadron Production Off Nuclei*, Phys. Rev. Lett. **88** (2002), 232303. 140

[Kar02] F. Karsch, *Lattice QCD at High Temperature and Density*, Lecture Notes in Physics **583** (2002), 209. 81, 86

[KF05] P. Koppenburg and L. Fernández, *HLT Exclusive Selections Design and Implementation*, LHCb Note 2005-015 (2005). 36

[Kli04] Esben Klinkby, *$\Lambda/\bar{\Lambda}$ polarisation studies in proton nucleus collisions at 920 GeV proton beam energy*, Master's thesis, Niels Bohr Institute, University Copenhagen, 2004. 92

[KM73] M. Kobayashi and T. Maskawa, *CP-Violation in the Renormalizable Theory of Weak Interaction*, Prog. Theor. Phys. **49** (1973), 652. 5

[L$^+$99] G. Lindström et al., *Radiation hardness of silicon detectors - a challenge from high-energy physics*, Nucl. Instr. Meth. **A426** (1999), 1. 46, 47

[L$^+$01] G. Lindström et al., *Radiation hard silicon detectors–developments by the RD48 (ROSE) collaboration*, Nucl. Instr. Meth. **A466** (2001), 308. 47, 59

[Leo92] W.R. Leo, *Techniques for Nuclear and Particle Physics Experiments*, Springer-Verlag Berlin, 1992. 39, 40, 42, 43

[LHC98] LHCb Collaboration, *LHCb Technical Proposal*, CERN-LHCC 98-4 (1998). 25, 29, 39

[LHC00a] LHCb Collaboration, *LHCb Calorimeters Technical Design Report*, CERN-LHCC-2000-036 (2000). 32, 34

[LHC00b] LHCb Collaboration, *LHCb Magnet Technical Design Report*, CERN-LHCC-2000-007 (2000). 31

[LHC00c] LHCb Collaboration, *LHCb RICH Technical Design Report*, CERN-LHCC-2000-037 (2000). 32

[LHC01a] LHCb Collaboration, *LHCb Muon System Technical Design Report*, CERN-LHCC-2001-010 (2001). 33, 35

[LHC01b] LHCb Collaboration, *LHCb Outer Tracker Technical Design Report*, CERN-LHCC 2001-024 (2001). 32, 39

[LHC01c] LHCb Collaboration, *LHCb Outer Tracker Technical Design Report*, CERN-LHCC-2001-024 (2001). 33

[LHC02] LHCb Collaboration, *LHCb Inner Tracker Technical Design Report*, CERN-LHCC 2002-029 (2002). 31, 39

[LHC03a] LHCb Collaboration, *Addendum to the LHCb Muon System Technical Design Report*, CERN-LHCC-2003-002 (2003). 33

[LHC03b] LHCb Collaboration, *LHCb Reoptimized Detector Design and Performance Technical Design Report*, CERN-LHCC 2003-030 (2003). 26, 28, 30, 31, 39, 50

[LHC03c] LHCb Collaboration, *LHCb Trigger System Design Report*, CERN-LHCC-2003-031 (2003). 34, 37

[LHC05] LHCb Collaboration, *Second Addendum to the Muon System Technical Design Report*, CERN-LHCC-2005-012 (2005). 33

[LHC06] LHCb Collaboration, *Status of the* LHCb *Experiment*, Tech. Report CERN-RRB-2006-039, CERN, 2006. 25

[LLV05] F. Lehner, C. Lois, and H. Voss, *Measurements on irradiated silicon sensor prototypes for the Inner Tracker of LHCb*, LHCb Note 2004-104 (2005). 59

[M+03] A. Mischke et al., *Energy dependence of Λ and $\bar{\Lambda}$ production at CERN-SPS energies*, Nucl. Phys. **A715** (2003), 453. 123, 125

[MBa06] *HERA-B Minimum Bias working group webpage* , http://www-hera-b.desy.de/subgroup/physics/herab/analysis/mb2003/welcome.html, 2006, retrieved January 2006. 87, 149

[Mil02] E. Milotti, *1/f noise: a pedagogical review.*, physics/0204033, 2002. 45

[MS99] R. Mankel and A. Spiridonov, *The Concurrent Track Evolution Algorithm: Extension for Track Finding in the Inhomogeneous Magnetic Field of the HERA-B Spectrometer*, Nucl. Instr. Meth. **A426** (1999), 268. 22

[Nö02] Michael Nörenberg, *Tracking Efficiency of the HERA-B First Level Trigger in the Single Lepton Mode*, Ph.D. thesis, Universitat Hamburg, 2002. 18

[N+03] T. Nunez et al., *The Second Level Trigger Algorithm*, HERA-B Internal Note 03-021 (2003). 19

[Nac91] O. Nachtmann, *Phänomene und Konzepte der Elementarteilchenphysik*, Vieweg Braunschweig, 1991. 5

[Now94] S. Nowak, *A Description of HERA-B GEANT*, HERA-B Internal Note 94-123 (1994). 90

[Ouc03] M. Ouchrif, *The HERA-B outer tracker*, Nucl. Instrum. Meth. **A513** (2003), 239. 14

[Per00] D.H. Perkins, *Introduction to High Energy Physics*, 4th edition ed., Cambridge University Press, 2000. 2

[Pes01] R. Pestotnik, *Identification of Pions, Kaons and Protons in the HERA-B Spectrometer*, Ph.D. thesis, University of Lljubljana, January 2001. 22

[Pi92] H. Pi, *An event generator for interactions between hadrons and nuclei – FRITIOF version 7.0*, Comp. Phys. Comm. **71** (1992), 173. 4, 77, 90

[PKR86] B. Müller P. Koch and J. Rafelski, *Strangeness in Relativisitic Heavy-Ion Collisions*, Phys. Rep. **142** (1986), 167. 83, 84

[Ple01] M.-A. Pleier, *Cloneremove V1.0*, HERA-B Internal Note 01-062 (2001). 23

[Pre92] William H. Press, *Numerical Recipes in C*, Cambridge University Press, 1992. 113

[RAK92] I. Dunietz R. Aleksan and B. Kayser, *Determining the CP-violating phase* γ, Z. Phys. **C54** (1992), 653. 25

[Rep06] *HERA-B Reprocessing webpage* , http://www-hera-b.desy.de/subgroup/software/datamgr/RP.html, 2006, retrieved January 2006. 22, 88

[RJG01] B. Jost R. Jacobsson and Z. Guzik, *Readout supervisor design specifications*, LHCb Note 2001-012 (2001). 35

[S+04] L. Sándor et al., *Hyperon production at the CERN SPS: results from the NA57 experiment*, J. Phys. G **30** (2004), 129. 123, 125, 126

[Sak67] A.D. Sakharov, *Violation of CP Invariance, C Asymmetry, and Baryon Asymmetry of the Universe.*, J. Exp. Theor. Phys. Lett. **5** (1967), 24. 3

[Sat03] H. Satz, *The First 15 Years of Ultra-Relativistic Heavy Ion Studies*, Nucl. Phys. **A715** (2003), 3. 86

[Sch01] M. Schmelling, *Specifications of the Front End Chip for the LHCb Vertex Detector*, LHCb Note 2001-048 (2001). 51

[Sch02] O. Schneider, *B physics prospects at the LHC*, talk given at the Flavour in the era of the LHC Workshop, CERN, November 2002. 26

[Sch06] B. Schwingenheuer, *Private communication*, May 2006. 18

[Sjö94] T. Sjöstrand, *High-energy-physics event generation with PYTHIA 5.7 and JETSET 7.4*, Comp. Phys. Comm. **82** (1994), 74. 4, 77

[Sma04] N.J. Smale, *Multi-Anode Photon-Multiplier Readout Electronics for the LHCb Ring Imaging Cherenkov Detectors*, Ph.D. thesis, University of Oxford, 2004. 44, 45

[SQ93] A. E. Snyder and H. R. Quinn, *Measuring CP asymmetry in $B \to \rho\pi$ decays without ambiguities*, Phys. Rev. D **48** (1993), 2139. 26

[T+53] R. W. Thompson et al., *The Disintegration of V_0 Particles*, Phys. Rev. **90** (1953), 329. 94, 96

[tar04] *Hera-B Target Homepage* , http://www-hera-b.desy.de/subgroup/detector/target/, 2004. 12

[vB06] M. van Beuzekom, *Identifying fast hadrons with silicon detectors*, Ph.D. thesis, Rijksuniversiteit Groningen, 2006. 44

[vE04] C. van Eldik, *$K^{*0}(892)$ production in proton-nucleus collisions*, Ph.D. thesis, Universität Dortmund, 2004. 77

[Wei95] S. Weinberg, *The quantum theory of fields, volume I: Foundations*, Cambridge University Press, 1995. 2

[Wol83] L. Wolfenstein, *Parametrization of the Kobayashi-Maskawa Matrix*, Phys. Rev. Lett. **51** (1983), 1945. 6

[Won94] C.-Y. Wong, *Introduction to High-Energy Heavy-Ion Collisions*, World Scientific, 1994. 81, 82

[WS50] C.S. Wu and I. Shaknov, *The Angular Correlation of Scattered Annihilation Radiation*, Phys. Rev. **77** (1950), 136. 2

[Z+00] J. Zimányi et al., *Quark liberation and coalescence at CERN SPS*, Phys. Lett. **B 472** (2000), 243. 84

[Z+01] J. Zimanyi et al., *Hyperon ratios at RHIC and the coalescence predictions at mid-rapidity.* 85

Danksagung

Mit einem lachenden und einem weinenden Auge blicke ich nun zurück auf die Jahre meiner Doktorarbeit am MPI für Kernphysik, gespannt auf all das Neue, aber gleichzeitig ein wenig traurig über Vieles, das ich zurücklassen muss. Herzlichen Dank an

Prof. Michael Schmelling für die Möglichkeit, meinen Horizont durch die Arbeit auf zwei Themengebieten zu erweitern, für die gewährte Freiheit, meine eigenen Fehler zu machen sowie für die Unterstützung, selbige zu beheben, kurz gesagt, für eine sehr angenehme Betreuung in all der Zeit,

Prof. Werner Hofmann für die Übernahme des Zweitgutachtens und die spontane Bereitschaft, zu Prüfung nach Dortmund zu fahren,

Mikhail Zavertiaev for sharing his experience in data analysis and his russian humour with me, Brigitte Villaumie für die willkommenen Ablenkungungen in Form von Gesprächen oder CDs,

Bernhard Schwingenheuer für all den Beistand in technischen Fragen,

Johan Blouw, Helge Voss und Christian Bauer für die gemeinsam erfolgreich gemeisterten Testbeams,

Sven Löchner für die Umsichtigkeit, bei Mountainbiketouren immer ein Erste-Hilfe-Set dabei zu haben,

Nigel Smale and Florin Maciuc for endless, mostly fruitless but very exhilarating discussions about english grammar, latin roots and cineastic highlights,

Thomas Kihm für seine partielle Geistesverwandschaft,

meinen Eltern für den starken Rückhalt, der mir viel Kraft gegeben hat, und ihren Humor

und meinem Freund Mike Bernhardt für all seine liebevolle Unterstützung, Aufmunterung und die gemeinsame Freude, für seine Sorge und seine ironischen Seitenhiebe auf uns "verrückte Physiker"...